Universidad Politécnica de Valencia
Departamento de Comunicaciones

Coupling techniques between dielectric waveguides and planar photonic crystals

Pablo Sanchis Kilders

Director: Dr. Javier Martí Sendra

Tesis Doctoral presentada en la Universidad Politécnica de Valencia para la obtención del título de Doctor Ingeniero de Telecomunicación

Valencia, Febrero 2005

Contents

Abstract

The aim of this work is to investigate coupling techniques and structures to minimize the coupling losses between dielectric waveguides and planar photonic crystals circuits. The modeling of the coupling between dielectric and photonic crystal waveguides has been carried out. Closed form expressions for the reflection and transmission matrices that completely characterize the scattering that occurs at the interface between dielectric and photonic crystal waveguides have been derived. The influence of the main parameters of the photonic crystal on the coupling efficiency has also been analyzed. To improve the coupling efficiency from both narrow and broad dielectric waveguides, a novel coupling technique based on setting a number of localized defects within a discrete photonic crystal taper has been proposed. Different approaches, including genetic algorithms, have been reported to design the optimum configuration of defects. Once efficient coupling from dielectric waveguides into photonic crystal waveguides has been achieved, efficient coupling into coupled-cavity waveguides has been pursued. An adiabatic coupling technique based on progressively varying the radii of the spacing defects between cavities has been proposed. Furthermore, a rigorous analysis of pulse propagation in frequency and time domains has been carried out for characterizing the influence of the coupling efficiency on the main parameters of the pulse. Finally, the fabrication and experimental demonstration of the proposed coupling techniques have been addressed.

Resumen

El objetivo de esta tesis es la investigación de estructuras y técnicas de acoplo para minimizar las pérdidas de acoplo entre guías dieléctricas y cristales fotónicos planares. En primer lugar se ha estudiado el modelado del acoplo entre guías dieléctricas y guías en cristal fotónico así como la influencia de los principales parámetros del cristal en la eficiencia de acoplo. Se han obtenido expresiones cerradas para las matrices de reflexión y transmisión que caracterizan totalmente el scattering que ocurre en el interfaz formado entre una guía dieléctrica y una guía en cristal fotónico. A continuación y con el fin de mejorar la eficiencia de acoplo desde guías dieléctrica de anchura arbitraria, se ha propuesto como contribución original una técnica de acoplo basada en la introducción de defectos puntuales en el interior de una estructura de acoplo tipo cuña realizada en el cristal fotónico. Diferentes soluciones, incluida los algoritmos genéticos, han sido propuestas con el objetivo de conseguir el diseño óptimo de la configuración de defectos. Una vez conseguido un acoplo eficiente desde guías dieléctricas a guías en cristal fotónico, se ha investigado el acoplo en guías de cavidades acopladas. Como contribución original se ha propuesto una técnica de acoplo basada en la variación gradual del radio de los defectos situados entre cavidades adyacentes. Además, se ha realizado un riguroso análisis en el dominio del tiempo y la frecuencia de la propagación de pulsos en guías acopladas de longitud finita. Dicho estudio ha tenido como objetivo la caracterización de la influencia de la eficiencia del acoplo en los parámetros del pulso. Finalmente, se han presentado los procesos de fabricación y resultados experimentales de las estructuras de acoplo propuestas.

Resum

L'objectiu d'esta tesi és la investigació d'estructures i tècniques d'acoblament per a minimitzar les pèrdues d'acoblament entre guies dielèctriques i cristals fotònics planars. En primer lloc s'ha estudiat el modelatge de l'acoblament entre guies dielèctriques i guies en cristal fotònic així com la influència dels principals paràmetres del cristal en l'eficiència d'acoblament. S'han obtingut expressions tancades per a les matrius de reflexió i transmissió que caracteritzen totalment el scattering que ocorre en l'interfície format entre una guia dielèctrica i una guia en cristal fotònic. A continuació i a fi de millorar l'eficiència d'acoblament des de guies dielèctrica d'amplària arbitrària, s'ha proposat com a contribució original una tècnica d'acoblament basada en la introducció de defectes puntuals en l'interior d'una estructura d'acoblament tipus falca realitzada en el cristal fotònic. Diferents solucions, inclosa els algoritmes genètics, han sigut proposades amb l'objectiu d'aconseguir el disseny òptim de la configuració de defectes. Una vegada s'ha aconseguit l'acoblament eficient des de guies dielèctriques a guies en cristal fotònic, s'ha investigat l'acoblament en guies de cavitats aclobades. Com a contribució original s'ha proposat una tècnica d'acoblament basada en la variació gradual del radi dels defectes situats entre cavitats adjacents. A més, s'ha realitzat una rigorosa anàlisi en el domini del temps i la freqüència de la propagació de polsos en guies adaptades de longitud finita. Tal estudi ha tingut com a objectiu la caracterització de la influència de l'eficiència de l'acoblament en els paràmetres del pols. Finalment, s'han presentat els processos de fabricació i resultats experimentals de les estructures d'acoblament proposades.

Preface

This work was carried out with the support of the Nanophotonics Technology Centre (NTC) within its nanophotonics research line. The NTC is the centre of photonic systems and technology in Spain and has been recently created as the hub for scientific research, technological development and innovation (R+D+I) in the field of advanced optical technologies and photonic systems for telecommunications and computing. Its mission is to explore and expand the existing knowledge, and to create and transfer technology to industry. The NTC facility is hosted by the Universidad Politécnica de Valencia at its Campus in Valencia city.

I would specially acknowledge the Spanish Ministry of Education, Culture and Sport for giving me the financial support for making this work possible. However, this work would not have been possible without the help of a number of people including all the one working in NTC, where I have enjoyed so many good moments. I would like to mention a number of people by their names hoping not to forget anyone.

First of all, I would like to give a special thank to the tutor of this work, Javier Martí, who gave me the opportunity to make this work and join the NTC, formerly Fiber-Radio Group. Thank you also to Alex, Jaime, Ico, Amadeo, Javi and recently Carlos for their fruitful discussions and for the stimulating work done together within the context of the nanophotonics research line. An additional thank to Javi for letting me supervise his master thesis. Thank you to Guillermo and Benito for their explanations of the fabrication process. I would also give a special thank to Jose Sánchez-Dehesa for his useful comments and to Andreas for collaborating in part of this work with his magic genetic algorithms. I can also not forget Andrés because of his help when I began my research in photonic crystals. Thank also to

Valentin for his corrections of this work and his useful comments and to Roberto and Rafa for ensuring that part of the used software in this work was always operative and updated.

I would also give special thank to Roel Baets for giving me the opportunity to join during six months the photonics research group at the University of Ghent (Belgium). Thank you, Peter, Bert, Wim, Pieter and Dirk for your fruitful discussions with special thank to Wim and Pieter for their time spent in the fabrication of my samples as well as for helping me during the first measurements. Of course, I will never forget all the people of the photonics research group that helped me in so many things during my stay in Ghent that made me feel like at home.

Finally, I would like to dedicate this thesis to my parents, brothers and sister, and especially Marian, who gave me the support and courage that I needed to finish this work.

Valencia, February 2005.

Chapter 1

Introduction

1.1 Motivation

The huge growth of data traffic during the last years is forcing next generation telecommunications networks to increase their capacity and performance. Basically, a telecommunication network consists of a number of nodes connected by links, as shown in figure 1.1. The information is first processed at the nodes and then transmitted through the appropriate link up to their final destination. Nowadays, almost all the links are optical connections whose key component is the optical fiber. Optical fibers offer a large range of benefits such as a high capacity, low propagation loss, immunity to electromagnetic interferences or low weight. Furthermore, optical fiber communications together with advanced multiplexing techniques such as wavelength division multiplexing (WDM) and optical time division multiplexing (OTDM) will permit to satisfy the growth of capacity demanded by the market [Blu03]. However, most of the processing functionalities performed at the nodes, such as routing and regeneration, are still performed in the electronic domain seriously limiting the maximum data rate achievable with fiber-based optical networks.

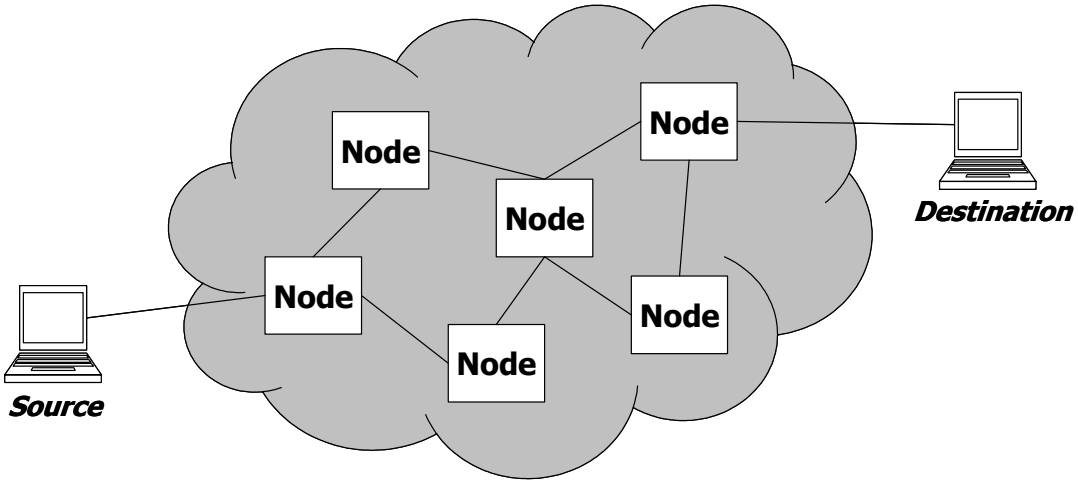

Figure 1.1.- Schematic of a telecommunications network. A number of nodes are connected by links. The information is first processed at the nodes and then transmitted through the appropriate link up to their final destination.

All-optical processing is therefore a must to avoid the bottleneck imposed by existing nodes based on an electronic processing. However, current photonic integrated circuits are not mature enough to replace microelectronics circuits, mainly because of their large size and relative simplicity. Recent results show that key components in photonic integrated circuits such as directional couplers and Mach–Zehnder interferometer have still lengths in the order of millimetres [Liu04]. Therefore, strong efforts are still needed to reduce the size of photonic integrated circuits.

Photonic crystals are expected to be one of the main candidates for the realization of highly integrated photonic integrated circuits because of their ability to control light propagation on a small scale [Joa97]. From their discovery till nowadays the research field related to photonic crystal has experienced an exponential interest. The initial expectation was so high that it was pointed out that photonic crystals could give rise to a technological revolution similar to that caused by semiconductors in the middle of the 20^{th} century.

Photonic crystals are periodic materials, typically dielectrics, in which the periodicity is on the order of the wavelength of light. The periodicity can extend into one, two or three dimensions. Several examples are shown in figure 1.2. In the left part, a one-dimensional (1D) photonic crystal is made by alternating layers of materials with different refractive indexes. In the middle part, a two-dimensional (2D) photonic crystal is made by circular shaped columns arranged in a periodic lattice. In the right part, a three-dimensional (3D) photonic crystal is made by an arrangement of dielectric spheres placed at each point of a periodic lattice.

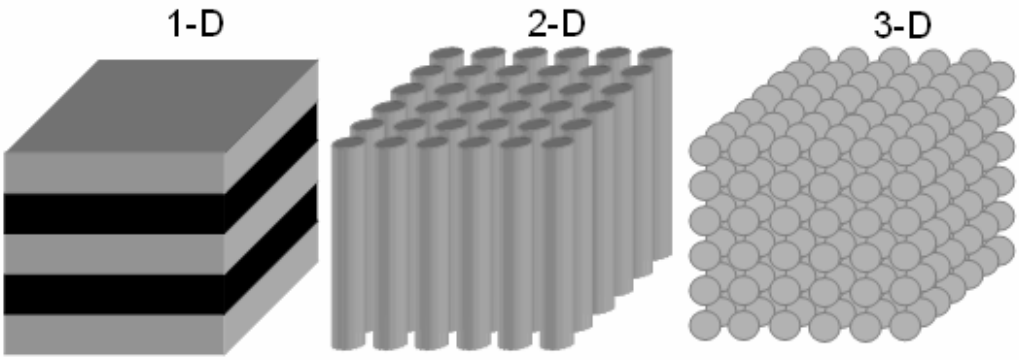

Figure 1.2.- Schematic of different kinds of photonic crystals, periodic materials, typically dielectrics, in which the periodicity is on the order of the wavelength of light. The periodicity can extend into one, two or three dimensions. In the left part, a one-dimensional (1D) photonic crystal is made by alternating layers of materials with different refractive indexes. In the middle part, a two-dimensional (2D) photonic crystal is made by circular shaped columns arranged in a periodic lattice. In the right part, a three-dimensional (3D) photonic crystal is made by an arrangement of dielectric spheres placed at each point of a periodic lattice.

The main feature that distinguishes photonic crystals from other photonic structures is that the periodicity of the material gives rise to a frequency region, known as the photonic band gap (PBG), where electromagnetic radiation is not allowed. The introduction of defects into the otherwise periodic structure gives rise to the appearance of localized modes inside the PBG. Thus, light is bound to the defect and can not radiate out of it due to the PBG effect. The simplest defect that can be created in a photonic crystal is the point defect, which has been used, for instance, to design high Q-value nano cavities [Joa97]. On the other hand, photonic crystal waveguides are implemented by creating line defects into the periodic structure.

In conventional dielectric waveguides, light propagation is due to the total internal reflection effect which restricts the minimum radius of curvature due to the radiation losses. Recent progress on high index contrast dielectric waveguides is giving rise to sharper bends [Man99]. However, 90-degree bends are only possible in photonic crystals where the excitation of radiation modes is forbidden [Mek96]. Such a feature has been one of the main reasons for justifying the capacity of photonic crystals to realize highly integrated photonic circuits. However, photonic crystals have also unique features such as a strong dispersion that can be used to implement novel functionalities as well as to enhance different phenomena such as the group delay, nonlinear effects or stimulated emission, which in turn implies an extra reduction of size.

In recent years, a large variety of functionalities based on photonic crystal structures have been reported. Furthermore, there has also been a considerable progress on the fabrication processes. However, there is still needed a great effort

to resolve several issues that permit the definitive industrial deployment of photonic crystal technology [Kra99]. Among them, the minimization of propagation losses and coupling losses between photonic crystal circuits and external media (fiber and dielectric waveguides) play a crucial role.

1.2 Objectives

The aim of this work is to investigate coupling techniques and structures to minimize the coupling losses between photonic crystal circuits and dielectric waveguides. A large variety of spot size converters have been developed in the past to resolve the mode mismatch between fibre and dielectric waveguides [see for e.g. Moe97]. Therefore, we have focussed on the coupling between dielectric and photonic crystal waveguides. Furthermore, efficient interfacing between dielectric and photonic crystal waveguides is also very important when photonic crystal circuits have to be inserted on a chip with other functional blocks implemented with conventional dielectric waveguides. The main objectives pursued in this work have been as follows:

- The modeling of the coupling between dielectric and photonic crystal waveguides and the influence of the main parameters of the photonic crystal on the coupling efficiency.
- The development of a novel coupling technique to improve the coupling efficiency from dielectric waveguides into line defect photonic crystal waveguides.
- The development of a novel coupling technique to improve the coupling efficiency into coupled-cavity waveguides.
- The fabrication and experimental demonstration of the proposed coupling techniques.

1.3 Outline of this work

The contents of this work are structured in seven chapters. In chapter 2, the fundamentals of photonic crystals are drawn. After a brief historical review of photonic crystals, light propagation in periodic media is described. Special emphasis is made in planar photonic crystals due to their easier fabrication at optical wavelengths. The modeling tools used along this work have also been described. Furthermore, the potential of photonic crystals to implement a large number of functionalities is analyzed.

In chapter 3, butt-coupling between narrow dielectric waveguides and single line defect photonic crystal waveguides is analyzed. Closed-form expressions for the reflection and transmission matrices are derived based on the mode matching

technique. Analytic expressions, validated by means of 2D simulations, are used to study coupling losses in two different kind of photonic crystals called rod and hole structures. In the former, the photonic crystal is formed by a lattice of high index rods surrounded by a material with lower refractive index while in the latter the photonic crystal is formed by an air hole lattice etched into a high refractive index material. Furthermore, it is shown that the obtained closed form expressions can also be used for analyzing coupling issues in more complex photonic crystals by means of a semi-analytic approach.

In chapter 4, a coupling technique between both narrow and broad dielectric waveguides and line defect waveguides is proposed and analyzed by means of 2D simulations. The coupling technique is based on the introduction of a number of localized defects within a photonic crystal taper. An initial approach has been proposed to design the optimum configuration of defects. However, when coupling from broader dielectric waveguides, larger photonic crystal tapers must be used that make much more complicated the design. Therefore, the usefulness of genetic algorithms to design the optimum configuration of defects has been proposed and assesed.

In chapter 5, an adiabatic coupling technique between conventional photonic crystal single line defect waveguides and coupled-cavity waveguides is proposed and analyzed by means of 2D simulations. Adiabatic coupling is achieved by progressively varying the radii of the spacing defects between cavities. Inefficient coupling into coupled-cavity waveguides can be a critical point in order to achieve an optimum dynamic performance because the propagation of ultra short pulses may be seriously distorted. Therefore, a rigorous analysis of pulse propagation in the frequency and time domains has been carried out.

In chapter 6, the experimental implementation of the coupling techniques proposed in chapter 4 and 5 is addressed. Two different planar photonic crystal structures based on a lattice of rods and air holes are considered. The fabrication processes for each structure are reviewed, although experimental results are only provided for the hole structure since fabrication of the rod structure is still under development. However, both structures have been analyzed by means of 3D finite-difference time-domain (FDTD) simulations and results have been compared to 2D FDTD simulations.

Finally, conclusions and future work are provided in chapter 7.

Chapter 2

Fundamentals of Photonic Crystals

2.1 The origin of photonic crystals

Photonic bands in a periodic arrangement of dielectric spheres were first discussed in 1979 by K. Ohtaka [Oht79]. However, the concept of photonic band gap was proposed in 1987 for the first time. E. Yablonovitch suggested that spontaneous emission could be inhibited in a dielectric medium with a periodic variation of the refractive index [Yab87]. In a different work also in 1987, S. John reported that strong localization of photons could occur in a predictable manner for a certain frequency range in particular disordered dielectric lattices [Joh87]. The term photonic band gap (PBG) was adopted in analogy to the electronic band gap ocurring in semiconductors. Just as a regular arrangement of atoms in a crystal gives rise to electronic band gaps, the periodicity of the spatial dielectric distribution in a photonic crystal gives rise to a frequency region where electromagnetic radiation is not allowed.

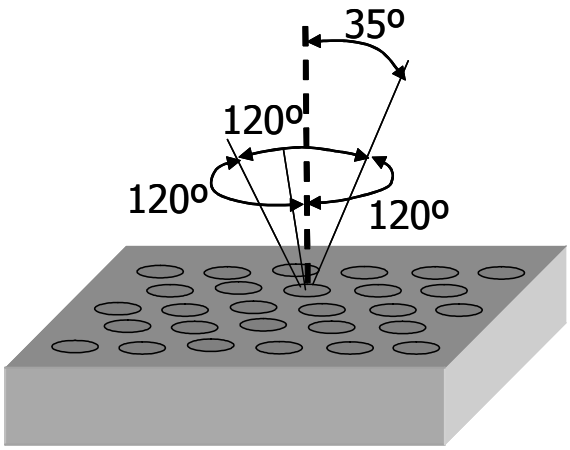

Figure 2.1.- The *Yablonovite*, first photonic crystal with a full three dimensional photonic band gap experimentally demonstrated in 1991. The structure is fabricated by drilling each hole of the lattice at three different angles separated 120 degree and 35 degree away from the normal. This results in a three dimensional structure with a diamond lattice.

The research after the works of E. Yablonovitch and S. John was intended to find a three-dimensional (3D) lattice that could allow a complete 3D PBG. The first choice was a face-centered cubic lattice of air spheres in a high-index dielectric material [Yab89]. Because of the lack of numerical tools for design, a number of structures were fabricated and tested with different filling factors and refractive indexes. For one of these structures, a 1 GHz bandwidth 3D PBG centered at 15 GHz was experimentally identified. These experimental results were later confirmed by two theoretical works [Leu90, Sat90]. However, after this apparent success several authors pointed out an inaccuracy in the theoretical procedure and showed that the PBG observed experimentally was only a pseudo-PBG, i.e. a PBG limited to a certain range of spatial directions [Leu90a, Zha90]. These disappointing theoretical results gave rise to some controversy but, in the end of 1990, the first structure that possessed a complete 3D PBG was discovered: the diamond lattice of dielectric spheres [Ho90]. The first experimental demonstration was reported in 1991 by E. Yablonovitch [Yab91]. The structure, later called as *Yablonovite* and illustrated in figure 2.1, consisted of a dielectric medium drilled along the three of the axes of the diamond lattice. This 3D structure showed a PBG for the transmission of microwave waves that extended from 13 GHz to about 15 GHz.

The microwave regime was initially chosen to fabricate photonic crystals owing to the easier fabrication and testing. However, it is in the optical regime where photonic crystals would find real applications that justify the interest that they had received. This imposed the adaptation of conventional semiconductor nanofabrication techniques to make photonic crystals. First experiments were carried out in the near infrared regime for two-dimensional (2D) photonic crystals.

Deeply etched structures were initially considered to overcome the lack of light confinement in the vertical direction [Grü95, Lin96]. However, this approach suffered large diffraction losses and a waveguide configuration was chosen to achieve light confinement [Kra96]. Following this approach, a one-dimensional (1D) photonic crystal that consisted of a series of tiny holes etched in a silicon strip was successfully demonstrated for optical communications wavelengths ($\lambda \sim 1.5\mu m$) in 1997 [For97].

Initial research on 3D photonic crystals was aimed to fabricate the *Yablonovite* structure at optical wavelengths [Che95]. However, the fabrication was too difficult and different approaches to make 3D photonic crystals were investigated. Layer by layer 3D photonic crystals formed by stacking one dimensional (1D) rods were demonstrated for silicon [Lin98, Fle99] and III-V semiconductor composites [Nod00]. Another promising approach was self-assembled colloidal 3D photonic crystals, which exploited the tendency of submicron spheres to spontaneously self-organize [Mig97, Bla00].

2.2 Light propagation in periodic media

2.2.1 Wave equations in mixed media

The propagation of light in electromagnetic periodic media is governed by Maxwell equations. For non conducting media without free charges these equations take the form

$$\nabla \times \mathbf{E}(r,t) = -\frac{\partial \mathbf{B}}{\partial t}(r,t) \tag{2.1}$$

$$\nabla \times \mathbf{H}(r,t) = \frac{\partial \mathbf{D}}{\partial t}(r,t) \tag{2.2}$$

$$\nabla \cdot \mathbf{D}(r,t) = 0 \tag{2.3}$$

$$\nabla \cdot \mathbf{B}(r,t) = 0 \tag{2.4}$$

where E and H are the electric and magnetic fields while D and B are the displacement and magnetic induction.

In order to solve the wave equations derived from Maxwell equations, the following so-called constitutive relations that relate D to E and B to H are needed

$$\mathbf{B}(r,t) = \mu_o \mathbf{H}(r,t) \tag{2.5}$$

$$\mathbf{D}(r,t) = \varepsilon_o \varepsilon(r) \mathbf{E}(r,t) \tag{2.6}$$

where μ_o is the magnetic permeability in free space, ε_o is the electric permittivity in free space and $\varepsilon(r)$ is the relative dielectric constant. Linear, isotropic and lossless no magnetic media are assumed as well as that there is no material dispersion. Therefore, the magnetic permeability is equal to that in free space and the electric permittivity is scaled by a scalar function which only depends on the spatial coordinate, r. With all these assumptions in place and substituting (2.5) and (2.6) into (2.1)-(2.4), the following wave equations are obtained

$$\frac{1}{\varepsilon(\mathbf{r})} \nabla \times \left\{ \nabla \times \mathbf{E}(r,t) \right\} = -\frac{1}{c^2} \frac{\partial^2}{\partial t^2} \mathbf{E}(r,t) \tag{2.7}$$

$$\nabla \times \left(\frac{1}{\varepsilon(\mathbf{r})} \nabla \times \mathbf{H}(r,t) \right) = -\frac{1}{c^2} \frac{\partial^2}{\partial t^2} \mathbf{H}(r,t) \tag{2.8}$$

where c stands for the light velocity in free space:

$$c = \frac{1}{\sqrt{\varepsilon_0 \mu_0}} \tag{2.9}$$

In general, both E and H are complicated functions of time and space. However, since Maxwell equations are linear, the time dependence can be separated out by expanding the fields into a set of harmonic modes and remembering to take the real part to obtain the physical fields. The harmonic modes can be written as

$$\mathbf{H}(\mathbf{r},t) = \mathbf{H}(\mathbf{r}) e^{j\omega t} \tag{2.10}$$

$$\mathbf{E}(\mathbf{r},t) = \mathbf{E}(\mathbf{r}) e^{j\omega t} \tag{2.11}$$

where ω is the angular frequency. Using (2.10) and (2.11) into the wave equations (2.7) and (2.8) results in

$$\zeta_E \mathbf{E}(\mathbf{r}) \equiv \frac{1}{\varepsilon(\mathbf{r})} \nabla \times \{\nabla \times \mathbf{E}(\mathbf{r})\} = \left(\frac{\omega}{c}\right)^2 \mathbf{E}(\mathbf{r}) \tag{2.12}$$

$$\zeta_H \mathbf{H}(\mathbf{r}) \equiv \nabla \times \left(\frac{1}{\varepsilon(\mathbf{r})} \nabla \times \mathbf{H}(\mathbf{r})\right) = \left(\frac{\omega}{c}\right)^2 \mathbf{H}(\mathbf{r}) \tag{2.13}$$

where the two differential operators ζ_E and ζ_H are defined by the first equality in each of the above equations. The eigenvector *E(r)* and *H(r)* are the field patterns of the harmonic modes while the eigenvalues $(\omega/c)^2$ are proportional to the squared frequencies of these modes.

2.2.2 Light propagation in homogeneous media

In homogeneous media, the relative dielectric constant, *ε(r)*, takes a constant value, *ε*. Therefore, the wave equations can be simplified to

$$\nabla^2 \mathbf{E}(\mathbf{r}) + n^2 \left(\frac{\omega}{c}\right)^2 \mathbf{E}(\mathbf{r}) = 0 \tag{2.14}$$

$$\nabla^2 \mathbf{H}(\mathbf{r}) + n^2 \left(\frac{\omega}{c}\right)^2 \mathbf{H}(\mathbf{r}) = 0 \tag{2.15}$$

where *n* is the refractive index obtained as the root square of the relative dielectric constant. These wave equations are usually expressed as

$$\nabla^2 \mathbf{E}(\mathbf{r}) + k^2 \mathbf{E}(\mathbf{r}) = 0 \tag{2.16}$$

$$\nabla^2 \mathbf{H}(\mathbf{r}) + k^2 \mathbf{H}(\mathbf{r}) = 0 \tag{2.17}$$

where *k* is called the wave number which is linearly dependent on *ω*:

$$k = n \frac{\omega}{c} \tag{2.18}$$

The above equation is called the *dispersion relation* that depends on the homogeneous medium through the refractive index. Therefore, the wavelength *λ* of the wave propagated through the medium depends on the free space wavelength λ_0 through the refractive index by

$$\lambda = \frac{\lambda_0}{n} \tag{2.19}$$

The general solution of (2.16) and (2.17) is a set of plane waves whose simplest solution for the electric field is given by

$$\mathbf{E}(\mathbf{r}) = \mathbf{E}_0 e^{j\mathbf{k}\cdot r} \tag{2.20}$$

where E_0 is a complex value, which describes the amplitude and phase of the plane wave, and **k** is the wave vector, which indicates the propagation direction of the wave and whose magnitude is the wave number. A monochromatic plane wave propagates at the velocity of ω/k. However, when the plane wave is modulated by a signal, this velocity is known as the phase velocity. The phase velocity, v_p, indicates the velocity that the phase fronts are propagated. On the other hand, the group velocity is defined as the velocity that the energy is propagated. The group velocity is calculated as

$$v_g = \frac{\partial \omega}{\partial k} \tag{2.21}$$

In linear, isotropic and homogeneous media, the phase velocity will equal the group velocity, $v_p=v_g$, however, this is no longer valid when the dielectric medium becomes periodic.

2.2.3 Light propagation in 1D periodic media

The simplest possible photonic crystal consists of alternating layers of materials with different refractive indexes, n_1 and n_2, which can have different thickness, d_1 and d_2, but the same periodicity of a, being $a = d_1 + d_2$ the lattice constant. This one-dimensional (1D) periodic structure is depicted in figure 2.2. The traditional approach for analyzing this structure is to allow a plane wave to propagate through the material and to consider the multiple reflections that take place at each interface. In this case, it can be obtained that the structure act as a perfect mirror for a certain wavelength range near $\lambda=2m(d_1n_1+d_2n_2)$, where m is an integer number. This condition is called the Bragg condition and therefore the structure shown in figure 2.2 is usually known as a Bragg mirror [Yeh98]. However, the properties of Bragg mirrors can also be analyzed following a different approach based on the analysis of the dispersion relation or, in other words, the band diagram. We will focus on this approach since it will permit us to further analyze the more complex two- and three-dimensional periodic media.

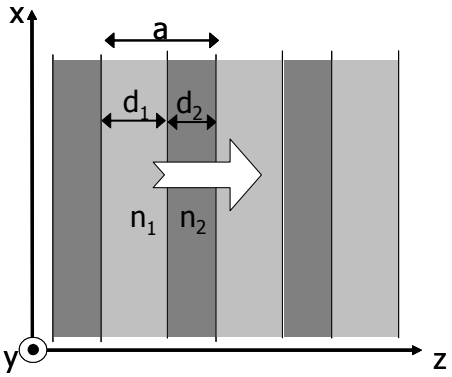

Figure 2.2.- One dimensional photonic crystal formed by alternating layers of materials with different refractive indexes, n_1 and n_2, and different thickness, d_1 and d_2, but with the same periodicity of a, being $a = d_1 + d_2$ the lattice constant.

In 1D periodic media, the solution of the wave equations (2.12) and (2.13) takes the form of a plane wave, as it would be in homogeneous media, but modulated by a periodic function $u_k(z)$ with the same periodicity of the periodic structure, i.e. $u_k(z) = u_k(z+a)$:

$$\mathbf{E}(z) = u_k(z)e^{j\mathrm{k}\cdot z} \tag{2.22}$$

This result is usually known as the *Bloch theorem* since it was proved by F. Bloch in 1928 when he studied wave propagation in three dimensional periodic structures [Blo28], unknowingly extending a similar theorem in one dimension proposed by G. Floquet in 1883 [Flo83].

One dimensional periodic structures are homogeneous in the plane perpendicular to the direction of periodicity. Therefore, the wave vector in these directions can take any value due to the continuous translational symmetry. However, let us consider that light propagation is in the direction of periodicity, i.e. the z-direction for the particular case shown in figure 2.2, so the wave vectors in the xy-plane are zero. One important attribute about Bloch states is that the solution with wave vector k_z, is identical from a physical point of view to the solutions with wave vector k_z+mG, where m is an integer number and $G=2\pi/a$ is known as the reciprocal lattice constant. Hence, the Bloch state may be considered as an infinite number of spatial harmonics with propagation constants separated by the reciprocal lattice constant. All these spatial harmonics that make up the Bloch state have multiple phase velocities but they propagate all together with the same group velocity. In the same way, the frequencies of the Bloch state are also periodic in k_z, i.e. $\omega(k_z) = \omega(k_z+mG)$. Therefore, it is only needed to consider k_z to exist in the range $-\pi/a < k_z \leq \pi/a$. This region is called the *first Brillouin zone* and can be further reduced to $0 < k_z \leq \pi/a$, the *irreducible Brillouin zone*, because of the reciprocity of Maxwell equations.

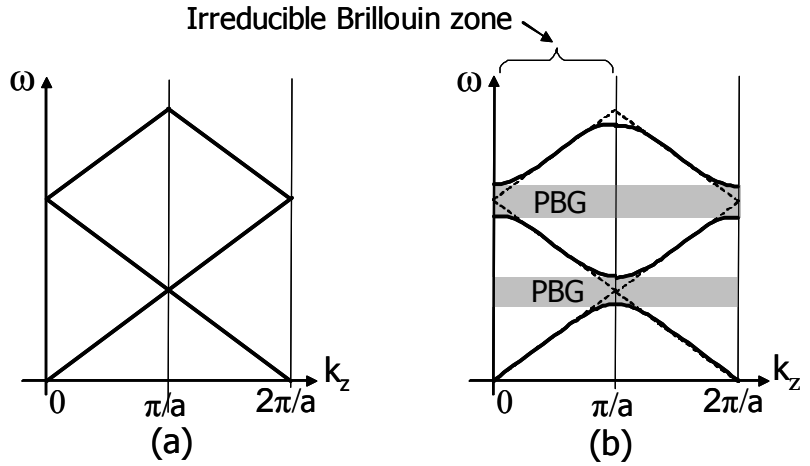

Figure 2.3.- Dispersion relation for (a) a homogeneous material and (b) a 1D periodic structure formed by two layers of alternating refraction indexes. In the periodic structure the dispersion line is split at the band edges giving rise to ranges of frequencies, called the *photonic bad gap* (PBG), in which no mode, regardless of k_z, can exist in the structure.

Figure 2.3(a) shows the dispersion relation, $\omega_n(k_z)$, of an homogeneous material while figure 2.3(b) shows the dispersion relation of a 1D periodic structure formed by two layers of alternating refraction indexes. In the former, an artificially periodicity of a has been assigned and therefore the dispersion line is folded back when it reaches the edges of the irreducible Brillouin zone. However, in the 1D periodic structures the dispersion line is split at the band edges, $k_z=0$ and $k_z=\pi/a$, giving rise to ranges of frequencies in which no mode, regardless of k_z, can exist in the structure. This frequency range is called the *photonic bad gap* (PBG) and is originated because the modes at the band edges are mixed each other in the presence of the periodic structure resulting in a frequency splitting. The PBG is generally larger when the index contrast between the alternating layers of the periodic structure is higher [Joa95].

2.2.4 Light propagation in 2D periodic media

A two-dimensional (2D) photonic crystal is a periodic dielectric medium along two of its axes being homogeneous along the third axis. The plane of periodicity is determined by the primitive lattice vectors that form the basic cell. The primitive lattice vectors are defined as the smallest vectors pointing from one lattice point to another. Therefore, any point of the plane can be obtained by an integer linear combination of the lattice vectors. Figures 2.4(a) and 2.4(b) show a cross section in the plane of periodicity of the most common lattices used in photonic crystals. Circular shaped columns are arranged in a triangular lattice for the former and in a square lattice for the latter. The dashed line shows the basic cell corresponding to each lattice. The lattice vectors, a_1 and a_2, in both lattices have the same modulus, a, but different directions.

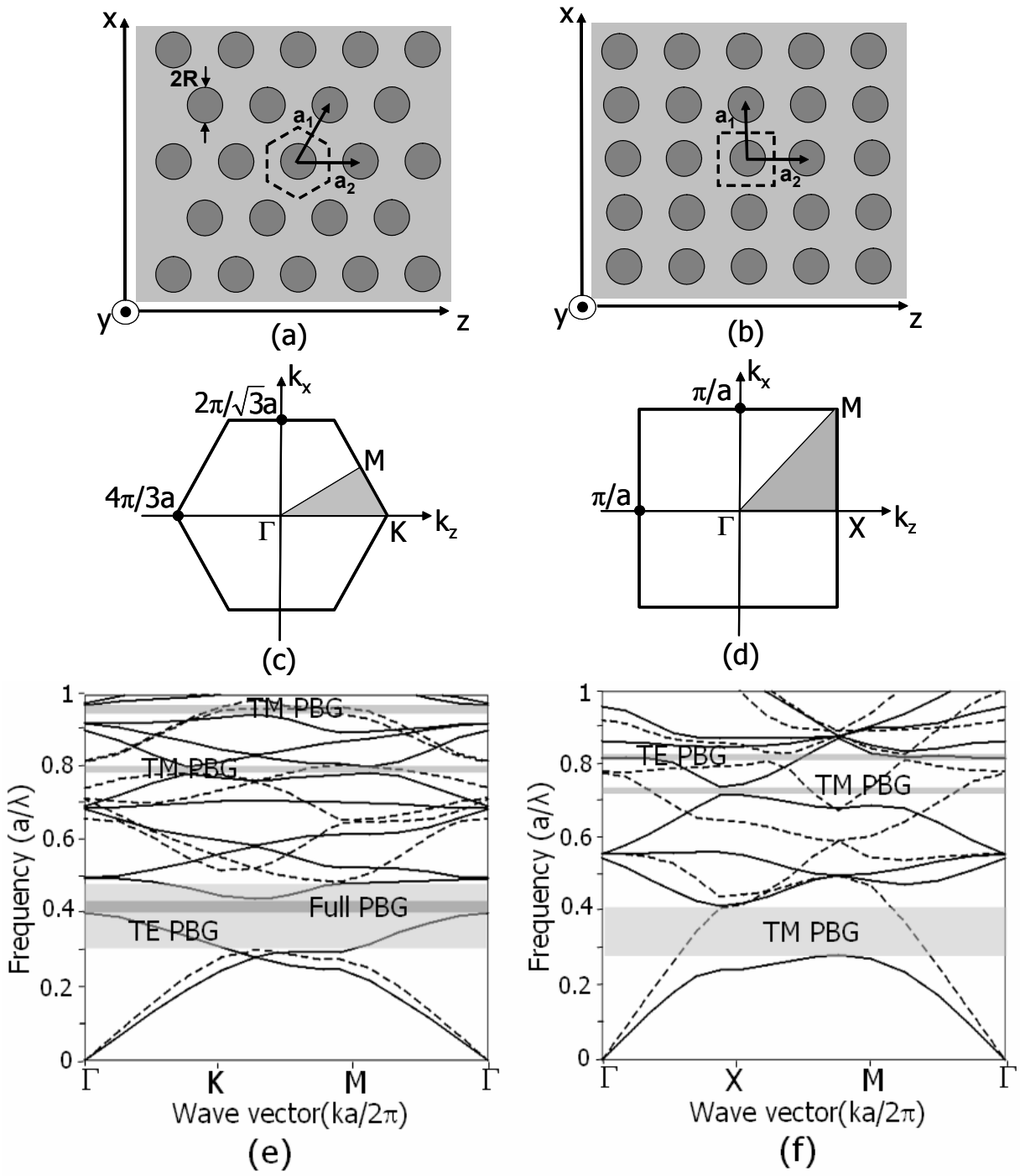

Figure 2.4.- (a) Triangular and (b) square lattices and their corresponding (c) hexagonal and (d) square shaped Brillouin zones. The band diagram is shown (e) for a triangular lattice of air holes with R=0.45a etched in a high-index material with n=3.45 and (f) for a square lattice of dielectric rods with n= 3.45 and R=0.2a embedded in air. The solid lines depict the propagating modes with TM polarization and the dashed lines depict the propagating modes with TE polarization.

Let us assume that the homogeneous direction is in the *y*-axis while the plane of periodicity is the *xz*-plane. In this case, the Bloch theorem gives us a similar solution of the wave equations as the one given for 1D periodic media expressed in (2.22). The function $u_k(\mathrm{r})$ is now periodic in the *xz*-plane but homogeneous in the *y*-direction. If light propagation is assumed to be in the plane of periodicity, the wave vector component in the *y*-direction will be zero, k_y=0. As occurs in 1D periodic media, the analysis of the *k* values is also restricted to the irreducible Brillouin zone.

The first Brillouin zones for the triangular and square lattices are shown in figures 2.4(c) and 2.4(d) respectively. It can be seen that the Brillouin zone has a hexagonal shape in the former while a square shape in the latter. In both cases, the shape of the Brillouin zone in the reciprocal space coincides with the shape of the basic cell in the real space. However, the Brillouin zone corresponding to the triangular lattice is rotated by 90 degrees with respect to the basic cell. The irreducible Brillouin zone corresponds to the highlighted region and is usually defined by the Γ, *M* and *X* points in the square lattice and by the Γ, *M* and *K* points in the triangular lattice. The frequency as a function of the wave vector, i.e. the band diagram, is only represented along the edge of the irreducible Brillouin zone, from Γ to *M* to *X* (*K*). The mirror symmetry of the structure permits to classify the modes by separating them into two uncoupled polarizations. The transverse-electric modes, *TE polarization*, have the magnetic field normal to the plane of periodicity and the electric field in the plane, (E_x, E_z, H_y). The transverse-magnetic modes, *TM polarization*, have just the reverse: the electric field normal to the plane of periodicity and the magnetic field in the plane, (H_x, H_z, E_y).

Figure 2.4(e) shows the band diagram for a triangular lattice of air holes etched in a high-index material. The solid lines correspond to the propagating modes with TM polarization and the dashed lines correspond to the propagating modes with TE polarization. A PBG appears for the TE polarization between the first and second band. Furthermore, narrower PBGs for TM polarization appear at higher frequencies. Figure 2.4(f) shows the band diagram for a square lattice of dielectric rods in air. In this case, the PBGs are mostly given for the TM polarization. It can be obtained that TM PBGs are usually predominant in high index rods lattices while TE PBGs are predominant in air holes lattices [Joa95].

In figure 2.4(e) it can be seen that there is also a PBG for the TM polarization between the first and second bands that overlaps with the TE PBG. The frequency range where the periodic structure has a PBG for both the TE and TM polarizations is called a *full photonic bandgap*. In this frequency range any propagating mode regardless of its polarization will be allowed inside the periodic structure. For practical applications, it is desirable to have the widest possible full PBG. To

achieve this goal, the PBG for both polarizations should be wide enough and centred at a similar frequency. Just as in 1D periodic media, the PBG is enlarged by increasing the index contrast of the periodic structure. On the other hand, the central frequency of the PBG can be controlled by varying the radius of the columns as well as the geometry of the lattice. A rounded shape of the Brillouin zone contributes to the appearance of full PBGs [Vil92]. Therefore, a larger full PBG is easier achieved by a triangular lattice rather than by a square lattice.

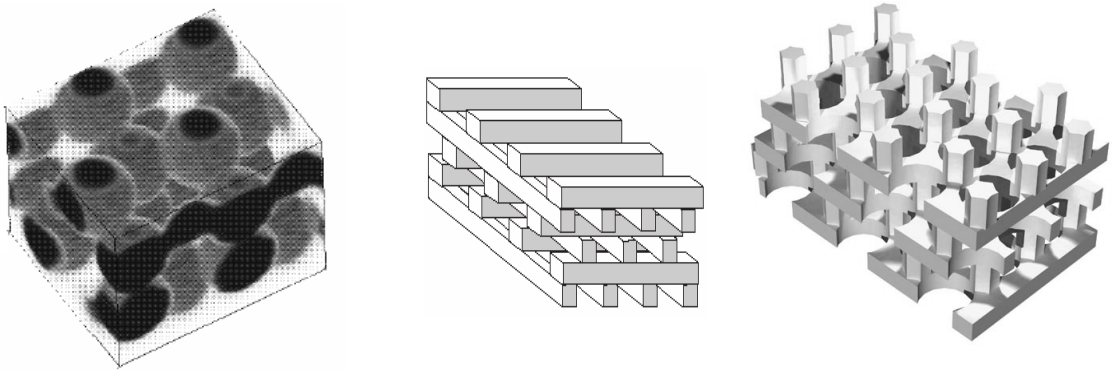

Figure 2.5.- Examples of three-dimensional periodic structures. From left to right, self-assembled colloidal spheres, a layer by layer structure and a sequence of planar layers with an horizontal offset.

2.2.5 Light propagation in 3D periodic media

Full control of light propagation by means of the PBG effect can only be achieved with three-dimensional periodic media. In this case, the structure is periodic along the three dimensions and light propagation can be forbidden in any spatial direction. There are a large number of possible geometries for realizing 3D periodic media. As in 2D periodic structures, the optical properties are analyzed from the band diagram calculated in the irreducible Brillouin zone. However, the Brillouin zone is a 3D figure that makes difficult its interpretation. The ability to confine light in three dimensions results of great interest to quantum optics and quantum-optical devices. For instance, the localization of light to a fraction of a cubic wavelength may permit the realization of efficient single-mode light-emitting diodes [Kra99].

The first experimental demonstration of photonic crystals was carried out in the microwave regime using a 3D structure [Yab89]. The structure consisted of a dielectric medium drilled along the three of the axes of a diamond lattice, which was the first geometry analyzed to achieve a full 3D PBG [Ho90]. However, the fabrication of this structure for optical wavelengths was too difficult and different approaches were investigated [Che95].

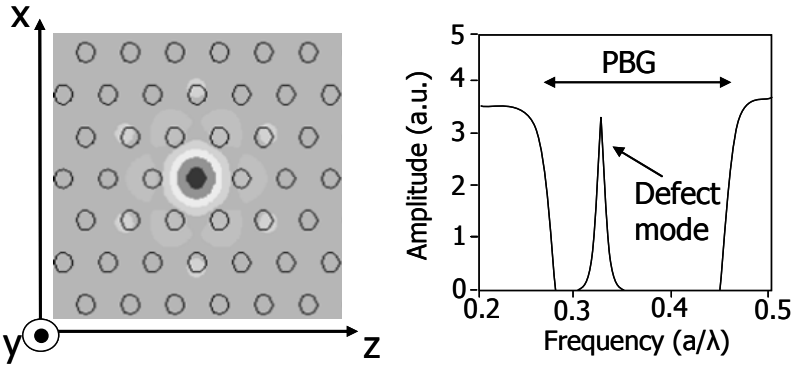

Figure 2.6.- Point defect created by removing a single column from the crystal that introduces a localized defect mode within the PBG in the transmission spectrum.

One of the most promising approaches is the self assembly of colloidal spheres placed at each lattice point [Bla00, Vla01], as shown in the left part of figure 2.5. The strategy behind this approach is to exploit the tendency of submicron spheres to spontaneously organize on a face-centred cubic lattice. The resulting material acts as a template into which a semiconductor material is infiltrated. The removal of the template leads to a 3D photonic crystal, known as inverted opal, which has a periodic arrangement of air spheres embedded inside the semiconductor.

There have also been alternative approaches like the layer by layer 3D photonic crystals shown in middle part of figure 2.5. This so-called woodpile structure consists of layers of one dimensional rods with a stacking sequence that repeats itself every four layers [Lin98, Fle99, Nod00]. A similar structure that has been proposed to achieve a full 3D PBG is shown in the right part of figure 2.5. In this case, the 3D periodic structure is made by a sequence of planar layers with an horizontal offset and repeated every three layers to form the lattice [Joh00].

2.2.6 Defects in photonic crystals

Previously, we have seen that infinite periodic structures could be conveniently designed to achieve a PBG so that no modes are allowed with frequencies inside this region. However, the introduction of defects that break the translational symmetry of the periodic structure may permit the existence of a localized mode or a set of closely spaced modes inside the PBG [Joa95].

The simplest defect that can be created in a photonic crystal is the point defect. Point defects can be created by removing or changing a single column from the crystal. Thus, localized defect modes may appear within the PBG in the transmission spectrum. An example is shown in figure 2.6.

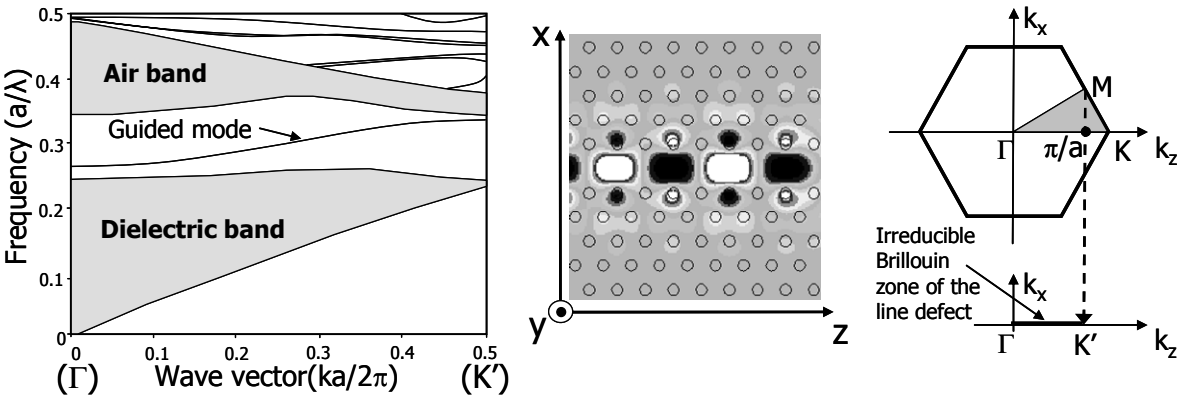

Figure 2.7.- Line defect created by removing a row of columns in the Γ*K* direction of a 2D photonic crystal formed in a triangular lattice of rods with R=0.2a and n=3.45 in a surrounding medium with n=1.45. The band diagram is shown in the left part in which the grey area depicts the projected band structure of the perfect 2D crystal. The projected band structure is calculated by projecting the reciprocal lattice of the photonic crystal into the reciprocal lattice of the line defect structure as depicted in the right part.

It can be seen that the light is trapped inside the point defect since light propagation is not allowed out of the defect. Therefore, point defects may be used in designing high Q-value nano cavities [Joa97].

Line defects can also be created by removing or changing one or more rows of columns into the otherwise periodic structure. By creating line defects well confined guided modes may appear inside the PBG. Therefore, a waveguide is created where light can only propagate back and forth along the line defect. Thus, light can also be guided around sharp bends as the radiation of energy in the cladding is prohibited [Mek96]. The ability of controlling the light in such a small scale has been one of the main reasons that has boosted the attraction on photonic crystals to develop micro scale photonic integrated circuits.

The introduction of line defects may also be analyzed by using the band diagram. However, line defects break the periodicity in one spatial direction so the Brillouin zone changes with respect to that of the original periodic structure. The band diagram for a line defect created along the Γ*K* direction is shown in figure 2.7. The grey area depicts the projected band structure of the perfect 2D crystal. This region contains the continuum of states that are extended in the surrounding crystal and it is calculated by projecting the reciprocal lattice of the perfect crystal into the reciprocal lattice of the line defect structure [Joh00a]. The edge of the Brillouin zone is the *K'* point, which is the projected image of the *M* point of the perfect crystal into the Γ*K* direction and therefore has a lower value than the *K* point of the perfect crystal, as depicted in the right part of figure 2.7.

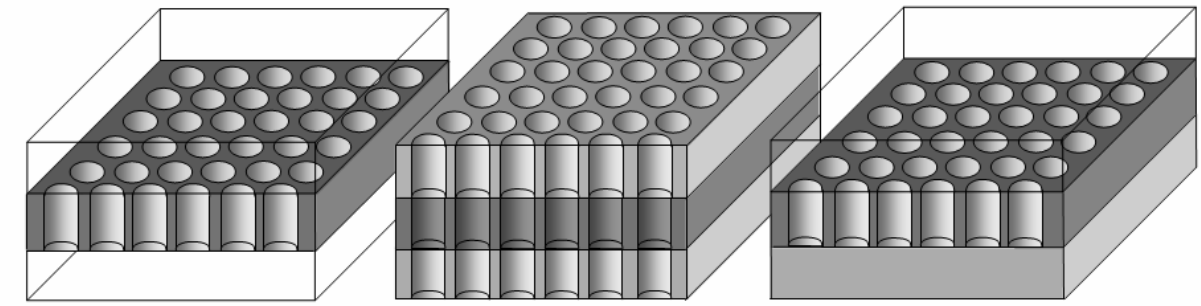

Figure 2.8.- Planar photonic crystals, also known as photonic crystal slabs, combine 2D photonic crystals with a slab waveguide in the vertical direction. They can be formed with uniform materials as claddings above and below the slab core, as shown in the left part, or with claddings with the same periodicity than the core but with a lower effective index, as shown in the middle part. On the other hand, it is also possible to have an asymmetric structure, as shown in the right part, in which the lower and upper claddings have different refractive indexes.

The band above the PBG is usually referred as the air band because the modes located at high frequencies concentrate their energy around the material with lower index. On the other hand, the band below the PBG is usually referred as the dielectric band because the modes located at the low frequencies concentrate their energy around the material with higher index [Joa95]. Therefore, the introduction of defects into the otherwise periodic structure can be distinguished in the form of either adding or removing a certain amount of dielectric material. Adding dielectric material pulls modes from the air band into the PBG while removing dielectric material pulls modes from dielectric band into the PBG [Yab91].

2.3 Planar photonic crystals

Although 3D photonic crystals can control light in the three dimensions, they are very difficult to fabricate at optical wavelengths. Therefore, *planar photonic crystals*, also known as *photonic crystal slabs*, have been proposed to allow an easier fabrication by using the current planar processing technologies developed by the microelectronics industry [Kra96, Joh99, Cho00].

Planar photonic crystals combine 2D photonic crystals with a slab waveguide in the vertical direction. Therefore, index confinement is used to bind the light in the third dimension. Several examples are shown in figure 2.8. This configuration has obvious advantages, such as growth of layered structures by established epitaxial methods. There are, however, several issues that need to be addressed when designing the structure. Among them, the vertical symmetry of the structure, the slab thickness and the index contrast between the slab core and the claddings will play a prominent role in determining the properties of planar photonic crystals.

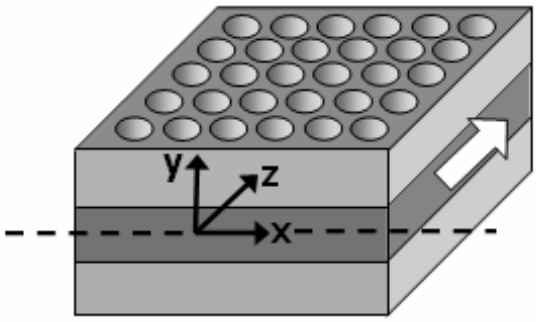

	E_x, E_z, H_y	H_x, H_z, E_y
Even modes (TE-like)	even	odd
Odd modes (TM-like)	odd	even

Figure 2.9.- The table shows the definition of the even and odd modes in terms of the individual electromagnetic fields components. Even or odd is defined with respect to the mirror horizontal plane, shown with a dashed line in the above figure, bisecting the symmetric planar photonic crystal. The horizontal plane is defined by the x- and z-axes and the vertical dimension is defined by the y-axis.

2.3.1 Influence of vertical symmetry on polarization

For 2D photonic crystal, the electromagnetic fields can be decoupled into two transversely polarized modes, the TE modes and the TM modes. However, the polarization in planar photonic crystals can not be so clearly defined because the structure becomes inhomogeneous in the vertical direction. Therefore, the symmetry or asymmetry of the structure in the vertical direction has a large influence on the polarization [Joh99, Qiu02].

In planar photonic crystals, the modes that are symmetric with respect to the horizontal plane bisecting the slab have a strong similarity to the modes that are originated in unperturbed slab waveguides. Guided modes in unperturbed slab waveguides are classified into TE and TM modes in spite of the slab symmetry. However, the modes can also be classified as even or odd modes according to their symmetry with respect to the horizontal mirror plane bisecting the slab. For the fundamental TE and TM modes, even modes correspond to TE modes while odd modes correspond to TM modes. This correspondence changes for higher order modes.

In symmetric planar photonic crystals, modes can not be considered as purely TM or TE polarized due to the lack of translational symmetry. However, modes can still be classified into even and odd modes that do no interact between them. Even and odd modes are usually called TE-like and TM-like respectively for the

fundamental mode. In fact, even and odd modes are purely TE and TM modes at the mirror plane itself. Figure 2.9 depicts the definition of the even and odd modes in terms of the individual electromagnetic fields components.

On the other hand, it is also possible to have an asymmetric structure in the vertical direction so that, for instance, the lower and upper claddings have different refractive indexes, as shown in the right part of figure 2.8. In these structures, the guided modes can no longer be classified as even or odd modes and they couple to each other due to the symmetry breaking. However, it is still possible to distinguish them as TE-like and TM-like when the guided modes are tightly confined in the slab core [Qiu02].

2.3.2 The light cone

A new band diagram analysis becomes necessary when planar photonic crystals are taken into account due to the finite height of the structure. The band diagram calculated for the corresponding 2D photonic crystal is no longer valid as only states that have no wave vector in the vertical direction are considered. The introduction of the third direction requires the inclusion of vertical wave vectors that produces a continuum of states which is called the *light cone*. The light cone consists of radiation modes that are extended infinitely in the region outside the slab.

However, a discrete number of guided modes can still exist below the light cone [Joh99]. These guided modes can not couple to the radiation modes above the light cone unless the periodicity of the structure is broken. The lower boundary of the light cone, which determines the boundary between guided and radiation modes, is called the *light line*. In case of having a uniform material above and below the slab core, the light line is simply the modulus of the wave vector divided by the refractive index. The refractive index must be lower than the averaged index of the slab core in order to confine the light in the vertical direction.

On the other hand, a material with the same periodicity but with a lower effective index may also be used to confine the light in the slab core. This configuration is depicted in the middle part of figure 2.8. In this case, the light line is the lowest band of the dispersion relation calculated for the corresponding 2D photonic crystal structure used in the cladding [Joh99]. Such a structure has the advantage that both slab core and claddings could be etched at the same time. It is also possible to have an asymmetric structure in the vertical direction, for instance if the lower and upper claddings have different refractive indexes. In this case, the light cone is calculated as the more restrictive of the two light cones imposed by each cladding.

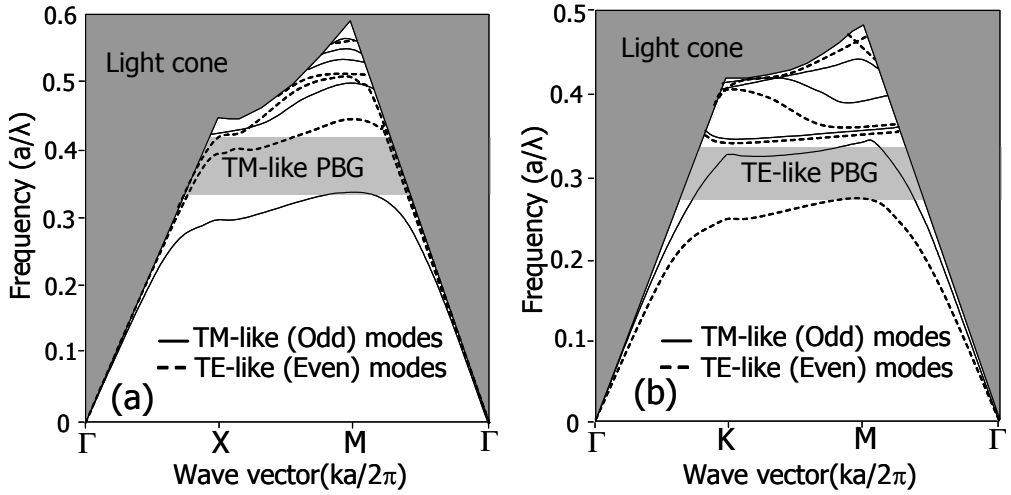

Figure 2.10.- Band diagrams of a planar photonic crystal formed by (a) a square lattice of dielectric rods with n=3.45, R=0.2a in air and (b) a triangular lattice of air holes with R=0.3a etched in a medium with n=3.45. The slab core thickness is 2a in the former and 0.5a in the latter.

Figure 2.10(a) shows the band diagram for a planar photonic crystal formed by a square lattice of dielectric rods in air while figure 2.10(b) shows the band diagram for a triangular lattice of air holes in a dielectric medium. The structure is symmetric in the vertical direction since an air cladding is considered above and below the slab. The slab core thickness is chosen so that it is not too small, because then guided modes will be weakly confined, or too large, because then higher-order modes will fill the PBG. The optimum thickness is around half a wavelength relative to an averaged index that depends on the polarization [Joh99].

Just like in 2D photonic crystals, TM-like PBGs are predominant in rod lattices while TE-like PBGs are predominant in air holes lattices. However, it should be pointed out that the PBG can not be considered anymore as a true PBG because there are radiation modes at every frequency due to the light cone. The presence of these radiating modes means that when translational symmetry is broken, for instance at a bend or a resonant cavity, vertical radiation losses are inevitable and strategies to minimize these losses will be required. However, in linear defect waveguides, where only one direction of translational symmetry is broken, ideally lossless guiding can be maintained.

2.3.3 Waveguides in planar photonic crystals

Planar photonic crystal waveguides are also made by the introduction of linear defects into the plane of periodicity. The differences to 2D photonic crystals arise from the fact that while light is still controlled in the horizontal direction using the PBG effect, the confinement in the vertical direction is achieved by index guiding.

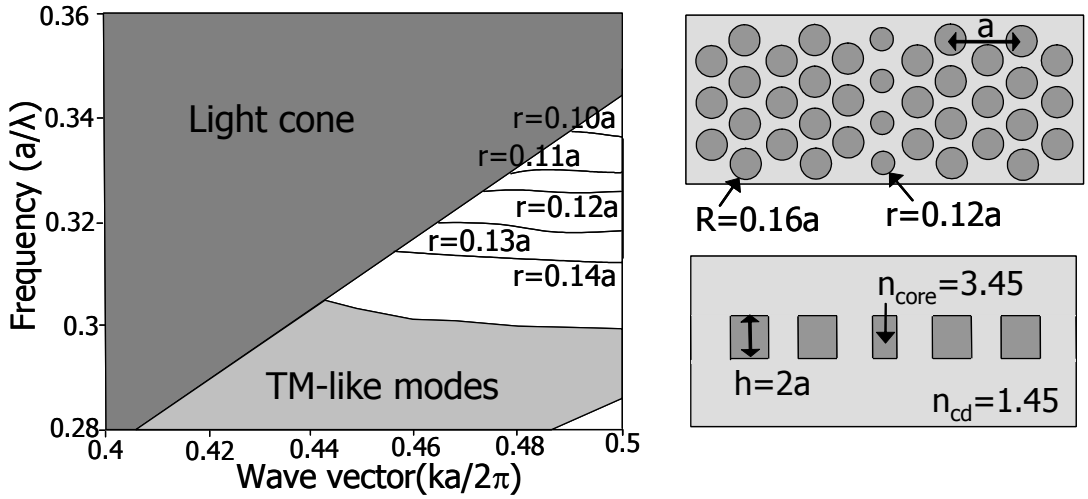

Figure 2.11.- Band diagram of planar photonic crystal waveguides created by reducing the radius of a row of columns. Numbers near the curves denote the radius of the row of columns that form the waveguide. Note that the structure is symmetric in the vertical direction.

A single mode behavior in the frequency range of interest is desired in order to achieve an optimal performance. Furthermore, the guided mode should be below the light cone and within the PBG to avoid radiation losses. Conventional waveguides formed by removing one or several row of columns usually result in multimode guiding, especially in air holes lattices. Therefore, alternative approaches, some of them described below, have been proposed to design more efficient waveguides [Joh00a].

Figure 2.11 shows the band diagram of planar photonic crystal waveguides created by reducing the radius of a row of columns instead of being removed. A triangular lattice of silicon rods embedded in a silica medium is considered. It can be seen that by appropriately designing the radius of the defects that form the waveguide a single guided mode below the light cone and located within the PBG, therefore a lossless guided Bloch mode, is achieved. However, it should be noticed that it has a narrow bandwidth as well as a very flat dispersion relation. While the former limits the frequency range of operation, the latter gives rise to a low group velocity, which may be useful for implementing optical functionalities such as optical delay lines or dispersion compensators. However, the low group velocity makes difficult the coupling from an external medium.

A large variety of different strategies to design waveguides with single mode transmission and increased bandwidth have been proposed during the last years. Several examples are illustrated in figure 2.12. In figure 2.12(a), the waveguide is designed by shifting the lattice so the distance between the adjacent rows of columns is reduced γ times the distance of the original waveguide [Not01].

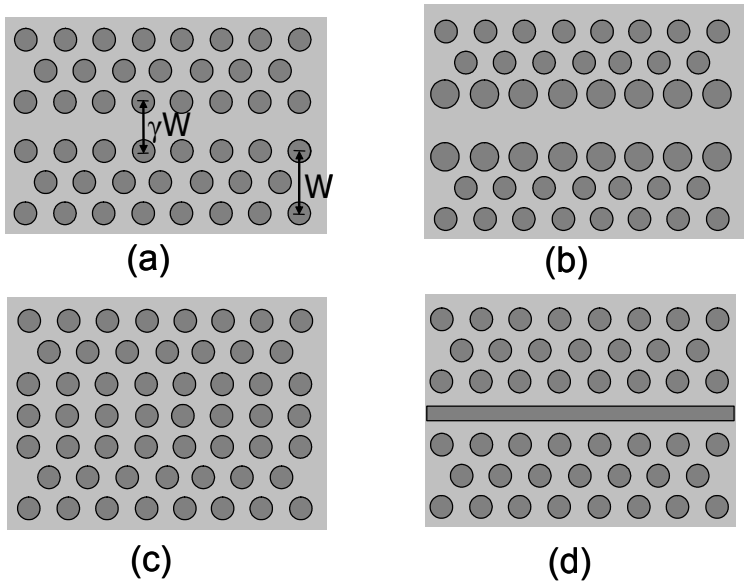

Figure 2.12.- Different kinds of waveguides designed to achieve single mode transmission. The waveguide is created (a) by reducing the core of the original waveguide, (b) by changing the radius of the adjacent rows of columns that form the waveguide, (c) by shifting the central row of columns and (d) by replacing the row of columns by a dielectric waveguide.

In figure 2.12(b), the radius of the adjacent rows of columns that form the waveguide is changed [Adi00]. In figure 2.12(c), the central row of columns is shifted up to be aligned with the adjacent rows [Yam02]. Finally, in figure 2.1.2(d), the row of columns is replaced by a dielectric waveguide to create the waveguide [Lau02]. One important point for any waveguide design is trying to maintain the periodicity of the lattice, which is only achieved in the above examples for the cases shown in figures 2.11, 2.12(b) and 2.12(d). The preservation of the lattice periodicity simplifies the implementation of bends and other discontinuities.

On the other hand, there is an important issue that should be taken into account in any design when the planar photonic crystal is asymmetric in the vertical direction. Figure 2.13 shows the band diagram of a planar photonic crystal waveguide formed by a triangular lattice of air holes etched in a silicon slab core on top of a silica layer. The core of the waveguide has been reduced in order to achieve single mode transmission, although it can also be seen another guided mode close to the lower PBG edge. On the other hand, the lowest mode located below the projected band of the TE-like modes is guided by total internal refraction in both the vertical and horizontal direction. This kind of mode can not exist in the structure shown in figure 2.11 because the core of the waveguide has a refractive index smaller than the surrounding medium, i.e. there is not index confinement in the horizontal direction.

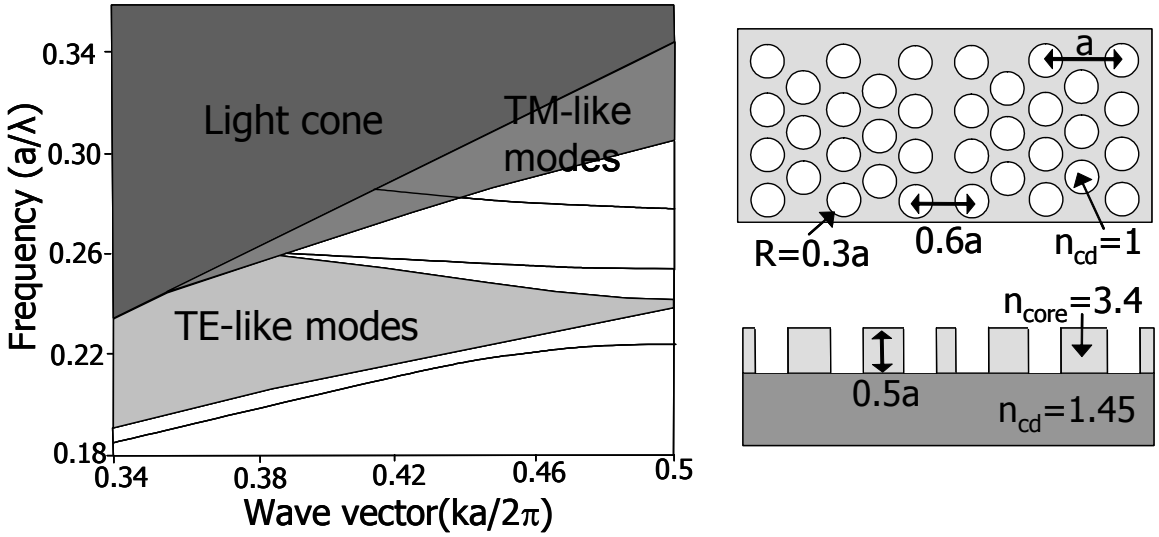

Figure 2.13.- Band diagram of a planar photonic crystal waveguide formed by reducing the core of the original waveguide. Note that the structure is asymmetric in the vertical direction and therefore both TE-like and TM-like polarizations can couple to each other increasing propagation losses.

The vertical asymmetry of the structure shown in figure 2.13 may give rise to an interaction between both TM-like and TE-like polarizations. This interaction will increase propagation losses because, if the TE-like mode is coupled to a TM-like mode, it will no longer experience the PBG and light will not be confined within the waveguide. This effect becomes stronger when the asymmetry of the structure increases. Therefore, when the PBG occurs only for one of the polarizations, the projected band of both TM-like and TE-like modes should be represented in the band diagram. The optimum performance is given when the guided mode is below the light cone but also below the projected band of the polarization for which the PBG does not exist. It is important to notice that even in symmetric planar photonic crystals, fabrication imperfections, such as tilted sidewalls, make the structure asymmetric so that both polarizations are no longer decoupled and can interact.

2.3.4 Index contrast between claddings and core

The highest index contrast between the slab core and claddings is *a priori* preferred in planar photonic crystals in order to achieve guided modes below the light cone thus allowing the implementation of lossless waveguides. The highest contrast is achieved by using a semiconductor membrane suspended in air. This membrane-type structure has been fabricated with slab cores of silicon [Lon00, Not01], Al_xGa_yAs composites [Kan97, Kaw01] or GaInAsP [Pai99]. However, this structure suffers from a poor mechanical stability, especially in air holes lattices with large filling ratios. Therefore, the support of a material with a lower index than the one used for the slab core becomes more suitable. The main benefit is that

the mechanical stability is improved but the light cone is pulled down reducing the space for guided modes. Normally, an air medium is still used above the slab core breaking the vertical symmetry of the structure. One example is Silicon-on-insulator (SOI) in which a silicon layer is used on top of a silica layer [Bog02, Pat02]. Another alternative is the use of a high index GaAs layer on top of an Al_xO_y layer [Rip99, Cho00].

Low vertical index contrast is the alternative to high index contrast. One example is GaAs-$Al_xGa_{1-x}As$ heterostructures where the index contrast depends on the fraction of Aluminium, x [Kra96]. In this case, the guided modes are usually above the light cone. Therefore, radiation modes are always excited making the structure inherently lossy due to out-of-plane radiation. This may be seen as a clear disadvantage with respect to high index contrast structures. However, out-of-plane radiation at discontinuities is much lower than in high index contrast structures. This is originated because light in high index contrast structures is more confined in the slab core. Therefore, the breakage of the translational symmetry at the discontinuities has a larger impact. On the other hand, larger aspect ratios are required at the etching process in low index contrast structures because light is less confined in the vertical direction. Furthermore, the buffer layer between the slab core and the substrate must be thick enough to avoid substrate leakage.

Losses due to out-of-plane radiation, known as out-of-plane losses, can significantly degrade the performance of the circuit [Bog01, Ben00]. The choice between low or high index contrast will depend on the particular problem and material system at hand. However, in both cases, different specific designs are required to minimize out-of-plane losses. It is worth to mention that low index contrast structures permit an approximated 2D analysis by using the effective index method. This method consists of replacing the material index in the corresponding 2D photonic crystal by the effective index of the fundamental guided mode in the unperturbed 3D slab structure [Qui02a]. The effective index method may also be used in planar photonic crystals with high index contrast but results will only be valid in a narrower frequency range. Therefore, in this kind of structures a 3D modelling tool should be used for a more rigorous analysis.

2.4 Modeling tools

Several methods have been proposed for analyzing the properties of photonic crystal structures. We will review the most important that have also been used throughout this work.

2.4.1 Finite-difference time-domain

The finite-difference time-domain (FDTD) method is one of the methods most widely employed for simulating photonic crystal circuits. The method is based on the discretization of Maxwell equations by replacing the partial differentials by finite differences [Taf95]. In general, the method is very accurate since no assumptions are made on the kind of solution of the Maxwell equations. Therefore, it has been employed for calculating electromagnetic fields distributions in structures of arbitrary geometry. Furthermore, FDTD is a time domain technique, which allows the analysis of pulse propagation in the structure. Therefore, when a pulse is used as source, the transmission spectrum can be obtained with only one simulation by applying the Fourier transform. The main weakness of FDTD is that long calculation times and huge memory requirements are usually needed, especially in 3D simulations.

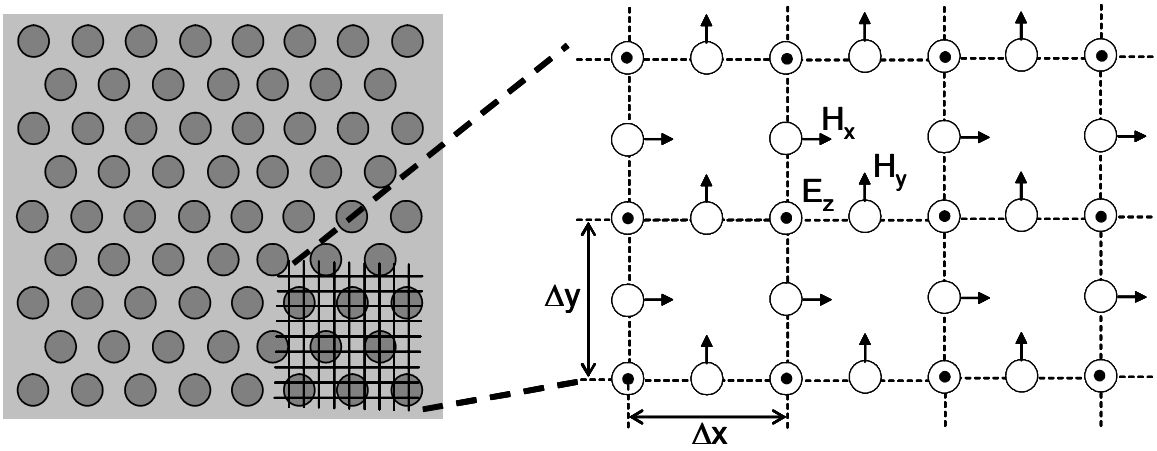

Figure 2.14.- Finite-difference time-domain (FDTD) method. The structure is discretized on a spatial grid and the time evolution of the electromagnetic field is determined at every point within the computational domain in an iterative process.

In order to use FDTD, a computational domain must be defined and discretized on a spatial grid, as shown in figure 2.14. The materials of the structure to be simulated must be specified at all points within the computational domain. Once the computational domain and the grid are established, a source is specified. The source will depend on the type of simulation. The time evolution of the electromagnetic field is then determined at every point within the computational domain in an iterative process. Thus, the resultant electromagnetic fields can be obtained anywhere on the structure for later analysis.

On the other hand, since the computational domain must end at some point, a boundary must be established. Different types of absorbing boundary conditions can be chosen to avoid undesired reflections in the computational domain. The so-

called perfectly matched layer (PML) condition is usually employed for simulating photonic crystals [Ber94]. In this work, we have used *FullWAVE* from *Rsoft Design Group Inc.*, which allows 1D, 2D and 3D FDTD simulations with PML boundary conditions[1].

2.4.2 Plane wave method

The plane wave method is a popular numeric technique used to solve periodic electromagnetic problems. This technique is based on the expansion of the electromagnetic fields into a superposition of plane waves [Leu90]. The Maxwell equations are represented in the frequency domain and transformed into an eigenvalue problem. By solving this eigenvalue problem, the electromagnetic fields and the frequencies corresponding to each plane wave, which provides the dispersion relation of the periodic structure, are obtained. The plane wave method is the most widely used method to calculate band diagrams in photonic crystals [Joh01].

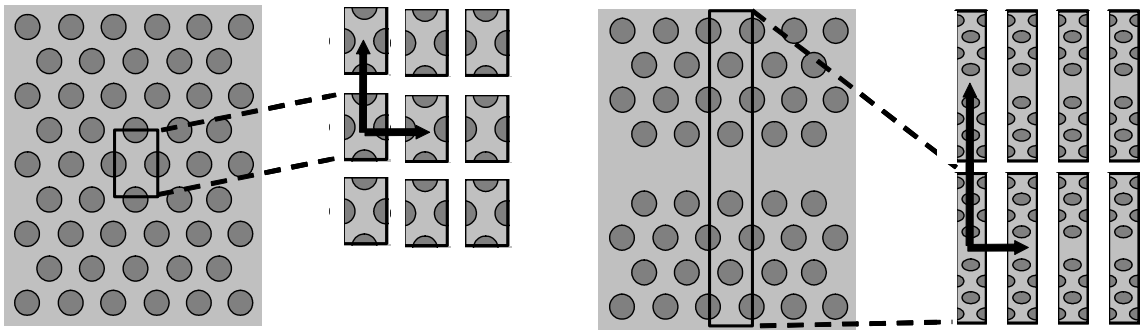

Figure 2.15.- Plane wave method. In the left part, the basic cell is periodically repeated modelling the structure that extends into infinity. In the right part, a supercell is defined to model the photonic crystal waveguide. Several lattice constants are considered in the transversal direction to avoid the interaction between neighbouring defects.

The basic cell of the photonic crystal determines the computational domain. Once the primitive lattice vectors and materials are defined, the basic cell is periodically repeated modelling the structure that extends into infinity, as depicted in the left part of figure 2.15. When modelling linear or point defects in photonic crystals, a supercell approach is needed. The right part of figure 2.15 shows the supercell used to model a photonic crystal waveguide. In this case, the computational domain is defined with several lattice constants in the spatial directions where the periodicity is broken. Because the electromagnetic fields are localized within the defect, this avoids the interaction between neighbouring defects. Therefore, the obtained band diagram will be a good approximation of that of the isolated defect.

[1] http://www.rsoftdesign.com/products/component_design/FullWAVE/

A similar approach is used to calculate the band diagram of planar photonic crystals but, in this case, an artificial periodicity is established in the vertical dimension. In the same way, the frequencies of the guided modes are not affected because the electromagnetic field is localized within the slab. The frequencies of radiation modes are affected but since they fall inside the light cone they are not of interest. In this work, we have used *BandSOLVE* from *Rsoft Design Group Inc.*[2] and the MIT Photonic-Bands (MPB) package developed by the Massachusetts Institute of Technology that can be freely downloaded from Internet[3].

2.4.3 Eigenmode expansion

Eigenmode expansion is also a frequency domain method based on the expansion of the electromagnetic fields, like in the plane wave method, but using a different set of basic functions [Bie01]. In this case, the photonic crystal is divided into a number of layers where the refractive index profile does not change in the propagation direction, as it is shown in figure 2.16. The electromagnetic field in each layer is written as a sum of the local eigenmodes of that particular layer, which can be considered as a natural optical field profile that can exist in this layer and therefore propagates indefinitely without changing its form. At the interfaces between layers, a scattering matrix is calculated describing the coupling between the eigenmodes of neighbouring layers.

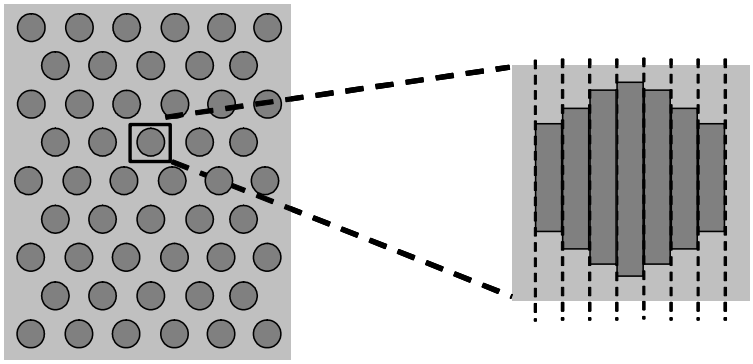

Figure 2.16.- Eigenmode expansion method in which the photonic crystal is divided in a number of layers where the refractive index profile does not change in the propagation direction.

Shorter computation times than FDTD are achieved because the fields in each layer are represented in a more compact form rather than specifying them explicitly at a number of grip points, as realized in FDTD. Furthermore, the calculation time of a layer is independent of the length of that layer and periodicity or quasi-periodicity can also be easily exploited. However, multiple simulations are needed to analyze a

[2] http://www.rsoftdesign.com/products/component_design/BandSOLVE/
[3] http://ab-initio.mit.edu/mpb/

certain frequency range since frequency domain methods can only handle a single frequency at the same time. In this work, we have used the modelling tool CAMFR developed by the photonics group at the INTEC department of Ghent University[4].

2.4.4 Multiple scattering

The multiple scattering method has also been proposed to simulate photonic crystals [Och02, Hak05a]. This frequency domain method is based on the expansion of the electromagnetic fields into series of orthogonal Bessel functions. The computational domain is defined as an array of scatterers located at arbitrary positions. The electromagnetic field induced by a particular scatter is obtained by multiplying the superposition of the external field and the field scattered by the array of scatterers with the so-called transition matrix, which is defined from the boundary condition at the interface of this particular scatter. Thus, the total electromagnetic field of the structure is obtained as the sum of the induced fields by every scatterer.

When circular scatterers are considered, as occurs in photonic crystals, the series expansion of the Bessel functions converges rather fast. This fast convergence yields to very short computation times. However, the computation time increases exponentially with the number of scatterers. Therefore, it is important to exclude scatterers that does not influence on the result. Furthermore, the scatterers can not overlap. In this work, we have used a self-made code developed by Prof. José Sánchez-Dehesa and co-workers.

2.5 Applications of photonic crystals

Resonant cavities and waveguides have been the subject of a significant research effort as they are the basic components in photonic integrated circuits. Based on these components, different passive functionalities have been proposed and demonstrated, such as sharp bends [Mek96, Bab99], Y junctions [Lin02, Bos02, Sug02], add drop filters [Nod00a, Fan98], demultiplexers and multiplexers [Kos01, Bos02a] or Mach-Zehnder interferometers [Mar03]. Several examples are shown in figure 2.17, which were fabricated on Silicon-on-insulator (SOI) [Bog02].

The ability of photonic crystals to control the flow of light and their capability to concentrate light and enhance the interaction between light and matter are also of interest to implement active functionalities based on nonlinear effects.

[4] http://camfr.sourceforge.net/

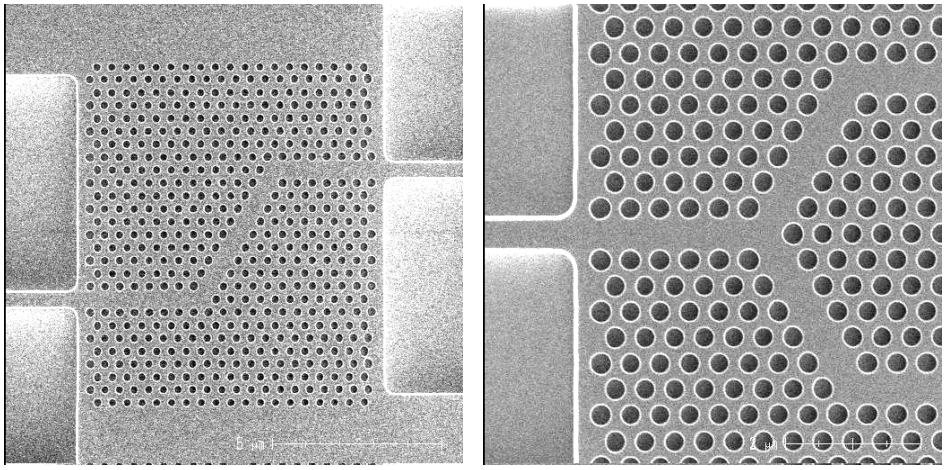

Figure 2.17.- Scanning electron microscopy (SEM) images of planar photonic crystals fabricated on Silicon-on-insulator (SOI). The left part shows a sharp bend and the right part shows a Y junction.

Several active functionalities have been proposed such as all-optical switches [Lan02, Cue04], second harmonic generation [Mar97] or novel light sources. In the latter, light emitted into unwanted directions is prohibited by the photonic crystal, which permits the design of high-efficiency light-emitting diodes (LEDs) [Fan97, Ryu02]. Furthermore, ultra-low-threshold semiconductor lasers in which the photonic crystal is designed to reduce the number of non-lasing modes have also been proposed [Pai99, Sak99].

The dispersion features of photonic crystals result also of interest to implement different functionalities. In a photonic crystal, the dispersion relation can noticeably change with the propagation direction and wavelength. This effect is known as the superprism effect because light dispersion is much stronger than in conventional glass prism [Kos99]. The angular dispersion can be useful to achieve highly collimators or spot size converters, as depicted in the left part of figure 2.18 [Kos00]. On the other hand, when an incident beam with multiple wavelengths impinges at the interface of the photonic crystal, each wavelength is refracted in a different angle, as shown in the right part of figure 2.18. Therefore, wavelength multiplexers and demultiplexers can also be designed [Wu02]. However, a careful design of the input and output interfaces is needed to avoid the high reflection originated due to the mode mismatch [Bab01].

On the other hand, under certain conditions, photonic crystals can have an anomalous behaviour in which an incident beam is diffracted in a direction different from that expected in homogeneous dielectric materials [Not00, Fot04]. This effect, known as negative refraction, has received an increasing interest in the last years due to their usefulness to implement novel applications, such as the realization of optical flat lenses that overcome the diffraction limit [Pen00, Mar04].

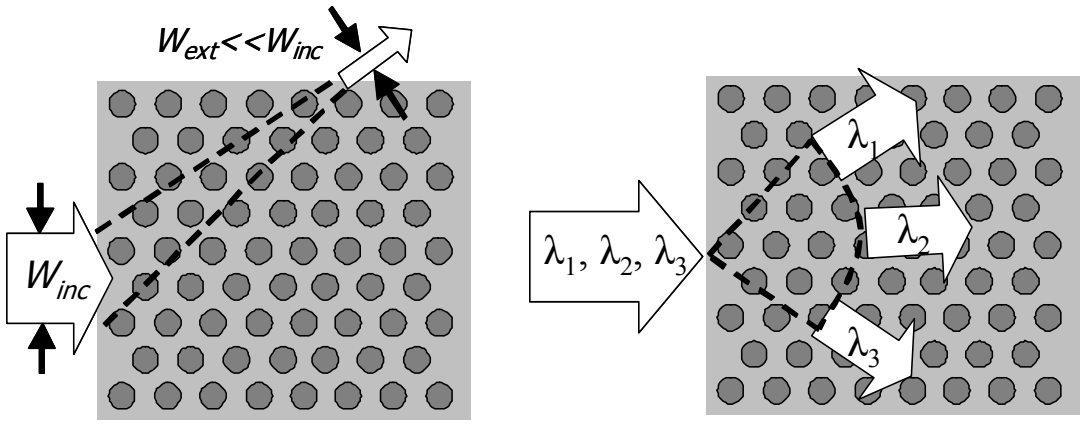

Figure 2.18.- Possible applications of the superprism effect. The left part shows a spot-size converter where W is the beam waist while the right part shows a wavelength demultiplexer where λ is the wavelength.

Photonic crystal waveguides can also support both strong positive and negative dispersion at the band edges of the guided mode where the dispersion relation is flattened. For the guided mode shown in figure 2.7, for instance, the group velocity increases with the frequency at the lower band edge while the group velocity decreases with the frequency at the higher band edge. Therefore, both strong positive and negative dispersion are possible which also means that the group velocity is significantly reduced at the band edges. These features may be useful to implement compact optical delay lines or dispersion compensators [Sca96, Hos02].

2.6 Conclusion

Photonic crystals have attracted great research interest because of their potential to achieve highly integrated photonic circuits with advanced functionality. A large number of applications has been proposed and demonstrated during the last years with special emphasis in planar photonic crystals due to their easier fabrication at optical wavelengths. However, a great effort is still needed in order to solve several issues that permit the definitive commercial deployment of photonic crystal technology. One of the most important is the reduction of propagation losses. To achieve this goal mainly depends on optimization of the fabrication process to reduce fabrication imperfections such as sidewall roughness and on the study of techniques to minimize out-of-plane losses. At the moment, propagation losses lower than 3 dB/mm have been reported [Mcn03, Tan04]. Another very important issue that must be addressed is the coupling losses between external media (fiber and dielectric waveguides) and photonic crystal circuits, which is the subject of study in this work.

Chapter 3

Butt-coupling in Photonic Crystals

3.1 Coupling losses in photonic crystals

Efficient coupling from optical fibres into and out of photonic crystal circuits is a key technological step for the definitive commercial deployment of photonic crystal technology. The core diameter of single mode optical fibres ranges from 8μm to 10μm. However, the size of photonic crystal waveguides is usually smaller than 1μm in both the vertical and horizontal dimensions. The different sizes of both waveguides are illustrated in figure 3.1. Because of the large mode profile mismatch, the coupling efficiency is very low when both waveguides are butt-coupled. However, a large variety of spot size converters between optical fibers and dielectric waveguides have been developed in the past to resolve the mode profile mismatch mainly in the horizontal dimension but also in the vertical dimension [see e.g. Moe97]. Recently, a promising approach based on an inverted dielectric taper has been proposed to achieve efficient coupling between narrow dielectric waveguides and fibres in relatively short coupling lengths [Alm03, Sho02, Mcn03].

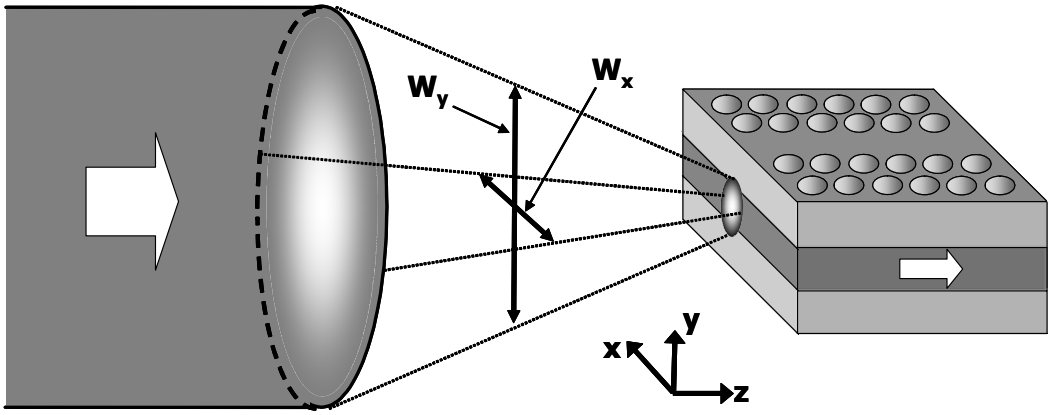

Figure 3.1.- Coupling from optical fibres into and out of photonic crystal circuits. Because of the large mode profile mismatch in both vertical, W_y, and horizontal, W_x, directions, the coupling efficiency is very low when both waveguides are butt-coupled.

Therefore, the problem of coupling in photonic crystal circuits may be simplified to achieve efficient coupling between dielectric waveguides and photonic crystal waveguides of a similar size in both the vertical and horizontal dimensions. Furthermore, efficient interfacing between dielectric and photonic crystal waveguides with a similar size may also be important if photonic crystal circuits have to be inserted on a chip with other functional blocks implemented with conventional dielectric waveguides.

However, the coupling efficiency can be still rather poor even when the dielectric and photonic crystal waveguide have similar sizes. The origin of coupling losses is basically due to the mode mismatch derived from the different guiding mechanism in both kinds of waveguides. Waveguides in photonic crystal circuits are usually formed by inserting line defects into the otherwise periodic structure. Propagation in this kind of waveguides is characterized by Bloch modes, as introduced in chapter two. On the other hand, propagation in conventional dielectric waveguides relies on index-contrast guiding.

Butt coupling losses are rather different depending on the nature of the photonic crystal considered. In rod structures, where the photonic crystal is formed by rods with a higher refractive index than the surrounding medium, the coupling efficiency is in general poor [Sto00, Mek01]. However, in hole structures, where the photonic crystal is formed by a lattice of air holes inserted in a high refractive index medium, the coupling efficiency is very high and transmission efficiencies near 100% can be achieved [Adi00a, Qiu01, Miy02, Mol03]. Coupling losses in both kinds of photonic crystal structures have been studied by means of simulations but to the best of our knowledge there has not been any systematic, all-encompassing analytic study at the moment.

The aim of this chapter is to obtain analytic expressions for the reflection and transmission matrices at an interface formed by a dielectric waveguide butt coupled to a photonic crystal waveguide. Closed form expressions have been obtained following the mode matching technique. Eigenmode expansion on the Bloch mode basis has been considered. The Bloch mode basis has been used for engineering gratings, propagation in finite photonic crystal waveguides or taper transitions in photonic crystals [Pal01, Joh02, Lan04, Bot03]. However, in this case, the coupling from a dielectric waveguide into a semi-infinite photonic crystal waveguide and vice versa has been considered. Previously, the mode matching technique has been introduced for an interface formed by two different dielectric waveguides. Analytic expressions, validated by means of simulations, have been used to study coupling losses in both rod and hole structures to get a qualitative insight into the origin of coupling losses. Furthermore, the obtained expressions have been extended for a semi-analytic treatment of complex photonic crystal structures.

3.2 Interface between two dielectric waveguides

Figure 3.2 shows the interface between two different media where the z-axis is oriented along the propagation direction. In this case we consider that both media are z-invariant. If the interface is placed at z=0 and a singlemode with index p is incident from medium I, this incident mode will give rise to a reflected field in medium I and a transmitted field in medium II. The following derivation is based on the well-known mode matching technique [Zak88, Ele94]. We expand the fields in terms of the eigenmodes of each medium and impose the continuity of the tangential components of the total field

$$\mathrm{E}_p^I + \sum_j R_{j,p}\mathrm{E}_j^I = \sum_j T_{j,p}\mathrm{E}_j^{II} \tag{3.1}$$

$$\mathrm{H}_p^I - \sum_j R_{j,p}\mathrm{H}_j^I = \sum_j T_{j,p}\mathrm{H}_j^{II} \tag{3.2}$$

where E_p^I and H_p^I are the incident electric and magnetic fields for the mode with index p, E_j^I, H_j^I, E_j^{II} and H_j^{II} are respectively the reflected and transmitted electric and magnetic fields for the eigenmode with index j and $R_{j,p}$ and $T_{j,p}$ are the reflection and transmission coefficients for the eigenmode with index j considering an incident mode with index p. The minus sign of the reflected magnetic field is due to the symmetries for the backward propagating modes. In order to calculate the unknown transmission and reflection coefficients, we take the right cross product of (3.1) with H_i^I and the left cross product of (3.2) with E_i^I, which are the expansion fields of medium I. Here, I is an arbitrary index. After integrating over the cross-section, we get

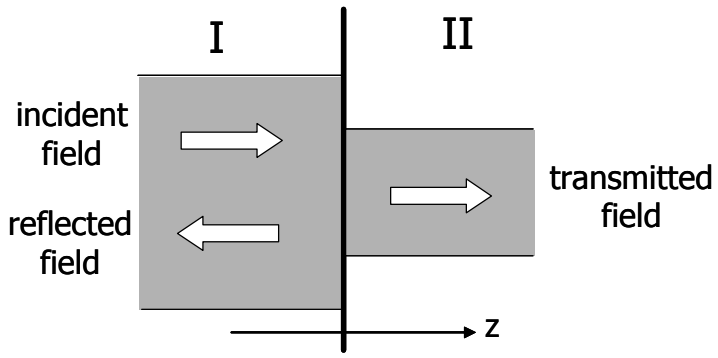

Figure 3.2.- Interface between two media where the *z*-axis is oriented along the propagation direction. The incident field impinging on the interface will give rise to a reflected field in medium I and a transmitted field in medium II.

$$\left\langle \mathrm{E}_p^I, \mathrm{H}_i^I \right\rangle + \sum_j R_{j,p} \left\langle \mathrm{E}_j^I, \mathrm{H}_i^I \right\rangle = \sum_j T_{j,p} \left\langle \mathrm{E}_j^{II}, \mathrm{H}_i^I \right\rangle \tag{3.3}$$

$$\left\langle \mathrm{E}_i^I, \mathrm{H}_p^I \right\rangle - \sum_j R_{j,p} \left\langle \mathrm{E}_i^I, \mathrm{H}_j^I \right\rangle = \sum_j T_{j,p} \left\langle \mathrm{E}_i^I, \mathrm{H}_j^{II} \right\rangle \tag{3.4}$$

where the scalar product is defined as the following overlap integral

$$\left\langle \mathrm{E}_n, \mathrm{H}_m \right\rangle = \iint_S \left(\mathrm{E}_n \times \mathrm{H}_m \right) \mathrm{u}_z \, dS$$

being u_z the unitary vector in the z-axis direction. By invoking the orthogonality relation and after some algebraic manipulations we get

$$2\delta_{ip} \left\langle \mathrm{E}_p^I, \mathrm{H}_p^I \right\rangle = \sum_j T_{j,p} [\left\langle \mathrm{E}_j^{II}, \mathrm{H}_i^I \right\rangle + \left\langle \mathrm{E}_i^I, \mathrm{H}_j^{II} \right\rangle] \tag{3.5}$$

$$R_{i,p} = \frac{1}{2\left\langle \mathrm{E}_i^I, \mathrm{H}_i^I \right\rangle} \sum_j T_{j,p} [\left\langle \mathrm{E}_j^{II}, \mathrm{H}_i^I \right\rangle - \left\langle \mathrm{E}_i^I, \mathrm{H}_j^{II} \right\rangle] \tag{3.6}$$

where δ_{ip} is the Kronecker delta. If the series expansion is truncated after N terms, the transmission coefficient will be calculated by solving an $N \times N$ linear system, and then the reflection coefficients will be obtained by a simple matrix multiplication. Although these coefficients are obtained upon incidence of a mode with index p, the whole procedure can be repeated using all modes p in $1 \rightarrow N$. Thereby, we will obtain the transmission and reflection matrices that completely characterize the scattering that occurs at the interface.

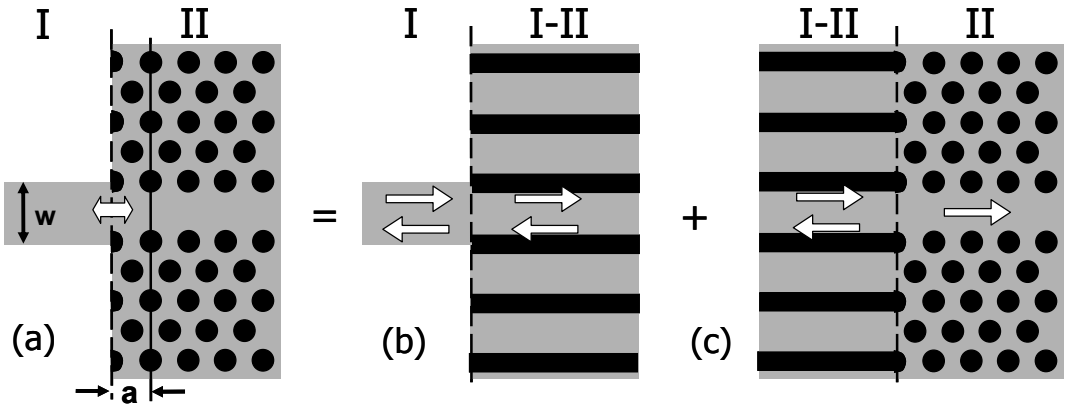

Figure 3.3.- Schematic of the analyzed structures. A dielectric waveguide is butt-coupled to a single line defect photonic crystal waveguide. The width of the input waveguide is *w* and the lattice constant is *a*. The structure shown in (a) can be decomposed into the two structures shown in (b) and (c) in order to calculate the transmission and reflection matrices.

3.3 Interface between dielectric and photonic crystal waveguides

The mode matching technique has been used to calculate the transmission and reflection matrices for an interface between a dielectric waveguide and a semi-infinite photonic crystal waveguide. Two different approaches, which yield to the same closed-form expressions, are presented.

3.3.1 First approach

Figure 3.3(a) shows the structure under study that is formed by a dielectric waveguide butt-coupled to a single line defect photonic crystal waveguide. In this case, medium II shown in figure 3.2 is not a *z*-invariant medium but a periodic medium, which consists of an infinitive number of repetitions of the same basic period in the *z*-direction. Propagation in the periodic medium is determined by Bloch modes [Blo28]. Mode properties can change significantly within the basic period. Therefore, the coupling efficiency will depend on the interface chosen among all the possible cuts within the basic period.

In order to calculate the transmission and reflection matrices of the structure shown in figure 3.3(a), we expand the fields of medium II in terms of the Bloch modes and use (3.5) and (3.6). These equations are still valid because the orthogonality relation is invoked by using the field expansions of the dielectric waveguide, which is a *z*-invariant medium. On the other hand, only forward-propagating Bloch modes are used in the series expansion because a semi-infinite photonic crystal waveguide

is considered. In order to distinguish the forward-propagating Bloch modes from the backward-propagating Bloch modes we look at the power flux for the guided mode and at the imaginary part of the wave vector for the evanescent modes [Bot01]. As described in the previous chapter, in eigenmode expansion, the structure is sliced up into layers where the index profile does not change in the propagation direction. In each of these individual layers, we can write the field as a sum of the eigenmodes. In the case of Bloch modes, the field in each layer is composed of forward and backward components. Eq. (3.5) and (3.6) can be simplified by expressing the Bloch modes in terms of their forward and backward components so that we get

$$\left\langle \mathrm{E}_j^{II}, \mathrm{H}_i^{I} \right\rangle = \sum_k \left(F_k^j + B_k^j \right) \cdot \left\langle \tilde{\mathrm{E}}_k, \mathrm{H}_i^{I} \right\rangle \tag{3.7}$$

$$\left\langle \mathrm{E}_i^{I}, \mathrm{H}_j^{II} \right\rangle = \sum_k \left(F_k^j - B_k^j \right) \cdot \left\langle \mathrm{E}_i^{I}, \tilde{\mathrm{H}}_k \right\rangle \tag{3.8}$$

where $\tilde{\mathrm{E}}_\mathrm{k}$ and $\tilde{\mathrm{H}}_\mathrm{k}$ are the eigenmodes of the individual layer that depend on the chosen cut position within the basic period. Adding and subtracting (3.7) and (3.8) results in

$$\begin{aligned} \left\langle \mathrm{E}_j^{II}, \mathrm{H}_i^{I} \right\rangle + \left\langle \mathrm{E}_i^{I}, \mathrm{H}_j^{II} \right\rangle = & \sum_k F_k^j \cdot \left(\left\langle \tilde{\mathrm{E}}_\mathrm{k}, \mathrm{H}_i^{I} \right\rangle + \left\langle \mathrm{E}_i^{I}, \tilde{\mathrm{H}}_\mathrm{k} \right\rangle \right) \\ & + \sum_k B_k^j \cdot \left(\left\langle \tilde{\mathrm{E}}_\mathrm{k}, \mathrm{H}_i^{I} \right\rangle - \left\langle \mathrm{E}_i^{I}, \tilde{\mathrm{H}}_\mathrm{k} \right\rangle \right) \end{aligned} \tag{3.9}$$

$$\begin{aligned} \left\langle \mathrm{E}_j^{II}, \mathrm{H}_i^{I} \right\rangle - \left\langle \mathrm{E}_i^{I}, \mathrm{H}_j^{II} \right\rangle = & \sum_k F_k^j \cdot \left(\left\langle \tilde{\mathrm{E}}_\mathrm{k}, \mathrm{H}_i^{I} \right\rangle - \left\langle \mathrm{E}_i^{I}, \tilde{\mathrm{H}}_\mathrm{k} \right\rangle \right) \\ & + \sum_k B_k^j \cdot \left(\left\langle \tilde{\mathrm{E}}_\mathrm{k}, \mathrm{H}_i^{I} \right\rangle + \left\langle \mathrm{E}_i^{I}, \tilde{\mathrm{H}}_\mathrm{k} \right\rangle \right) \end{aligned} \tag{3.10}$$

Using (3.9) and (3.10) into (3.5) and (3.6) we obtain the transmission and reflection matrices for the structure shown in figure 3.3(a), which can be expressed by the following matrix equations

$$T_{IN} = F^{-1} \left(I + T_{12} R_{12} T_{12}^{-1} B F^{-1} \right)^{-1} T_{12} \tag{3.11}$$

$$R_{IN} = \left(R_{12} T_{12}^{-1} F + T_{12}^{-1} B \right) T_{IN} \tag{3.12}$$

where the transmission matrix can be simplified to

$$T_{IN} = F^{-1}\left(I - R_{21}^{T} B F^{-1}\right)^{-1} T_{12} \tag{3.13}$$

It can be shown that T_{ij} and R_{ij} are the transmission and reflection matrices of the structure shown in figure 3.3(b), which are calculated using (3.5) and (3.6). In figure 3.3(b), the medium I-II is the individual layer corresponding to the interface chosen within the basic period of the photonic crystal. Therefore, it can be deduced that the problem shown in figure 3.3(a) can be decomposed in the two sub-problems shown in figures 3.3(b)-(c) and a similar derivation can be followed to obtain the scattering matrices.

3.3.2 Second approach

In this subsection, we demonstrate that another approach to calculate the scattering matrices of the structure shown in figure 3.3(a) is to separate the basic structure into two structures, shown in figures 3.3(b)-(c), and then combine the transmission and reflection matrices of each structure. Medium I and I-II are *z*-invariant media so that we expand the fields in terms of the eigenmodes of each medium. On the other hand, medium II is a periodic medium so that we expand the fields in terms of the Bloch modes.

In the first structure, shown in figure 3.3(b), the forward and backward propagating modes are related by a transfer matrix

$$F_{I-II} = T_{12} F_I + R_{21} B_{I-II} \tag{3.14}$$

$$B_I = R_{12} F_I + T_{21} B_{I-II} \tag{3.15}$$

where T_{ij} and R_{ij} are the transmission and reflection matrices calculated using (3.5) and (3.6). On the other hand, in the second structure, shown in figure 3.3I, there are no backward propagating Bloch modes in medium II so that

$$F_{II} = T_{23} F_{I-II} \tag{3.16}$$

$$B_{I-II} = R_{23} F_{I-II} \tag{3.17}$$

In this case, T_{23} and R_{23} can also be simplified by expressing the Bloch modes in terms of forward and backward components. Moreover, it can be seen that as the interface layer of medium II is the same as that of medium I-II, the eigenmodes expansion will be the same in both media allowing us to take advantage of the orthogonality relation. Therefore, it can be shown that

$$\left\langle \mathrm{E}_j^{II}, \mathrm{H}_i^{I-II} \right\rangle = \left(F_i^j + B_i^j\right) \cdot \left\langle \widetilde{\mathrm{E}}_i, \widetilde{\mathrm{H}}_i \right\rangle \tag{3.18}$$

$$\left\langle \mathrm{E}_i^{I-II}, \mathrm{H}_j^{II} \right\rangle = \left(F_i^j - B_i^j\right) \cdot \left\langle \widetilde{\mathrm{E}}_i, \widetilde{\mathrm{H}}_i \right\rangle \tag{3.19}$$

Thus, inserting (3.18) and (3.19) into (3.5) and (3.6) we get

$$T_{23} = F^{-1} \tag{3.20}$$

$$R_{23} = BF^{-1} \tag{3.21}$$

These results are in agreement with those reported in [Bot01, Bot03] where a plane-wave expansion was used to describe the input field as well as the Bloch modes.

The transmission and reflection matrices of the full structure can be easily calculated by relating (3.14)-(3.17) and inserting (3.20) and (3.21) which yields

$$T_{IN} = F^{-1}\left(I - R_{21}BF^{-1}\right)^{-1} T_{12} \tag{3.22}$$

$$R_{IN} = R_{12} + T_{21}BT_{IN} \tag{3.23}$$

It can be seen that the transmission matrices given by (3.13) and (3.22) are the same because $R^T_{21}=R_{21}$ due to reciprocity. Furthermore, the reflection matrices given by (3.12) and (3.23) are also identical as it is next demonstrated. First, we can put (3.23) into the form

$$R_{IN} = \left(R_{12}T_{12}^{-1}\left(I - R_{21}BF^{-1}\right)F + T_{21}B\right)T_{IN} \tag{3.24}$$

After some algebraic manipulations we get

$$R_{IN} = \left(R_{12}T_{12}^{-1}F + T_{12}^{-1}\left(T_{12}T_{21} + R_{21}R_{21}\right)B\right)T_{IN} \tag{3.25}$$

where it can be shown that

$$T_{12}T_{21} + R_{21}R_{21} = I \tag{3.26}$$

by using the self-inverting property of the scattering matrix and relating it with the transfer matrix [Ele94]. Thus, it can be shown that (3.25) is equal to (3.12).

The transmission and reflection matrices involve the scattering properties of guided, radiation and evanescent modes. Thus, if the modes are normalized, the transmitted and reflected power from the fundamental mode of the dielectric waveguide into the fundamental guided propagating Bloch mode are given by

$$\eta_{IN}^{T} = \left| T_{IN}[0,0] \right|^2 \tag{3.27}$$

$$\eta_{IN}^{R} = \left| R_{IN}[0,0] \right|^2 \tag{3.28}$$

where $T_{IN}[0,0]$ is the first element of (3.22) while $R_{IN}[0,0]$ is the first element of (3.23).

3.4 Interface between photonic crystal and dielectric waveguides

Transmission and reflection matrices have also been obtained for the reverse interface between a semi-infinite photonic crystal waveguide and a dielectric waveguide. On the contrary regarding to the previous derivation, in this case both forward and backward propagating Bloch modes inside the photonic crystal waveguide need to be considered. Figure 3.4 shows the analyzed interface formed by a line defect photonic crystal waveguide butt-coupled to a dielectric waveguide. The transmission and reflection matrices have also been calculated by using the mode matching technique. Therefore, let us consider that the interface is placed at z=0 and a single Bloch mode with index p is incident from medium I. This incident mode originates a reflected field in medium I and a transmitted field in medium II. We expand the fields in terms of the Bloch modes in medium I and in terms of the eigenmodes in medium II. Imposing the continuity of the tangential components of the total field at the interface yields

$$\mathrm{E}_p^{I+} + \sum_j R_{j,p} \mathrm{E}_j^{I-} = \sum_j T_{j,p} \mathrm{E}_j^{II} \tag{3.29}$$

$$\mathrm{H}_p^{I+} + \sum_j R_{j,p} \mathrm{H}_j^{I-} = \sum_j T_{j,p} \mathrm{H}_j^{II} \tag{3.30}$$

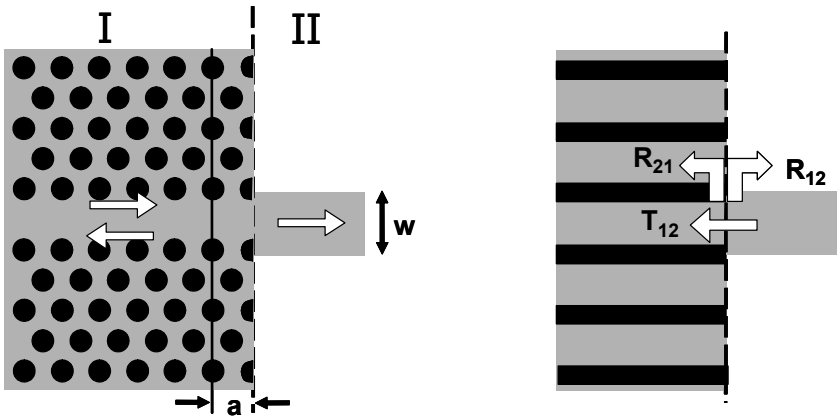

Figure 3.4.- Schematic of the analyzed structure for coupling out of photonic crystals. The right part shows the definition of R_{21}, R_{12} and T_{12} which is the same as in the previous derivation.

Where the plus and minus signs represent the forward and backward propagating Bloch modes respectively. The unknown transmission and reflection coefficients are calculated by taking the right cross product of (3.29) with H_i^{II} and the left cross product of (3.30) with E_i^{II}, which are the expansion fields of medium II. Here, I is an arbitrary index. After integrating over the cross-section and by invoking the orthogonality relation in medium II, we get

$$\left\langle \mathrm{E}_p^{I+}, \mathrm{H}_i^{II} \right\rangle + \sum_j R_{j,p} \left\langle \mathrm{E}_j^{I-}, \mathrm{H}_i^{II} \right\rangle = T_{i,p} \left\langle \mathrm{E}_i^{II}, \mathrm{H}_i^{II} \right\rangle \qquad (3.31)$$

$$\left\langle \mathrm{E}_i^{II}, \mathrm{H}_p^{I+} \right\rangle + \sum_j R_{j,p} \left\langle \mathrm{E}_i^{II}, \mathrm{H}_j^{I-} \right\rangle = T_{i,p} \left\langle \mathrm{E}_i^{II}, \mathrm{H}_i^{II} \right\rangle \qquad (3.32)$$

The reflection can be easily obtained by subtracting (3.31) to (3.32) yielding

$$\left\langle \mathrm{E}_p^{I+}, \mathrm{H}_i^{II} \right\rangle - \left\langle \mathrm{E}_i^{II}, \mathrm{H}_p^{I+} \right\rangle = \sum_j R_{j,p} (\left\langle \mathrm{E}_j^{I-}, \mathrm{H}_i^{II} \right\rangle - \left\langle \mathrm{E}_i^{II}, \mathrm{H}_j^{I-} \right\rangle) \qquad (3.33)$$

This equation can be simplified by decomposing the Bloch modes in terms of their forward, F_k, and backward, B_k, components. It should be noticed that the forward and backward components are different for the forward and backward propagating Bloch modes. Furthermore, the forward and backward components depend on the chosen cut position within the basic period of the photonic crystal waveguide. The chosen cut position will determine the index profile of the interface layer in medium I, shown at the right part of figure 3.4.

Therefore, we get

$$\begin{aligned}\left\langle \mathrm{E}_j^{I+}, \mathrm{H}_i^{II} \right\rangle - \left\langle \mathrm{E}_i^{II}, \mathrm{H}_j^{I+} \right\rangle = \sum_k F_k^{j+} \cdot (\left\langle \widetilde{\mathrm{E}}_\mathrm{k}, \mathrm{H}_i^{II} \right\rangle - \left\langle \mathrm{E}_i^{II}, \widetilde{\mathrm{H}}_\mathrm{k} \right\rangle) \\ + \sum_k B_k^{j+} \cdot (\left\langle \widetilde{\mathrm{E}}_\mathrm{k}, \mathrm{H}_i^{II} \right\rangle + \left\langle \mathrm{E}_i^{II}, \widetilde{\mathrm{H}}_\mathrm{k} \right\rangle)\end{aligned} \tag{3.34}$$

where $\widetilde{\mathrm{E}}_\mathrm{k}$ and $\widetilde{\mathrm{H}}_\mathrm{k}$ are the electric and magnetic field at the interface layer. Eq. (3.34) can be expressed with the following matrix equation

$$\left\langle \mathrm{E}_j^{I+}, \mathrm{H}_i^{/II} \right\rangle - \left\langle \mathrm{E}_i^{II}, \mathrm{H}_j^{I+} \right\rangle \equiv 2\left(R_{12} T_{12}^{-1} F_+ + T_{12}^{-1} B_+\right) \tag{3.35}$$

where T_{12} and R_{12} are defined as depicted in figure 3.4. It should be noticed that these terms are the same as those used in the previous derivation. A similar expression can be obtained for the right hand side of (3.33) so that we obtain

$$-2\left(R_{12} T_{12}^{-1} F_+ + T_{12}^{-1} B_+\right) = 2\left(R_{12} T_{12}^{-1} F_- + T_{12}^{-1} B_-\right) R_{OUT} \tag{3.36}$$

that results in the reflection matrix

$$R_{OUT} = -\left(B_- - R_{21} F_-\right)^{-1} \left(B_+ - R_{21} F_+\right) \tag{3.37}$$

The transmission matrix is obtained by adding (3.31) to (3.32) and following a similar procedure as that used from (3.34) to (3.37)

$$T_{OUT} = T_{12}^{-1} \left(F_+ - R_{21} B_+\right) + T_{12}^{-1} \left(F_- - R_{21} B_-\right) R_{OUT} \tag{3.38}$$

If the modes are normalized, the transmitted and reflected power from the fundamental guided propagating Bloch mode into the fundamental mode of the dielectric waveguide are given by

$$\eta_{OUT}^T = \left| T_{OUT}[0,0] \right|^2 \tag{3.39}$$

$$\eta_{OUT}^R = \left| R_{OUT}[0,0] \right|^2 \tag{3.40}$$

where $T_{OUT}\left[0,0\right]$ is the first element of (3.38) while $R_{OUT}\left[0,0\right]$ is the first element of (3.37).

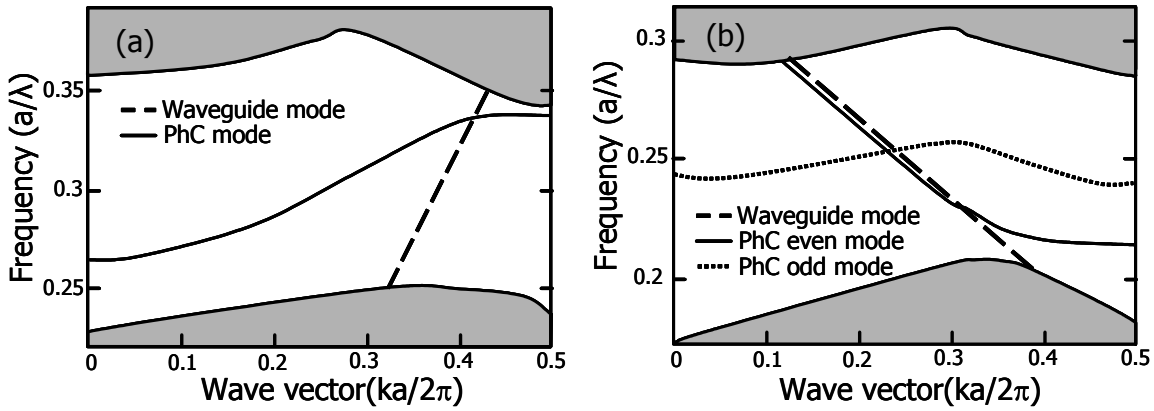

Figure 3.5.- Dispersion relation for the dielectric and photonic crystal waveguides for the (a) rod and (b) hole structures.

Structure	$n_{defects}$	n_{medium}	R	f_n (a/λ)	a @ λ=1.55μm	Polarization
Rod	3.4	1.45	0.2a	0.3	465 nm	TM
Hole	1	3.4	0.3a	0.235	364.2 nm	TE

Table 3.1.- Description of the main parameters of the two photonic crystal structures considered. $N_{defects}$ and n_{medium} are the refractive index of the defects (rods or holes) and the surrounding medium respectively, R is the defect radius, f_n is the normalized frequency and a is the lattice constant to achieve transmission at 1.55μm for the normalized frequency considered.

3.5 Butt-coupling in photonic crystals

3.5.1 Description of the analyzed structures

The analytic results were obtained with a frequency-domain model based on a vectorial eigenmode expansion technique and a staircase approximation of the index profile [Bie01]. This modeling tool, known as CAMFR, is freely available from the Internet[5]. For the photonic crystal waveguide, the Bloch modes were calculated from the eigenstates of the scattering matrix associated to the basic period. Afterwards, the field profiles and the forward and backward components of the Bloch modes were obtained at the chosen cut position within the basic period in order to calculate analytic expressions. Analytic results have been compared to simulation results. Simulations were performed with CAMFR as well as with the finite-difference time-domain (FDTD) method.

Two different photonic crystal structures formed by a dielectric waveguide butt-coupled to a single line defect photonic crystal waveguide have been analyzed. The first, hereafter named rod structure, consists of a 0.5μm-wide dielectric waveguide

[5] http://camfr.sourceforge.net/

with a silica core and an air cladding. The considered photonic crystal structure is a two-dimensional triangular lattice of dielectric rods of silicon surrounded by a homogeneous dielectric medium of silica. The second, hereafter named hole structure, consists of a 0.5μm-wide dielectric waveguide with a silicon core and an air cladding. The photonic crystal structure in this case is a two-dimensional triangular lattice of air holes surrounded by a homogeneous dielectric medium of silicon. The main parameters of both photonic crystal structures are summarized in table 3.1.

Figure 3.5 shows the dispersion relation of the rod and hole photonic crystal waveguides and of the dielectric waveguides considered in each case. The dispersion relations have been obtained by plane wave expansion method [Joh01] for the photonic crystal waveguides and by CAMFR for the dielectric waveguides. For the rod structure, it can be seen that both the dielectric and the photonic crystal waveguide are singlemode. The lattice constant has been calculated to get transmission at λ=1.55 μm for the central normalized frequency of the guided mode.

For the hole structure, it can be seen in figure 3.5 that the dielectric waveguide is singlemode while two guided modes, with odd and even symmetries in the transversal direction, appear for the photonic crystal waveguide. The lattice constant has been calculated to get transmission at λ=1.55 μm for a normalized frequency where only the even mode exists. However, as the dielectric waveguide mode has even symmetry, only the even mode can be excited in the photonic crystal waveguide.

3.5.2 Coupling efficiency dependence on cut position

Coupling losses between conventional dielectric and photonic crystal waveguides are caused due to the different guiding mechanism in both waveguides, which gives rise to a mode mismatch. Modal properties in dielectric waveguides are unaltered along the propagation direction but, in photonic crystals, they change within the basic period that defines the photonic crystal. Therefore, the mode mismatch between both waveguides will depend on the chosen cut position within the basic period.

Figures 3.6(a) and 3.7(a) show the transmission efficiency as a function of the chosen cut position within the basic period normalized to the lattice constant (z/a) for the rod and hole structure respectively. The frequency of operation is the one shown in table 3.1.

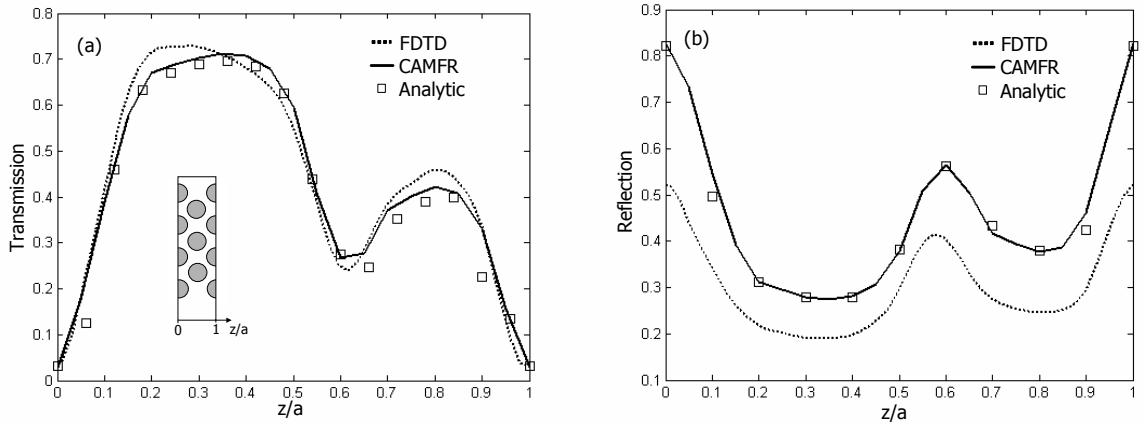

Figure 3.6.- (a) Transmission and (b) reflection efficiency for the butt-coupling between the dielectric waveguide and the photonic crystal waveguide as a function of the chosen cut position within the basic period normalized to the lattice constant (z/a) for the rod structure. The inset shows the basic period used, the propagation direction is in the z-axis.

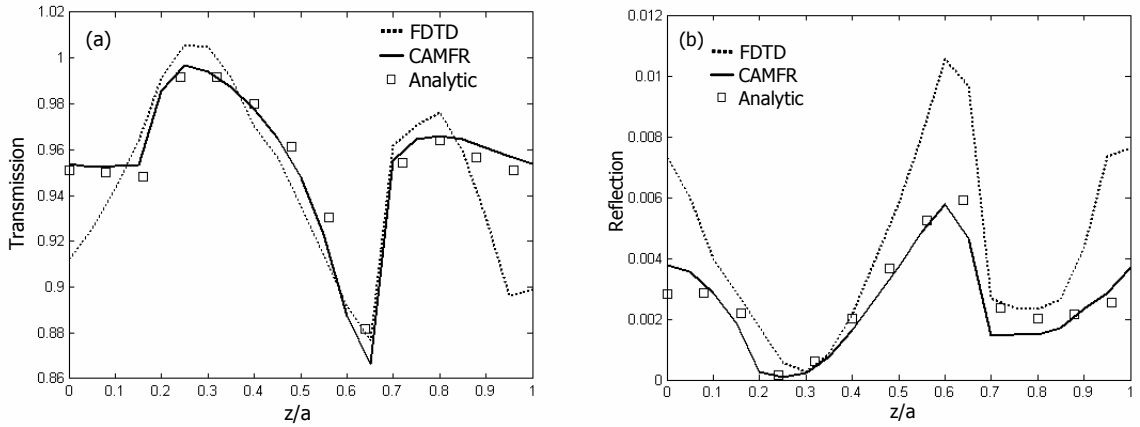

Figure 3.7.- (a) Transmission and (b) reflection efficiency for the butt-coupling between the dielectric waveguide and the photonic crystal waveguide as a function of the chosen cut position within the basic period normalized to the lattice constant (z/a) for the hole structure.

The inset of figure 3.6(a) shows the basic period considered where the propagation direction is along the z-axis. It should be noticed that the cut position is only varied along the ΓK direction. Results are shown for CAMFR, FDTD and the analytic expressions derived in section 3.3. It can be seen that analytic and simulation results show an excellent agreement especially with CAMFR as the parameters in both simulation and analytic calculations are the same. Reflection into the dielectric waveguide has also been calculated and is shown in figure 3.6(b) and 3.7(b) for the rod and hole structure respectively. It can be seen that analytic and simulation results are also in agreement. However, FDTD results are somewhat different for the rod structure. This is because in this case, the reflection was calculated by integrating the power only along the width of the input waveguide.

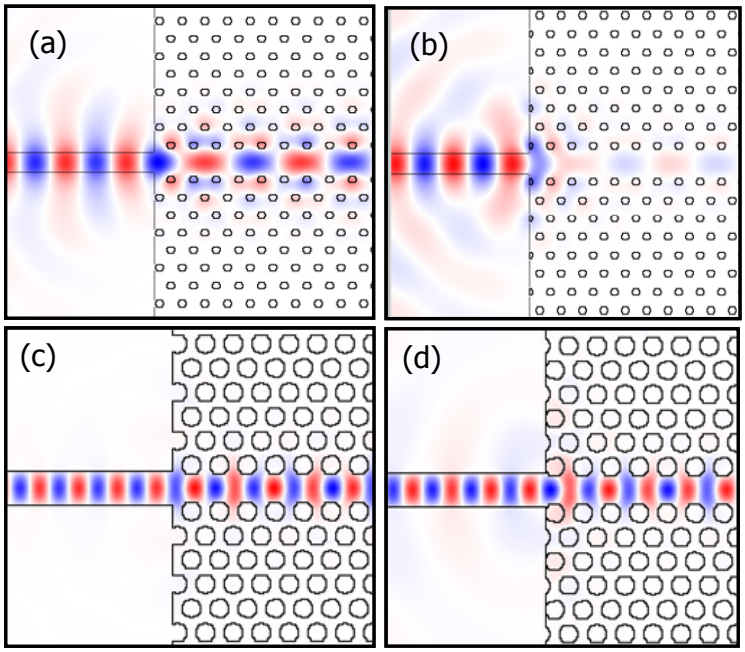

Figure 3.8.- Electric field diagram in the rod structure for (a) *z/a*=0.3 and (b) *z/a* =0.0 and magnetic field diagram in the hole structure for (c) *z/a* =0.3 and (d) *z/a*=0.66.

However, in the rod structure, as the index contrast of the dielectric waveguide is lower, the mode will be less confined and it will expand into the cladding. Therefore, the power calculation is underestimated but the shape remains unaltered.

From figures 3.6 and 3.7, it can be seen that the transmission response is asymmetric in both structures although the absolute value of the total field is symmetric within the basic period. This behaviour can be interpreted from the transmission expression (see Eq. (3.22)), in which the forward and backward components of the Bloch modes are responsible for the asymmetric response as they have different values depending on the chosen cut position. It is also interesting to notice that the transmission expression is similar to the Airy formula [Yeh98] but without any propagation terms as medium I-II has zero length. On the other hand, it can be seen that the reflection is proportional to the backward components multiplied by the transmission (see Eq. (3.23)). In the hole structure, the transmission is very high while the reflection is maintained very low. Therefore, the low reflection implies that the backward components should be very low in order to counteract the high transmission. On the other hand, a good mode profile matching is expected at the optimum cut position due to the coupling efficiency improvement. In order to show this effect the field diagrams have been calculated at different cut positions.

Figures 3.8(a)-(b) show the electric field diagrams in the rod structure for z/a=0.3 and z/a=0.0 respectively, which corresponds to the maximum and minimum transmission efficiency shown in figure 3.6(a).

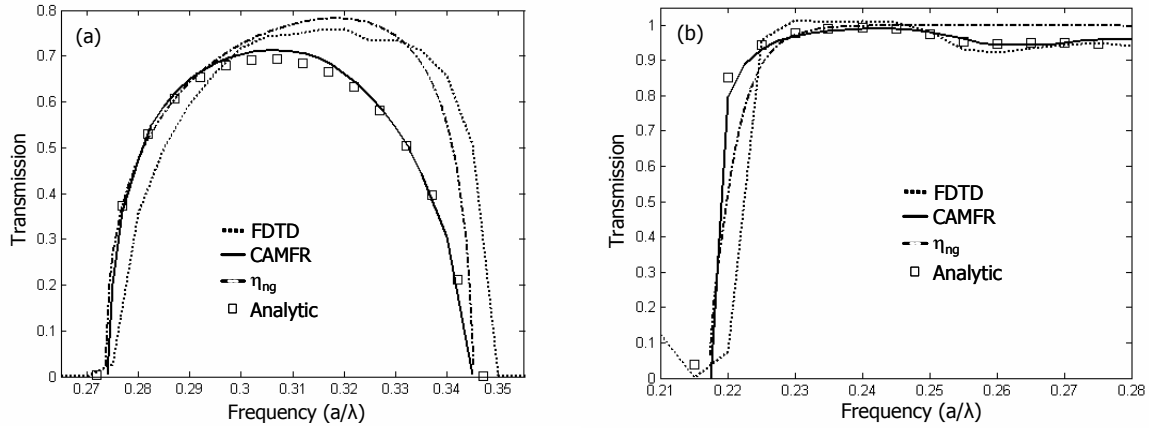

Figure 3.9.- Transmission efficiency for the butt-coupling between the dielectric waveguide and the photonic crystal waveguide as a function of the normalized frequency for (a) the rod structure with z/a=0.3 and (b) the hole structure with z/a=0.3.

Figures 3.8I-(d) show the magnetic field diagram in the hole structure for z/a=0.3 and z/a=0.66 respectively, which again corresponds to the maximum and minimum transmission efficiency shown in figure 3.7(a). It can be seen that at the optimum cut position a high coupling efficiency is achieved which reflects in a good mode profile matching. However, at the non optimum cut position the reflection increases and the coupling efficiency decreases, which is reflected in a poor mode profile matching. It is also interesting to point out that the higher reflection in the rod structure could be attributed to the fact that the waveguide mode is less confined, because of the smaller index contrast, which increases the mode profile mismatch. However, the reflection is also highly dependent on the modal properties of the photonic crystal waveguide, as it can be deduced from the results shown in figure 3.6, so that it can not be stated that a more confined waveguide mode will reduce the reflection.

3.5.3 Coupling efficiency dependence on frequency

We have seen that the transmission efficiency can be significantly improved at a fixed frequency by choosing the optimum interface. Now, we will study the dependence of transmission efficiency on frequency which is mainly determined by the difference in the dispersion relations between the dielectric and photonic crystal waveguides. In figure 3.5(b), it can be seen that for the hole structure the dispersion relations of the dielectric and photonic crystal waveguide are very similar. This will result in an efficient coupling and high transmission will be achieved over the whole bandwidth of the photonic crystal mode. On the other hand, in the rod structure the dispersion relations of both waveguides differ more (see figure 3.5(a)) and therefore the frequency response will be worse.

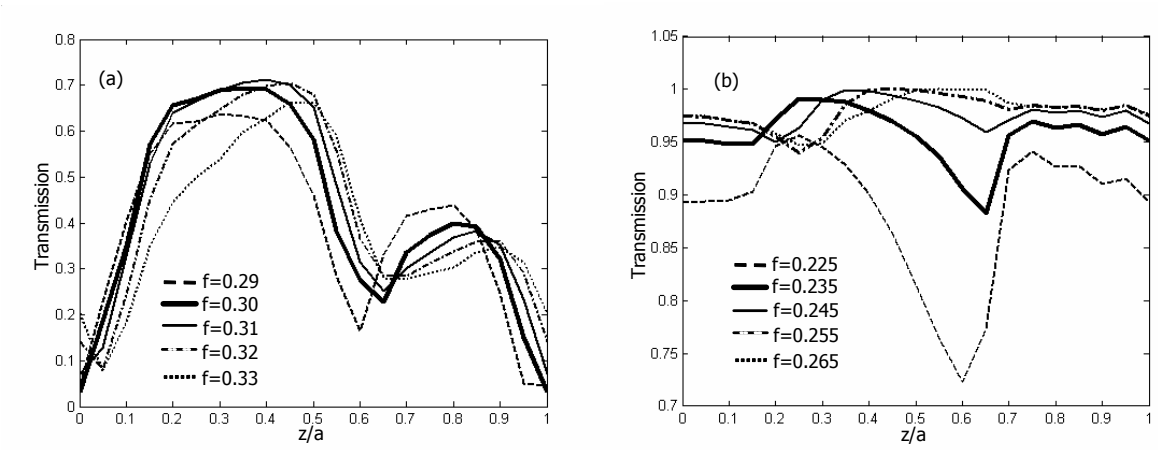

Figure 3.10.- Transmission efficiency for the butt-coupling between the dielectric waveguide and the photonic crystal waveguide as a function of the chosen cut position within the basic period normalized by the lattice constant (z/a) for different normalized frequencies and for (a) the rod structure and (b) the hole structure.

Figures 3.9(a)-(b) show the transmission spectra for the hole and rod structures respectively considering in both cases the optimum interface position (z/a=0.3) which corresponds to the maximum transmission. Analytic results are compared to CAMFR and FDTD simulations showing a good agreement. However, it can be seen that FDTD results are slightly shifted to higher frequencies especially in the rod structure. We attribute this shifting to an artifact of FDTD as the results obtained by CAMFR are also in agreement with the band diagrams shown in figure 3.5, which were calculated with the plane wave expansion method. On the other hand, the dash-dotted results shown in figure 3.9 have been calculated with the scalar Fresnel equation but involving the group indexes of the dielectric and photonic crystal waveguide and given by

$$\eta_{ng} = 4\, n_g^{phc} n_g^{wg} \Big/ \left(n_g^{phc} + n_g^{wg}\right)^2 \tag{3.41}$$

where n_g^{phc} and n_g^{wg} are the group index of the photonic crystal and dielectric waveguides respectively. The group index is inversely related to the group velocity and the group velocity is determined by the variation of the frequency with respect to the wave vector, i.e. the slope of the dispersion relation. Therefore, the group indexes can be easily calculated from the dispersion curves.

From the results presented in figure 3.9, it can be seen that the transmission spectrum presents a parabolic shape in the rod structure while it is relatively flat in the hole structure. In both cases, it is very remarkable to notice that even though the optimum cut position has been obtained for a fixed frequency, the transmission spectrum shape is similar to the one obtained with Eq. (3.41).

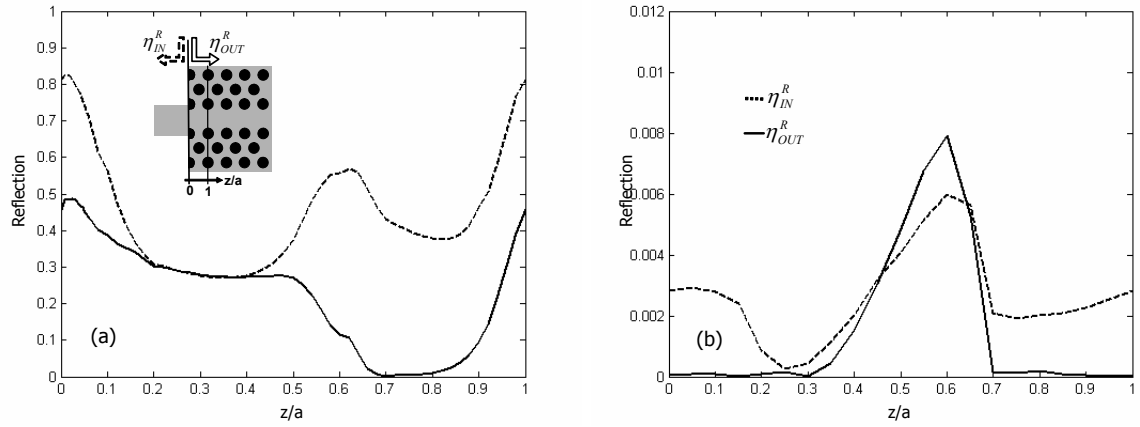

Figure 3.11.- Reflection as a function of the chosen cut position within the basic period normalized by the lattice constant (z/a) for different normalized frequencies and for (a) the rod structure and (b) the hole structure. The reflection is different depending on if the light is transmitted into or out of the photonic crystal.

This indicates that the transmission efficiency dependence on frequency mainly stems from the group index mismatch. However, the influence of the frequency on the cut position has also been analyzed. Figures 3.10(a)-(b) show the transmission efficiency as a function of the cut position for the rod and hole structure respectively and considering different frequencies. Results have only been calculated with the analytic expression showing the advantages of the developed formulation as the computation time was significantly reduced. In both structures, it can be seen that the transmission response does not change significantly with frequency and the optimum cut position is only slightly shifted. It is interesting to notice that the maximum transmission efficiency in all cases is similar to that predicted with Eq. (3.41). On the other hand, it can be seen that the transmission efficiency variation with the chosen cut position in the hole structure increases as the frequency is close to the band edge. We will show that this behaviour can be partly explained by looking at the forward and backward components of the fundamental guided Bloch mode.

3.5.4 Reflection into photonic crystals

Because of the reciprocity theorem, the transmission matrix that characterizes the transmission from the dielectric waveguide into the photonic crystal waveguide, T_{IN}, is equal to the transpose of the transmission matrix that characterizes the transmission from the photonic crystal waveguide into the dielectric waveguide, T_{OUT}. However, this is not the case for the reflection matrices, R_{IN} and R_{OUT}, which are different. Thus, the transmission efficiency from the fundamental mode of the dielectric waveguide into the fundamental guided Bloch mode and vice versa, i.e. Eqs. (3.24) and (3.38), are the same while the reflection, i.e. Eqs. (3.25) and (3.37), are different.

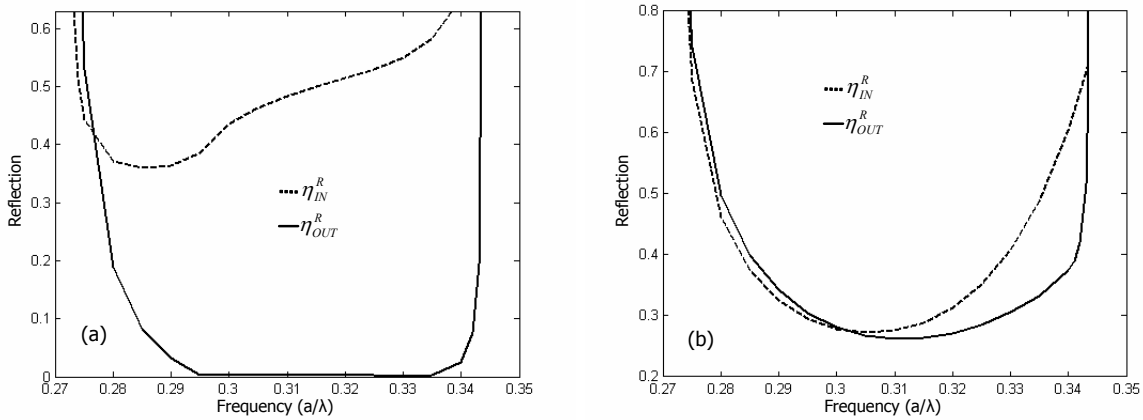

Figure 3.12.- Reflection as a function of the normalized frequency for the input and output coupling of the photonic crystal waveguide at the cut positions (a) z/a=0.7 and (b) z/a=0.3.

Figure 3.11 shows the reflection as a function of the chosen cut position for the rod and hole structures considering two different cases: (i) input coupling where the light is propagated from the dielectric waveguide into the photonic crystal waveguide and (ii) output coupling where the light is propagated from the photonic crystal waveguide into the dielectric waveguide. It is important to notice that the reflection for the input coupling case is into the dielectric waveguide while the reflection for the output coupling case is into the photonic crystal waveguide. In the hole structure, the reflection is very low in both cases and the responses have a similar shape, as it is shown in figure 3.11(b). However, it can be seen in figure 3.11(a) that the reflection for the rod structure as a function of the cut position is different for both cases except for the range of z/a between 0.2 and 0.4, which corresponds to the range where the transmitted power is maximum. However, the minimum reflection for the output coupling is not achieved for the maximum transmission. The former is obtained at z/a=0.7 while the latter is obtained at z/a=0.3.

Hereafter, we will focus on the rod structure. Figure 3.12 shows the reflection spectra for the input and output coupling cases at the cut positions that give the minimum reflection into the photonic crystal waveguide (z/a=0.7) and the maximum transmission efficiency (z/a=0.3). The transmission efficiency at z/a=0.3 is around 70% while the reflection into the dielectric waveguide (input coupling) is around 30% at the normalized frequency of 0.3(a/λ). Therefore, coupling losses are mainly due to reflection, while scattering losses are negligible. Scattering losses are due to the coupling to radiation modes which can only be excited in the dielectric waveguide, as depicted in figure 3.13(a). Therefore, it can be expected that radiation modes will also not excited for the output coupling which could explain the similarity of the reflection spectra between both input and output coupling shown in figure 3.12(b).

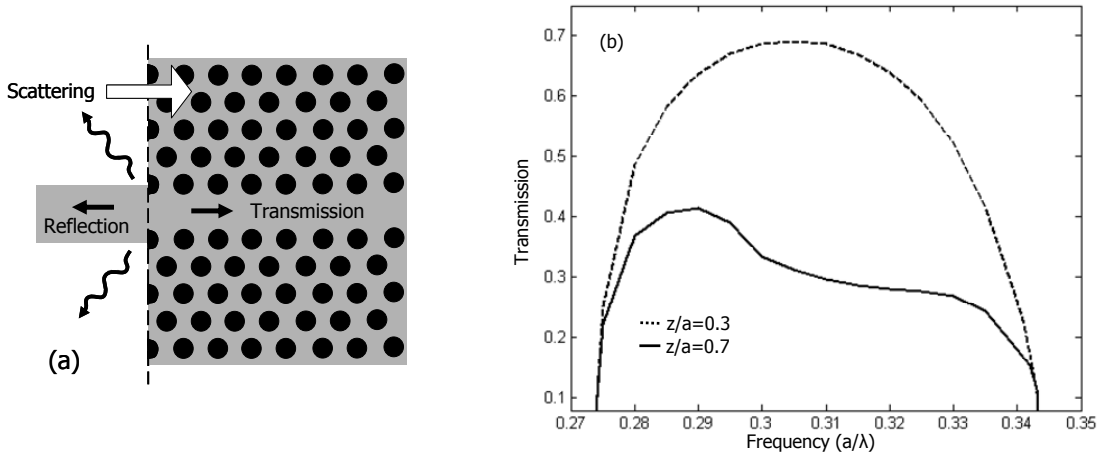

Figure 3.13.- (a) Transmission, reflection and scattering at the interface between the dielectric waveguide and the photonic crystal waveguide when light propagates from the former into the latter. (b) Transmission efficiency as a function of the normalized frequency for the rod structure considering the cut positions that give the minimum reflection into the photonic crystal waveguide (z/a=0.7) and the maximum transmission efficiency (z/a=0.3).

However, a higher mode mismatch occurs at z/a=0.7 which significantly increases the coupling to radiation modes, i.e. scattering losses. In this case, the transmission is around 30% at the normalized frequency of 0.3(a/λ) while the reflection into the dielectric waveguide is around 40% so that scattering losses will be around 30%. Therefore, a high coupling to radiation modes can be expected for the output coupling, which could explain the very low reflection achieved into the photonic crystal waveguide.

The minimization of the reflection that occurs when the light is extracted from the photonic crystal waveguide may be useful to avoid Fabry-Perot resonances in the transmission spectrum of photonic crystal structures of finite length. However, the transmission efficiency is reduced so a trade-off between maximum transmission and low reflection will exist. Figure 3.13(b) shows the transmission efficiency as a function of the normalized frequency for z/a=0.3 and z/a=0.7 and considering a semi-infinite photonic crystal waveguide. The left part of figure 3.14 shows the considered photonic crystal structure of finite length where the optimum cut positions can be designed for both input and output interfaces. The transmission efficiency as a function of the normalized frequency for this photonic crystal structure is shown at the right part of figure 3.14 for different cut positions. The transmission spectra were calculated by means of FDTD simulations. An incident pulsed field was launched at an input dielectric waveguide so that the transmission spectrum was obtained by calculating the overlap integral between the launched field and the measured field at output dielectric waveguide.

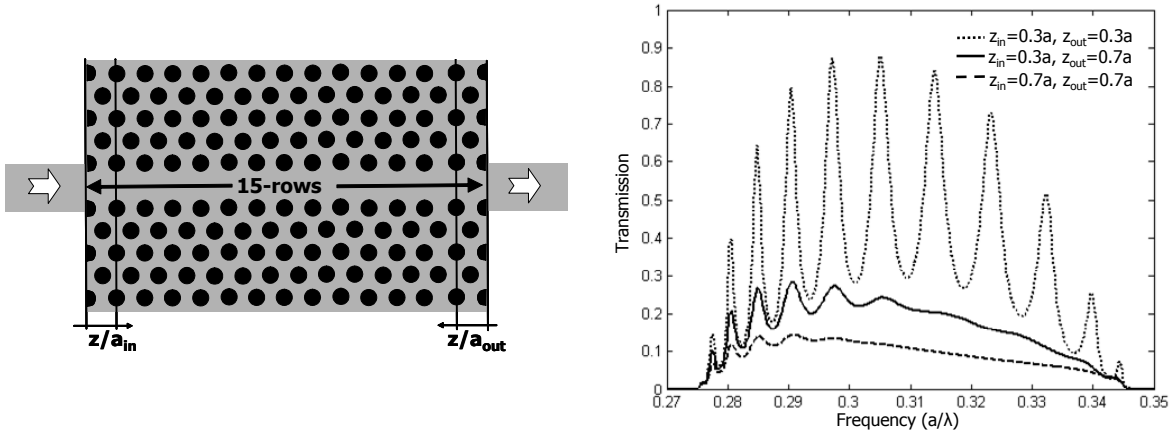

Figure 3.14.- Photonic crystal structure of finite length considered and the corresponding transmission efficiency as a function of the normalized frequency calculated by means of FDTD simulations. Different cut positions in both interfaces of the finite length photonic crystal waveguide are analyzed.

When the input and output interfaces are chosen to achieve the maximum transmission efficiency ($z/a_{in}= z/a_{out}$ =0.3), notable Fabry-Perot resonances appear in the transmission spectrum as the reflection into the photonic crystal waveguide is significant. It can be seen that the transmission at the resonance peaks is near unity at the frequencies where scattering is negligible. Another possibility is to choose the input and output interfaces to minimize the reflection into the photonic crystal waveguide ($z/a_{in}= z/a_{out}$=0.7). In this case, it can be seen that the Fabry-Perot resonances are eliminated but the overall transmission efficiency is very low.

One possible approach to improve the transmission efficiency without increasing Fabry-Perot resonances is to use at the output interface the cut position which gives minimum reflection into the photonic crystal waveguide (z/a_{out}=0.7) and use at the input interface the cut position which gives maximum transmission (z/a_{in}=0.3). Thus, the transmission efficiency is improved without increasing the Fabry-Perot peaks as the reflection at the output interface is still negligible. However, it can be seen that some resonances appear at the frequency range between 0.275(a/λ) and 0.3(a/λ), which is in agreement with the increase of reflection that can be seen in figure 3.12(a). The agreement between FDTD results and the analytic results for the corresponding semi-infinite photonic crystal structure prove the validity of the derived expressions.

3.5.5 Differences between rod and hole structures

We have seen that the coupling is much better for the hole structure than for the rod structure. As already mentioned, coupling losses between dielectric and photonic crystal waveguides are derived from the different guiding mechanism in the two

waveguides. In the dielectric waveguide, the guiding mechanism relies only on the index-contrast effect. On the other hand, the guiding mechanism in photonic crystals is determined by the propagation of Bloch modes. In principle, the properties of the guided Bloch mode are due to distributed Bragg reflections but they can also be affected by the total internal reflection effect depending on the features of the photonic crystal [Joh00a, Adi01]. In the hole structure, the core refractive index of the photonic crystal waveguide is higher than in the surrounding medium. In this case, the properties of the Bloch mode will be affected by the total internal reflection effect so that the modal properties in the dielectric and photonic crystal waveguides will be more similar, yielding to a high efficient coupling. This explains the similarity of the dispersion relations shown in figure 3.5(b).

On the other hand, the photonic crystal waveguide in the rod structure has a core refractive index smaller than the surrounding medium. In this case, the properties of the guided Bloch mode are only affected by the photonic band gap (PBG) effect so modal properties in the dielectric and photonic crystal waveguides will differ more, yielding to a worse coupling. However, we have seen that the transmission efficiency in the rod structure is highly dependent on the chosen cut position with values that go from lower than 5% to near 70%. On the other hand, the transmission efficiency variation with the chosen cut position is very low in the hole structure with values near 100% although it increases if frequencies close to the band edge are considered. In order to give an explanation of this behavior, we have analyzed the forward and backward components of the fundamental guided Bloch mode. The following factor for the forward component has been defined

$$\gamma_{FW} = \frac{\left|\left\langle \mathrm{E}_{FW}, \mathrm{H}^{*}_{FW} \right\rangle\right|}{\left|\left\langle \mathrm{E}_{FW}, \mathrm{H}^{*}_{FW} \right\rangle\right| + \left|\left\langle \mathrm{E}_{BW}, \mathrm{H}^{*}_{BW} \right\rangle\right|} \tag{3.42}$$

where the subscript *FW* and *BW* denotes the forward and backward components of the total field respectively. A similar expression has been used for the backward component. Figure 3.15 shows the factor values as a function of the chosen cut position within the basic period normalized to the lattice constant for the rod and hole structures. Results are only shown for the frequency of operation shown in table 3.1, for the sake of simplicity. A strong interaction between forward and backward components can be observed in the rod structure, which gives rise to a large difference between the Bloch mode and the waveguide mode. Thereby, the mode profiles in the dielectric and photonic crystal waveguide are rather different, as it is shown in figure 3.8(a), so that a higher mode mismatch exists which increases reflection and scattering.

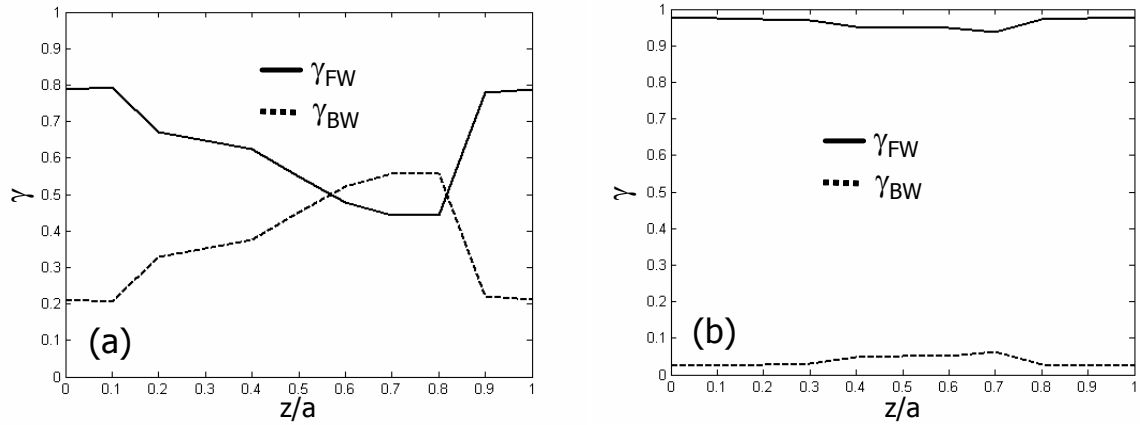

Figure 3.15.- Influence of forward and backward components as a function of the cut position within the basic period normalized to the lattice constant (z/a) for the (a) rod and (b) hole structures.

The results shown in figure 3.15(a) are only related with to the fundamental Bloch mode. However, the increase of scattering means that coupling losses are also due to interaction with higher order modes. Therefore, clear correspondence can not be established between the results shown in figure 3.6(a) and figure 3.15(a). On the other hand, it can be seen that the Bloch mode in the hole structure is mainly determined by the forward component. Furthermore, the γ_{FW} and γ_{BW} values are mainly constant along the different cut positions within the basic period, which explains the low dependence of the transmission efficiency with the chosen cut position shown in figure 3.7(a). We attribute this behaviour to the total internal reflection effect that results in a large similarity between the Bloch mode and the waveguide mode. This similarity can also be shown in the mode profiles shown in figure 3.8(c) and explains the results reported in [Adi01] where it was shown that the properties of the photonic crystal waveguide can be similar to those obtained from an effective corrugated waveguide.

For different frequencies we obtained similar curves for both rod and hole structures. In the later, we observed that, for frequencies close to the band edge, the reduction of the transmission efficiency as well as the higher variation with the chosen cut position, shown in figure 3.10(b), was associated with an increase of the backward components indicating a higher mode mismatch. However, we noticed that the reflection was maintained very low indicating that coupling losses mainly arose due to scattering. Therefore, the steep dip, shown in figure 3.10(b) and accentuated for frequencies close to the band edge, can be attributed to the complex interplay between mode mismatch and interaction with higher order modes.

3.5.6 Relation to classical approximate formula

We have also studied the usefulness of the classical approximate formula employed to study fiber-coupling issues (see e.g. [Mur88]) for interfaces involving photonic crystal structures. This formula can also be derived from Eq. (3.1) and (3.2) considering that medium I and II are *z*-invariant. In this case, the reflection is neglected and the transmission is obtained by taking the right cross product of (3.1) with H_i^{II} and the left cross product of (3.2) with E_i^{II}. However, as the reflection has been neglected, the transmission coefficients obtained from (3.1) and (3.2) will be different

$$\left\langle \mathrm{E}_p^I, \mathrm{H}_i^{II} \right\rangle = \sum_j T_{j,p}^E \left\langle \mathrm{E}_j^{II}, \mathrm{H}_i^{II} \right\rangle \tag{3.43}$$

$$\left\langle \mathrm{E}_i^{II}, \mathrm{H}_p^I \right\rangle = \sum_j T_{j,p}^H \left\langle \mathrm{E}_i^{II}, \mathrm{H}_j^{II} \right\rangle \tag{3.44}$$

The transmission from the incident mode into the desired transmitted mode is obtained using the orthogonality relation in (3.43) and (3.44) which yields

$$T_E = \left\langle \mathrm{E}_I, \mathrm{H}_{II} \right\rangle \Big/ \left\langle \mathrm{E}_{II}, \mathrm{H}_{II} \right\rangle \tag{3.45}$$

$$T_H = \left\langle \mathrm{E}_{II}, \mathrm{H}_I \right\rangle \Big/ \left\langle \mathrm{E}_{II}, \mathrm{H}_{II} \right\rangle \tag{3.46}$$

The power coupling efficiency is then described by

$$\eta = \frac{\mathrm{Re}\{T_E T_H^* \left\langle \mathrm{E}_{II}, \mathrm{H}_{II}^* \right\rangle\}}{\mathrm{Re}\{\left\langle \mathrm{E}_I, \mathrm{H}_I^* \right\rangle\}} \tag{3.47}$$

where *Re* denotes the real part. However, the above derivation is normally followed by using the conjugated magnetic field, which gives rise to the same results provided we have lossless materials. Thus, (3.47) results in

$$\eta = \frac{\mathrm{Re}\{\left\langle \mathrm{E}_I, \mathrm{H}_{II}^* \right\rangle \left\langle \mathrm{E}_{II}, \mathrm{H}_I^* \right\rangle \Big/ \left\langle \mathrm{E}_{II}, \mathrm{H}_{II}^* \right\rangle\}}{\mathrm{Re}\{\left\langle \mathrm{E}_I, \mathrm{H}_I^* \right\rangle\}} \tag{3.48}$$

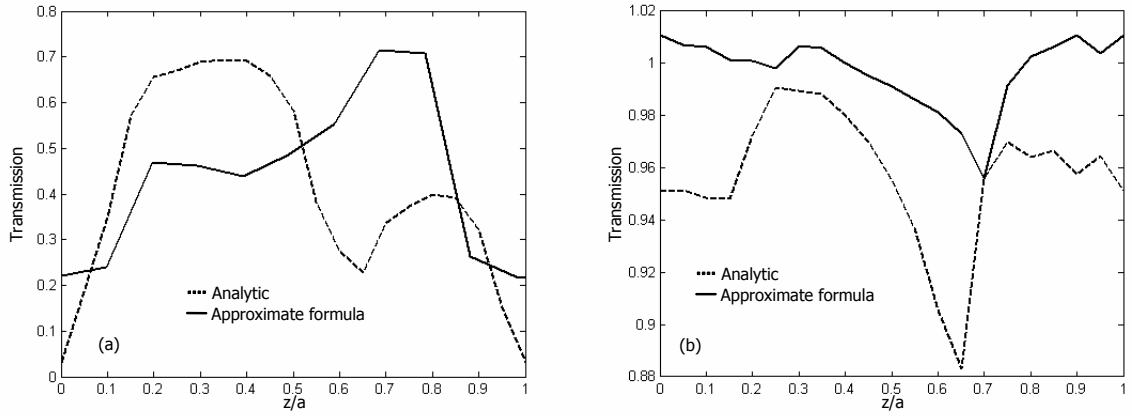

Figure 3.16.- Comparison between the results obtained with the analytic expression and the classical approximate formula employed to study fiber-coupling issues. The transmission is shown as a function of the chosen cut position normalized to the lattice constant (z/a) for the (a) rod and (b) hole structures.

In conventional index-guiding waveguides, the tangential component of the magnetic and electric fields are related by the wave impedance allowing us to simplify (3.48) into the well-known formula

$$\eta = \frac{\left|\left\langle \mathrm{E}_I , \mathrm{E}_{II}^* \right\rangle\right|^2}{\left\langle \mathrm{E}_I , \mathrm{E}_I^* \right\rangle \left\langle \mathrm{E}_{II} , \mathrm{E}_{II}^* \right\rangle} \tag{3.49}$$

The general expression (3.48) was successfully used to study radiation losses of a structure formed between a dielectric waveguide and a semi-infinite Bragg mirror [Pal01]. In that work, the non-propagating fundamental Bloch mode operating in the PBG was considered and it was obtained that the reflection of the structure could be calculated as η^2 but using the forward field of the Bloch mode instead of the total field. The prove of this assessment is out of the scope of this work, however, the fact of using only the forward field in order to calculate η can be understood from Eq. (3.20) that shows that the transmission only involves the forward components when the input waveguide has the same index profile than the interfacing layer of the photonic crystal waveguide, as occurs in [Pal01]. In our case, we have analyzed the usefulness of (3.48) in order to calculate the transmission efficiency in the rod and hole structure. As a difference to [Pal01], the transmission in this case relies on the fundamental guided propagating Bloch mode. In principle, the above derivation is not valid when medium II is a photonic crystal because the orthogonality relation is not true if the cross product is taken with the forward field of the Bloch mode. This implies that the coupling to higher order Bloch modes in addition to the backward components of the fundamental Bloch mode should be negligible to ensure the validity of the formula.

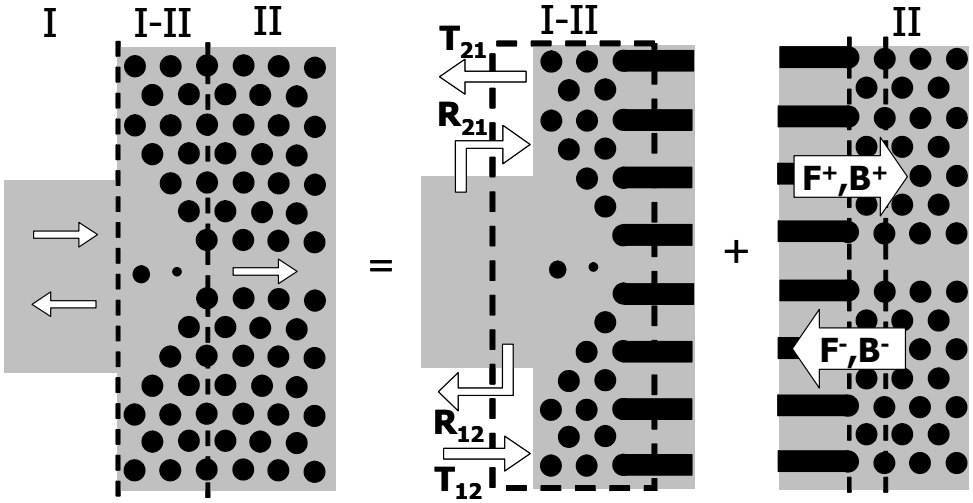

Figure 3.17.- Analyzed structure to prove the proposed semi-analytic approach. The structure is formed by a dielectric waveguide coupled to a semi-infinite photonic crystal waveguide by using an especially designed two-defect configuration placed within a photonic crystal taper. T_{12}, R_{21}, T_{21} and R_{12} are the transmission and reflection matrixes calculated in medium I-II while F_+ (F_-) and B_+ (B_-) are the forward and backward components of the forward (backward) propagating Bloch modes calculated at the interface layer between medium I-II and medium II.

Therefore, we obtained more or less consistent results for the hole structure but not for the rod structure, as it can been in figure 3.16. This result can also be interpreted by looking at the forward and backward components of the fundamental guided Bloch mode. As previously shown, the fundamental guided Bloch mode in the hole structure is mainly determined by the forward components however a stronger interaction between the forward and backward components exists in the rod structure. Furthermore, a high transmission is achieved in the former case so that the coupling to higher order Bloch modes as well as the reflection can be neglected. However, the results obtained with (3.48) also begin to disagree with exact analytic results when the reflection increases, as it can be seen in figure 3.16(b). Therefore, we conclude that only in very specific cases, Eq. (3.48) can be used for coupling issues in photonic crystals.

3.6 Semi-analytic treatment of complex structures

In recent years, coupling losses in photonic crystal circuits have been mainly studied by means of simulations. Only a few works have been focused in the modeling of the interface between photonic crystal circuits and external media such as free space of dielectric waveguides [Pal01, Bot03, Ush03, Bis04]. The modeling of photonic crystal circuits with efficient and accurate approaches may significantly reduce the computation time, which is usually very long in conventional numerical methods such as the FDTD method. The previously

derived closed-form expressions for the transmission and reflection at an interface between a dielectric waveguide and a semi-infinite photonic crystal waveguide can also be used for analyzing coupling issues in more complex photonic crystal structures by means of a semi-analytic approach. The proposed approach is valid for any kind of complex structure as long as the input medium has an invariant index profile along the propagation direction and the output medium is semi-infinitely periodic along the propagation direction or vice versa. The transmission and reflection matrices are

$$T = F_+^{-1}\left(I - R_{21}B_+F_+^{-1}\right)^{-1}T_{12} \tag{3.50}$$

$$R_{IN} = R_{12} + T_{21}B_+T \tag{3.51}$$

$$R_{OUT} = -\left(B_- - R_{21}F_-\right)^{-1}\left(B_+ - R_{21}F_+\right) \tag{3.52}$$

where F_+ and B_+ are the forward and backward components of the forward propagating Bloch modes while F_- and B_- are the forward and backward components of the backward propagating Bloch modes. These expressions are identical to (3.22), (3.23) and (3.37) respectively. The transmission matrix is (3.22) instead of (3.38) because we obtained a much better numerical stability. The semi-analytic character of the proposed approach is because, in this case, the transmission and reflection matrices T_{12}, T_{21}, R_{12} and R_{21} depend on the structure placed between the invariant medium and the semi-infinite periodic medium so it must be calculated by means of a numerical tool. Here, we use CAMFR to calculate the T_{12}, T_{21}, R_{12} and R_{21} matrices as well as the forward and backward components of the Bloch modes.

Figure 3.17 shows an example of structure that can be analyzed. T_{12}, T_{21}, R_{12} and R_{21} are calculated for medium I-II considering that the input interface is a dielectric waveguide and the output interface is the layer with an invariant index profile that depends on the cut position in the photonic crystal waveguide, as depicted in the middle part of figure 3.17. The transmission, T, and reflection, R_{IN}, matrices describe the coupling for light propagating from the invariant medium (medium I in figure 3.17) into the periodic structure (medium II in figure 3.17) while the reflection matrix, R_{OUT}, describes the coupling for light propagating from the periodic medium into the invariant medium. In the latter case, the transmission matrix can be simply obtained by the transpose of T due to the reciprocity theorem. Thus, if the modes are normalized, the transmitted and reflected power of the j-Bloch mode into the i-mode of the dielectric waveguide and vice versa is given by

$$\eta_T = \left|T_{i,j}\right|^2 \tag{3.53}$$

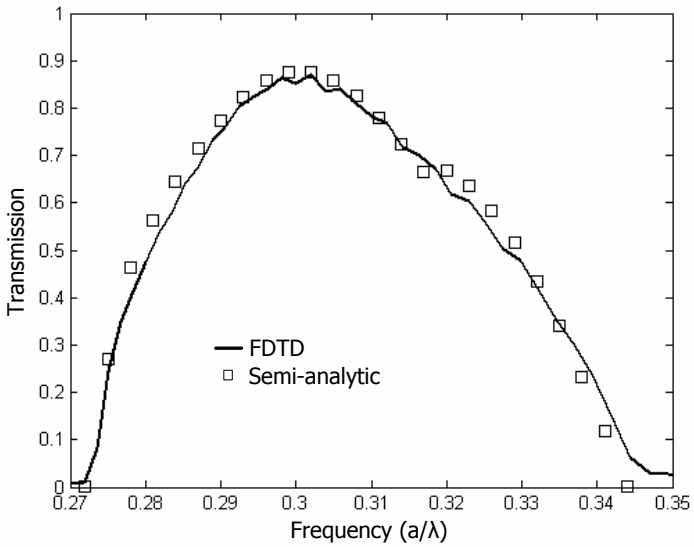

Figure 3.18.- Transmitted power as a function of the normalized frequency for the structure shown in figure 3.17. Semi-analytic results are compared to FDTD simulations.

$$\eta_R = \left| R_{i,j} \right|^2 \tag{3.54}$$

where $T_{i,j}$ and $R_{i,j}$ are the *i*-row and *j*-column of the corresponding transmission and reflection matrices.

The proposed semi-analytic approach has been first proven for the structure shown in figure 3.17 considering a 3μm-wide dielectric waveguide of silica surrounded by an air cladding and a photonic crystal formed by a two-dimensional triangular lattice of dielectric rods of silicon embedded in silica. The dielectric waveguide is coupled to a semi-infinite photonic crystal waveguide by using an especially designed two-defect configuration placed within a photonic crystal taper to improve the coupling efficiency. The structure shown in figure 3.17 will be carefully studied in the next chapter. The transmitted power as a function of the normalized frequency is shown in figure 3.18. Semi-analytic results are compared with FDTD simulations. In the latter, the fundamental mode of the dielectric waveguide was excited by a monochromatic continuous wave with normalized power. The transmitted power was then calculated by integrating the power flux inside the photonic crystal waveguide. It can be seen that there is a very good agreement between semi-analytic results and FDTD simulations.

Figure 3.19 shows the spectrum of the reflected power into the dielectric waveguide. Semi-analytic results were calculated by substituting (3.51) into (3.54). It is important to notice that the 3μm-wide dielectric waveguide is multimode for the frequency range of interest.

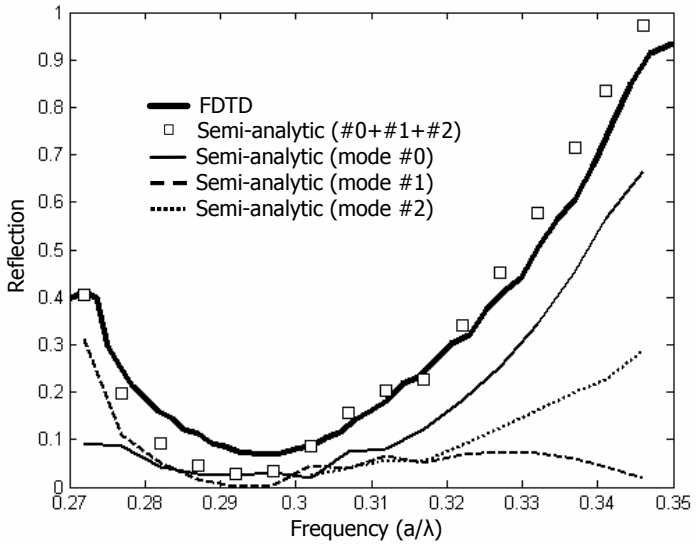

Figure 3.19.- Reflected power into the dielectric waveguide as a function of the normalized frequency for the structure depicted in figure 3.17. Semi-analytic results are shown for each of the guided modes in the dielectric waveguide as well as for the total sum of the power, which is compared to that calculated by FDTD simulations.

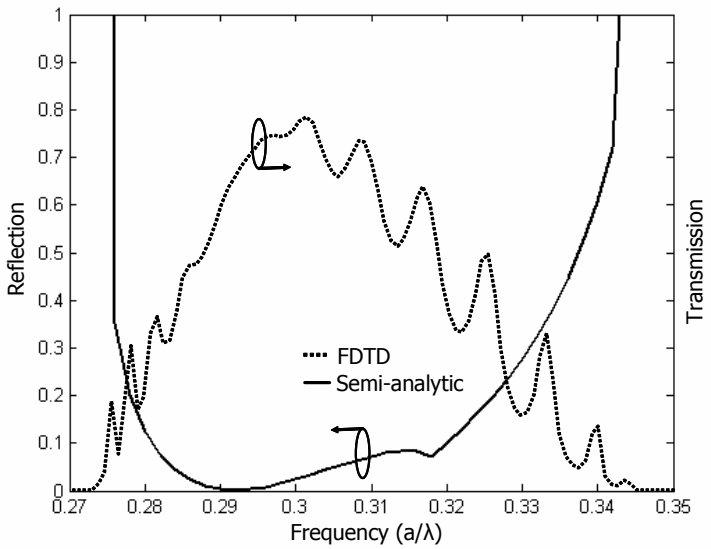

Figure 3.20.- Reflected power into the photonic crystal waveguide as a function of the normalized frequency for the structure shown in figure 3.17 but considering that the light propagates from the photonic crystal to the dielectric waveguide. The transmitted power is also shown for the same structure used to couple light into and out of a photonic crystal waveguide of finite length.

The waveguide supports two even guided modes below the frequency of 0.3(a/λ) but three even guided modes above this frequency. In FDTD, the reflected power was obtained by integrating the power flux along the dielectric waveguide at a certain distance before the position of the light source. Therefore, the power carried by each of the guided modes can not be separately calculated and only the total power is obtained. However, the proposed semi-analytic approach allows calculating the reflection into each one of the guided modes. In figure 3.19, it can be seen that the power is not only reflected into the fundamental mode but it is spread into the different guided modes that the dielectric waveguide supports. Furthermore, it can also be seen that the sum of the power carried by each of the guided modes is in good agreement with the reflected power calculated by FDTD.

The reflection into the photonic crystal waveguide when the light propagates from the photonic crystal into the dielectric waveguide has also been analyzed by using (3.52) into (3.54). Figure 3.20 shows the reflected power as a function of the normalized frequency. In this case, FDTD simulations results by using a monochromatic continuous wave were not accurate because the fundamental guided Bloch mode could not be excited within the photonic crystal waveguide. However, semi-analytic results can still be validated by calculating with FDTD the transmitted spectrum of a photonic crystal waveguide of finite length coupled to input and output dielectric waveguides using the optimized photonic crystal taper. Semi-analytic results (solid line) show that there is a frequency range between 0.285(a/λ) and 0.3(a/λ) where the reflection is almost negligible. Therefore, Fabry-Perot resonances do not appear in the transmission spectra calculated by FDTD (dashed line) at these frequencies.

The proposed approach can also be used to analyze the transmission and reflection properties of more complex structures such as a coupled-cavity waveguide (CCW) [Yar99] coupled to a conventional single line defect photonic crystal waveguide by using an adiabatic taper based on progressively varying the radii of the spacing defects between the cavities that form the CCW. The details of the coupling technique will be shown in chapter five. In this case, we are interested in calculating the reflection into the CCW when the light propagates from the CCW into the photonic crystal waveguide through the adiabatic taper.

In principle, both media are periodic so the proposed semi-analytic approach can not be used. However, a simple trick can avoid this situation. Figure 3.21(a) shows the analyzed structure. The dashed square corresponds to medium I-II in which R_{21} have to be numerically calculated. The photonic crystal waveguide has been butt coupled to a 0.5μm-wide dielectric waveguide by conveniently choosing the cut position to achieve negligible reflection (see figure 3.11(a)) in the whole bandwidth of the CCW.

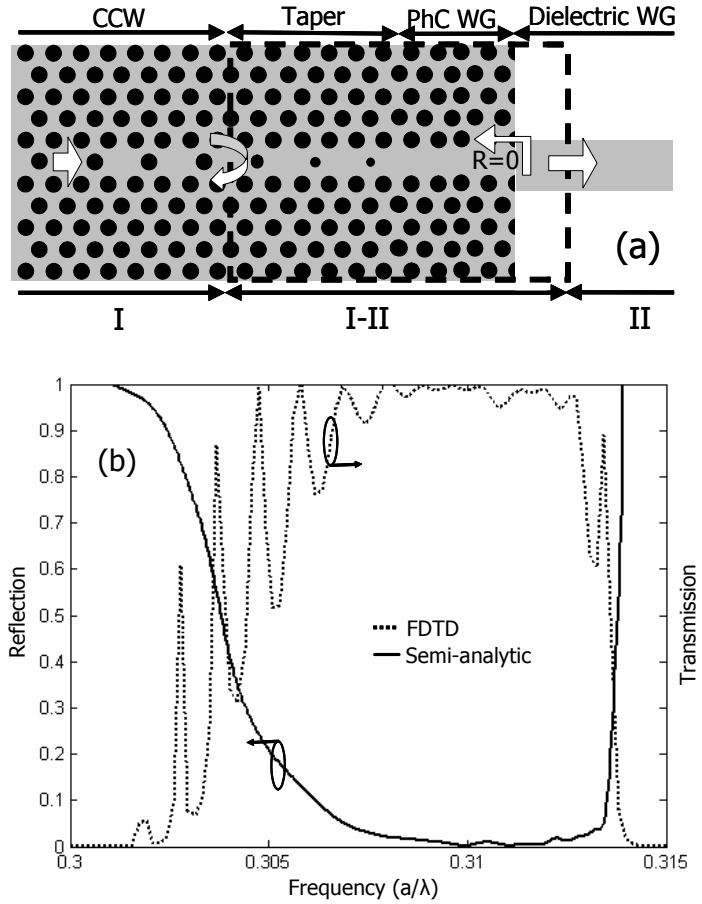

Figure 3.21.- (a) Coupled-cavity waveguide (CCW) coupled to a conventional single line defect photonic crystal (PhC) waveguide by using an adiabatic taper based on progressively varying the radii of the spacing defects between the cavities that form the CCW. The photonic crystal waveguide is butt coupled to a 0.5μm-wide dielectric waveguide by conveniently choosing the cut position to achieve negligible reflection back to the CCW. (b) Reflected power into the CCW as a function of the normalized frequency considering an adiabatic taper formed by 9 intermediate rods with a linear variation of their radius. The transmitted power is also shown for the same structure used to couple light into and out of a CCW of finite length.

This is possible since the bandwidth of the photonic crystal waveguide is much broader than that of the CCW. Therefore, the reflection into the CCW will only be the one originated due to inefficient coupling between the CCW and the single line defect photonic crystal waveguide. Once more, the validity of semi-analytic results has been demonstrated by comparing with the transmitted power obtained by means of FDTD for a CCW of finite length coupled to the input and output photonic crystal waveguide by using the adiabatic taper. The considered adiabatic taper is formed by 9 intermediate rods with a linear variation of their radius. In figure 3.21(b), it can be seen that Fabry-Perot resonances appear in the transmission spectrum, calculated by FDTD, at the frequencies in which the reflection, calculated by using the semi-analytic approach, increases.

3.7 Conclusion

Coupling losses have been analyzed at an interface formed by a dielectric waveguide butt coupled to a photonic crystal waveguide and vice versa. The main contribution is the derivation of closed form expressions for the reflection and transmission matrices that completely characterize the scattering that occurs at the interface. Analytic expressions are based on an eigenmode expansion technique but the same derivation can be followed by using other field expansions. The derived expressions can be very useful to analyze the influence of different parameters on the coupling efficiency as well as for efficient designing novel photonic crystal structures.

Analytic expressions, validated by means of CAMFR and FDTD simulations, have been used to analyze coupling losses in two different photonic crystal structures. We have shown that the transmission efficiency can be significantly improved by choosing the optimum cut position within the basic period of the photonic crystal. Thereby, the transmission efficiency can be increased from values lower than 5% to values near 70% for the rod structure while efficiency near 100% can be achieved for the hole structure. On the other hand, it has been obtained that even choosing the optimum interface the maximum transmission efficiency is limited by the group index mismatch. We have also shown that the reflection into a photonic crystal waveguide can be minimized by choosing the appropriate cut interface. Furthermore, it has been obtained that the behaviour of the coupling efficiency can be partly predicted by analyzing the forward and backward components of the guided propagating Bloch mode and it has also been demonstrated that the classical approximate formula employed to study fiber-coupling issues can only be used for interfaces involving photonic crystal structures in very specific cases.

An efficient approach has also been proposed for a semi-analytic treatment of complex photonic crystal structures based on the previously derived closed-form expressions. The proposed approach introduces several advantages with respect to other conventional numerical methods such as a shorter computation time and the possibility to calculate parameters, such as the reflection into photonic crystal structures, difficult to obtain with other methods.

Part of the obtained results has been published in the following peer-reviewed journals:

- P. Sanchis, P. Bienstman, B. Luyssaert, R. Baets, and J. Marti, “Analysis of Butt-Coupling in Photonic Crystals”, *IEEE Journal of Quantum Electronics*, vol. 40, pp. 541-550, 2004.

- P. Sanchis, J. Martí, B. Luyssaert, P. Dumon, P. Bienstman and R. Baets, "Analysis and design of efficient coupling in photonic crystal circuits", to be published in *Optical and Quantum Electronics*.

And in the following conferences:

- P. Sanchis, J. Martí, P. Bienstman, B. Luyssaert, R. Baets, "Analytic expressions for transmission and reflection from semi-infinite photonic crystal waveguides", *Photonic and Electromagnetic Crystal Structures (PECS-V)*, Tu-P31, Kyoto, Japan, March 2004.

- P. Sanchis, J. Marti, B. Luyssaert, P. Dumon, P. Bienstman, R. Baets, "Analysis and design of efficient coupling into photonic crystal circuits", *XII Int. Workshop on Optical Waveguide Theory and Numerical Modelling*, Ghent, Belgium, pp.27, March 2004.

- P. Sanchis, J. Martí, J. García, P. Bienstman, R. Baets, "Semi-analytic analysis of complex photonic crystal structures", *12th European Conference on Integrated Optics*, FrB1-4, pp. 347-350, Grenoble, France, 2005.

- P. Sanchis, J. Martí, J. García, P. Bienstman, R. Baets, "Semi-analytic approach for coupling issues in photonic crystal structures", *Photonic and Electromagnetic Crystal Structures (PECS-VI)*, Crete, Greece, 2005.

Chapter 4

Coupling into Line Defect Photonic Crystal Waveguides

4.1 Coupling techniques in photonic crystals

In chapter three, the improvement of the coupling efficiency between dielectric waveguides and single line defect photonic crystal waveguides was achieved by choosing the optimum cut interface. However, it was shown that this improvement is still rather low in rod structures, where the photonic crystal is formed by a rod lattice with a higher refractive index than the surrounding medium, when compared to that achieved for hole structures, where the photonic crystal is formed by a lattice of air holes etched in a high refractive index medium. Furthermore, the coupling efficiency is considerably degraded in both rod and hole structures when the width of the dielectric waveguide increases. Therefore, alternative approaches to butt-coupling become necessary in order to improve the coupling efficiency independently of the width of the dielectric waveguide. It is important to point out that an efficient coupling from broad dielectric waveguides would also imply a reduction of the conversion ratio in the horizontal direction needed to couple from a fiber, thus allowing the design of compact spot size converters.

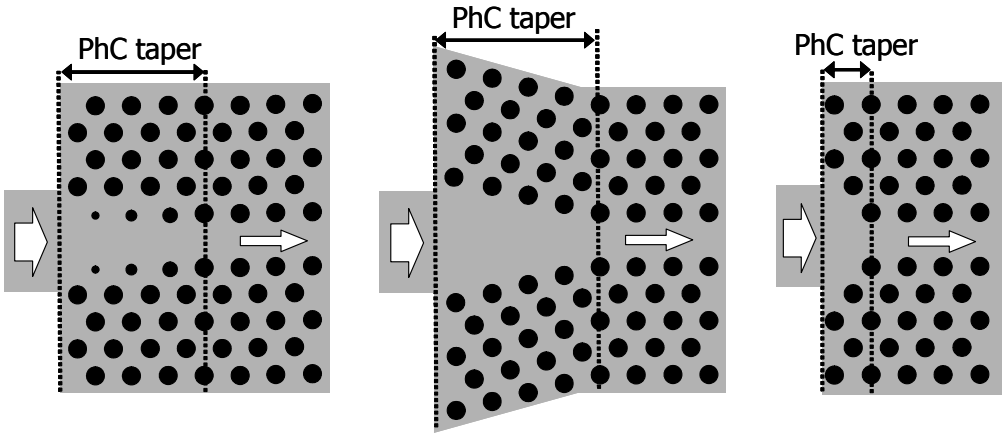

Figure 4.1.- Different kinds of photonic crystal tapers. In the left part, the taper is based on progressively varying the defects radii. In the middle part, the taper is based on a continuous tapering of the periodic lattice. In the right part, the taper is formed by removing some defects from the original photonic crystal waveguide.

A large variety of coupling structures and techniques has been proposed during the last years to minimize the coupling losses between photonic crystal waveguides and dielectric waveguides. First approaches relied on tapering the dielectric taper into the photonic crystal waveguide achieving simulated transmission efficiencies over 90% [Xu00, Mek01]. However, this approach is not very useful because the refractive index of the material surrounding the defects in the photonic crystal must be different from that of the dielectric waveguide, which does not usually occur in real structures. An original alternative approach was the so-called J-coupler that basically consisted of an offset parabolic mirror dielectric structure used to focus the light into the narrower photonic crystal waveguide. This structure was fabricated but experimental results failed to demonstrate the high transmission efficiencies achieved by means of simulations [Pra02].

Coupling from dielectric waveguides perpendiculars to the photonic crystal waveguides have been proposed by using grating coupler structures but the obtained simulated transmission efficiencies were smaller than 75% [Pot02]. It is also interesting to remark that grating couplers have been demonstrated for efficient coupling from tapered fibers parallel to the photonic crystal waveguides [Kua02, Bar02] and for out-of-plane coupling between fibers and compact planar waveguides [Tai02].

However, among all the proposed solutions, one of the most promising approaches are photonic crystal tapers mainly due to its small coupling length and high coupling efficiencies achieved over a large frequency range. Different kinds of photonic crystal tapers are possible, which are depicted in figure 4.1. In the right part of figure 4.1, the taper is based on progressively varying the defects radii to ensure an adiabatic mode transformation [Lal02]. Although transmission

efficiencies above 90% have been predicted by means of simulations, experimental results have only demonstrated efficiencies of 70% [Tal03, Tal04]. The main weakness of this approach is that the taper becomes useless when the dielectric waveguide is much broader than the photonic crystal waveguide. In the middle part of figure 4.1, the taper is based on a continuous tapering of the periodic lattice to also achieve an adiabatic mode transformation [Joh02, Bie03]. Transmission efficiencies above 90% have been experimentally demonstrated [Pot03]. However, the parameters of the photonic crystal taper, such as the angle with respect to the taper axis, must be carefully designed to achieve a broad bandwidth. Furthermore, the coupling length is still very long, especially when the width of the dielectric waveguide increases. In the right part of figure 4.1, the taper is formed by removing some defects from the original photonic crystal waveguide [Hap01]. In this case, the shortest coupling length is achieved but the transmission efficiency is generally worse than the other two approaches. Transmission efficiencies smaller than 80% have been demonstrated for this kind of photonic crystal taper [Din03].

4.2 Defects based photonic crystal tapers

4.2.1 Proposed coupling technique

A coupling technique based on setting a number of localized defects within a discrete photonic crystal taper, as the one shown in the right part of figure 4.1, is proposed. Coupling losses between conventional dielectric waveguides and photonic crystal waveguides are originated due to the mode mismatch between both kinds of waveguides. Although a mode transformation is achieved by employing the photonic crystal taper, the condition of adiabaticity is not satisfied resulting in a mode mismatch that decreases the coupling efficiency and increases reflection losses. The introduction of localized defects within the photonic crystal taper modifies the modal properties of the guided mode so that mode matching can be achieved by determining the optimum number of defects as well as their optimum parameters (radii and relative position within the photonic crystal taper) thus improving the transmission efficiency.

Multiple localized defects were also employed in photonic crystal waveguides to maximize the transmission efficiency in sharp bends and Y-junction [Bos02, Bos02c]. But while the effect of introducing defects inside a photonic crystal waveguide was modelled by means of the transmission line theory [Bos02c], a different approach is necessary for setting localized defects into photonic crystal tapers due to the variation of the modal properties along the taper. In order to analyze the proposed coupling technique, a photonic crystal structure formed by a two-dimensional (2D) triangular array of dielectric rods with a lattice constant of a=465nm surrounded by a homogeneous dielectric medium has been considered.

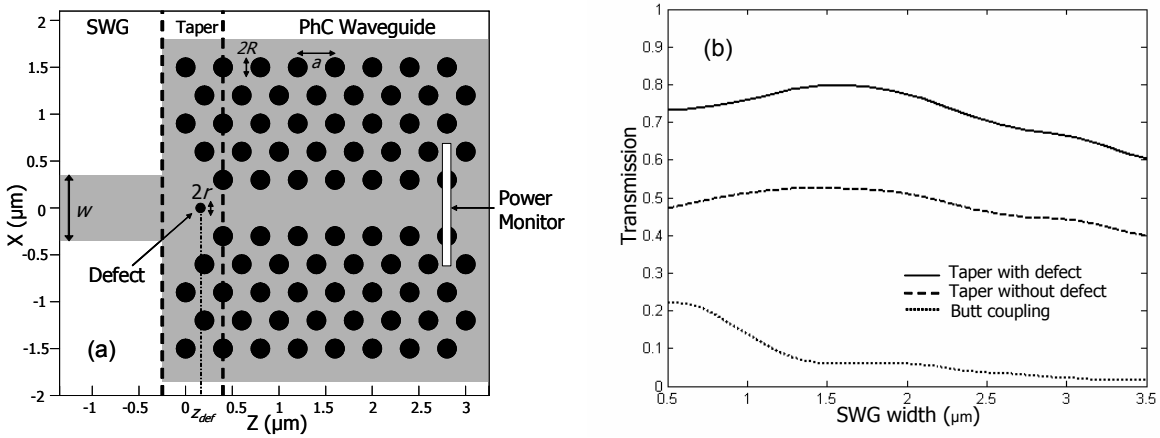

Figure 4.2.- (a) Schematic of the analyzed structure. A novel coupling technique based on setting a number of localized defects within the photonic crystal taper is proposed to achieve efficient coupling between a silica dielectric waveguide (SWG) of width w and a photonic crystal (PhC) waveguide. (b) Transmission efficiency as a function of the SWG width for the butt-coupling case and considering a photonic crystal taper without and with a defect of radius r_{def}=0.5R located in the centre of the taper.

Rods with a radius of R=0.2a and a refractive index of 3.45, which corresponds to silicon at optical wavelengths, are embedded in a medium of an refractive index of 1.45, which corresponds to silica at optical wavelengths. The photonic crystal structure considered is the same than the rod structure of the previous chapter and has a photonic band gap (PBG) for TM polarized modes between 1.34μm and 1.71μm for the considered lattice constant value, which corresponds to the normalized frequencies of 0.272(a/λ) and 0.347(a/λ). A single mode guided by a truly PBG effect appears by forming a linear defect along the ΓK direction in the photonic crystal. On the other hand, a silica waveguide (SWG) is used as the external dielectric waveguide. The SWG has a dielectric index of 1.45 and an air cladding.

Figure 4.2(a) shows the proposed coupling structure which consists of a SWG coupled to the photonic crystal waveguide by using a photonic crystal taper with a dielectric defect rod placed within it. Figure 4.2(b) shows the transmission efficiency as a function of the SWG width, w, at the normalized frequency of 0.3(a/λ). This normalized frequency is located close to the mid-gap frequency and corresponds to 1.55μm for the lattice value considered. The transmission into the photonic crystal waveguide was calculated by using the two dimensional finite-difference time-domain (FDTD) method. A monochromatic continuous-wave with normalized power corresponding to the fundamental mode of the SWG was used as light source in the z-direction. Then, the optical power transmitted through the photonic crystal waveguide was measured using a power monitor placed inside the waveguide, as shown in figure 4.2(a).

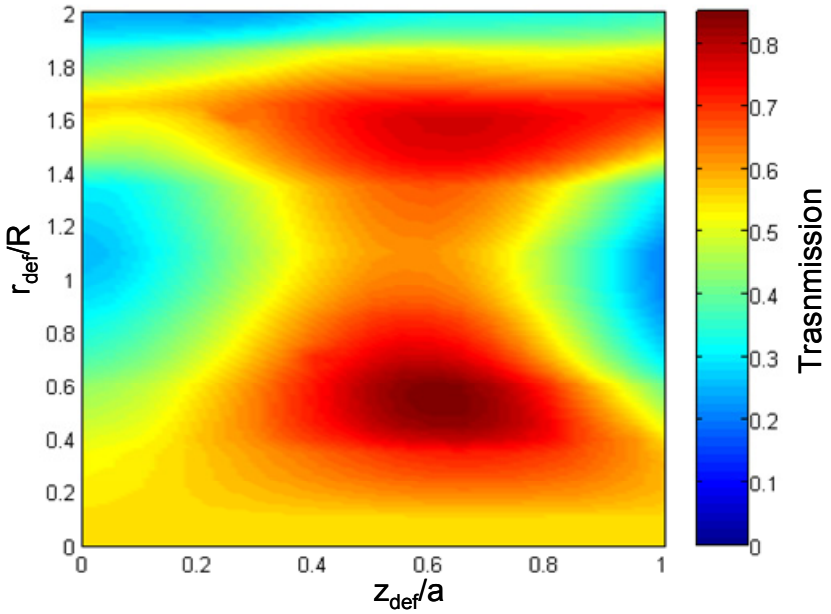

Figure 4.3.- Transmission efficiency as a function of the defect radius normalized to the rod radius of the photonic crystal, r_{def}/R, and of the relative position in the z-axis within the taper normalized to the lattice constant, z_{def}/a.

Three cases are considered: the butt-coupling case and the photonic crystal taper, shown in figure 4.2(a), without and with a defect of radius r=0.5R located in the centre of the photonic crystal taper. It can be seen that the transmission for the butt-coupling case is very low and only a maximum transmission of 22% is achieved when the SWG width is similar to the photonic crystal waveguide width. It is important to point out that the transmission could be improved by choosing the optimum cut position within the basic period of the photonic crystal, as it was shown in chapter three. However, it can be obtained that even at the optimum cut position the transmission decreases as the SWG broadens due to the mode profile mismatch. Therefore, the interface position has been chosen at a distance of a/2 with respect to the centre of the rods located at the border of the photonic crystal, as depicted in figure 4.2(a).

In figure 4.2(b), it can be seen that the transmission sharply increases with respect to the butt-coupled case when the photonic crystal taper without defect is used, achieving a transmission above 50% for a SWG width ranging from around 1μm to 2μm. However, the introduction of a defect within the photonic crystal taper improves the transmission up to 75% for a SWG width ranging from around 0.8μm to 2μm. It should be noticed that the transmission responses obtained in both cases using the photonic crystal taper are very similar, which indicates that the defect only acts as a mode matching technique improving the transmission efficiency but without modifying the shape of the response. The optimum SWG width to achieve the maximum transmission (81%) is 1.5μm.

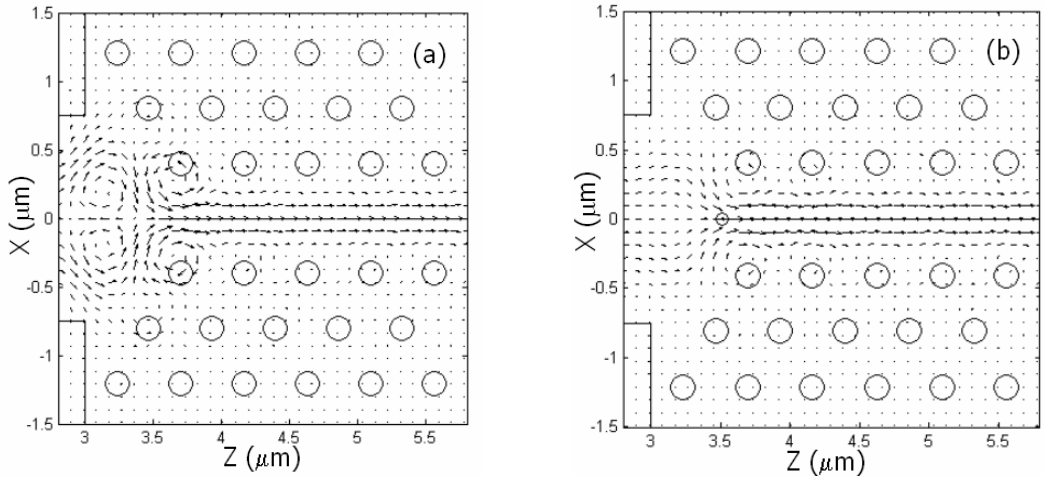

Figure 4.4.- Diagram of the Poynting vector for the photonic crystal taper (a) without and (b) with the optimized defect at the normalized frequency of 0.3(a/λ).

4.2.2 Optimization of the defect parameters

Once that the SWG width has been fixed (w=1.5μm), the radius, r_{def}, and position, z_{def}, of the defect placed within the photonic crystal taper can be further optimized to achieve the highest coupling efficiency. The optimum radius and z-position was initially obtained by means of FDTD on a trial an error basis [San02]. However, the semi-analytic method proposed in chapter three permits to obtain the map of all the possible solutions for a single defect in a very short computation time. Thus, the true optimum position can be determined. Figure 4.3 shows the transmission efficiency as a function of the defect radius normalized to the rod radius and of the relative position in the z-axis within the taper normalized to the lattice constant. It can be seen that the transmission efficiency can significantly vary from values very low up to values above 80% depending on the defect parameters. The maximum transmission efficiency (84%) is achieved for a defect of radius r_{def}=0.5R located at z_{def}=0.6a. The optimum parameters coincide with the ones obtained on a trial an error basis [San02]. Furthermore, there is another transmission maximum of 77% for a defect of radius r_{def}=1.6R located at z_{def}=0.6a. This solution could be useful in case the fabrication constraints limit the minimum achievable rods size. On the other hand, the optimum relative position of the defect along the x-axis has also been investigated. Variations in the x-axis indicate that the optimum position is x_{def}=0, which corresponds to the mirror symmetry axis (see figure 4.2(a)), with a parabolic-like decreasing of the transmission efficiency.

The introduction of the defect within the photonic crystal taper matches the modes of the dielectric and photonic crystal waveguides improving the coupling efficiency. The diagram of the Poynting vector has been calculated to achieve a better understanding of the defect behaviour.

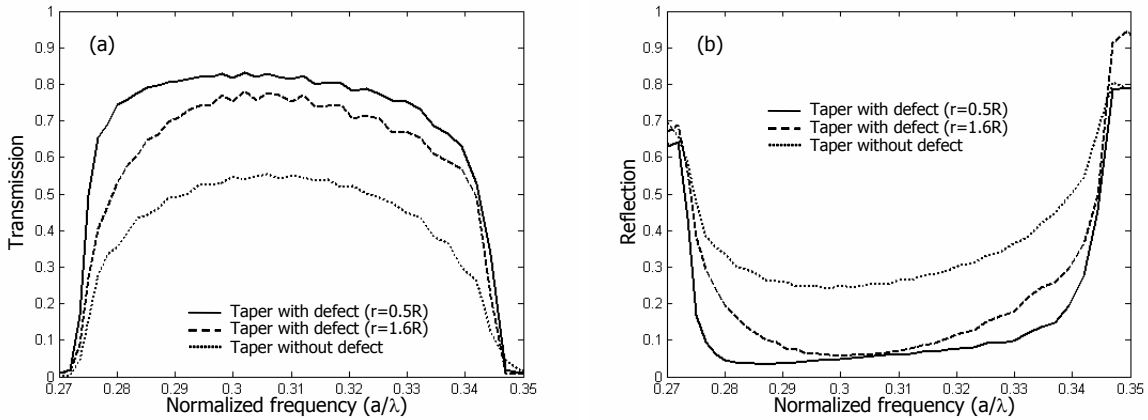

Figure 4.5.- (a) Transmission and (b) reflection efficiency as a function of the normalized frequency for the photonic crystal taper without and with defect. In the latter, two cases with a different radius of the defect (r_{def}=0.5R and r_{def}=1.6R) but located at the same z-position (z_{def}=0.6a) have been considered.

Figure 4.4 shows the Poynting vector for the photonic crystal taper without and with the optimum defect (r_{def}=0.5R, z_{def}=0.6a) at the normalized frequency of 0.3(a/λ). It can be seen that large backscattering occurs when no defects are considered. However, when the defect is placed within the taper, the power flux is concentrated around the defect and focused inside the photonic crystal waveguide. This behavior can be explained by the fact that the field is mostly concentrated around the regions of high refractive index. Therefore, the power flux is concentrated around the defect due to the higher refractive index with respect to the surrounding medium.

So far, the defect parameters have been optimized to achieve the highest transmission for a normalized frequency of 0.3(a/λ). However, the optimum calculated parameters have also been used to obtain the frequency response of the whole structure shown in figure 4.2(a). The transmission and reflection efficiencies as a function of the normalized frequency are shown in figure 4.5(a) and 4.5(b) respectively for the photonic crystal taper without and with defect. Furthermore, a defect of a radius of r_{def}=1.6R, corresponding to the second highest maximum of transmission, has also been considered in addition to the optimum radius. It can be seen that the introduction of the defect for both radii significantly improves the transmission efficiency with respect to the photonic crystal without defect. Furthermore, a high transmission efficiency and low reflection are obtained for a large frequency band corresponding to the band of the guided mode excited in the photonic crystal waveguide. The sum of transmission and reflection spectrum levels does not exactly equal the unity because the reflected power is only measured at the SWG neglecting the reflection in other directions. On the other hand, the transmission is lower for r_{def}=1.6R than for r_{def}=0.5R, as expected from the previously obtained results.

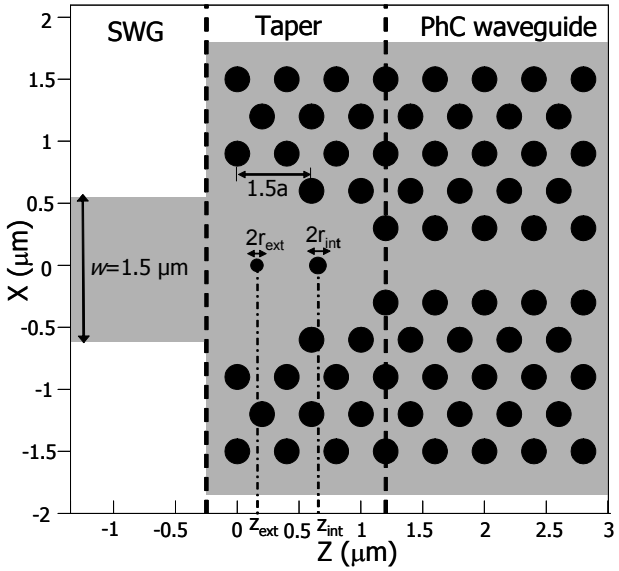

Figure 4.6.- Schematic of the analyzed structure. The photonic crystal taper is formed by 1.5*a*-spacing between adjacent rows and it is used for coupling light from a 1.5µm-wide silica dielectric waveguide (SWG) into the photonic crystal (PhC) waveguide.

4.2.3 Modification of the taper length

Just as occurs in conventional dielectric tapers, the transmission efficiency depends on the length of the photonic crystal taper [Hap01]. Therefore, higher transmission efficiency could be achieved by using a photonic crystal taper longer than the previous one. In order to investigate this fact, the structure shown in figure 4.6 has been analyzed. The photonic crystal taper is formed by 1.5*a*-spacing between adjacent rows. The total length of the taper is 3*a*, which corresponds to a length of 1.4µm for the considered lattice constant. The transmission efficiency without any defect is of only 56% similar to that obtained with the previous shorter photonic crystal taper. However, the proposed coupling technique can also be used to improve the transmission efficiency.

The semi-analytic method proposed in chapter three have also been used to obtain the transmission map of all the possible solutions in terms of the radius and *z*-position within the taper for a single defect. Figure 4.7(a) shows the transmission efficiency from the SWG into the photonic crystal waveguide as a function of the defect radius normalized to the rod radius and of the relative position in the *z*-axis normalized to the lattice constant. The maximum transmission efficiency (85%) is achieved for a defect of radius r=0.55R located at z=2.55a. It is interesting to notice that the defect parameters are similar to that obtained for the previous *a*-long photonic crystal taper. However, the transmission map is more complex than that shown in figure 4.3 and it can be seen that there are several maximums of transmission.

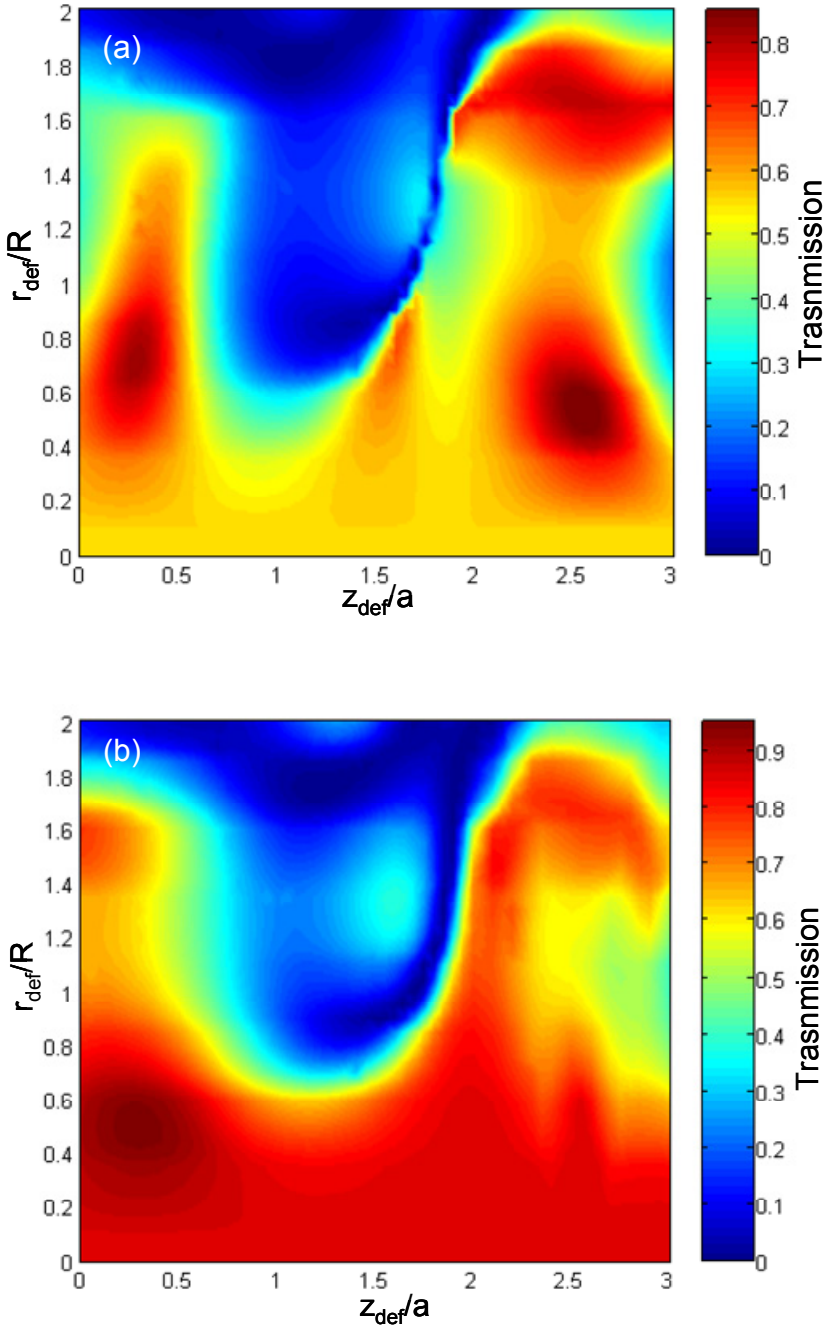

Figure 4.7.- (a) Transmission efficiency as a function of the defect radius normalized to the rod radius of the photonic crystal, r_{def}/R, and of the relative position in the z-axis within the taper normalized to the lattice constant, z_{def}/a. (b) Transmission efficiency map of an additional single defect considering that a defect of radius r_{def}=0.55R is placed at z_{def}=2.55a within the photonic crystal taper.

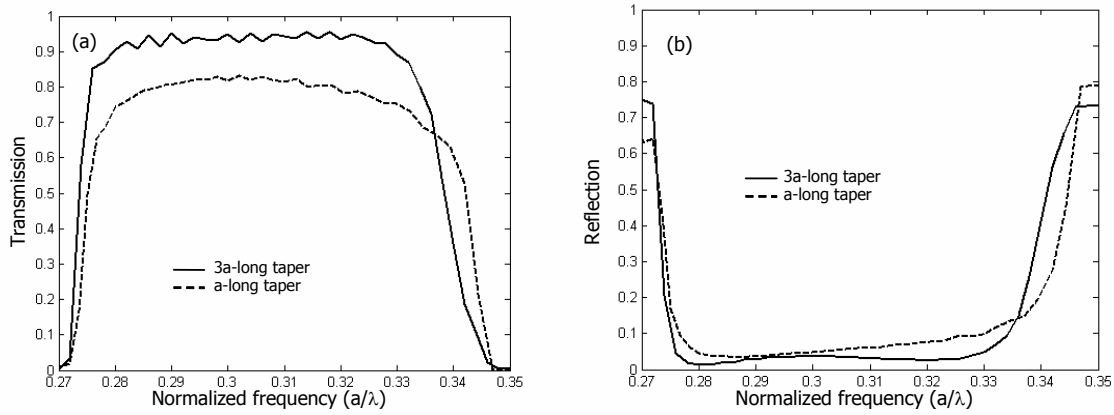

Figure 4.8.- (a) Transmission and (b) reflection efficiencies as a function of the normalized frequency for the *a*-long and 3*a*-long photonic crystal tapers shown in figure 4.2(a) and 4.6 respectively. In the former, an one defect configuration (r_{def}=0.5R, z_{def}=0.6a) placed within the taper is used to achieve the maximum transmission while in the latter a two-defect configuration (r_{int}=0.5R, z_{int}=2.6a and r_{ext}=0.6R, z_{ext}=0.2a) is used.

Therefore, the introduction of an additional defect within the taper has been analyzed in order to improve the transmission efficiency. The transmission map has been calculated for an additional defect considering that a defect of radius r_{def}=0.55R is placed at z_{def}=2.55a within the photonic crystal taper. Figure 4.7(b) shows the result. The transmission efficiency is improved up to 94% when the additional defect of radius r_{def}=0.5R is placed at z_{def}=0.3a.

Figure 4.8 shows the transmission and reflection efficiencies as a function of the normalized frequency for the 3*a*-long and *a*-long photonic crystal tapers considering in each case its optimum configuration of defects. It can be seen that a broad flat transmission band is also achieved for the 3*a*-long photonic crystal taper. In this case, the transmission efficiency is above 90% for a transmission band from 0.28(a/λ) to 0.329(a/λ), which corresponds to a wavelength range between 1.41 and 1.66μm. However, a similar transmission spectrum was obtained for both tapers without defects so the transmission is sharply improved when the appropriate configuration of defects is placed within each taper. On the other hand, it can be seen in figure 4.8(b) that the reflection into the SWG is similar for both the 3*a*-long and *a*-long photonic crystal tapers.

Figure 4.9 shows the electric field for the 3*a*-long taper with and without the optimized two defects configuration at the normalized frequency of 0.3(a/λ). It can be seen that almost perfect coupling to the photonic crystal waveguide is achieved when the proposed coupling technique is employed (see figure 4.9(a)). However, there is significant reflection when the taper is used without defects, as it can be seen in figure 4.9(b).

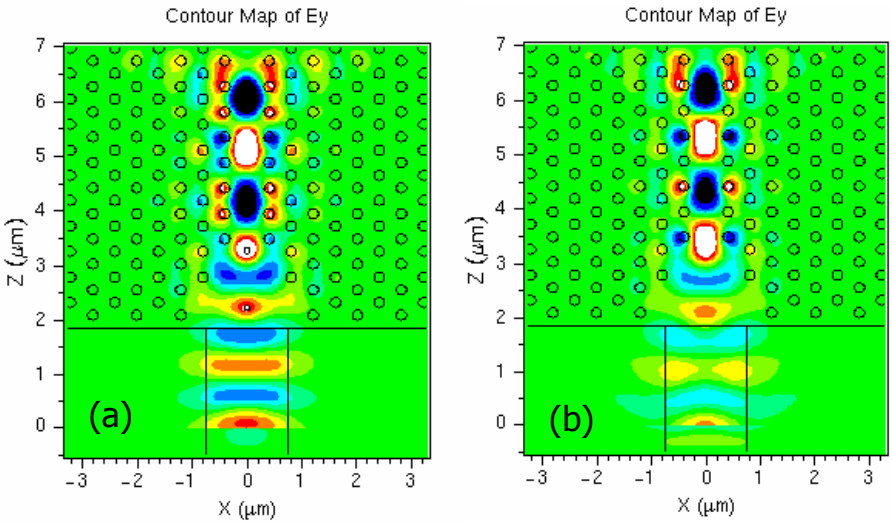

Figure 4.9.- Electric field intensity for the 3*a*-long photonic crystal taper (a) with and (b) without the optimized two defect configuration at the normalized frequency of 0.3(a/λ) and calculated by means of 2D FDTD simulations. It can be seen that almost perfect coupling to the photonic crystal waveguide is achieved when the proposed coupling technique is employed, which does not occur when the conventional taper without defects is used.

4.2.4 Transmission through photonic crystals of finite length

The transmission through photonic crystals of finite length has been analyzed by using the proposed coupling technique. The photonic crystal taper with the corresponding optimized configuration of defects is firstly used to couple the light from the SWG into the photonic crystal waveguide. Light is then propagated through a photonic crystal waveguide of finite length and coupled again into the SWG by using the same taper with the optimized configuration of defects. The analyzed structure is illustrated in figure 4.10. In this figure, the *a*-long photonic crystal taper is used to couple light into and out of a 16-rows photonic crystal waveguide. However, the 3*a*-long photonic crystal taper has also been considered by taking into account a photonic crystal waveguide with the same length.

Figure 4.11(a) shows the transmission efficiency as a function of the normalized frequency using the *a*-long taper with and without the optimized defect while figure 4.11(b) shows the transmission spectra of the *a*-long and 3*a*-long tapers each one with its corresponding optimized configuration of defects. The transmission spectra have been calculated by means of the FDTD method as follows. The fundamental mode of the SWG is excited by a pulsed wave that propagates along the z-direction. The transmission spectrum is then calculated by the overlap integral between the launched field and the field measured at the output SWG. Therefore, the transmission spectrum of the fundamental mode in the SWG can be calculated by only one simulation.

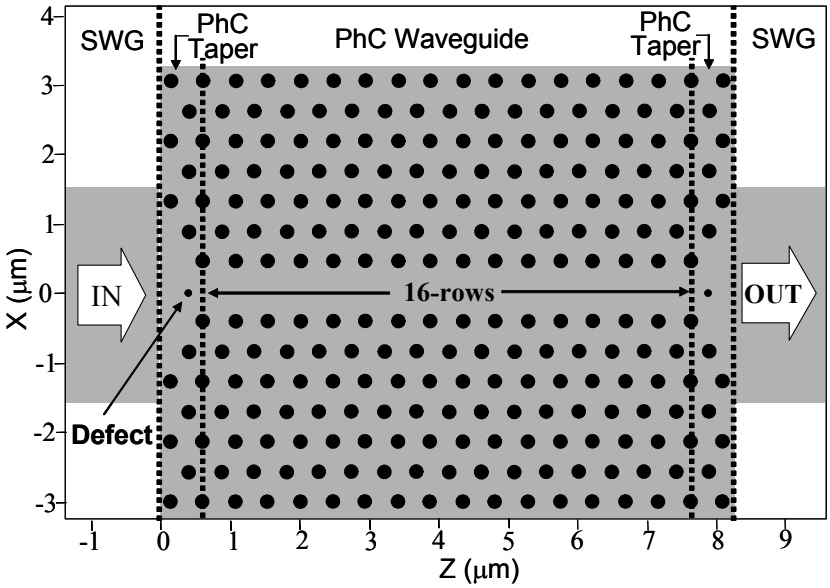

Figure 4.10.- Schematic of the analyzed structure. The photonic crystal taper with the corresponding optimized configuration of defects is used for efficient coupling from the silica dielectric waveguide into and out of a photonic crystal waveguide of finite length.

The resonance peaks that appear in the transmission spectrum of the *a*-long photonic crystal taper without defect (see dotted line in figure 4.11(a)) are due to the Fabry-Perot-like cavity originated due to the mode mismatch at the interfaces between the SWG and the photonic crystal waveguide. Therefore, the number and position of the resonance peaks depend on the photonic crystal length. On the other hand, the variation of the oscillation period with the normalized frequency is originated due to the dispersive behaviour of the photonic crystal. The period of the resonant peaks in a Fabry-Perot cavity is calculated by

$$\Delta f = c/2Ln_g \tag{4.1}$$

where c is the light velocity in free space, L is the cavity length, and n_g is the group index. Thus, the increase or decrease of the oscillation period is inversely proportional to the group index. The group index of the guided mode in the photonic crystal waveguide increases as the normalized frequency is close to the band edge. Therefore, the oscillation period decreases at those frequencies.

When the corresponding configuration of defects is placed within the a-long and 3*a*-long photonic crystal tapers, the resonances peaks are partly eliminated even though lower transmission efficiency is achieved by the *a*-long taper. The resonance peaks that appear near the band edges are due to the increase of the reflection into the photonic crystal waveguide, which in turn also implies a reduction of the transmission efficiency.

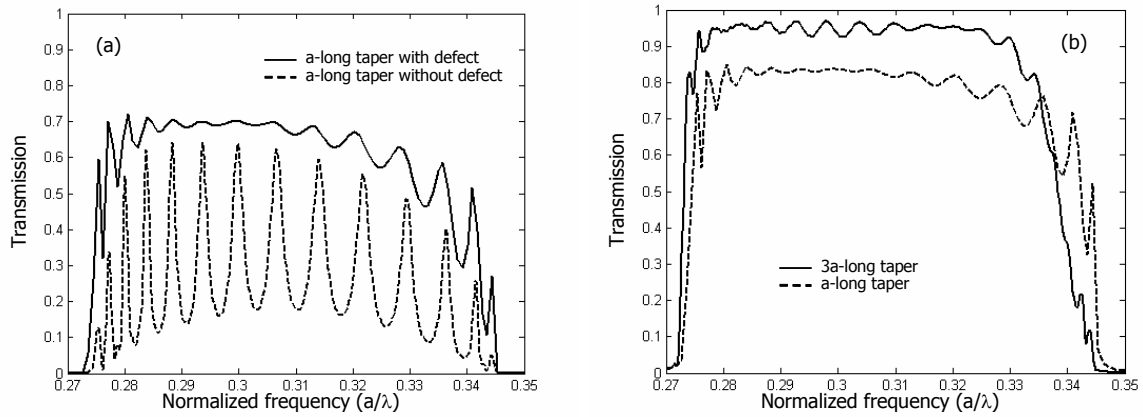

Figure 4.11.- Transmission efficiency as a function of the normalized frequency using (a) the a-long photonic crystal taper each one with and without the optimized defect and (b) the a-long and $3a$-long photonic crystal tapers with their corresponding optimized configuration of defects. In the former, the optimized configuration of defects consists of a single defect (r_{def}=0.5R, z_{def}=0.6a) while in the latter it consists of two defects (r_{int}=0.5R, z_{int}=2.6a and r_{ext}=0.6R, z_{ext}=0.2a).

The reflection into the photonic crystal waveguide for both tapers was also analyzed by using the semi-analytic method proposed in the chapter three. High reflection around 35% was obtained for the whole transmission band when no defects were placed within the photonic crystal taper. Therefore, the resonance peaks that appear in the transmission spectrum shown in figure 4.11(a) have a large peak-to-valley ratio. On the other hand, the reflection was similar and almost negligible in a broad transmission band when the corresponding optimized configuration of defects was used for both the a-long and $3a$-long photonic crystal tapers. Therefore, the transmission spectra shown in figure 4.11(b) are similar and almost flat in a broad frequency range. On the other hand, the lower transmission efficiency in the a-long photonic crystal taper implies that higher radiation losses occur for this taper since both the reflection into the SWG and the reflection into the photonic crystal waveguide are similar to those obtained for the $3a$-long taper.

4.3 Defects design based on a genetic algorithm

4.3.1 Coupling from broad dielectric waveguides

We have seen that very high transmission efficiency, above 90%, into single line defect photonic crystal waveguides can be achieved by using the proposed coupling technique. A compact photonic crystal taper of a length of only 1.4μm was sufficient to maximize the transmitted light from a 1.5μm-wide dielectric waveguide into a photonic crystal waveguide. However, the transmission efficiency decreases when the dielectric waveguide becomes broader due to the mode profile mismatch.

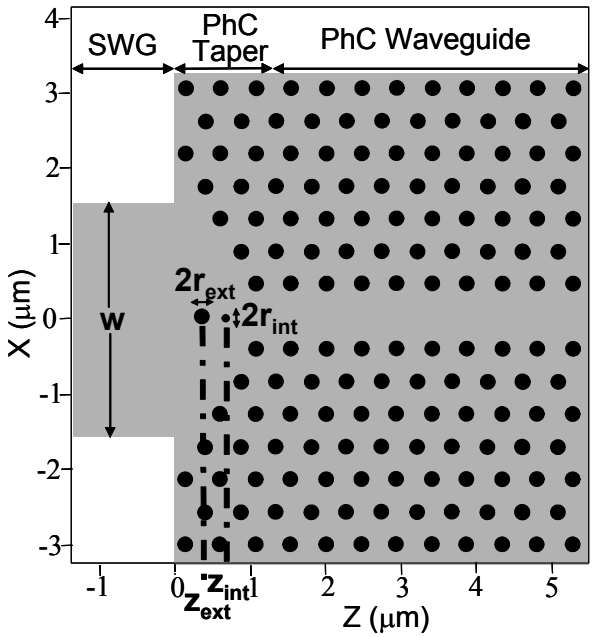

Figure 4.12.- Schematic of the structure used to analyze the coupling from broad dielectric waveguides into the narrow line defect photonic crystal waveguide by using the proposed coupling technique.

Therefore, a wider photonic crystal taper is required to maximize the transmission efficiency between the broad dielectric waveguide and the narrow photonic crystal waveguide. To prove the usefulness of the proposed coupling technique for efficient coupling from broad dielectric waveguides, the photonic crystal structure shown in figure 4.12 have been considered. A 2a-long photonic crystal taper is used to couple light from a 3μm-wide SWG. The photonic crystal taper is wider than the ones previously analyzed. However, its length is similar to that shown in figure 4.6. Therefore, it is expected that the optimum coupling performance will also obtained by setting two defects with different radii.

Figure 4.13(a) shows the transmission efficiency at the normalized frequency of 0.3(a/λ) as a function of the defect radius normalized to the rod radius and of the relative position in the z-axis normalized to the lattice constant. It can be seen that there is a dominant maximum of 79% for a radius of r_{def}=1.1R and at a position of z_{def}=0.65a. After fixing a defect with these parameters within the taper, the transmission map has been obtained for an additional single defect. The result is shown in figure 4.13(b). The transmission is improved up to 87% when the additional defect of a radius of r_{def}=0.35R is placed at z_{def}=1.7a. Therefore, by setting the two defects within the photonic crystal taper at the optimum positions and with their optimum radii (r_{int}=0.35R, z_{int}=1.7a, r_{ext}=1.1R, z_{ext}=0.65a), the transmission efficiency at the normalized frequency of 0.3(a/λ) is improved from around 40%, when no defects are considered, up to 87%.

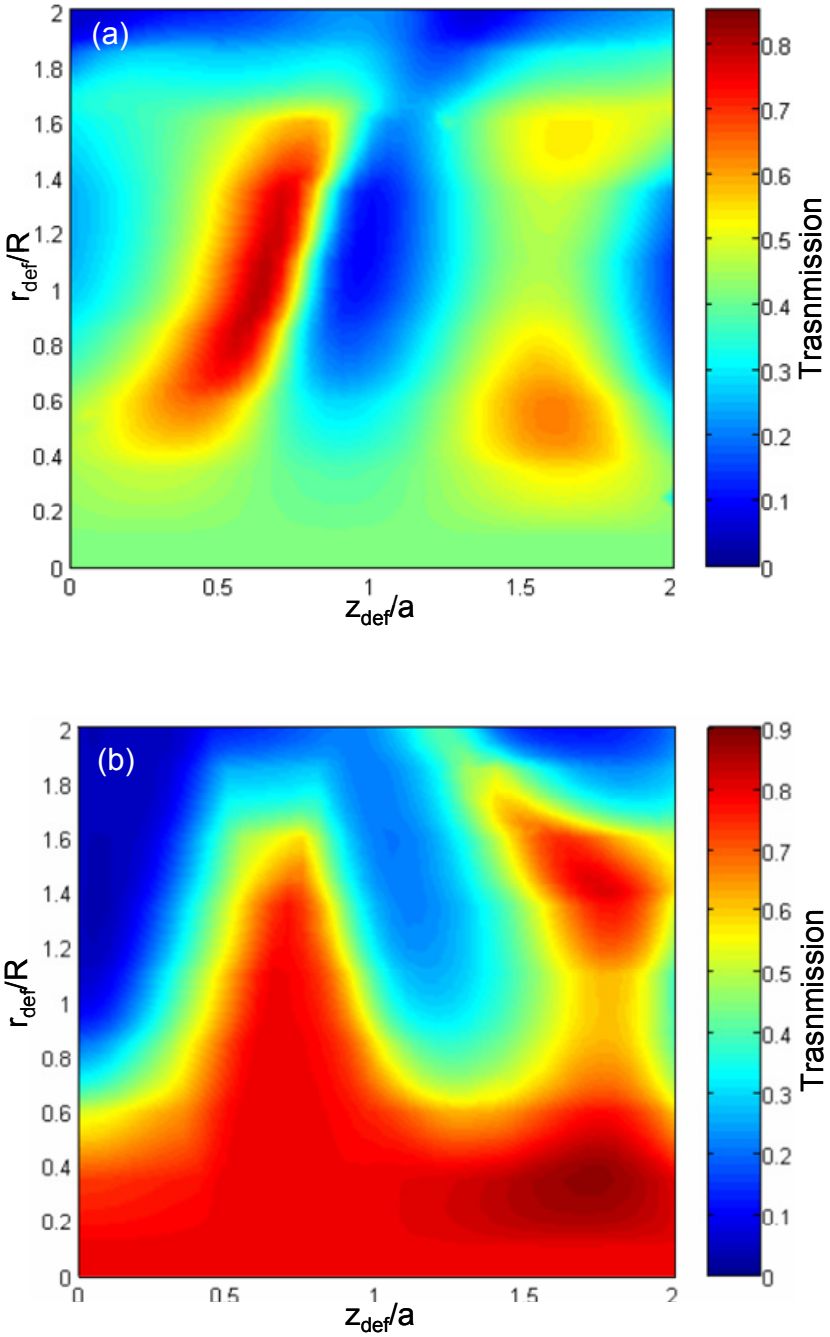

Figure 4.13.- (a) Transmission efficiency as a function of the defect radius normalized to the rod radius of the photonic crystal, r_{def}/R, and of the relative position in the z-axis within the taper normalized to the lattice constant, z_{def}/a. (b) Transmission efficiency map of an additional single defect considering that a defect of radius r=1.1R is placed at z=0.65a within the photonic crystal taper.

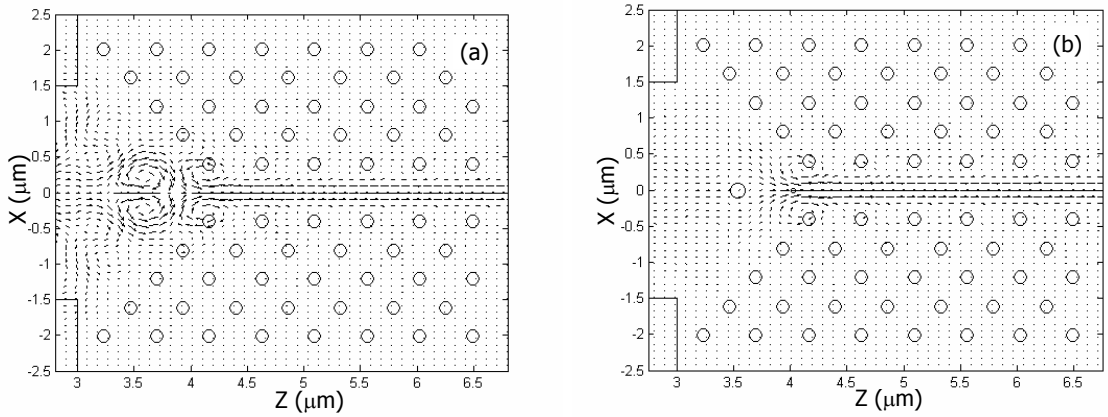

Figure 4.14.- Diagram of the Poynting vector at the normalized frequency of 0.3(a/λ) for the photonic crystal taper (a) without and (b) with the two defects configuration.

The diagram of the Poynting vector has been calculated to analyze the two defects configuration behaviour. Figure 4.14 shows the diagrams for the photonic crystal taper without and with the optimized two defects configuration. It can be seen that there is a large backscattering when no defects are placed within the taper. However, efficient mode matching is achieved when the two defects configuration is considered. It can be seen again that the power flux is concentrated around the higher refractive index defects and focused inside the photonic crystal waveguide.

Figure 4.15 shows the transmission and reflection efficiencies as a function of the normalized frequency for the photonic crystal taper with and without defects. It can be seen that the transmission is significantly improved when the defects are placed within the photonic crystal taper. The high transmission efficiency is achieved at the expense of a bandwidth reduction, which becomes more sensitive to the normalized frequency employed to optimize the parameters of the defects. However, the optimization process can be repeated by using other normalized frequency. For instance, the optimum two defects configuration considering a normalized frequency of 0.32(a/λ) is obtained for z_{int}=1.7a, r_{int}=0.4R and z_{ext}=0.8a, r_{ext}=1.1R. The transmission spectrum is also shown in figure 4.15. It can be seen that the transmission efficiency is also above 80%, however the spectrum is shifted towards the normalized frequency used in the optimization.

The previous analysis has been made possible because the computation time needed to calculate the maps shown in figure 4.13 (as well as those depicted in figures 4.3 and 4.7) is rather short by using the semi-analytic method proposed in chapter three. Notice that the total number of possible solutions is N= $(2a/\Delta z)\cdot(2R/\Delta r)$, where Δz and Δr are the steps related to the position and radius of the defect, respectively. Thus, for steps values of Δz= 0.1a and Δr= 0.1R, the total number of solutions is 400.

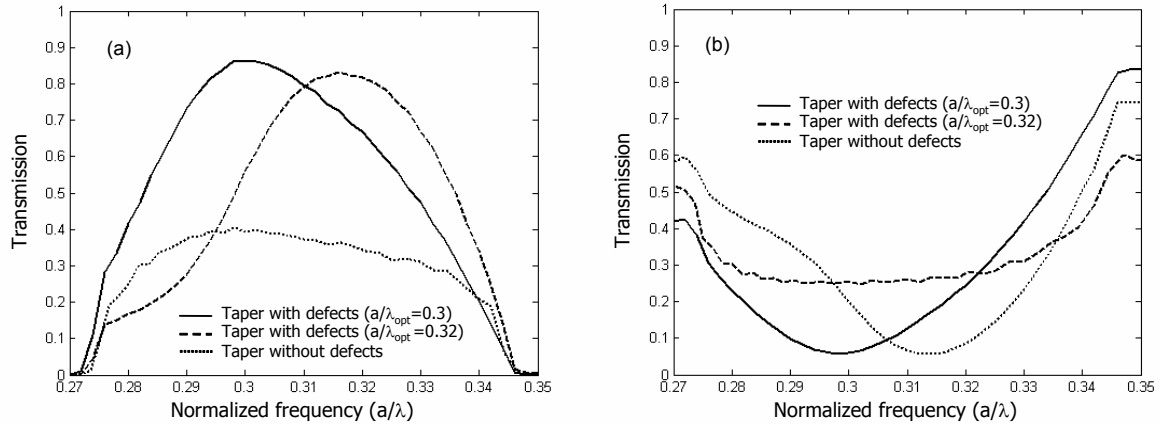

Figure 4.15.- (a) Transmission and (b) reflection efficiency as a function of the normalized frequency for the structure shown in figure 4.12 using the photonic crystal taper with and without the optimized two defects configuration defects. The two defects configuration is different depending on the normalized frequency used in the optimization process.

However, if one wants to explore the full set of solutions for the two defects configuration, the number N increases to 160,000, which makes unfeasible the calculation due to the huge computation time required. Because of this computational effort, the map in figure 4.13(b) has been calculated under the approach of fixing one of the defects at the position where a single defect configuration maximizes the transmission (see figure 4.13(a)). Fortunately, the correlation between defects is not very large for this 2*a*-long photonic crystal taper. Thus, a similar configuration of defects was obtained by using a heuristic approach [San03]. The heuristic approach was based on firstly deciding the number and relative position of the defects that should be placed into the photonic crystal taper and then optimizing the radius of each defect by considering both defects placed within the photonic crystal taper [San03]. However, the correlation between defects becomes an important issue either when the photonic crystal taper is made longer or when the number of the defects increases. In other words, the possible correlation between the defect parameters could be an important drawback in order to determine the true maximum transmission efficiency. Therefore, although high transmission efficiency is achieved by following the previous approach, alternative efficient approaches that simultaneously optimize the whole configuration of defects would be more suitable in order to take into account the correlation among the different defects.

4.3.2 Genetic algorithms

Genetic algorithms were formally introduced in the 1970s by John Holland [Holl75]. The goal was trying to improve the understanding of the natural adaptation process in order to design artificial systems having properties similar to natural systems [Gol89].

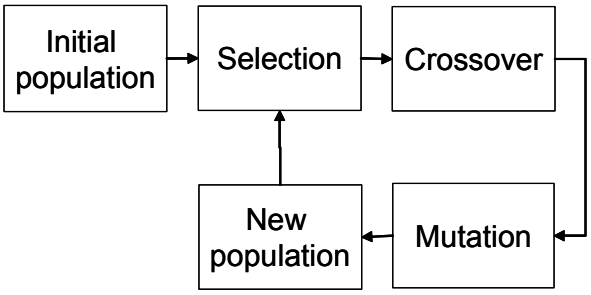

Figure 4.16.- Typical process flow used by genetic algorithms. The algorithm starts from a initial population of normally random individuals. In each generation, multiple individuals are stochastically selected from the current population and modified (crossover and mutation) to form a new population, which becomes the initial population in the next iteration of the algorithm.

During generations, natural populations have evolved according to the principles of natural selection. Thus, new populations are better adapted to the environment and they are best suited for survival than the previous generations. Genetic algorithms are adaptive methods aimed to find approximate solutions to difficult to solve problems by using the principles of natural evolution. They work with a population of individuals, each representing a possible solution to the optimization problem. A fitness function is assigned to each individual to evaluate the quality of the solution. For instance, in our case the fitness function is the transmitted power from the dielectric waveguide into the photonic crystal waveguide. Genetic algorithms are one of the best approaches to solve complex problems in which there is a very large set of possible solutions. Therefore, they have been used for different applications in many science fields such as engineering, physics, medicine or robotics.

Genetics algorithms have also been proven to be very effective to tackle complex problems in photonic crystals [Jia03, She03, San04, Bor04]. The algorithm starts from an initial population of normally random individuals. In each generation, multiple individuals are stochastically selected from the current population and modified to form a new population, which becomes the initial population in the next iteration of the algorithm. Thereby, the population of individuals evolve toward the better solution during each successive generation.

Typically, three operators are used to obtain the new population: selection, crossover and mutation that are iteratively applied, as shown in figure 4.16. The selection operator selects the individuals of the population that have better fitness, i.e. they that are better solutions to the given problem.

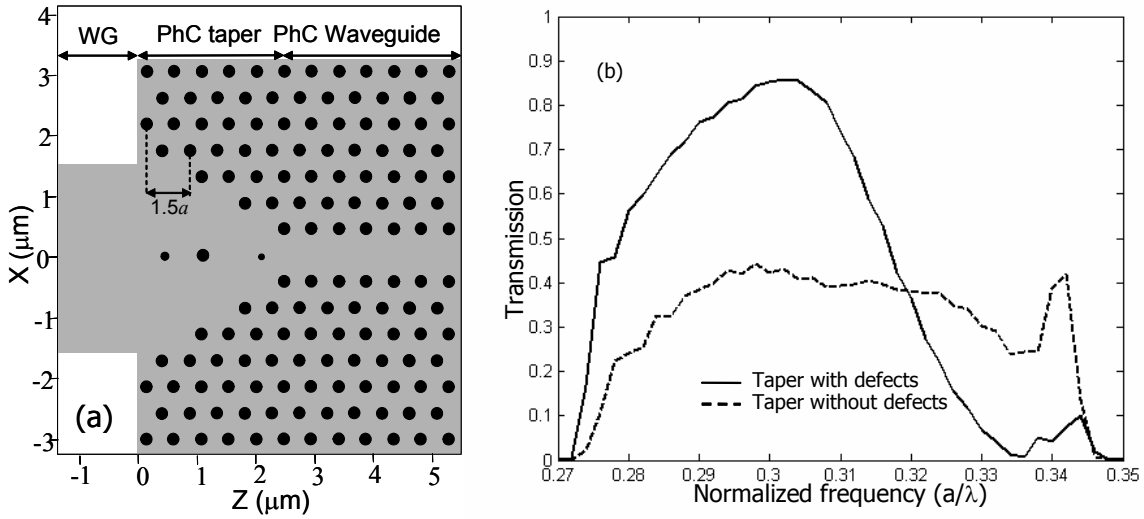

Figure 4.17.- (a) Schematic of the analyzed structure. A photonic crystal taper formed by a 1.5*a*-spacing between the successive discrete steps is used for coupling light from a 3μm-wide dielectric waveguide into the photonic crystal waveguide. (b) Transmission efficiency as a function of the normalized frequency using the photonic crystal taper without and with the optimized three defects configuration reported in table 4.1.

	Position	Radius
Defect 1	1.77*a*	0.38*R*
Defect 2	2.09*a*	1.03*R*
Defect 3	4.68*a*	0.64*R*

Table 4.1.- Optimum radius and position of the three defects configuration obtained by means of the genetic algorithm for the structure shown in figure 4.17(a) considering a frequency of 0.3(*a*/*λ*).

The crossover operator mixes two or more solutions creating a new solution with mixed properties from the previous ones. The mutation operator introduces random effects into the new solution to ensure that it differs from the previous ones. Therefore, this process results in a new population that is different from the initial generation. The solutions are usually represented by a digital string formed by a number of bits, where each bit codes one parameter of the problem.

4.3.3 Modification of the taper length

In the same spirit that the work in [San03], a micro genetic algorithm was recently used to design the optimum configuration of defects within a photonic crystal taper [Jia03]. The proposed defects had an elliptical symmetry and they were placed out of the mirror horizontal plane of the taper. However, only the same kind of photonic crystal taper as the one proposed in [San03] was investigated and no dependence on frequencies was reported.

In this work, a genetic algorithm have been used for properly designing the optimum configuration of defects considering photonic crystal tapers of different lengths and geometries in order to improve the transmission efficiency. One of the most popular genetic algorithms used in combination with multiple scattering theory has been considered to evaluate the transmission across the photonic crystal structures [San04, Hak05a]. The same design approach based on this genetic algorithm was successfully employed in different optimization problems [Hak04, Hak05]

Initially, the genetic algorithm has been used to optimize the configuration of defects for the previous photonic crystal taper shown in figure 4.12. The optimum two defects configuration is achieved for z_{int}=1.48a, r_{int}=0.38R and z_{ext}=0.6a, r_{ext}=0.84R. These parameters are somewhat different to those previously reported but the transmission efficiency is not improved. The optimization was also carried out for a three defects configuration but the transmission efficiency was also not substantially improved. Therefore, longer photonic crystals tapers have been analyzed with the aim of improving the transmission efficiency.

The structure shown in figure 4.17(a) has been first analyzed. The photonic crystal taper has a staircase-like profile, due to the periodicity nature imposed by the photonic crystal, with a 1.5a-spacing between the successive discrete steps. The taper length is of 5a. The optimum configuration of defects was searched by means of the genetic algorithm considering one, two, three and four defects. On the one hand, the case of a four defects configuration resulted in a transmission efficiency slightly higher than the three defects case but in a much narrower frequency band. On the other hand, the one and two defects configurations gave lower efficiencies than the three defects configurations. Therefore, the three defects configuration has been chosen.

The optimum radius and position of the defects at a normalized frequency of 0.3(a/λ) are given in table 4.1. The achieved transmission efficiency is of 86% not improving the 87% achieved with the previously considered photonic crystal taper depicted in figure 4.12. The transmission spectrum is shown in figure 4.17(b) considering the taper with and without the optimized three defects configuration. The FDTD method was used to calculate the transmission spectrum thus corroborating the results obtained by means of the genetic algorithm implemented by using the multiple scattering method. In figure 4.17(b), it can be seen that a broad bandwidth with transmission efficiencies above 80% is achieved for the taper with defects. Although the bandwidth for the taper with defects is narrower than that for the taper without defects, the transmission efficiency is significantly improved in the former.

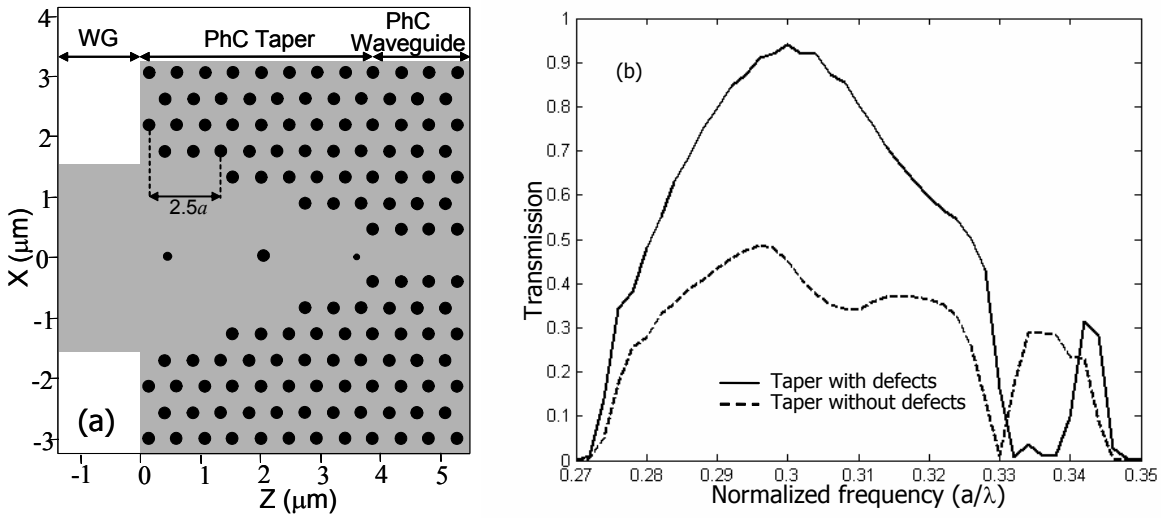

Figure 4.18.- (a) Schematic of the longer photonic crystal taper formed by a 2.5*a*-spacing between the successive discrete steps. (b) Transmission efficiency as a function of the normalized frequency using the photonic crystal taper without and with the optimized three defects configuration reported in table 4.2.

	Position	Radius
Defect 1	0.76*a*	0.45*R*
Defect 2	2.92*a*	0.77*R*
Defect 3	7.49*a*	0.45*R*

Table 4.2.- Optimum radius and position of the three defects configuration obtained by means of the genetic algorithm for the structure shown in figure 4.18(a) considering a frequency of 0.3(*a*/*λ*).

The transmission efficiency can be further improved by considering a longer photonic crystal taper, as the one shown in figure 4.18(a). In this case, the taper has a 2.5*a*-spacing between the successive discrete steps that form the taper. The taper length is of 8*a*. As before, the best results were obtained for a three defects configuration. The optimum radius and position of the defects calculated at the normalized frequency of 0.3(*a*/*λ*) are given in table 4.2. The transmission efficiency achieved in this case is 94% improving the transmission efficiency achieved by the previously considered photonic crystal tapers.

The transmission spectrum is shown in figure 4.18(b) for the photonic crystal taper with and without the optimized three defects configuration. It can be seen that there is also a broad bandwidth with transmission efficiencies above 80% for the taper with defects. However, it can also be observed that the transmission efficiency is rather worse at the high frequencies of the transmission band.

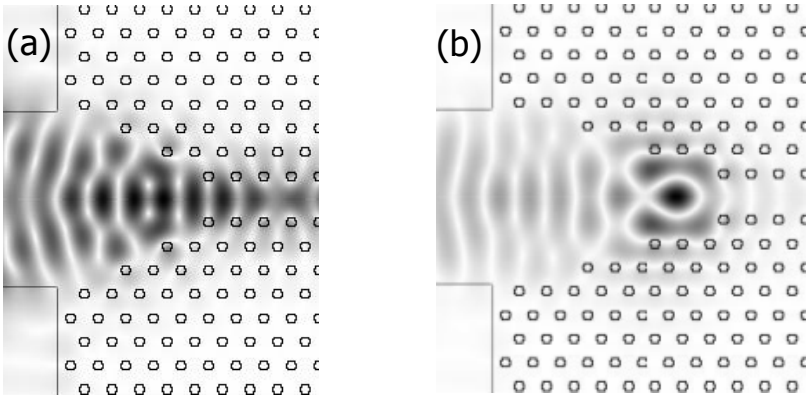

Figure 4.19.- Modulus of the electric field for (a) the structure shown in figure 4.17(a) at a normalized frequency of 0.336(a/λ) and for (b) the structure shown in figure 4.18(a) at a normalized frequency of 0.329(a/λ) both without considering defects within the photonic crystal taper.

Furthermore, the transmission efficiency for the photonic crystal taper without defects suddenly drops at the normalized frequency of 0.329(a/λ). A similar effect is also observed for the 5a-long photonic crystal taper shown in figure 4.17(a). In figure 4.17(b), it can be seen that the transmission efficiency for the taper with defects is also very low at the same frequency range while the transmission efficiency also drops for the photonic crystal taper without defects although with a lower strength and at a slightly higher frequency of 0.336(a/λ).

4.3.4 Modification of the taper geometry

In order to analyze more in depth this effect, the modulus of the electric field has been obtained for the 5a-long and 8a-long photonic crystal tapers without defects at the normalized frequency where the transmission efficiency drops. Figure 4.19(a) shows the modulus of the electric field for the 5a-long photonic crystal taper at the normalized frequency of 0.336(a/λ) while figure 4.19(b) shows the modulus of the electric field for the 8a-long photonic crystal taper at the normalized frequency of 0.329(a/λ). The results, which were calculated with CAMFR, indicate that a resonant mode is excited near the end of the photonic crystal taper, thus reducing the transmitted power into the photonic crystal waveguide.

The resonant effect is stronger for the 8a-long photonic crystal taper as expected due to the sharper notch with almost zero transmission that can be seen in the transmission spectrum. In order to avoid the excitation of the resonant mode, the section of the taper closer to the photonic crystal waveguide has been suppressed.

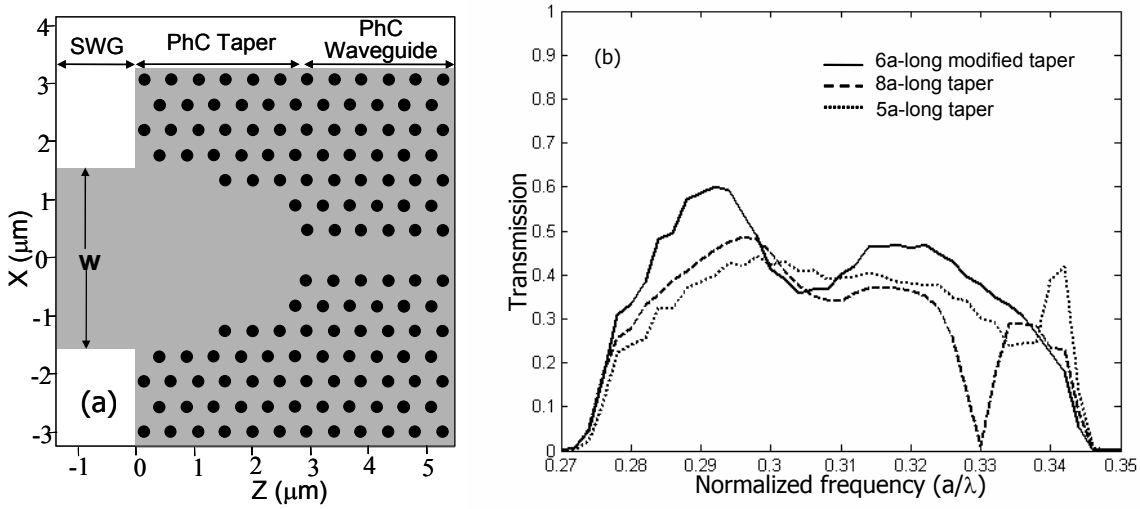

Figure 4.20.- (a) Schematic of the photonic crystal taper proposed to avoid the excitation of the resonant mode shown in figure 4.19(b). (b) Transmission efficiency as a function of the normalized frequency using the photonic crystal tapers shown in (a), named 6*a*-long modified taper, and the 5*a*-long and 8*a*-long photonic crystal tapers shown in figures 4.17(a) and 4.18(b) respectively. In all cases, no defects were placed within the photonic crystal taper.

	F=0.30(a/λ)		f=0.32(a/λ)		f=0.335(a/λ)	
	Position	Radius	Position	Radius	Position	Radius
Defect 1	0.76*a*	0.45*R*	1.01*a*	0.45*R*	2.54*a*	0.45*R*
Defect 2	2.92*a*	0.77*R*	2.92*a*	0.77*R*	3.05*a*	0.71*R*
Defect 3	7.49*a*	0.45*R*	6.22*a*	0.77*R*	7.62*a*	1.22*R*

Table 4.3.- Optimum radius and position of the three defects configuration obtained by means of the genetic algorithm for the structure shown in figure 4.18(a) considering different optimization frequencies.

	F=0.30(a/λ)		f=0.32(a/λ)		f=0.335(a/λ)	
	Position	Radius	Position	Radius	Position	Radius
Defect 1	0.57*a*	0.71*R*	1.14*a*	0.64*R*	0.00*a*	0.77*R*
Defect 2	2.95*a*	0.64*R*	2.85*a*	0.64*R*	4.86*a*	0.45*R*
Defect 3	5.62*a*	0.71*R*	5.52*a*	1.16*R*	5.71*a*	1.03*R*

Table 4.4.- Optimum radius and position of the three defects configuration obtained by means of the genetic algorithm for the structure shown in figure 4.20(a) considering different optimization frequencies.

The resulting photonic crystal taper, named as 6a-long modified taper is depicted in figure 4.20(a). The spectrum transmission of this new taper is shown in figure 4.20(b) and it is compared to those obtained for the 5*a*-long and 8*a*-long photonic crystal tapers shown in figures 4.17(a) and 4.18(a), respectively, with no defects in

them. It can be seen that the transmission does not present the drop at the high frequency of the band because the resonant mode can not be excited.

The huge reduction of transmission efficiency observed at frequencies around 0.335(a/λ) for the 5a-long and the 8a-long photonic crystal tapers when defects are considered within the photonic crystal taper can also be explained due to a similar resonant effect. For the sake of comparison, the optimization of a three defects configuration at the frequency of 0.3(a/λ) has also been carried out for the so-called 6a-long modified photonic crystal taper shown in figure 4.20(a). Results are given in table 4.4 and the transmission spectrum is shown in figure 4.21(a) and compared to that obtained for the 8a-long photonic crystal taper. The maximum transmission efficiency is also above 90%. However, it can be seen that in this case the transmission is not degraded at frequencies around 0.335(a/λ).

4.3.5 Coupling dependence on the frequency of optimization

The transmission efficiency can be improved at different frequencies since the defect parameters depend on the frequency used in the optimization process. To prove the usefulness of the proposed coupling technique, the optimization of the three defects configuration has been repeated for the 8a-long photonic crystal taper at the frequencies of 0.32(a/λ) and 0.335(a/λ). The parameters are given in table 4.3 and the corresponding transmission spectra are plotted in figure 4.21 with dashed lines. It is interesting to notice that the radius and position of the defect 3, located within the section of the taper closer to the photonic crystal waveguide, are the ones that differ more noticeable among the different optimization frequencies. This result corroborates that this section of the taper has a large influence on the coupling efficiency. On the other hand, the optimization of the three defects configuration has also been carried out at the same frequencies for the 6a-long modified photonic crystal taper. The defects parameters are given in table 4.4 and the solid lines in figure 4.21 represent the corresponding transmission spectra. In this case, the parameters of all the defects differ more or less for the different optimization frequencies.

In figure 4.21(b), it can be seen that the transmission efficiency at frequencies around 0.32(a/λ) is above 80% and almost the same for both the 8a-long and the 6a-long modified photonic crystal tapers. However, the transmission for the 8a-long photonic crystal taper sharply drops at frequencies above and below 0.32(a/λ). This does not occur for the 6a-long modified photonic crystal taper and, in this case, a much broader bandwidth is achieved although a drop of the transmission efficiency can still be seen near 0.34(a/λ).

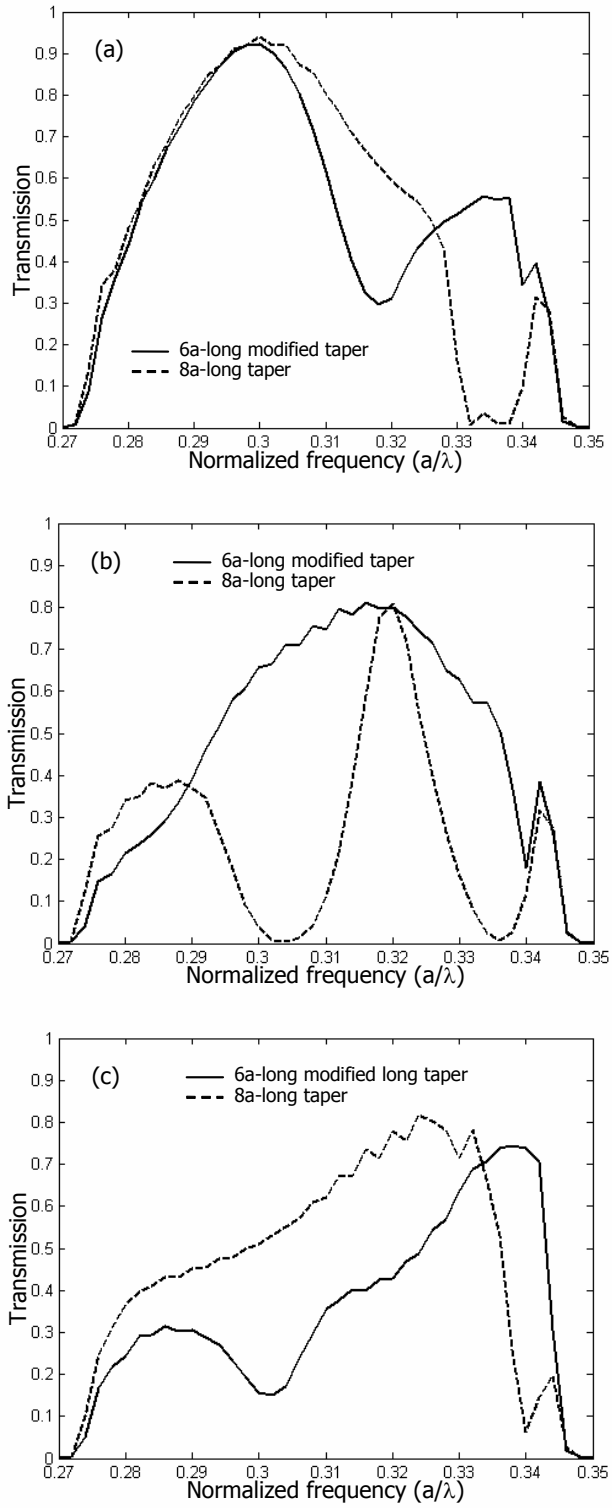

Figure 4.21.- Transmission efficiency as a function of the normalized frequency using the 8*a*-long photonic crystal taper shown in figure 4.18(a) and the 6*a*-long modified photonic crystal taper shown in figure 4.20(a) each one with its corresponding three defects configuration optimized at the frequency of (a) 0.3(*a/λ*), (b) 0.32(*a/λ*) and (c) 0.335(*a/λ*).

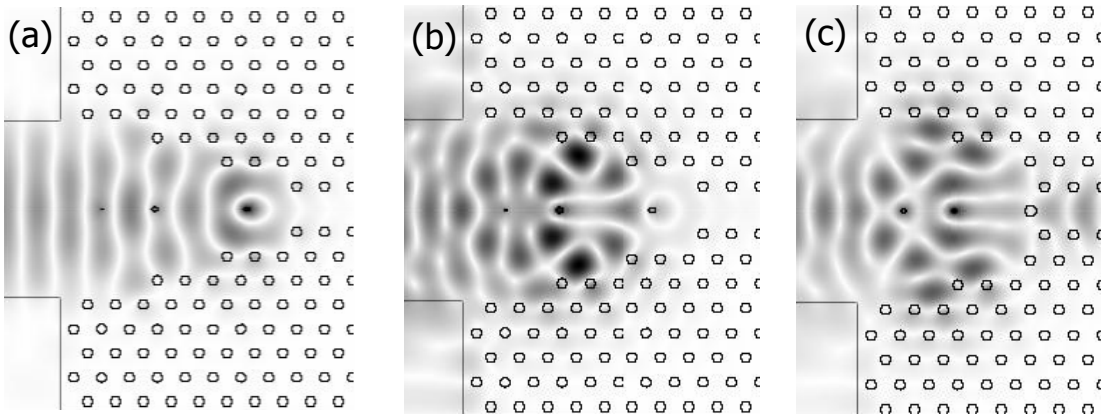

Figure 4.22.- Modulus of the electric field for the 8*a*-long photonic crystal taper at the normalized frequencies of (a) 0.303(*a*/λ) and (b) 0.3355(*a*/λ) and for the 6*a*-long modified photonic crystal taper at the normalized frequency of (c) 0.339(*a*/λ). The corresponding three defects configuration optimized at the normalized frequency of 0.32(*a*/λ) are used within each taper.

To analyze this behaviour, the modulus of the electric field has been first obtained for the 8*a*-long photonic crystal taper at the frequencies in which the transmission is minima. Figure 4.22(a) and 4.22(b) shows the plots at the normalized frequencies of 0.303(*a*/λ) and 0.3355(*a*/λ) respectively. It can be seen that for both frequencies a resonant mode is excited within the photonic crystal taper and therefore the transmission efficiency is significantly reduced. The resonant mode is located at a different place within the photonic crystal taper depending on the frequency. Figure 4.22(c) shows the modulus of the electric field for the 6*a*-long modified photonic crystal taper at the normalized frequency of 0.339(*a*/λ) in which the transmission drop occurs. A resonant mode is also excited which is very similar to that excited in the 8*a*-long photonic crystal taper at a nearby frequency.

On the other hand, it can be seen in figure 4.21I that the transmission efficiency at frequencies around 0.33(*a*/λ) is above 70% for both the 8*a*-long and the 6*a*-long modified photonic crystal tapers. The transmission efficiency is lower than that obtained at the frequencies of 0.3(*a*/λ) and 0.32(*a*/λ) because the optimization frequency is closer to the band edge where the mode mismatch between the dielectric and photonic crystal waveguides is higher. However, higher transmission efficiencies at frequencies closer to the band edge are achieved by using the 6*a*-long modified photonic crystal taper.

Finally, it is important to point out that no minimum transmission are found in the transmission spectra of the shortest photonic crystal tapers considered along this chapter (see for instance figure 4.15(a)). This occurs independently if there are or not are defects placed within the taper because of no resonant states are excited in the different sections that form the taper.

4.4 Conclusion

A coupling technique has been proposed for efficient light coupling between dielectric waveguides and line defect photonic crystal waveguides. The proposed coupling technique is based on setting a number of localized defects within a discrete photonic crystal taper. Therefore, mode matching at the interface between both kinds of waveguide is achieved reducing reflection losses and improving significantly the transmission efficiency over a large frequency band.

The optimum number of defects as well as their radii and position within the photonic crystal taper need to be carefully designed depending on the size of the photonic crystal taper. For small photonic crystal tapers, useful for coupling from narrow dielectric waveguides, the optimum parameters have been chosen by making a scan of all the possible solutions using the semi-analytic method proposed in chapter three. However, the optimization of the configuration of defects by using this approach can not lead to the best solution either when a large photonic crystal taper or a high number of defects are required, for instance for coupling from broad dielectric waveguides. Therefore, in this case, the optimization of the configuration of defects has been carried out by means of a genetic algorithm.

On the other hand, the influence of the photonic crystal taper length on the coupling efficiency has also been analyzed. We have obtained that resonant modes can be excited when the length of the taper is increased thus degrading the coupling efficiency. The origin of these resonant modes depends on the geometry of the photonic crystal taper. Therefore, it has been shown that the resonant modes can be avoided by modifying the design of the photonic crystal taper geometry. Furthermore, the transmission efficiency is maximized when the proposed coupling technique is used.

In summary, transmission efficiencies above 90% have been demonstrated by using the proposed coupling technique for both narrow and broad dielectric waveguides coupled to single line defect photonic crystal waveguides. In all the different analyzed tapers, the transmission efficiency was significantly improved with respect to the case of using the same photonic crystal taper without defects.

Part of the obtained results has been published in the following peer-reviewed journals:

- P. Sanchis, J. Martí, A. García, A. Martínez and J. Blasco, “High efficiency coupling technique for planar photonic crystal waveguides”, *Electron. Lett.*, vol. 38, pp. 961-962, 2002.

- P. Sanchis, J. Martí, J. Blasco, A. Martínez and A. García, "Mode matching technique for highly efficient coupling between dielectric waveguides and planar photonic crystal circuits", *Opt. Express*, vol. 10, pp. 1391-1397, 2002.

And in the following conferences:

- P. Sanchis, J. Martí, A. Martínez J. Blasco and A. Griol, "A novel high efficiency coupling technique for planar photonic crystal circuits", *Conferencia de dispositivos electrónicos (CDE)*, pp. IV10.1-IV10.4, Calella, Barcelona, 2003.

- P. Sanchis, A. Håkansson, J. Sánchez-Dehesa, and J. Marti, "High efficiency defect-based photonic-crystal-tapers designed by a genetic algorithm", *Photonic and Electromagnetic Crystal Structures (PECS-VI)*, Crete, Greece, 2005.

Chapter 5

Coupling into Coupled Cavity Waveguides

5.1 Coupled cavity waveguides

Waveguides in photonic crystals are usually created by forming line defects into the otherwise periodic structure. In the previous chapters, we have seen that these waveguides may be efficiently coupled to conventional index-guiding dielectric waveguides. Furthermore, efficient coupling between line defect waveguides of arbitrary widths has also been experimentally demonstrated [Tal02]. In a different kind of photonic crystal waveguide, known as coupled cavity waveguide (CCW) or coupled-resonator optical waveguide (CROW), only some evenly spaced point defects or cavities are created along a crystal direction [Ste98, Yar99]. The defect cavities are designed such that their eigenfrequency falls within the PBG of the surrounding photonic crystal. Hence, the waveguide can be considered as a chain of strongly confined defect cavities embedded in the photonic crystal.

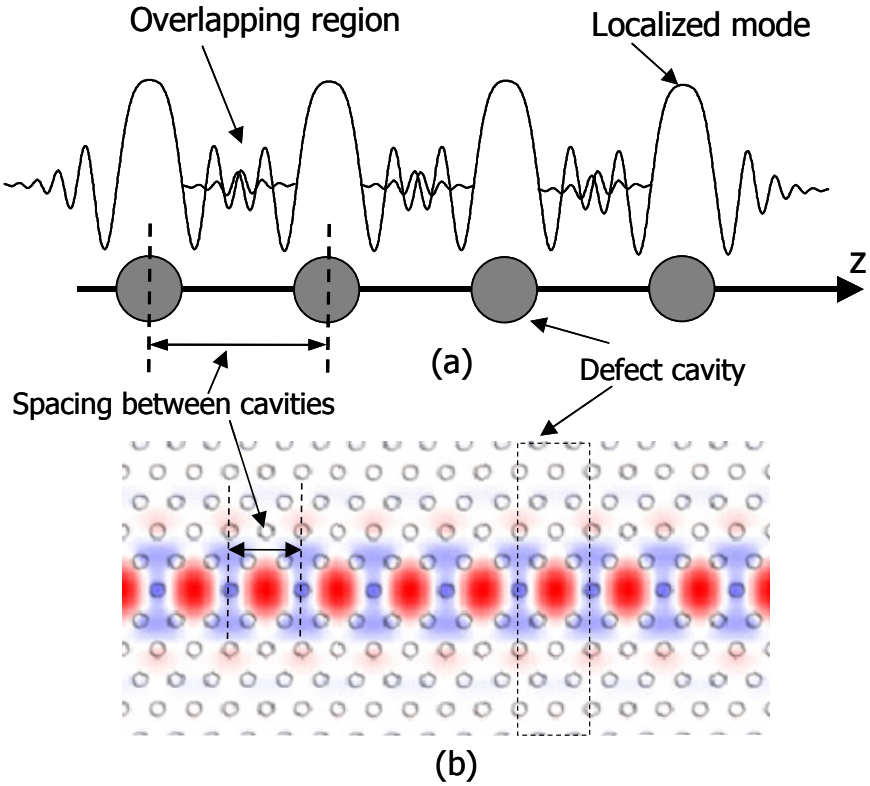

Figure 5.1.- (a) Schematic of a coupled-cavity waveguide (CCW). The waveguide is formed as a chain of strongly confined point defects or cavities created along a crystal direction. Light propagation can be explained as photon hopping from a cavity to its next neighbour due to the overlapping of the evanescent tails of the tightly confined modes. (b) modulus of the electrical field in a CCW created in a 2D photonic crystal and formed by single missing defect cavities with a spacing of two lattice constants between next neighbouring cavities.

Figure 5.1(a) illustrates the basics of transmission in CCWs. Although the cavity modes are tightly confined at the defect cavities, the overlapping between neighbouring cavities is enough to provide light propagation as photon hopping from a cavity to its next neighbour [Bay00]. The coupling between the strongly localized cavity modes originates a frequency splitting of the single cavity mode into a number of resonance peaks that depend on the number of coupled cavities. Therefore, a guided band appears when the CCW has an infinite length. The central frequency of the guided band can be tuned by modifying the cavities shape while the bandwidth can be varied by adjusting the spacing between cavities. A longer spacing between cavities leads to a narrower bandwidth. The physics behind light propagation in CCW is the classical wave analogous to the tight-binding approach employed in solid-state physics. Hence, the tight-binding formalism has been used to analyze the properties of CCWs and to derive a closed form expression of the dispersion relation of the guided mode [Lid98, Bay00a, Ozb02].

Waveguiding through CCWs has been experimentally demonstrated at microwave and optical frequencies [Bay00, Oli01]. Figure 5.1(b) shows the modulus of the electrical field in a CCW created in a 2D photonic crystal and formed by single missing defect cavities with a spacing of two lattice constants between next neighbouring cavities. One of the main features of the CCW is a very small group velocity, mainly near the band edges, which gives rise to the enhancement of phenomena such as group delay, nonlinear effects and stimulated emission. Therefore, CCW results of great interest for the design of optical functionalities such as optical delay lines [Lan01], dispersion compensators [Hos02], pulse compression [Moo02], second harmonic generation [Xu00] or Mach-Zehnder interferometers [Mar03]. Furthermore, lossless transmission through sharp bends is achieved if the cavity mode has a proper symmetry [Yar99].

However, when the CCW has finite length, as occurs in reality, the resonance peaks that appear in the transmission spectrum originate ripples in both group velocity and group delay responses that may distort the transmission of ultrashort pulses through the structure [Lan01]. The peak-to-valley ratio of these undesired resonant peaks is determined by the coupling efficiency at the two ends of the CCW. Therefore, proper mode matching may be achieved by designing the CCW interfaces in order to avoid the abrupt change in the reflectivity at the input and output of the chain of resonant cavities [Kar02]. An efficient coupling will result in eliminating the resonant peaks of the transmission spectrum so that flat transmission bands will be achieved.

5.2 Adiabatic coupling

Efficient coupling into conventional line defects photonic crystal waveguides have been widely investigated in the last years. However only a few works have focused on CCWs. Flat transmission bands were obtained by adding a number of additional defect cavities, carefully designed, at both ends of the waveguide in 1D [Ye04] and 2D CCW [Lan01]. It was also proposed that flat transmission bands could be achieved by a proper design of the filling ratio, i.e. the ratio of the defect radius to the lattice constant [Yan03]. In this work, adiabatic coupling between conventional photonic crystal single line defect waveguides (SLWGs) and CCWs is proposed. Adiabatic coupling is achieved by progressively varying the radii of the spacing defects between cavities. Therefore, the SLWG and CCW guided modes are gradually matched and an efficient coupling is achieved [Sum03].

5.2.1. Band diagram analysis

Figure 5.2 depicts the structure under study. An adiabatic taper is used to couple light from a SLWG into and out of a CCW of finite length.

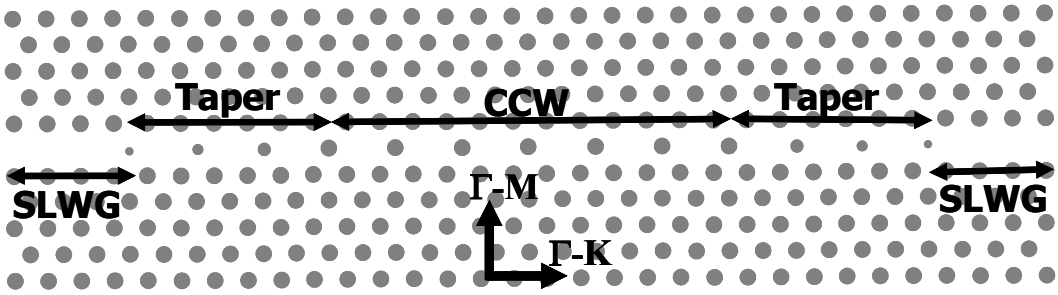

Figure 5.2.- Adiabatic coupling into CCWs. A taper, formed by gradually varying the radius of the spacing defect between cavities, is used to couple light from single-line-defect waveguides (SLWGs) into and out of a CCW of finite length.

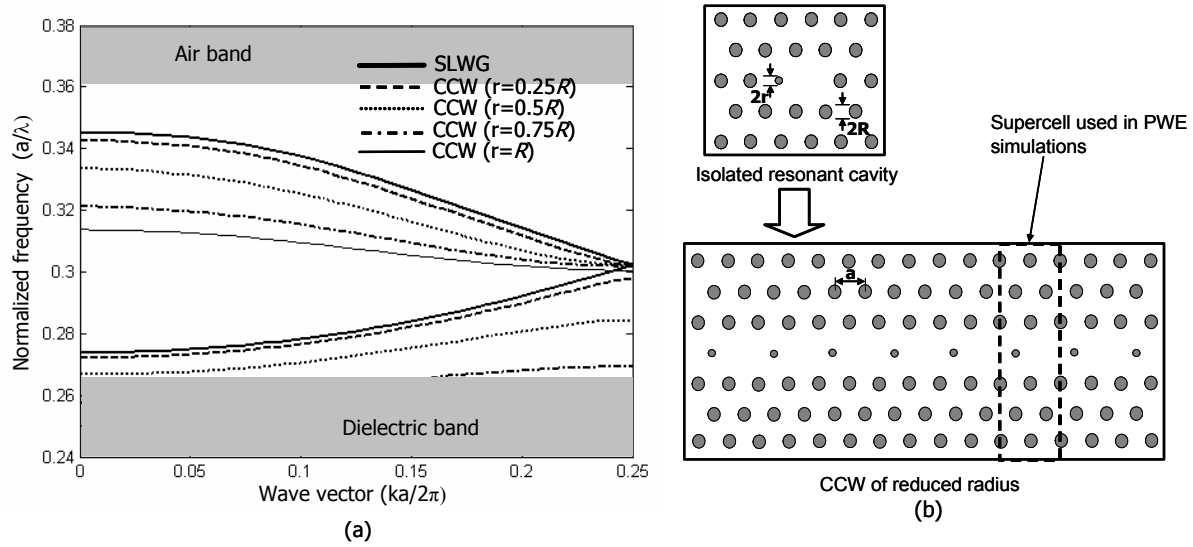

Figure 5.3.- (a) Dispersion diagrams for the SLWG and CCWs with r=0.25*R*, r=0.5*R*, r=0.75*R* and r=*R*. The parameter *r* refers to the radius of the spacing rod between cavities while *R* is the rod radius of the photonic crystal. (b) Isolated cavity and the corresponding CCW of reduced radius used to obtain the dispersion diagram.

The bulk photonic crystal structure considered here is a two-dimensional triangular lattice of dielectric rods of silicon surrounded by a homogeneous dielectric medium of silica. The refractive index value is of 3.45 for the former and of 1.45 for the latter. A TM gap appears between the normalized frequencies of 0.266(a/λ) and 0.361(a/λ) for a rod radius R=0.2a, a being the lattice constant. This is the same structure used in previous chapters. The SLWG is created by removing a row of rods along the ΓK direction while the CCW is formed by single missing rod cavities with a spacing of one rod between next neighbouring cavities. Initially, a taper formed by three rods of radius r=0.25*R*, r=0.5*R* and r=0.75*R* has been considered. Adiabatic transmission in photonic crystals may be achieved if it is ensured that the operating mode for every intermediate point in the taper is propagating (non evanescent) and guided [Joh02]. Therefore, the taper behavior may be predicted by calculating the independent dispersion diagrams at intermediate points in the taper.

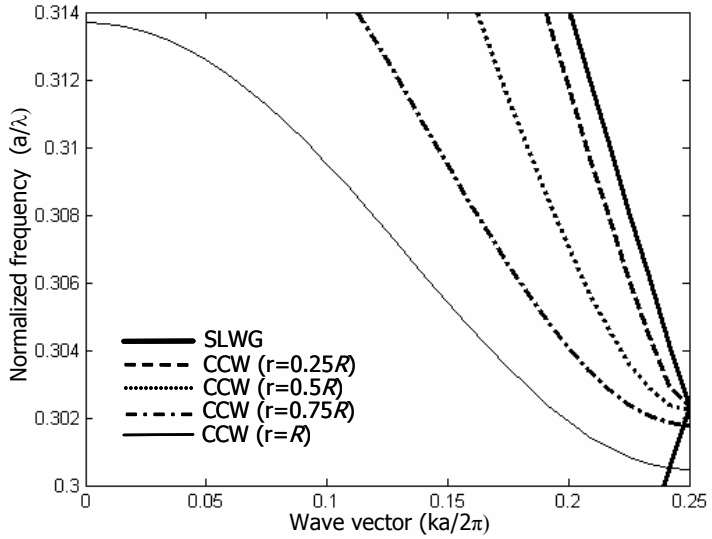

Figure 5.4.- Detailed view of the dispersion diagrams shown in figure 5.3(a). It can be observed that the mode splitting at the edge of the Brillouin zone originates frequency ranges in which propagation is not allowed.

The intermediate dispersion diagrams for the taper under study are obtained by CCWs formed by reducing the radius, *r*, of the spacing single rod between cavities. Figure 5.3(a) shows the dispersion diagrams of the SLWG and the CCWs with r=0.25*R*, r=0.5*R*, r=0.75*R* and r=*R*, calculated by means of the plane wave expansion method. Figure 5.3(b) shows the isolated cavity and the corresponding CCW of reduced radius as well as the supercell used in the plane wave expansion (PWE) simulations to obtain the dispersion diagrams [Joh01]. For the SLWG, a single mode appears that is folded back because a supercell of a periodicity of 2*a* in the ΓK direction, the same as that used for the CCW, was considered in the calculation. However, for the CCWs a mode splitting at the edge of the Brillouin zone, k=0.25($2\pi/a$), occurs, which is enlarged as the radius of the spacing rod increases. As described later, mode splitting degrades the transmission at those frequencies close to the edge band because the required condition of being a propagation mode at every point of the taper is not met. The violation of this condition is shown in figure 5.4, in which a detailed view of the dispersion diagrams represented in figure 5.3(a) is depicted. On the other hand, it can be seen in figure 5.3(a) that the high-frequency waveguide mode is the one giving rise to the CCW band while the low-frequency waveguide mode is rapidly pulled down toward the dielectric band. To understand this phenomenon, transmission spectra and field distributions of the corresponding isolated cavities, which form each of the CCWs with different radius, have been calculated by means of two-dimensional finite-difference time-domain (FDTD) simulations. A grid size of a/50 was employed in the FDTD simulations and perfectly matched layers conditions were considered at the boundary regions.

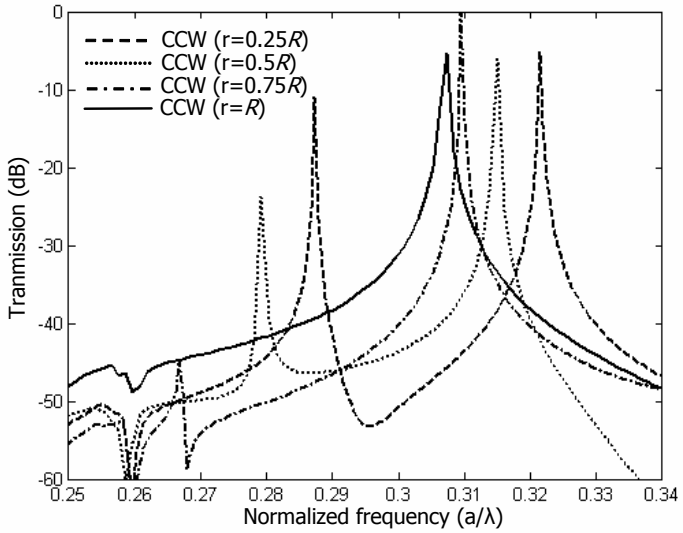

Figure 5.5.- Transmission responses of the isolated cavities that form the CCWs with different rod radius as a function of the normalized frequency. The considered isolated cavity is shown in figure 5.3(b).

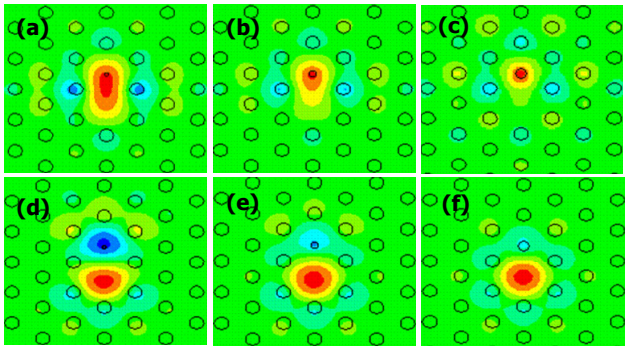

Figure 5.6.- Electrical field distribution for r=0.25*R*, r=0.5*R* and r=0.75*R* is shown at (a)-(c) the low-frequency and (d)-(f) the high-frequency resonant modes respectively.

5.2.2. Transmission spectra analysis

Figure 5.5 shows the transmission spectra of the different isolated cavities that form the CCWs as a function of the normalized frequency. The isolated cavity is created by two adjacent point defects: a missing rod and a rod of radius *r* smaller than the radius of the rest of the rods, as illustrated in figure 5.3(b). In figure 5.5, it may be observed that for r=*R* one resonant mode appears while for r<*R* two resonant modes result due to the two adjacent defects. It should be noticed that these two resonant modes are those that give rise to the two waveguides modes shown in figure 5.3(a) and the eigenfrequencies of each isolated cavity are in agreement with the central frequencies of the waveguide modes.

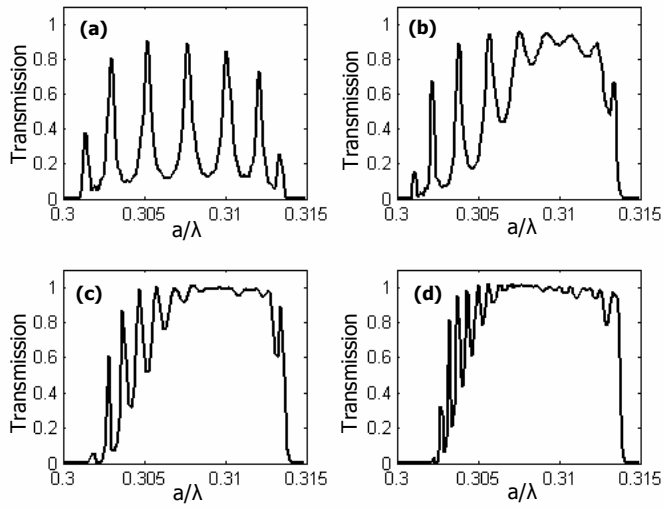

Figure 5.7.- Transmission efficiency as a function of the normalized frequency for the structure shown in figure 5.2 for several cases: (a) without taper and with taper with (b) L=3, (c) L=9 and (d) L=14. The parameter *L* refers to the number of intermediate rods, with a linear variation of their radius, used in the taper.

The electric field distributions of the two resonant modes for r=0.25*R*, r=0.5*R* and r=0.75*R* cases are shown in figure 5.6. In figure 5.6(a)-(c), it can be clearly seen that the field distribution of the low-frequency mode is concentrated around the small rod of reduced radius, i.e. in the region of high refractive index, while the field in the high-frequency resonant mode is concentrated around the missing rod, i.e. in the region of low refractive index, as depicted in figure 5.6(d)-(f). This result is consistent with the fact that high-frequency modes concentrate their energy in low dielectric constant regions while low-frequency modes concentrate their energy in high dielectric constant regions [Joa95]. These results also explain why the low-frequency waveguide modes (see figure 5.3(a)) are rapidly pulled down toward the dielectric band. As the radius of the spacing rod increases, the region of high refractive index, where the mode is concentrated, also increases and thus the waveguide mode is shifted to lower frequencies.

Figure 5.7 shows the transmission efficiency as a function of the normalized frequency for the structure shown in figure 5.2. The vertical scale is in linear units to enhance the variations of the transmission spectra shape. To obtain the presented results an incident pulsed field was launched at an input dielectric waveguide and coupled to the SLWG by employing the coupling technique proposed in chapter four. This coupling technique was also used to extract light at the end of the structure shown in figure 5.2 and allowed us to calculate the transmission spectrum with the overlap integral between the launched and measured field at the input and output dielectric waveguides respectively. The transmission spectrum was then

obtained with a simple rescaling to remove external coupling losses from the results.

Transmission spectra have been calculated for a 7-cavities CCW coupled to an 8-rows SLWG without taper, shown in figure 5.7(a), and by using three tapers of different length formed by L rods with a linear variation of their radius, shown in figure 5.7(b)-(d), where $r=nR/(L+1)$, n values ranging from 1 to L. It should be noticed that the number of resonant peaks that appears in the transmission spectra depends on both the taper and the CCW length. However, only the taper length has been varied keeping the CCW length constant to show that, although the number of resonance peaks increases for longer tapers, the peak-to-valley ratio is reduced due to the improvement of the coupling efficiency. Thereby, flat transmission bands with coupling efficiencies above 90% are achieved. However, it can be seen that the transmission is degraded at the low frequencies of the band appearing significant resonance peaks. The reason of this behavior is twofold. Firstly, the group index mismatch is especially large at those frequencies because the modes of the CCWs with reduced radius are flattened at the band edge unlike the SLWG mode, which is simply folded back as shown in figure 5.4. Therefore, efficient transmission can only be achieved by using slowly varying tapers as it can be seen in figure 5.7 in which the transmission response is improved at low frequencies as the taper length increases. Secondly, the imposed requirement for a proper adiabatic coupling of being a propagation mode for every intermediate point in the taper is not ensured near the band edge (see figure 5.4). This gives also rise to a slight bandwidth reduction at lower frequencies, which is enhanced as the taper length increases. For the shorter taper (L=3) this reduction is negligible because the tails of the evanescent field, which is not allowed to propagate within the taper at those frequencies, achieve to excite the CCW mode.

5.3 Pulse propagation analysis

It has been seen that an inefficient coupling originates a number of undesired resonance peaks in the transmission spectrum that coincides with the number of cavities that form the CCW. Efficient coupling into CCWs can be a critical point in order to achieve an optimum dynamic performance because the propagation of ultra short pulses may be seriously distorted due to the oscillations in the transmission spectrum. In recent years, pulse propagation has been analyzed by means of simulations and experiments in bulk photonic crystals [Imh99, Tan02], line defects photonic crystal waveguides [Yam03, Asa04] as well as in CCW [Lan01, Moo02a, Kar04]. In almost all the works, pulse propagation has been analyzed to study the dispersion features of photonic crystals. However, only the work of S. Lan *et al*. is, to the best of our knowledge, focused on the analysis of pulse propagation from the coupling point of view [Lan01].

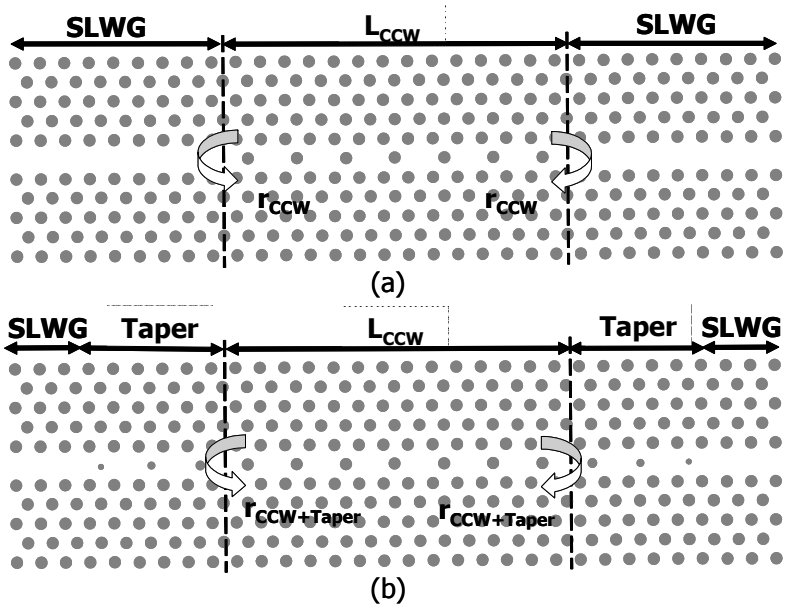

Figure 5.8.- Schematic of the analyzed structures. A coupled cavity waveguide (CCW) of finite length is (a) butt coupled and (b) adiabatically coupled to single line defect waveguides (SLWGs).

A rigorous analysis of pulse propagation in frequency and time domains is carried out in order to analyze the influence of the coupling efficiency on the main parameters of the pulse. Results by using the proposed adiabatic coupling technique are compared to the case of butt coupling between the SLWGs and the CCW of finite length. A comprehensive explanation of the origin of the pulse degradation when the CCW is inefficiently coupled is provided. A different explanation from that provided by S. Lan *et al*. is given in order to explain the origin of pulse degradation when the CCW is inefficiently coupled. It is shown that pulse degradation is simply originated due to the overlapping between the transmitted pulse and the reflected pulses produced due to the high reflection at the CCW interfaces. Furthermore, the Fabry-Perot formula has been used to study a large variety of parameters dramatically reducing the computation time with respect to FDTD simulations.

5.3.1 Theoretically model

The photonic crystal structure and parameters are the same that the ones used in the previous section. The SLWG is used to couple light into and out a CCW of finite length. Both waveguides are created along the Γ*K* direction. The CCW consists of neighbouring cavities formed by removing individual rods and the spacing between cavities is of one rod. Figure 5.8(a) shows the butt coupled CCW while figure 5.8(b) shows the adiabatically coupled CCW. The well-known Fabry-Perot formula has been used for modeling the pulse propagation along the CCW of finite length [Hau84].

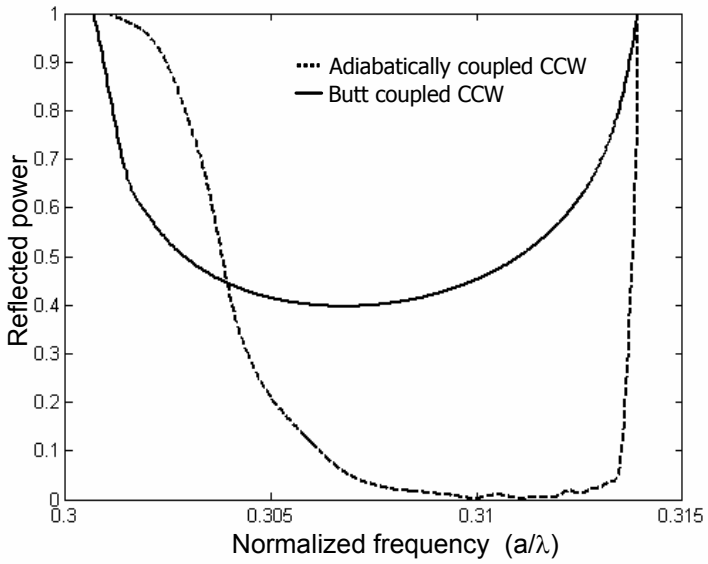

Figure 5.9.- Reflected power, *R*, as a function of the normalized frequency for the butt coupled and adiabatically coupled CCW. The adiabatic taper is formed by 9 intermediate rods with a linear variation of their radius.

The transmission response in amplitude can be written as

$$t_{FP}(f_n) = \frac{-t^2 \exp(-j\frac{2\pi}{a}kL)}{1-r^2 \exp(-j\frac{4\pi}{a}kL)} \tag{5.1}$$

where f_n is the normalized frequency, k is the normalized wave vector, L is the cavity length and t and r are the transmission and reflection coefficients. The relation between f_n and k is determined by the dispersion diagram, which is shown in figure 5.4 with thin solid line. The reflection coefficients for the butt coupled and the adiabatically coupled CCW, depicted in figure 5.8, were calculated with the semi-analytic method described in chapter three. The reflected power, *R*, as a function of the normalized frequency is shown in figure 5.9 for both structures. The adiabatic taper considered hereafter is formed by 9 intermediate rods with a linear variation of their radius. It can be seen that the reflection is almost negligible for a broad frequency range in agreement with the results shown in figure 5.7.
The reflection is calculated as

$$r = \sqrt{R} \tag{5.2}$$

and the transmission is obtained from (5.2) as

$$t = \sqrt{1 - r^2} \tag{5.3}$$

because radiation modes are not allowed in the photonic crystal and both the CCW and the SLWG are single mode.

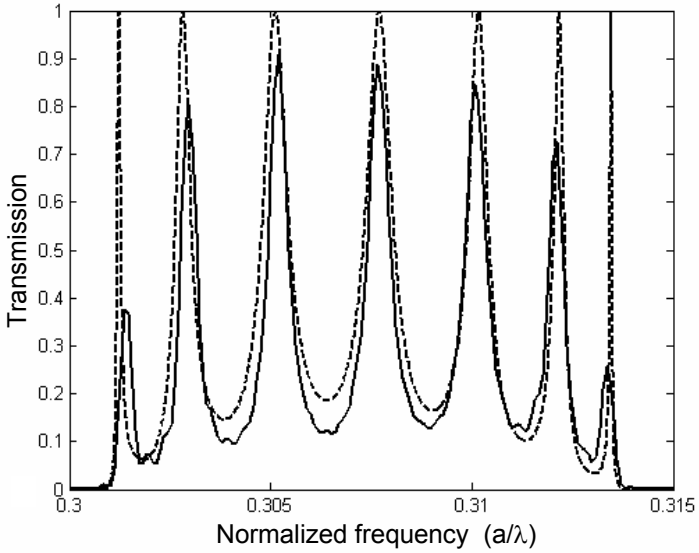

Figure 5.10.- Transmission spectra calculated by the Fabry-Perot formula (dashed line) and by the finite-difference time-domain method (solid line) for the butt coupled CCW.

The power transmission spectrum is calculated as

$$T_{FP}(f_n) = \left|t_{FP}(f_n)\right|^2 \tag{5.4}$$

Figures 5.10 and 5.11 show the transmission spectra calculated with (5.4) (dashed line) and the transmission spectra calculated by using the FDTD method (solid line) for the butt coupled and the adiabatically coupled CCW respectively. The CCW has a length of $L = 16a$ in both cases. A very good agreement can be seen between the Fabry-Perot model and FDTD simulation for the butt coupled CCW shown in figure 5.10. The amplitude of the resonance peaks, principally at the band edges, is lower in the FDTD simulation because a higher frequency resolution would require a very long simulation time. On the other hand, the number of resonances in the adiabatically coupled CCW, shown in figure 5.11, is higher in the FDTD spectrum compared to the theoretical results. This is because the total cavity length will not only depend on the CCW length but also on the input and output tapers length. The taper sections can not be modelled by using the Fabry-Perot model since the dispersion relation is also modified along the taper. However, we are mainly interested in the range of frequencies in which flat transmission occurs, where the Fabry-Perot model and FDTD simulations agree quite well. Even in this case, it is important to notice that the taper sections may introduce an additional broadening and group delay on the propagated pulse that is not taken into account by the Fabry-Perot model. However, the broadening is usually negligible due to the short length of the taper while the group delay can be theoretically estimated, as it will be shown later.

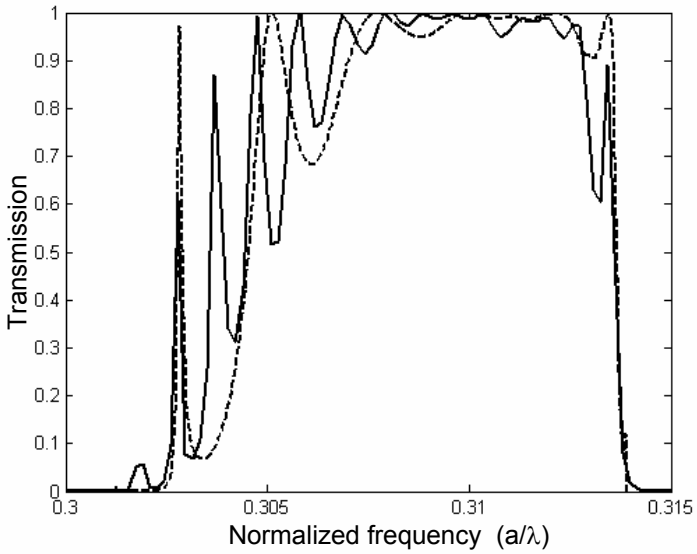

Figure 5.11.- Transmission spectra calculated by the Fabry-Perot formula (dashed line) and by the finite-difference time-domain method (solid line) for the adiabatically coupled CCW.

The main advantage of using the theoretical model is that the computational time is significantly reduced compared to FDTD simulations. Therefore, a large variety of parameters can be easily analyzed. The procedure is the following. A Gaussian source is used as input pulse. The input pulse is Fourier transformed and multiplied by the Fourier transform of (5.1). Thereby, the spectrum response of the output pulse is obtained and the time response is calculated by the inverse Fourier transform. The main parameters of the input pulse that can be adjusted are the full-width at half-maximum (FWHM) and the central frequency while the amplitude is normalized.

5.3.2 Frequency domain analysis

The influence on group delay, FWHM and peak amplitude of a pulse propagated through a CCW of finite length (L=16a) has been investigated. Results were obtained by using the Fabry-Perot model. Three input pulses of different FWHM have been considered: 250, 500 and 1000 femtoseconds (fs). In this case, a lattice constant of 465nm has been considered. First of all, it can be seen in figure 5.12(a) that when the input pulse is propagated through the adiabatically coupled CCW, the group delay is almost the same for the three widths of the input pulse. The thicker solid line shows the theoretical group delay calculated from the dispersion relation of the CCW particularized for the CCW length of L=16a. A very good agreement with the results obtained by using the Fabry-Perot model is observed. The increase of group delay at the band edges is due to the low group velocity of the guided mode at those frequencies.

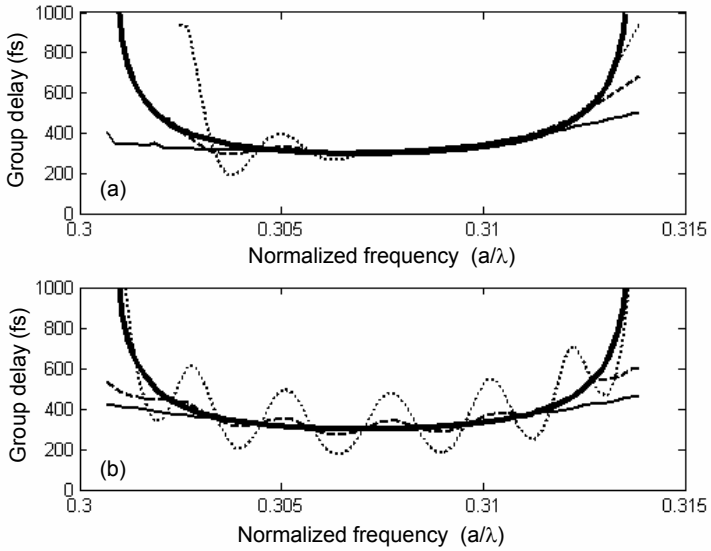

Figure 5.12.- Group delay of the output pulse as a function of the normalized central frequency of the input pulse for (a) the adiabatically and (b) butt coupled CCW of length L=16*a*. The solid, dashed and dotted lines show the results for FWHMs of the input pulse of 250fs, 500fs and 1000fs respectively. The thicker solid line shows the theoretical group delay calculated from the dispersion relation of the CCW.

However, it can be seen in figure 5.12(b) that the group delay oscillates with frequency when the input pulse is propagated through the butt coupled CCW. The origin of this oscillation, which can also be seen as an oscillation of the group velocity, is due to the overlapping between the transmitted pulse and the successive reflected pulses, which are transmitted out of the CCW after they travel a number of times back and forth along the CCW depending on the reflection at the interfaces.

Figure 5.13 explains more clearly this effect. The increase or decrease of group delay with respect to the ideal case depends on the constructive or destructive interference between the transmitted and reflected pulses, which depends on the CCW length and the central frequency of the input pulse, but also on the width of the input pulse. Therefore, the group delay in the adiabatically coupled CCW, shown in figure 5.12(a), begins to oscillate at the low frequencies of the band due to the increase of reflection that occurs at these frequencies. The group delay oscillations have also higher amplitude as the FWHM of the input pulse increases in both the butt coupled and adiabatically coupled CCW. Figure 5.14(a) shows the transmitted and successive reflected pulses in the butt coupled CCW considering an input pulse with a FWHM of 1000fs and a central frequency of 0.3101(a/λ). The amplitude of the successive reflected pulses is attenuated each time the pulse travels back and forth along the CCW due to the reflection losses.

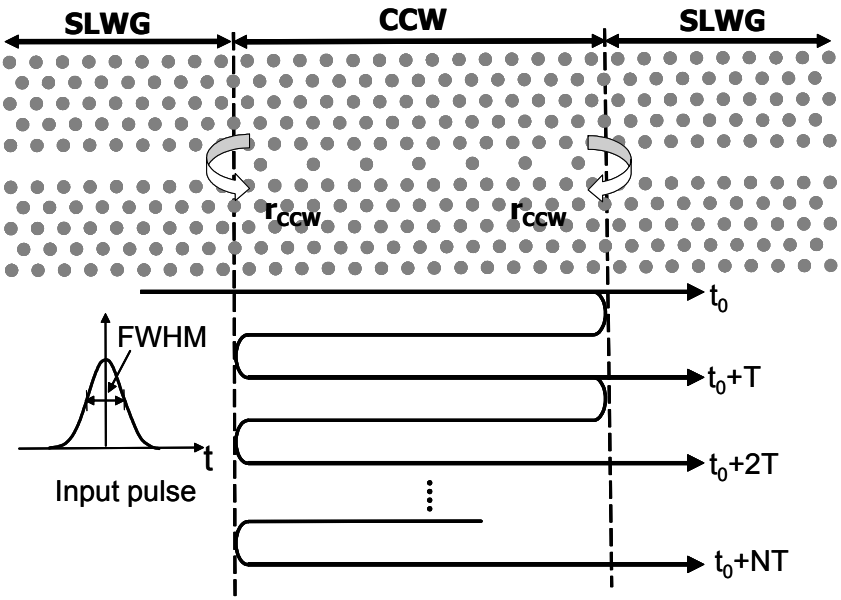

Figure 5.13.- Effect of the overlapping between pulses due to the inefficient coupling at the CCW interfaces. The transmitted pulse, t_o, and successive reflected pulses, t_o+NT, which are transmitted out of the CCW after they travel back and forth along the CCW, interfere among them forming the total transmitted pulse. T is the round-trip delay.

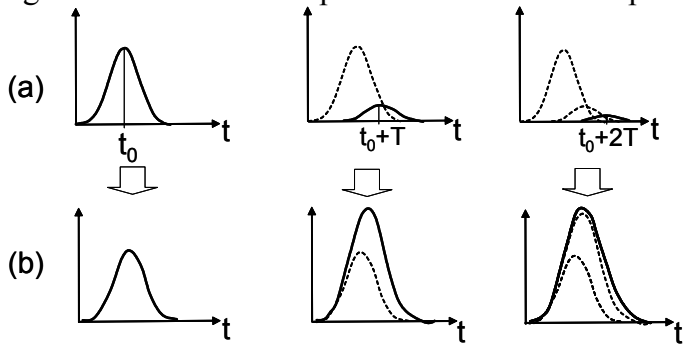

Figure 5.14.- (a) Transmitted and successive reflected pulses and (b) the output pulse evolution in time after each reflected pulse is transmitted out the butt coupled CCW. In this example, the input pulse has a FWHM of 1000fs and a central frequency of 0.3101(a/λ) while the CCW length is 16a.

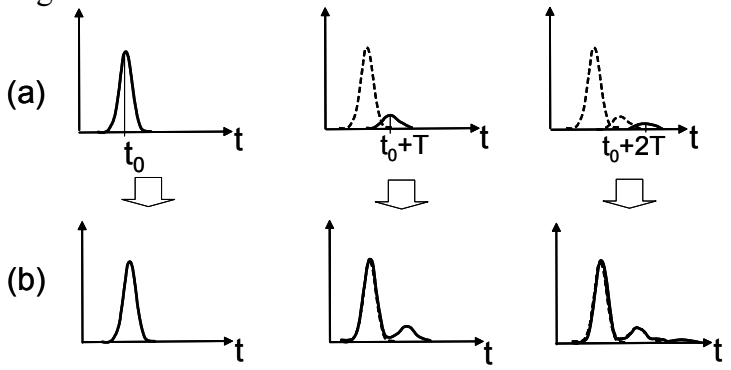

Figure 5.15.- The same as above figure but considering an input pulse with FWHM=250fs.

However, it can be seen that due to the short length of the CCW (L=16a), the transmitted and reflected pulses overlap when they are transmitted out of the CCW. This overlapping distorts the total output pulse affecting to the group delay as well as to the FWHM and pulse attenuation, as it will be shown later. Figure 5.14(b) shows the output pulse evolution in time after each reflected pulse is transmitted out of the CCW. The distortion of the output pulse is higher as the number of successive reflected pulses transmitted out of the CCW increases.

On the other hand, when the input pulse is narrower, the overlapping becomes almost negligible. This can be seen in figure 5.15 that shows the transmitted and successive reflected pulses considering an input pulse with a FWHM of 250fs and a central frequency of 0.3101(a/λ) as well as the output pulse evolution after each reflected pulse is transmitted out the CCW. In this case, the group delay and FWHM of the main output pulse is not altered independently of the reflection at the CCW interfaces. Therefore, the group delay responses considering an input pulse with a FWHM of 250fs, shown with solid lines in figure 5.12, are the same for the adiabatically and butt coupled CCW. However, a train of successive pulses appears at the output of the CCW when high reflection exists at the interfaces, as shown in the right part of figure 5.15(b). Furthermore, the amplitude of the output pulse depends also on the transmission efficiency at the CCW interfaces. When the overlapping between successive pulses is negligible, the pulse amplitude will be approximately twice the transmission efficiency between the SLWG and the CCW. Therefore, the highest transmission efficiency, or in other words the lowest reflection, is desirable even when narrow input pulses are used.

The effect of the overlapping between successive pulses can be theoretically estimated by comparing the FWHM and the round trip delay, which is defined as $2L/v_g$ where L is the CCW length and v_g is the group velocity. For the particular case of L=16a (7.44μm) and a central frequency of the input pulse of 0.3101(a/λ) that corresponds to a v_g~0.02fs/μm, the round trip delay is 744fs. When the FWHM is lower than the round trip delay, the overlapping will be minimized. Therefore, there is a significant overlapping when the FWHM of the input pulse is 1000fs, as depicted in figure 5.14(a), but it is insignificant when the FWHM of the input pulse is 250fs, as depicted in figure 5.15(a).

The same behavior than that of the group delay response can be observed for the FWHM and peak amplitude of the output pulse, as shown in figures 5.16 and 5.17. The FWHM is similar to that of the input pulse, as shown figure 5.16(a), when the reflection at the CCW interfaces is negligible, but it becomes to oscillate with frequency, as shown in figure 5.16(b), when the reflection grows up.

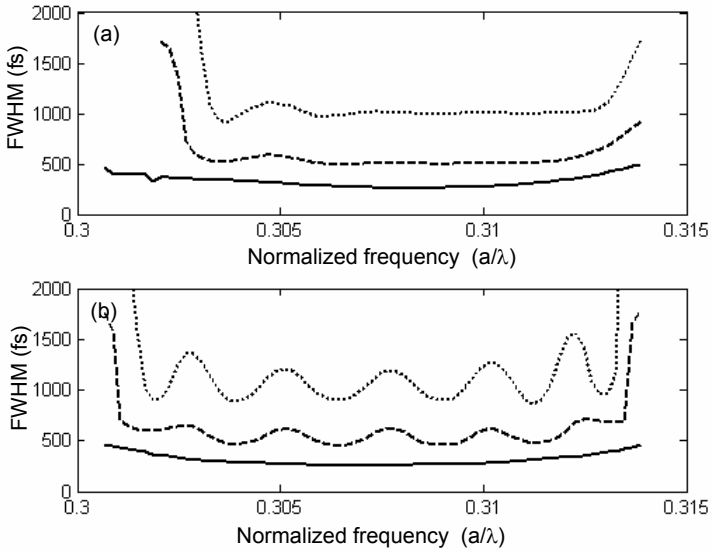

Figure 5.16.- Full-width at half-maximum (FWHM) of the output pulse as a function of the normalized central frequency of the input pulse for (a) the adiabatically and (b) butt coupled CCW. The solid, dashed and dotted lines show the results considering an input pulse of 250fs, 500fs and 1000fs respectively.

The increase of the FWHM at the band edges is due to the larger group velocity dispersion (GVD). Furthermore, there is also an additional broadening because part of the bandwidth of the pulse is filtered by the transmission spectrum. This reduction of the bandwidth implies that the output pulse suffers an extra broadening that adds to that derived from the effect of GVD. On the other hand, when narrower input pulses are considered, the FWHM of the output pulse at frequencies located in the middle of the band is slightly higher than that of the input pulse because the bandwidth of the pulse covers a higher frequency range thus increasing the effect of GVD.

The attenuation of the output pulse is very low when the adiabatically coupled CCW is used, as it can be seen in figure 5.17(a), except at the low frequencies of the band, which is again expected due to the higher reflection at these frequencies. Furthermore, there is a slight bandwidth reduction at low frequencies compared to the butt coupled CCW response, shown in figure 5.17(b), which can also be seen in the results shown in figures 5.12(a) and 5.16(a). The origin of this bandwidth reduction was discussed in section 5.2.2. On the other hand, although the group delay and FWHM responses in both the butt coupled and the adiabatically coupled CCW are the same when narrower input pulses are considered due to the lower overlapping between the transmitted and reflected pulses, the attenuation of the output pulse is much higher in the butt coupled CCW than in the adiabatically coupled CCW due to the lower transmission efficiency.

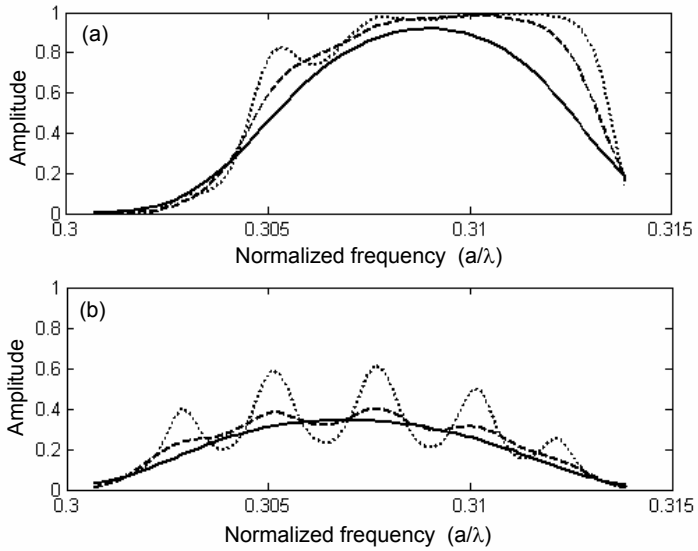

Figure 5.17.- Peak amplitude of the output pulse as a function of the normalized central frequency of the input pulse for (a) the adiabatically and (b) butt coupled CCW. The solid, dashed and dotted lines show the results considering an input pulse of 250fs, 500fs and 1000fs respectively.

5.3.3 Time domain analysis

Comparing the results shown in figures 5.12(b), 5.16(b) and 5.17(b) to the transmission spectrum of the butt coupled CCW, shown in figure 5.10, it can be observed that the maximums and minimums in the transmission spectrum correspond to maximums and minimums of group delay, FWHM and peak amplitude of the output pulse. This behavior is due to the fact that when the central frequency of the input pulse coincides with a maximum of the transmission spectrum, the transmitted pulse interferes constructively with the reflected pulses so the width of the output pulse is increased as well as the group delay. Furthermore, the pulse attenuation decreases because the transmission efficiency is higher. The opposite performance occurs when the central frequency of the input pulse coincides with a minimum of the transmission spectrum. In order to analyze in depth this behavior, time domain pulse propagation has been analyzed at two different normalized central frequencies of the input pulse, 0.3089(a/λ) and 0.3101(a/λ), which correspond to a minimum and a maximum of the transmission spectrum, respectively, for the butt coupled CCW. The input pulse spectra corresponding to FWHMs of 250fs, 500fs and 1000fs are shown in figure 5.18(a) for the central frequency of 0.3089(a/λ) and in figure 5.18(b) for the central frequency of 0.3101(a/λ). The transmission spectrum of the adiabatically coupled CCW is also shown in figure 5.18. The group delay, FWHM and amplitude of the output pulse have been obtained by means of FDTD simulations as well as with the Fabry-Perot model.

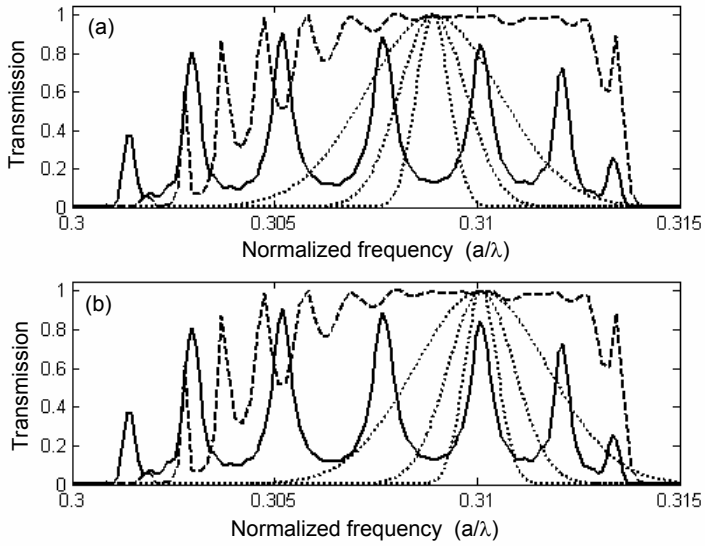

Figure 5.18.- Transmission spectra of the input pulse for a normalized central frequency of (a) 0.3089(a/λ) and (b) 0.3101(a/λ). The FWHM of the input pulse is 250fs (broader spectrum), 500fs and 1000fs (narrower spectrum). The solid and dashed lines show the transmission spectra of the butt coupled and adiabatically coupled CCW.

FWHM	Fabry-Perot model			FDTD simulations		
	FWHM	Delay	Amplitude	FWHM	Delay	Amplitude
250	264.281	650.117	0.3096	258.923	672.758	0.2905
500	456.464	617.405	0.3021	449.696	635.064	0.2712
1000	897.418	513.253	0.2147	876.925	512.112	0.1827

Table 5.1.- Full-width at half-maximum (FWHM) (fs), group delay (fs) and peak amplitude of the output pulse as a function of the FWHM of the input pulse considering the butt coupled CCW. Results of FDTD simulations and the Fabry-Perot model are compared. Regarding the group delay, the excess delay (~330fs) introduced by the input and output SLWGs have been added to the group delay obtained from the Fabry-Perot model to better compare to FDTD simulations. The central frequency of the input pulse is 0.3089(a/λ) and the CCW length is L=16a.

Tables 5.1 and 5.2 show the results for the butt coupled CCW for the two different central frequencies considered while tables 5.3 and 5.4 show the results for the adiabatically coupled CCW. First of all, it can be seen that FDTD simulations and theoretical results agree quite well. Regarding the group delay, the excess delay introduced by the input and output SLWGs have been added to the group delay obtained from the Fabry-Perot model to better compare to FDTD simulations. This additional delay can be theoretically estimated from the dispersion relation of the SLWG.

FWHM	Fabry-Perot model			FDTD simulations		
	FWHM	Delay	Amplitude	FWHM	Delay	Amplitude
250	281.295	669.549	0.2528	291.447	697.809	0.2557
500	621.622	699.535	0.3128	654.569	745.185	0.3514
1000	1266.51	873.341	0.5028	1214.06	897.606	0.5670

Table 5.2.- Full-width at half-maximum (FWHM) (fs), group delay (fs) and peak amplitude of the output pulse as a function of the FWHM of the input pulse considering the butt coupled CCW. Results of FDTD simulations and the Fabry-Perot model are compared. Regarding the group delay, the excess delay (~328fs) introduced by the input and output SLWGs have been added to the group delay obtained from the Fabry-Perot model to better compare to FDTD simulations. The central frequency of the input pulse is 0.3101(a/λ) and the CCW length is L=16a.

FWHM	Fabry-Perot model			FDTD simulations		
	FWHM	Delay	Amplitude	FWHM	Delay	Amplitude
250	263.858	784.347	0.9193	263.200	814.886	0.9344
500	499.704	774.101	0.9698	502.195	799.799	0.9856
1000	995.46	767.521	0.9609	1000.830	797.309	0.9905

Table 5.3.- Full-width at half-maximum (FWHM) (fs), group delay (fs) and peak amplitude of the output pulse as a function of the FWHM of the input pulse considering the adiabatically coupled CCW. Results of FDTD simulations and the Fabry-Perot model are compared. Regarding the group delay, the excess delay (~460fs) introduced by the input and output SLWGs and tapers have been added to the group delay obtained from the Fabry-Perot model to better compare to FDTD simulations. The central frequency of the input pulse is 0.3089(a/λ) and the CCW length is L=16a.

FWHM	Fabry-Perot model			FDTD simulations		
	FWHM	Delay	Amplitude	FWHM	Delay	Amplitude
250	276.877	806.466	0.8843	278.005	835.848	0.8299
500	503.981	797.912	0.9816	503.464	827.071	0.9716
1000	1002.79	795.374	0.9937	1002.79	817.329	0.9807

Table 5.4.- Full-width at half-maximum (FWHM) (fs), group delay (fs) and peak amplitude of the output pulse as a function of the FWHM of the input pulse considering the adiabatically coupled CCW. Results of FDTD simulations and the Fabry-Perot model are compared. Regarding the group delay, the excess delay (~455fs) introduced by the input and output SLWGs and tapers have been added to the group delay obtained from the Fabry-Perot model to better compare to FDTD simulations. The central frequency of the input pulse is 0.3101(a/λ) and the CCW length is L=16a.

Furthermore, the input and output tapers also introduce an additional delay in the adiabatically coupled CCW, which has also been added in tables 5.3 and 5.4 to the group delay obtained from the Fabry-Perot model. This delay can be estimated for a particular normalized frequency with

$$\Delta\tau_{taper}(f_n) = \sum_{i=1}^{LT} 4a / v_g^i(f_n) \tag{5.5}$$

where $4a$ is twice the length of the intermediate sections that form the taper being a the lattice constant, $v^i_g(f_n)$ is the group velocity at the corresponding normalized frequency calculated from the intermediate dispersion diagrams of the taper and LT is the taper length. For instance, the additional delay for the butt coupled CCW due to the input and output SLWGs, whose total length is $51a$, at the normalized frequency of $0.3089(a/\lambda)$ will be around 330fs while the additional delay for the adiabatically coupled CCW will be around 460fs being 360fs due to the input and output tapers, calculated with (5.5) and whose total length is $36a$, and being 100fs due to the input and output SLWGs, whose total length is $15a$. On the other hand, the results shown in tables 5.1 and 5.2 corroborate that the group delay, FWHM and amplitude of the output pulse decrease with respect to the ideal performance when the central frequency of the input pulse coincides with a minimum of the transmission spectrum while they increase when the central frequency of the input pulse coincides with a maximum of the transmission spectrum. Furthermore, this effect becomes more noticeable as the input pulse is wider.

The input pulse (FWHM=1000fs) as well as the output pulses propagated through the butt coupled CCW when the central frequency of the input pulse is $0.3101(a/\lambda)$ and $0.3089(a/\lambda)$ are shown in figures 5.19(a)-(c) respectively. It should be noticed that only the pulse envelope is shown and therefore the time response of the input pulse for both central frequencies will be the same. From the results shown in figure 5.19, it can be seen that an excellent agreement between FDTD results, shown with solid line, and theoretical results, shown with dashed line, is achieved. On the other hand, it can be observed that at both frequencies the rising time of the output pulse is the same than that of the input pulse. However, the falling time increases at $0.3101(a/\lambda)$, as it can be seen in figure 5.19(b), due to the constructive interference between the transmitted and reflected pulses while it decreases at $0.3089(a/\lambda)$, as it can be seen in figure 5.19(c), due to the destructive interference between the transmitted and reflected pulses. Therefore, the FWHM as well as the group delay increases in the former while decreases in the latter. Furthermore, the attenuation of the output pulse is much lower in the former than in the latter.

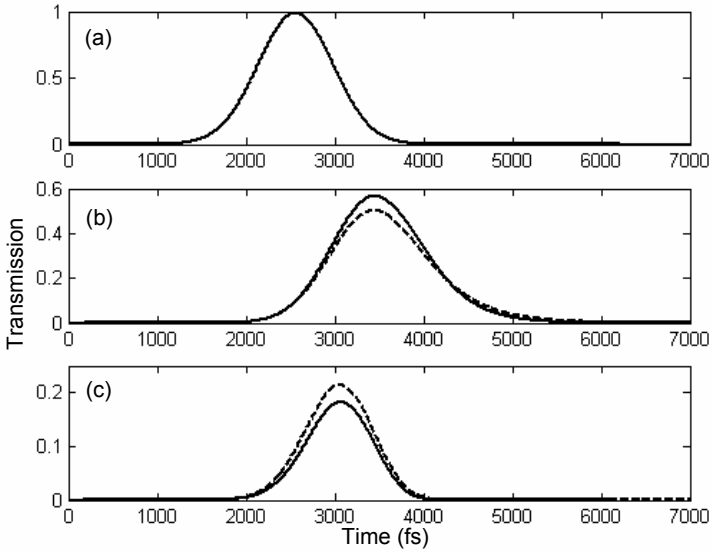

Figure 5.19.- Pulse propagation through the butt coupled CCW for an input pulse, shown in (a), with FWHM=1000fs and central frequencies (b) 0.3101(a/λ) and (c) 0.3089(a/λ). The solid line shows FDTD simulations while the dashed line shows the results obtained with the Fabry-Perot model.

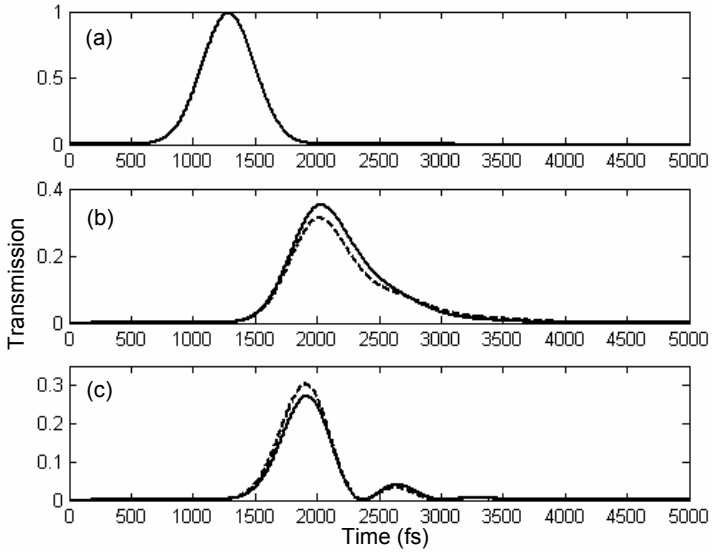

Figure 5.20.- Pulse propagation through the butt coupled CCW for an input pulse, shown in (a), with FWHM=500fs and central frequencies (b) 0.3101(a/λ) and (c) 0.3089(a/λ). The solid line shows FDTD simulations while the dashed line shows the results obtained with the Fabry-Perot model.

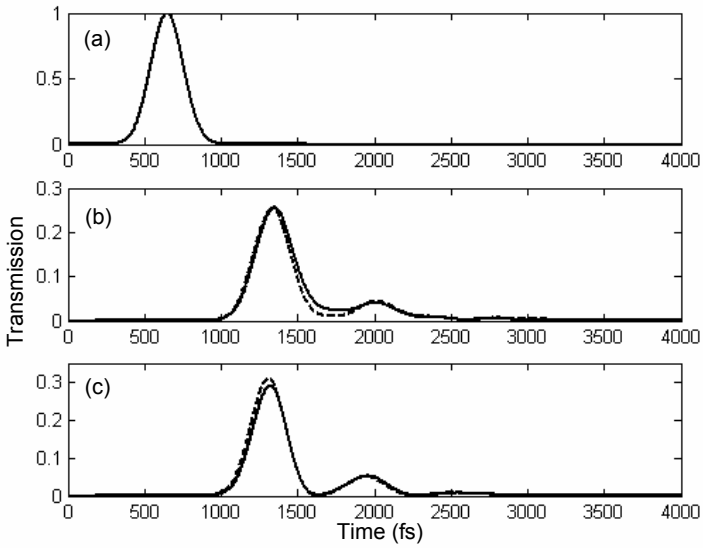

Figure 5.21.- Pulse propagation through the butt coupled CCW for an input pulse, shown in (a), with FWHM=250fs and central frequencies (b) 0.3101(a/λ) and (c) 0.3089(a/λ). The solid line shows FDTD simulations while the dashed line shows the results obtained with the Fabry-Perot model.

It is important to point out that the increase or decrease of FWHM and group delay is an artificial artifact due to the overlapping between the transmitted and reflected pulse and not due to a variation of the dispersion relation associated to the finite length of the CCW.

The same behavior takes place when the input pulse has a FWHM of 500fs, as shown in figure 5.20. However, in this case the reflected pulses, which travel several times back and forth along the CCW and therefore suffer a higher delay, do not entirely overlap with the transmitted pulse due to the lower width of the input pulse. Therefore, the variation of the FWHM and group delay of the output pulse regarding the ideal performance is diminished. The successive reflected pulses that suffer a higher delay are seen when the central frequency of the input pulse is 0.3089(a/λ), shown in figure 5.20I, because the destructive interference of the reflected pulses that overlap shortens the falling time of the output pulse.

This performance can be clearly observed in figure 5.21, which shows the propagated pulses when the input pulse has only a FWHM of 250fs. In this case, the reflected pulses practically do not overlap with the transmitted pulse and therefore they can be seen independently of the central frequencies of the input pulse. Therefore, the FWHM, group delay and pulse attenuation of the output pulse is similar in figures 5.21(b) and 5.21(c). The slight differences in the FWHM and group delay are those determined due to the different behaviour of the dispersion relation at both frequencies.

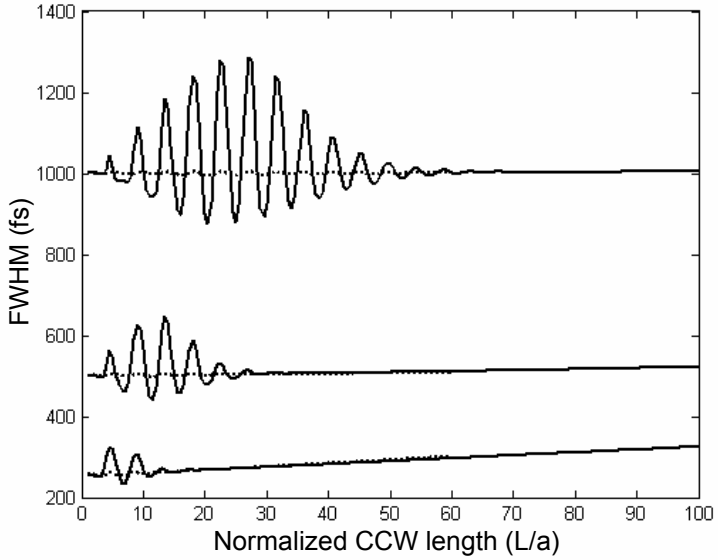

Figure 5.22.- Full-width at half-maximum (FWHM) of the output pulse as a function of the normalized CCW length for an input pulse of FWHMs of 250fs, 500fs and 1000fs and a central frequency of 0.3101(a/λ). The solid line shows the results for the butt coupled CCW while the dashed line shows the results for the adiabatically coupled CCW.

5.3.4 Variation of the CCW length

Figure 5.22 shows the FWHM as a function of the normalized CCW length for the butt coupled (solid line) and the adiabatically coupled CCW (dotted line) considering that the central frequency of the input pulse is 0.3101(a/λ). Three input pulses of different FWHM have been considered: 250fs, 500fs and 1000fs. It can be seen that the FWHM of the output pulse does not oscillate when the adiabatic taper is used independently of the FWHM of the input pulse. However, the FWHM oscillates when the reflection into the CCW increases, i.e. for the butt coupled CCW. Furthermore, the oscillations have higher amplitude and occur in a larger range of CCW lengths when the FWHM of the input pulse increases due to the fact that the overlapping between the transmitted and reflected pulses will be larger. The highest amplitude of the oscillations arises when the round trip delay of the CCW is similar to the FWHM of the input pulse. On the other hand, the maximum or minimum of the oscillations depends on if the central frequency of the input pulse coincides or not with a maximum or minimum of the transmission spectrum. Note that the resonances in the transmission spectrum are located at different frequencies and their number decreases or increases as the CCW length is shorter or longer respectively. It is also interesting to notice that if the CCW is very short, the transmitted and reflected pulses will almost entirely overlap and therefore the FWHM of the output pulse will not be affected although the amplitude of the output pulse will still be attenuated with respect to the adiabatically coupled CCW.

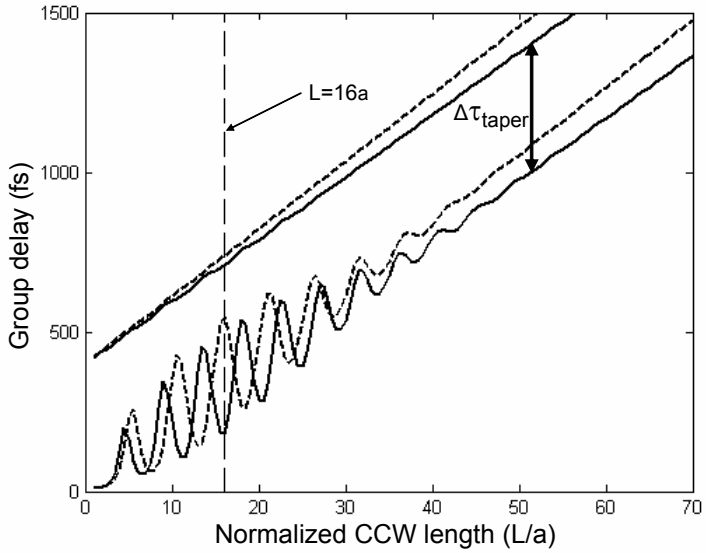

Figure 5.23.- Group delay of the output pulse as a function of the normalized CCW length for the butt coupled and adiabatically coupled CCW. The input pulse has a FWHM of 1000fs and a central frequency of 0.3089(a/λ) (solid line) and 0.3101(a/λ) (dashed line).

From the results shown in figure 5.22, it can also be seen that the FWHM of the output pulse increases with the CCW length due to the GVD. The effect of the GVD is higher, i.e. the slope of FWHM as a function of CCW length increases, as the input pulse is narrower due to the broader spectral width.

Figure 5.23 shows the group delay as a function of the normalized CCW length for the butt coupled and the adiabatically coupled CCW considering that the input pulse has a FWHM of 1000fs and the central frequency is 0.3101(a/λ) (dashed line) and 0.3089(a/λ) (solid line). The group delay of the adiabatically coupled CCW is increased by $\Delta\tau_{taper}$, which can be estimated with Eq. (5.5), due to the excess of delay introduced by the input and output tapers. In figure 5.23, we have taken an arbitrary $\Delta\tau_{taper}$ in order to better interpret the results. It can be seen that the group delay in both the butt coupled and adiabatically coupled CCW increases linearly with the CCW length. However, it oscillates at shorter lengths for the former due to the overlapping between the transmitted and reflected pulses. In this case, the group delay is maximum at 0.3101(a/λ) and minimum at 0.3089(a/λ) only when the CCW length of 16a. Obviously, this behavior does not occur for other CCW lengths because the frequency response, i.e. the number and position of resonances, is modified.

On the other hand, it should be noticed that although the group delay response of both the butt coupled and the adiabatically CCW is the same for long CCWs, apart from the $\Delta\tau_{taper}$ factor, the time response of the propagated pulse will not be the same, as discussed in the previous sections.

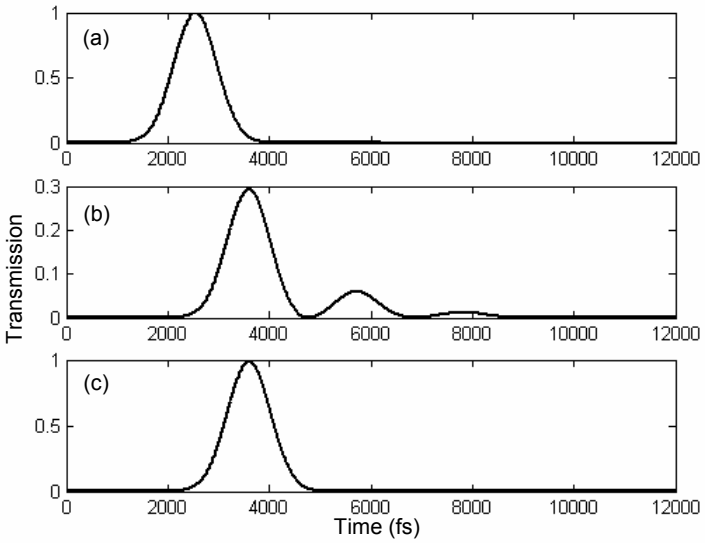

Figure 5.24.- (a) Input pulse of a FWHM of 1000fs and a central frequency of 0.3101(a/λ) propagated through the (b) butt coupled and (c) adiabatically coupled CCW of a length of 50a.

Figure 5.24 shows the propagated pulse as a function of time considering a CCW length of 50a for the butt coupled CCW (see figure 5.24(b)) and the adiabatically coupled CCW (see figure 5.24(c)). The input pulse (FWHM=1000fs) is shown in figure 5.24(a) and in this case $\Delta\tau_{taper}$=0. It can be seen that while the shape and group delay of the main transmitted pulse is the same in both cases, there are several additional pulses of lower amplitude in the butt coupled CCW corresponding to the successive reflected pulses. Furthermore, the output pulse is significantly attenuated for the butt coupled CCW while it is not attenuated for the adiabatically coupled CCW.

Figure 5.25 shows the peak amplitude of the output pulse as a function of the normalized CCW length for the butt coupled CCW. The input pulse has a FWHM of 250fs (solid line), 500fs (dashed line) and 1000fs (dotted line) and a central frequency of 0.3089(a/λ). It can be seen that the peak amplitude also oscillates with the normalized CCW length due to the overlapping between the transmitted and reflected pulses. As occurred in figure 5.22, the oscillations have higher amplitude and arise in a larger range of CCW lengths when the FWHM of the input pulse increases. Furthermore, the maximum or minimum peak amplitude for each particular CCW length depends on the coincidence or not of the central frequency of the input pulse with a maximum or minimum of the transmission spectrum. Therefore, the maximums and minimums appear at the same value of the CCW length independently of the FWHM of the input pulse.

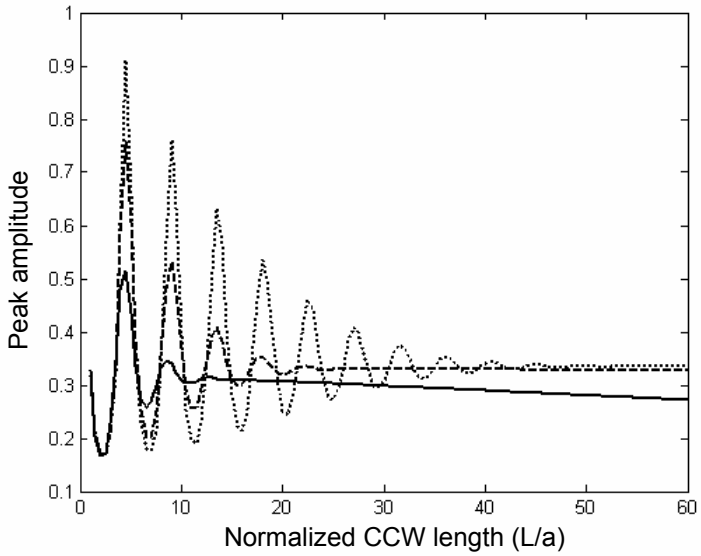

Figure 5.25.- Peak amplitude of the output pulse as a function of the normalized CCW length for the butt coupled CCW. The FWHM of the input pulse is 250fs (solid line), 500fs (dashed line) and 1000fs (dotted line) and the central frequency is 0.3089(a/λ).

When the CCW is long enough so that there is not overlapping between the transmitted and reflected pulses, the attenuation is higher for narrower input pulses because the bandwidth of the pulse becomes broader thus increasing the attenuation due to the parabolic shape of the transmission spectrum.

5.4 Conclusion

The interesting features of CCWs, such as a very small group velocity, make this kind of photonic crystal waveguide a key component for the development of compact photonic integrated devices such as optical delay lines or dispersion compensators. However, we have seen that an efficient coupling becomes mandatory in order to ensure their optimum dynamic performance. The proposed adiabatic coupling technique between SLWGs and CCWs based on progressively varying the radii of the spacing defects between cavities has been shown to be a promising approach. Flat transmission spectra with transmission efficiencies above 90% may be achieved with relatively short tapers, although longer tapers are necessary to achieve good transmission at the low frequencies of the band.

Furthermore, the causes of distortion of ultra short pulses that are propagated through inefficiently coupled CCW have been analyzed and discussed. It has been shown that pulse degradation is simply originated due to the overlapping between the transmitted pulse and the successive reflected pulses originated due to the high reflection at the CCW interfaces. This overlapping yields to undesired oscillations in the group delay, FWHM and peak amplitude frequency responses of the output

pulse, which can seriously limit the dynamic performance for a particular application. On the other hand, a theoretical model based on the Fabry-Perot formula has also been proposed and used to analyze a large variety of parameters. We want to point out that such a model could be extended for easily testing the performance of other devices based on CCW.

Part of the obtained results has been published in the following peer-reviewed journals:

- P. Sanchis, J. Garcia, A. Martínez, F. Cuesta, A. Griol, J. Martí, "Analysis of adiabatic coupling between photonic crystal single-line-defect and coupled-resonator optical waveguides", *Optics Letters*, vol. 28, pp. 1903-1905, 2003.

- P. Sanchis, J. García, A. Martinez, J. Martí, "Pulse Propagation in Adiabatically Coupled Photonic Crystal Coupled Cavity Waveguides", *Journal of Applied Physics*, vol. 97, pp. 013101, 2005.

Chapter 6

Fabrication and Measurements

6.1 Fabrication and characterization of photonic crystals

Photonic crystals have been mainly fabricated in the form of planar structures, known as planar photonic crystals or photonic crystal slabs, due to the easier fabrication at optical wavelengths and most suitable integration into photonic integrated circuits [Kra96]. However, their submicron size increases the difficulty of both the fabrication and characterization processes. For the characterization, very precise alignments tolerances are required, which demands the use of translation stages with submicron control. On the other hand, resolutions with accuracies of the order of nanometres are required for their fabrication.

Currently, most photonic integrated circuits are fabricated by optical lithography, where a mask with the pattern of the structure is projected onto a photosensitive film and then the pattern on the film is developed and transferred into the structure.

The resolution of the fabrication depends on the illumination wavelength used in the lithography process. Higher resolutions are achieved with shorter wavelengths. However, the resolution achieved by using current optical or near-UV wavelengths does not meet the accuracies required for photonic crystal circuits. Therefore, shorter illumination wavelengths are needed.

Deep UV lithography uses illumination wavelengths shorter than 250 nm, which provide the required resolution accuracies but at expenses of much higher costs that limit its use for research purposes. Nowadays, deep UV lithography is widely used for the mass manufacturing of complementary metal-oxide-semiconductor (CMOS) circuits at the microelectronic industry. However, the adaptation of CMOS techniques to the fabrication of photonic crystal circuits is far from being straightforward [Bog04].

The schematic of the process flow followed from the initial design of the photonic crystal structures until their characterization is depicted in figure 6.1. The design of the structures is carried out by means of theoretical studies and simulations. Several modelling tools, as those described in chapter 2, may be used for the design. Once the design stage is finished, the mask layout is defined before fabrication. The mask contains the pattern of the different designed structures that are transferred into a photoresist during the lithography process. The length of photonic crystal structures is usually very short. However, narrow dielectrics waveguides are coupled to the photonic crystal thus increasing the sample length. These waveguides are tapered up to broad waveguides more suitable for efficient coupling into and out of the samples. The whole structure is defined in the mask layout.

The fabrication process basically consists of a lithography process followed by an etching process. The lithography transfers the mask layout onto the photoresist, which was previously coated on top of the wafer. The photoresist is then developed and transferred into the structure by the etching process. Finally, the photoresist is removed from the structure. After fabrication, a post processing is carried out to obtain the sample of interest from the whole wafer. The samples are then ready to be measured.

One alternative to deep UV lithography is electron beam (e-beam) lithography. In this case, the pattern of the structure is written in a sequential way onto the photoresist by using a focused narrow electron beam in a vacuum system [Mar99]. Higher resolution and lower costs than deep UV lithography are achieved. However, the slower speed of the process makes this technique not suitable for mass manufacturing. Therefore, e-beam lithography has been mainly focussed to research purposes.

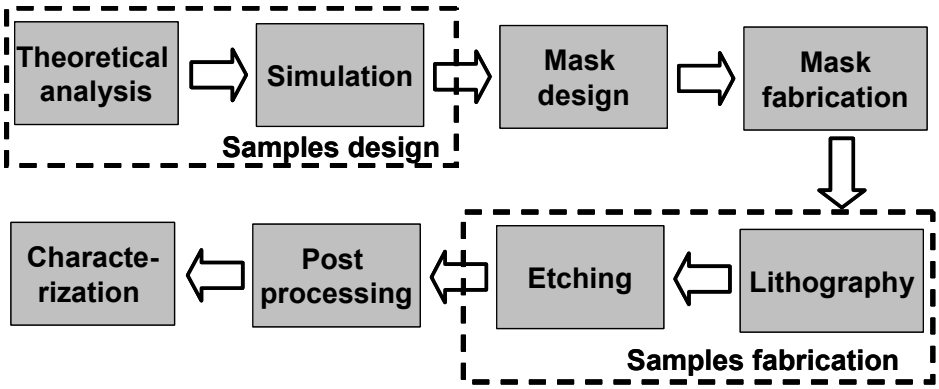

Figure 6.1.- Schematic of the photonic crystal fabrication process flow. The structures are first designed by means of theoretical studies and simulations. The mask layout, needed for the lithography process, is then designed and fabricated. The samples are basically fabricated following lithography and etching processes. A post processing is carried out to obtain the sample of interest from the wafer. Finally, samples are characterized.

6.2 Rod or hole structure?

Planar photonic crystals based on a hole structure, hereafter named hole structures, are usually formed by a lattice of air holes etched into a high refractive index material. On the other hand, planar photonic crystals based on a rod structure, hereafter named rod structures, are formed by a lattice of high index rods surrounded by a material with lower refractive index. In both kinds of structures, illustrated in figure 6.2, light is confined in the vertical direction due to the total internal reflection effect.

The main difference between hole and rod structures is the field polarization. TE polarization is normally used in hole structures while TM polarization is used in rod structures. The different polarization has several implications. Firstly, the optimum thickness of the slab core depends strongly on the polarization. Therefore, it is much larger in the rod structure (~1μm) than in the hole structure (~250nm) [Joh99, Mar03a]. This means that larger aspect ratios are required in the rod structure making the fabrication process more difficult. However, the mode mismatch in the vertical dimension to external optical fibers is lower so coupling losses will be reduced.

On the other hand, it has been predicted that TM modes are more sensitive to sidewall roughness [Bog04]. This means that rod structures would suffer from higher propagation losses. However, the sidewall roughness depends on the optimization of the fabrication process. In fact, low propagation losses (below 5dB/mm) comparable to those obtained in hole structures have been recently reported in a rod structure similar to that used in this work [Tok04].

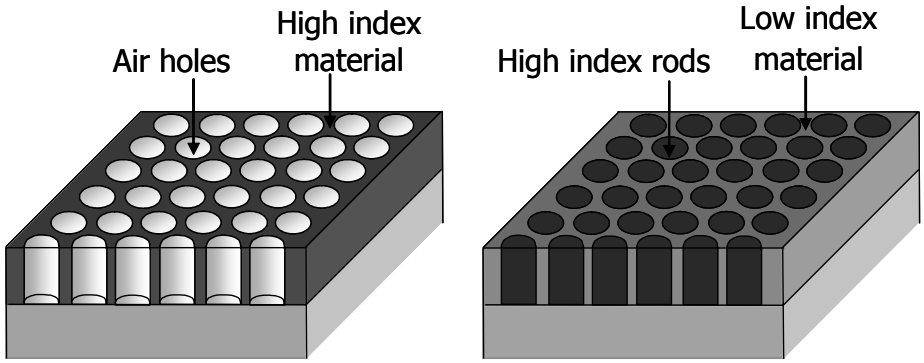

Figure 6.2.- Planar photonic crystal based on a hole structure (left part) and on a rod structure (right part). In the former, a lattice of air holes is usually etched into a high refractive index material. In the latter, the lattice is formed by high index rods surrounded of a material with lower refractive index.

Another important difference between hole and rod structures is the index contrast between the waveguide and the surrounding lattice in the horizontal dimension. In the so-called reduced-index waveguides, where the average refractive index of the waveguide is lower than the refractive index in the cladding, the total internal reflection effect is not present and therefore it is easily to achieve single mode transmission. Furthermore, better mode coupling, i.e. lower transmission losses, is expected at discontinuities because the number of undesired spurious modes that may be excited is also reduced [Chu00].

In hole structures, reduced-index waveguides are only achieved by increasing the amount of air in the waveguide, for instance by using holes of a larger size than the holes of the photonic crystal. However, the confinement in the vertical direction is then very weak pushing the guided modes above the light line. Furthermore, the influence of sidewall roughness is stronger increasing out-of-plane losses. On the other hand, waveguides in the rod structure are inherently of reduced index. The most obvious case are waveguides formed by completely removing a row of rods. However, in this case the guided modes are usually above the light line because low index contrast is given in the vertical dimension. Therefore, alternative waveguide designs, such as using rods of a smaller size, are required to achieve high vertical index contrast thus giving rise to guided modes below the light line. To summarize, it can be stated that single mode transmission with lossless Bloch modes may be easily achieved in rod structures.

At the moment, planar photonic crystals have been almost uniquely fabricated based on a hole structure due to the easier fabrication process. There has only been a few works that have recently reported the fabrication of a planar photonic crystal formed by a lattice of rods [Tok04, Ass04, Che05, Chu05]. Therefore, the lack of experimental results for the rod structure makes difficult to judge which structure is preferred and only time will answer to this question.

The fabrication of planar photonic crystals based on a rod structure is planned at the Nanophotonics Technology Centre, where this work has been carried out. Therefore, although both hole and rod structures were initially analyzed (chapter 3), the proposed coupling techniques for efficient coupling into photonic crystal line defect waveguides (chapter 4) and coupled-cavity waveguides (chapter 5) were analyzed and designed considering a rod structure. However, the proposed coupling techniques are also useful for hole structures, as it will be shown in this chapter. The fabrication processes of both rod and hole structures are still under development at the Nanophotonics Technology Centre. However, the fabrication of the hole structure was possible thank to a collaboration with the photonics research group at the INTEC department of the University of Ghent and within the framework of the IST-PICCO project[6]. Thus, experimental results have been obtained for the hole structure.

On the other hand, the complete analysis of previous chapters was carried out by using two-dimensional (2D) modelling tools. However, three-dimensional (3D) simulations are required for a rigorous design of planar photonic crystals. We did not have the facilities to perform 3D simulations until recently because of the high complexity and huge resources requirements of 3D modelling tools. Therefore, 3D simulations have only been obtained in this last chapter for comparing with experimental results as well as for analyzing the discrepancies with 2D simulation results. A cluster of four machines with parallel computing capabilities has been used to achieve 3D finite-difference time-domain (FDTD) simulations. A single simulation usually takes from 24 to 48 hours depending on the size of the computational domain.

6.3 Measurement set-up

To characterize the fabricated structures, light has to be coupled into and out of the fabricated sample. The end-fire technique shown in figure 6.3(a) has been used. Figure 6.3(b) shows a photo of the measurement set-up. Light is focussed from a polarization maintaining lensed fiber into the sample at a cleaved facet. Similarly, the transmitted light is coupled out of the sample at a cleaved facet and collected by using an objective with a high numerical aperture. Instead of coupling the light directly into and out of the photonic crystal structure, a 3μm-wide ridge waveguide is used at both ends of the sample to improve the coupling efficiency. A linear taper narrows the 3μm-wide ridge waveguide down to a 500nm-wide photonic wire, more suitable for coupling into and out of the photonic crystal structure. On the other hand, the total length of the samples is around 5mm, which simplifies the cleaving process.

[6] IST-PICCO Project web site: http://www.intec.ugent.be/picco

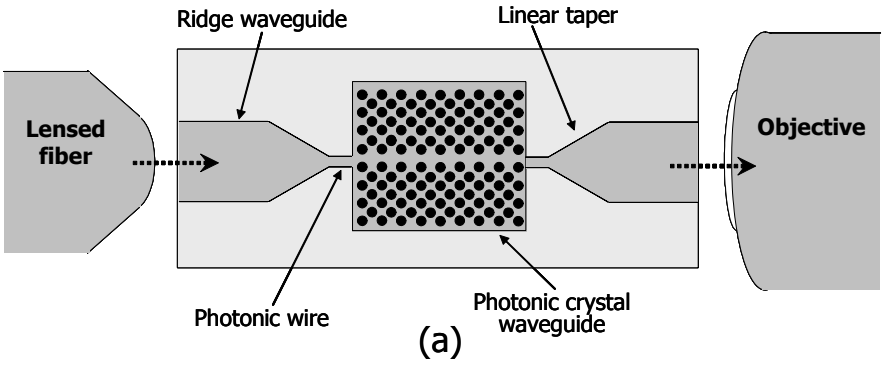

(a)

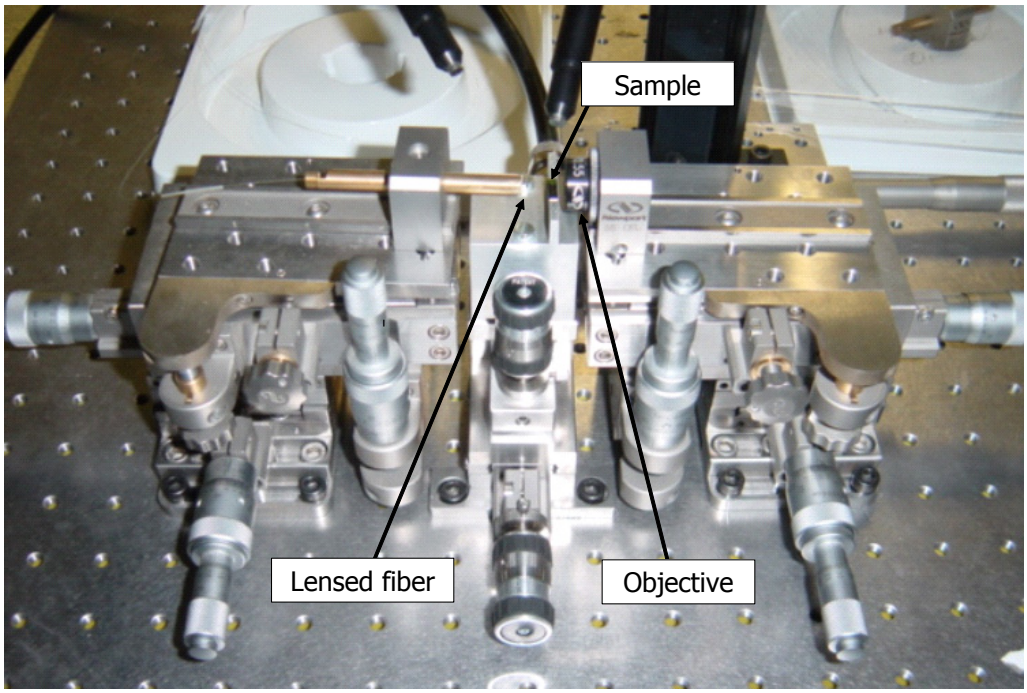

(b)

Figure 6.3.- (a) Detailed view of the sample and (b) photo of the measurement set-up. The sample is formed by a 3μm-wide ridge waveguide that is narrowed down by using a linear taper to a 500nm-wide photonic wire, more suitable for coupling into and out of the photonic crystal. Light is coupled into the sample by using a lensed fiber and it is collected at the end of the sample by using an objective.

Figure 6.4 shows the schematic of the measurement set-up. Light from a tunable laser is used as input source. In our measurements, we use the TSL-210F laser from SANTEC. The laser has four internal cavity lasers thus covering a very broad wavelength range from 1260 to 1630nm. Firstly, the sample has to be aligned with the lensed fiber and the objective. An infrared (IR) camera is needed to control the alignment, as depicted in figure 6.4(a). The observation of the interference pattern indicates if the light is being transmitted through the substrate or the air instead of being transmitted through the core.

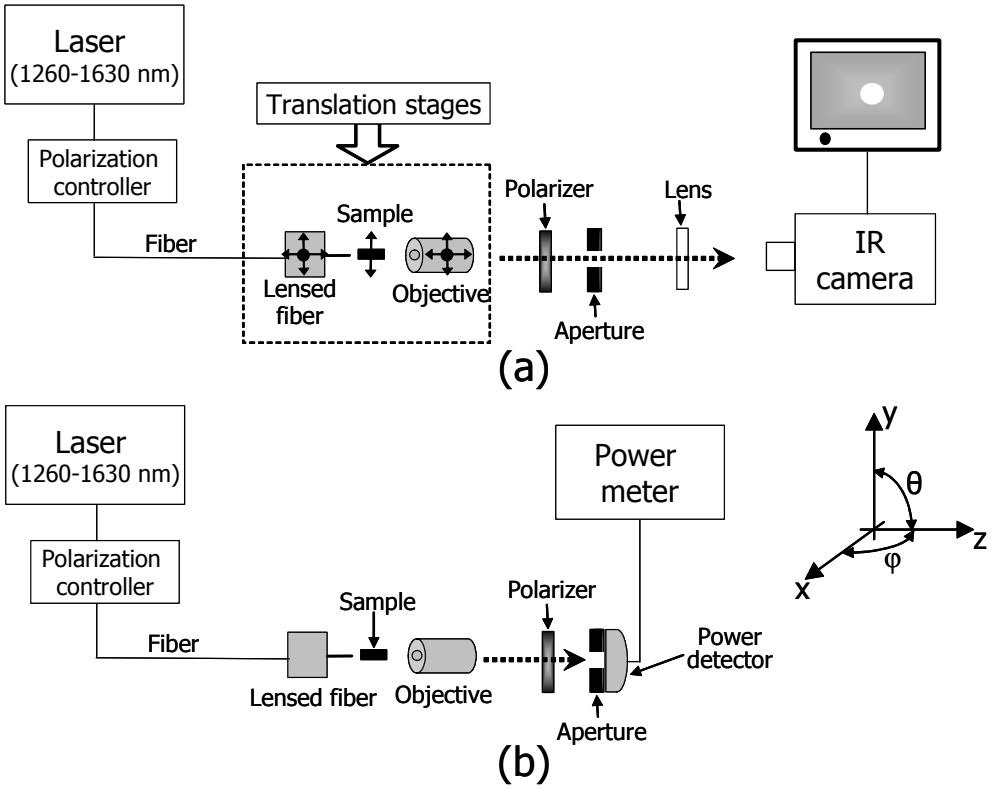

Figure 6.4.- Schematic of the measurement set-up. (a) Firstly, the sample has to be aligned with the lensed fiber and the objective. Translation stages with submicron resolution and an infrared (IR) camera are used to achieve proper alignment. (b) The transmitted power is then measured as a function of the wavelength by using a power detector.

When a spot appears in the screen, as shown in figure 6.4(a), the sample is correctly aligned. The alignment is achieved by using translation stages with submicron resolution. For the lensed fiber and objective, the translation stages can be moved along the three spatial axes (*x,y,z*) as well as in angular positions of the *yz*-plane (θ) and the *xz*-plane (φ), taking into account that light propagates in the *z*-direction. On the other hand, the sample is fixed to another translation stage with a vacuum holder and, in this case, it can be moved only along the *xy*-plane perpendicular to the direction of light propagation.

Once the sample is properly aligned, an aperture is used to get rid of the remaining scattered light. After the aperture, the transmitted light is detected using a power detector and finally measured by using a power meter. A polarizer is placed between the objective and the aperture in order to select the polarization state. Therefore, the polarization maintaining lensed fiber has to be conveniently rotated to align its polarization to the desired polarization. Furthermore, a polarization controller is needed to ensure that light has the proper polarization state at the input of the lensed fiber. Finally, the transmitted power is measured as a function of the wavelength by remote control via GPIB using a personal computer.

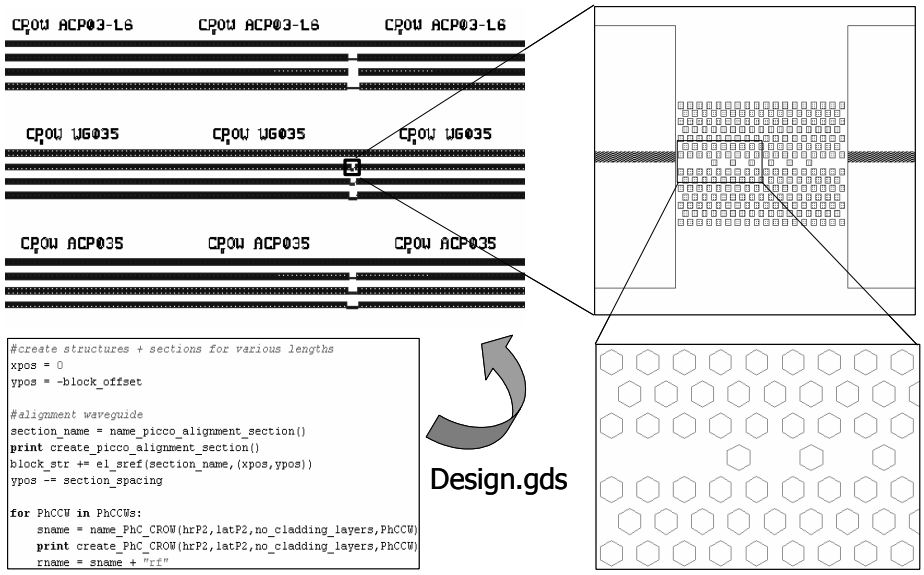

Figure 6.5.- Illustration of the procedure followed to design the mask layout of the fabricated planar photonic crystal on Silicon-on-insulator technology.

6.4 Hole structure: Silicon-on-insulator

6.4.1 Fabrication process

Silicon-on-insulator (SOI) consists of a thin silicon layer on top of an oxide cladding layer deposited on a bare silicon substrate. In this work, 200mm (8 inches) SOI wafers were used with a top silicon layer of a thickness of 220nm and an underlying silica layer of a thickness of 1μm. The photonic crystal is formed by a lattice of air holes etched on the silicon layer. As depicted in figure 6.1, the mask layout has to be designed before fabrication. The mask design was created with a script-based tool as illustrated in figure 6.5.

The photonic crystal structure is coupled to narrow dielectric waveguides which are tapered up to broad waveguides more suitable for efficient coupling into and out of the sample. The air holes were defined by hexagons with restrictions imposed by the fabrication process on the minimum diameter as well as on the spacing between holes. A large number of photonic crystal structures are usually defined on a single die. Therefore, similar structures are grouped together and labelled with text to help to identify them during measurements.

Deep UV lithography at the standard wavelength of 248nm is used for the fabrication process. This technique offers both the resolution and speed required for the mass manufacturing of photonic crystals. The fabrication process flow is illustrated in figure 6.6 [Bog02, Bog03, Bog04].

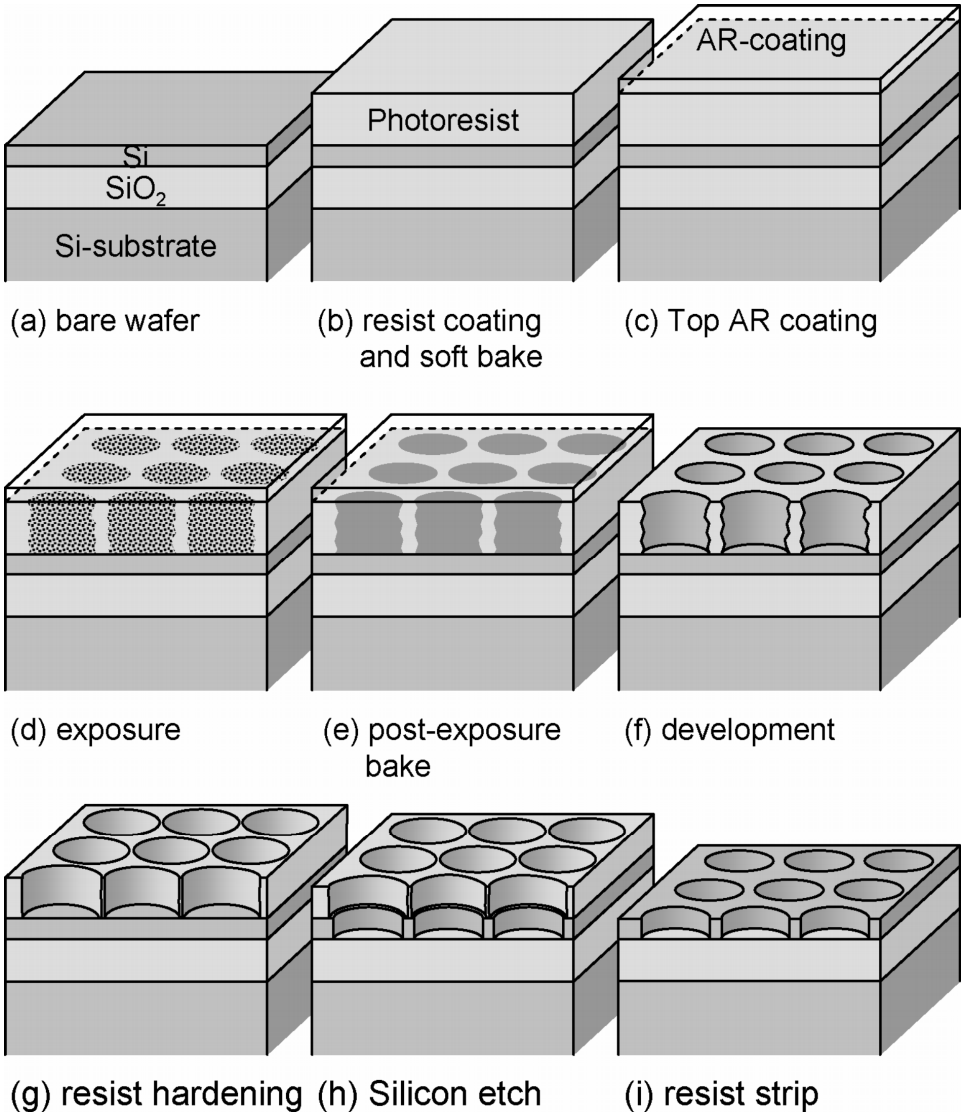

Figure 6.6.- Description of the fabrication process of the planar photonic crystal based on a hole structure on Silicon-on-insulator (SOI). SOI consists of a thin silicon layer on top of an oxide cladding layer deposited on a bare silicon substrate. *Courtesy of Wim Bogaerts* [Bog04].

First, the photoresist is coated on top of the SOI wafer, and then pre-baked. On top of the resist, an antireflective coating is spun to eliminate reflections at the interface between the air and the photoresist. These reflections increase standing waves in the photoresist and therefore inhomogeneous illumination. The following step is to process the wafer by a stepper, which illuminates the photoresist with the pattern on the mask. After lithography, the resist goes through a post-exposure bake, and is then developed. The developed photoresist is used directly as a mask for etching. Only the top silicon layer is etched in order to reduce propagation losses due to sidewall roughness [Bog04]. Resist hardening is used prior to etching to compensate the litho-etch bias.

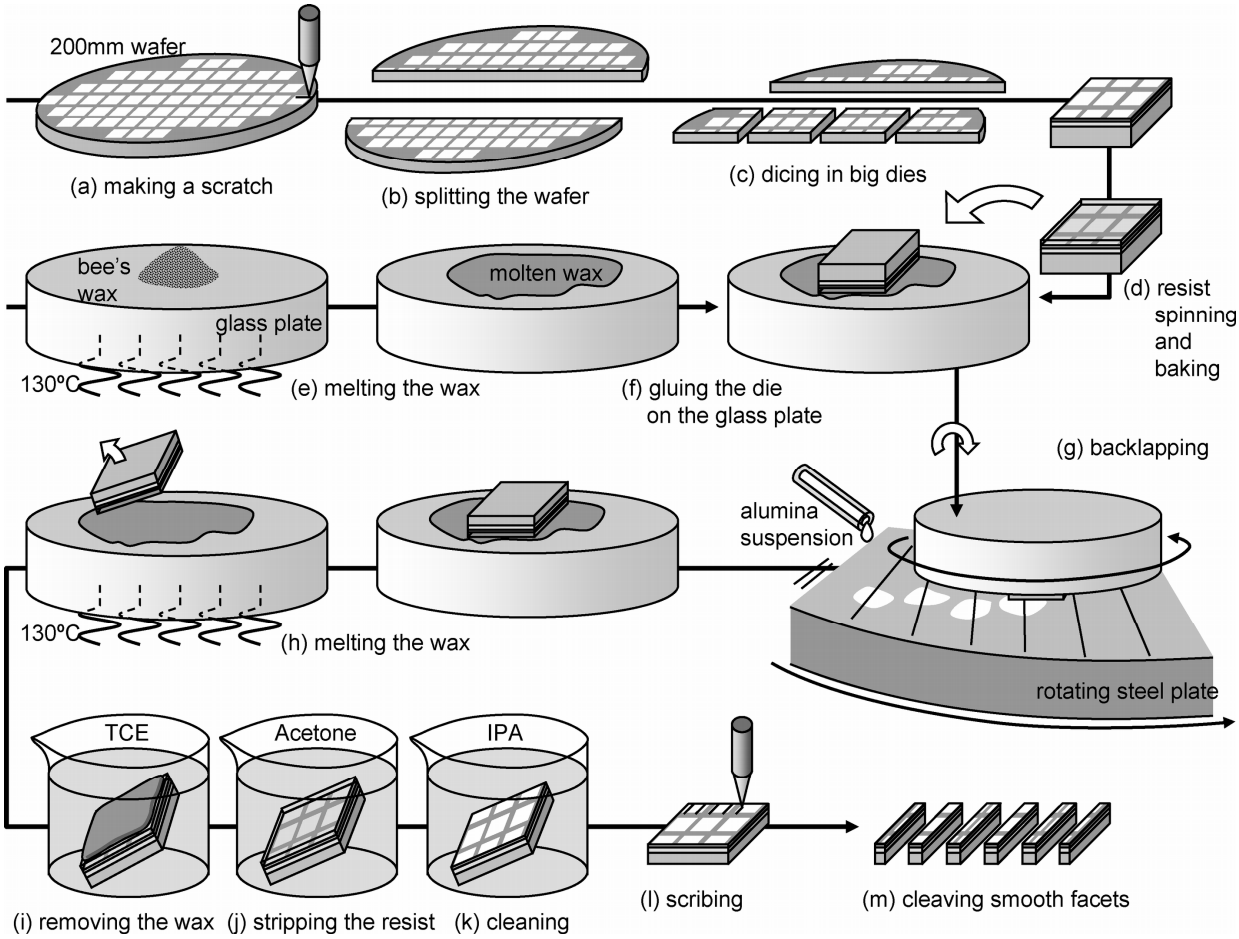

Figure 6.7.- Post processing to obtain the samples from the wafer. The amorphous nature of the silica as well as the large thickness (725µm) of the silicon substrate makes very difficult to achieve smooth facets by directly cleaving onto the wafer. Therefore, the thick substrate has to be thinned before making the cleaving. *Courtesy of Wim Bogaerts* [Bog04].

As a 200mm wafer can contain many structures, the die with the pattern is repeated across the wafer. Furthermore, not all structures have the same dose-to-target. Therefore, they are fabricated with a variety of exposure doses. As the dose can be changed from die to die on a wafer, a linear scan of the dose is done in the horizontal direction so that repetitions of the same structures with different hole radius are achieved. In the vertical direction, all dies in a column are identical. Therefore, a large variety of structures is achieved on a single wafer, while still keeping multiple dies with the same structure parameters.

6.4.2 Post processing

Once the photonic crystal structures have been fabricated, a post processing is needed to obtain the samples to be measured from the wafer. As previously described, an end-fire measurement set-up has been used so that the light is coupled into and out of the ridge waveguides at cleaved facets. Smooth facets at

both extremes of the sample are needed to reduce coupling losses. However, the amorphous nature of the silica as well as the large thickness (725µm) of the silicon substrate makes very difficult to achieve smooth facets by directly cleaving onto the wafer. Therefore, the thick substrate has to be thinned before making the cleaving.

The procedure is illustrated in figure 6.7. Firstly, the wafer is divided into big dies of approximately $4 \times 4 cm^2$. To thin the substrate, each die has to be glued upside down on a glass plate. Therefore, a resist is previously coated and baked on top of the dies to protect them. Bee wax is used to glue the die on the glass plate. The glass plate is then fixed with a vacuum holder and turned on top of the thinning machine. Several hours are usually needed to thin the substrate from 725µm down to 250µm. The time depends on the area of the die, the kind of alumina powder used for the thinning and the rotating speed of the steel plate. Once the thinning is finished, the dies are taken off from the glass plate by heating the wax. TCE (C_2HCl_3) is used to get rid of the remaining wax. Then, the resist is removed by using acetone and the die is cleaned by using isopropanol (IPA) and distilled water. Finally, the die is cleaved to obtain the different samples that contain each die.

6.4.3 Coupling into photonic crystal waveguides

The coupling technique proposed in chapter four has also been used to achieve efficient coupling into photonic crystals circuits formed by an air holes lattice etched into a high-index dielectric background. The structure considered is shown in figure 6.8. An input dielectric waveguide is coupled to a line defect photonic crystal waveguide by using a photonic crystal taper. The bulk photonic crystal is a two-dimensional triangular array of air holes in a dielectric background of silicon. We use the effective index approximation (n_{eff}=2.8) for the vertical direction [Qiu02a] and a hole radius of R=0.3a. A lattice constant of a=435nm has been used for transmission at the wavelength band around 1.55µm. The effective index was calculated for a thickness of the silicon layer of 220nm in agreement with that of the fabricated structure. This approach allows us to initially design the fabricated structures by means of two-dimensional (2D) finite-difference time-domain (FDTD) simulations.

A line defect photonic crystal waveguide of a reduced width of 0.6W, W being the width of the single-line missing-hole defect waveguide, has been chosen in order to obtain singlemode transmission [Not01]. The width of the dielectric waveguide is 3µm with a surrounding medium of air. In order to design the optimum parameters of the defect, the transmission efficiency as a function of the position along the waveguide axis of a defect placed with radius r=R within the photonic crystal taper has been first calculated. Figure 6.9(a) shows the obtained results.

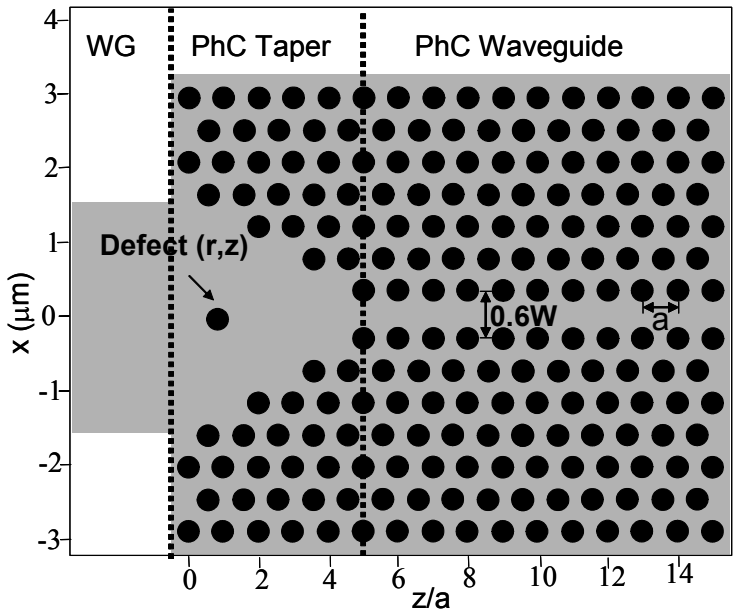

Figure 6.8.- Schematic of a the analyzed structure. An input dielectric waveguide is coupled to a line defect photonic crystal (PhC) waveguide by using a photonic crystal taper. The coupling efficiency is significantly improved by placing a single defect within the taper.

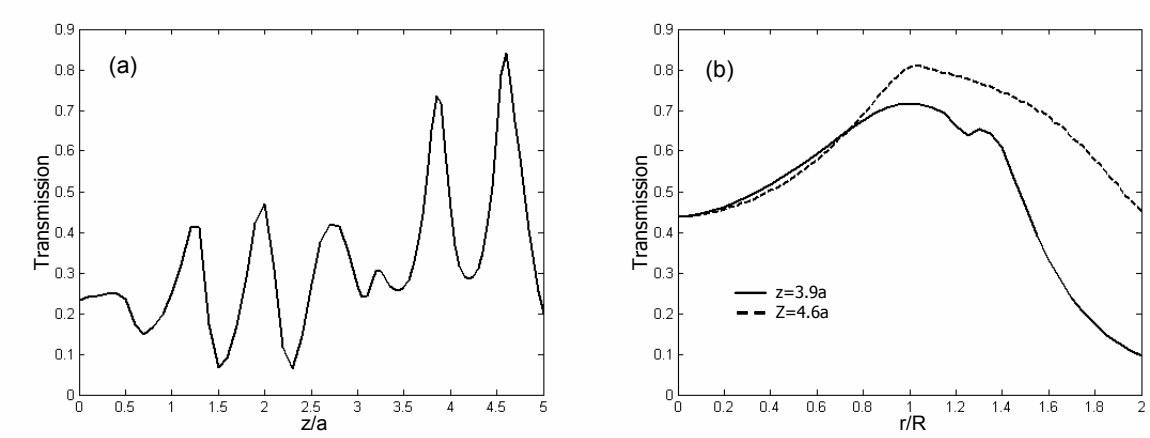

Figure 6.9.- (a) Transmission efficiency as a function of the position in the *z*-axis normalized to the lattice constant for a defect of radius *R* placed within the taper. (b) Transmission efficiency as a function of the radius of the defect normalized to the hole radius of the photonic crystal and located at z=0.39a.

It can be seen that several peaks of high transmission efficiency appear in the transmission response at different positions. The peak of maximum transmission (84%) is achieved at z=4.6a. However, this position is too close to the photonic crystal waveguide not meeting the fabrication constraint of minimum separation between holes. Therefore, the nearest peak, located at z=3.9a and of a lower transmission efficiency of 72%, has been chosen.

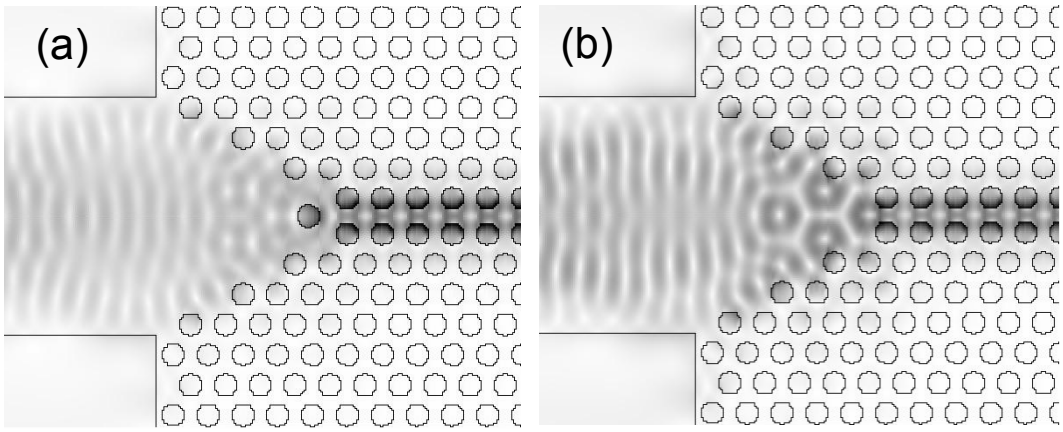

Figure 6.10.- Modulus of the electric field at 1.55 μm for the photonic crystal taper (a) with and (b) without the optimized defect located at z=3.9a.

The next step is to optimize the defect radius at the previously calculated optimum position. Figure 6.9(b) shows the transmission efficiency as a function of the radius of the defect normalized to the hole radius of the photonic crystal and located at z=3.9a and also at z=4.6a It can be seen that the optimum defect radius coincides in both cases to the one used in the defect position scan, i.e. r=R. The introduction of the defect significantly improves the transmission efficiency up to 72% regarding the photonic crystal taper without defect, in which the transmission efficiency is only 44%, and the butt-coupled case, in which the transmission efficiency is 36%.

In principle, the optimum width of the dielectric waveguide to achieve the maximum transmission by means of butt-coupling is 1.5μm, however even in this case the transmission efficiency is still of 60%. An efficient coupling from a wider dielectric waveguide implies a reduction of the conversion ratio in the horizontal direction needed to couple from a fiber, which typically has a thickness between 8 and 10 μm, allowing the design of compact spot size converters. Although, alternative approaches will be required to resolve the mode mismatch between the fiber and the photonic crystal circuit in the vertical direction.

As discussed in chapter four, the introduction of the defect within the photonic crystal taper modifies the modal properties of the modes so that mode matching is achieved. This can be seen in figure 6.10 that shows the modulus of the electric field for the photonic crystal taper without defect and with the optimized defect located at z=3.9a. The diagrams were obtained with CAMFR. In figure 6.10(b), it can be seen that resonant modes are excited within the photonic crystal taper, which increase coupling losses. Resonant modes are eliminated by the introduction of the defect (see figure 6.10(a)) thus improving the coupling efficiency.

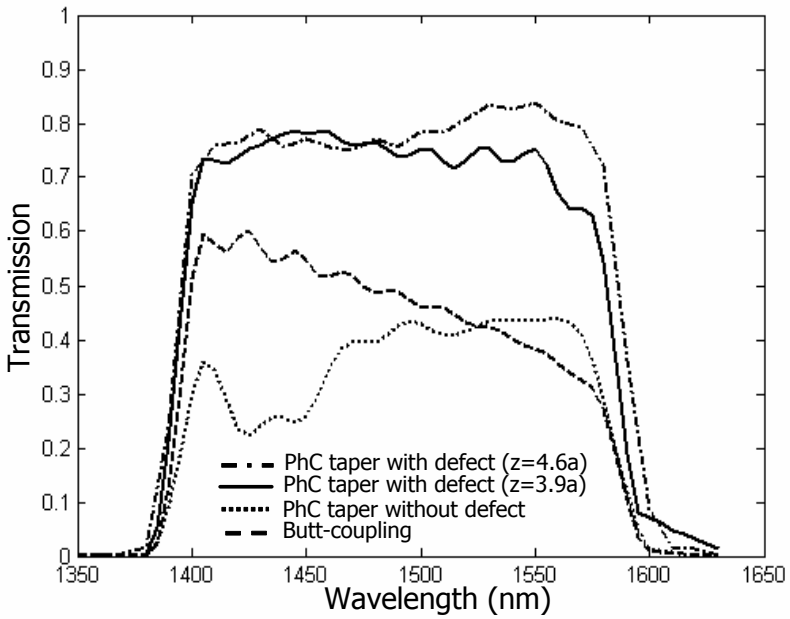

Figure 6.11.- Transmission efficiency as a function of the wavelength for a photonic crystal (PhC) waveguide of finite length considering the butt-coupled and photonic crystal taper structures without and with defect.

The optimum parameters of the defect have been designed to achieve the highest transmission at 1.55μm. Figure 6.11 shows the transmission efficiency as a function of the wavelength for the butt-coupled and the photonic crystal taper structures without and with the optimized defect. Both cases of the defect located at z=3.9a and z=4.6a have been considered for the sake of comparison. It can be seen that the transmission spectrum for the photonic crystal taper with defect, either located at z=3.9a or z=4.6a, significantly improves the transmission achieved for the taper without defect and butt-coupled structure. For the photonic crystal taper with defect, the transmission is only improved by 10% at wavelengths around 1.55μm when the defect with radius R is placed at the more optimum position of z=4.6a instead of at the position of z=3.9a.

The butt-coupled and photonic crystal taper without and with the optimized defect structures have been fabricated. Figure 6.12 shows SEM images of the photonic crystal taper with defect and butt-coupled structures. A 3μm-wide ridge dielectric waveguide is used to couple light into and out of the line defect photonic crystal waveguide. The photonic crystal waveguide has a length of 23a for the butt-coupled structure and of 13a for the photonic crystal taper structures. Thus, the total length of the photonic crystal is the same in the three analyzed structures. The radius is approximately the same (R=0.3a) to that used in the previous 2D analysis, i.e. 130nm for the considered lattice value.

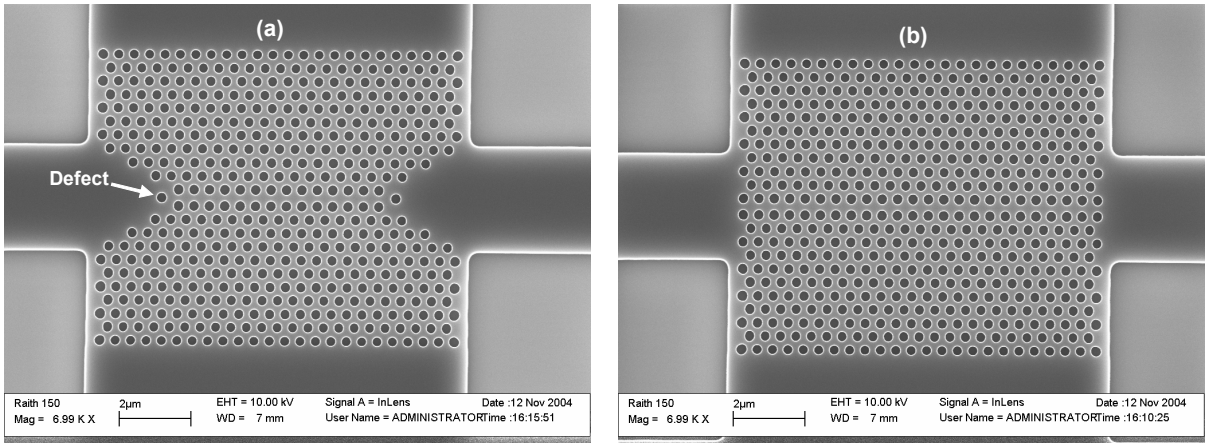

Figure 6.12.- Scanning electronic microscope (SEM) images of the (a) photonic crystal taper with defect structure and the (b) butt-coupled structure. The total length of the photonic crystal is the same in both cases.

Experimental results are shown in figure 6.13. The transmission as a function of wavelength was measured using the measurement set-up described in section 6.3. The output power of the laser was 1mW (0dBm) and the polarizer was adjusted for only measuring TE polarized light. Figure 6.13(a) shows the transmitted power as a function of the wavelength for the unpatterned sample which consists only of the ridge waveguide without the photonic crystal. Figures 6.13(b)-6.13(d) show respectively the transmitted power as a function of the wavelength for the butt-coupled and the photonic crystal taper without and with defect structures. Although there are noticeable Fabry-Perot resonances in the transmission spectra due to the inefficient coupling into and out of the ridge waveguide, experimental results demonstrate a power transmission improvement when the photonic crystal taper with defect is used compared to the butt-coupled and photonic crystal taper without defect cases. Furthermore, it can be seen that a reduction of the Fabry-Perot resonances comparable to those obtained for the unpatterned sample is achieved for the photonic crystal taper with defect structure.

Experimental results have been compared to three (3D) and two dimensional (2D) FDTD simulation results. Figure 6.14 shows the results for the photonic crystal taper with and without defect structures while figure 6.15 shows the results for the photonic crystal with taper and butt-coupled structures. Experimental results have been normalized by the averaged transmission spectrum of the unpatterned structure. It can be seen that a good agreement is achieved between experimental and 3D simulation results. Transmission efficiencies above 30% over a rather large wavelength range are achieved for the photonic crystal taper with defect structure. However, the transmission efficiency is lower than 25% and 15% for the taper without defect and butt-coupled structures respectively. Furthermore, the higher transmission efficiencies for the taper without defect structure are only achieved at very small wavelength ranges.

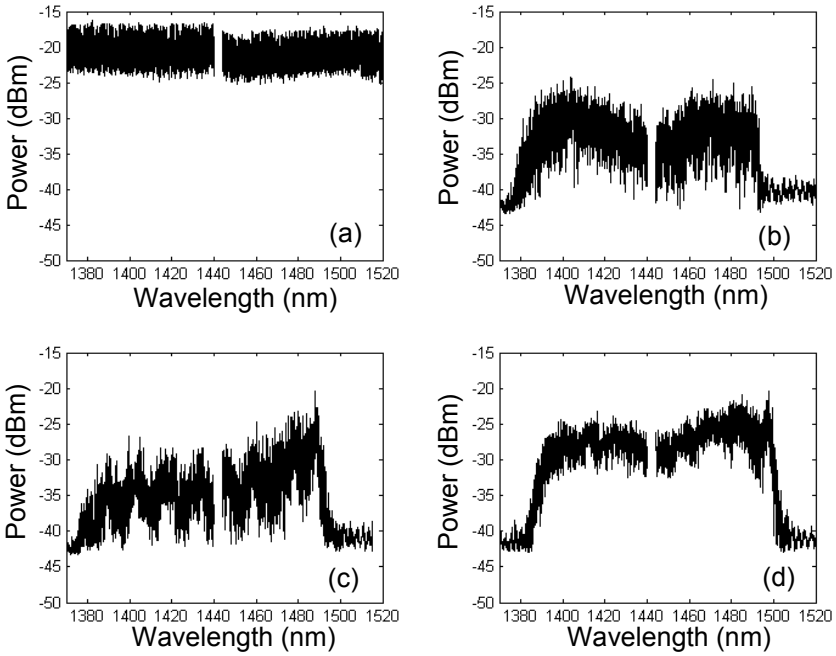

Figure 6.13.- Experimental transmission spectrum for (a) the unpatterned structure, (b) the butt-coupled structure and the photonic crystal taper structure (c) without and (d) with the optimized defect. The photonic crystal is formed by a triangular lattice of air holes. The hole radius is R=130nm while the lattice constant is a=435nm.

On the other hand, although similar transmission behaviour of the three analyzed structures is achieved for 2D and 3D simulation results, there are also important discrepancies between them such as a smaller bandwidth shifted to lower wavelengths as well as a lower transmission for the 3D results. These discrepancies indicate that the effective index method used for the calculation of 2D results is valid but gives only approximated 3D results. It is important to notice that out-of-plane losses are not modelled by the effective index method. Therefore, the decrease of the transmission efficiency in about 25% for 3D results compared to 2D results is mainly attributed due to out-of-plane losses in the photonic crystal waveguide.

The photonic crystal waveguide supports a guided mode below the light line. However, the wavelength range in which the mode is below the light line is very narrow so that almost all the bandwidth of the mode is above the light line. The grey area shown in figure 6.14(b) and 6.15(b) and located close to the upper band edge corresponds to the wavelength range in which the mode is below the light line. This wavelength range was obtained by calculating the 3D band diagram of the photonic crystal waveguide by means of the plane wave method [Joh01].

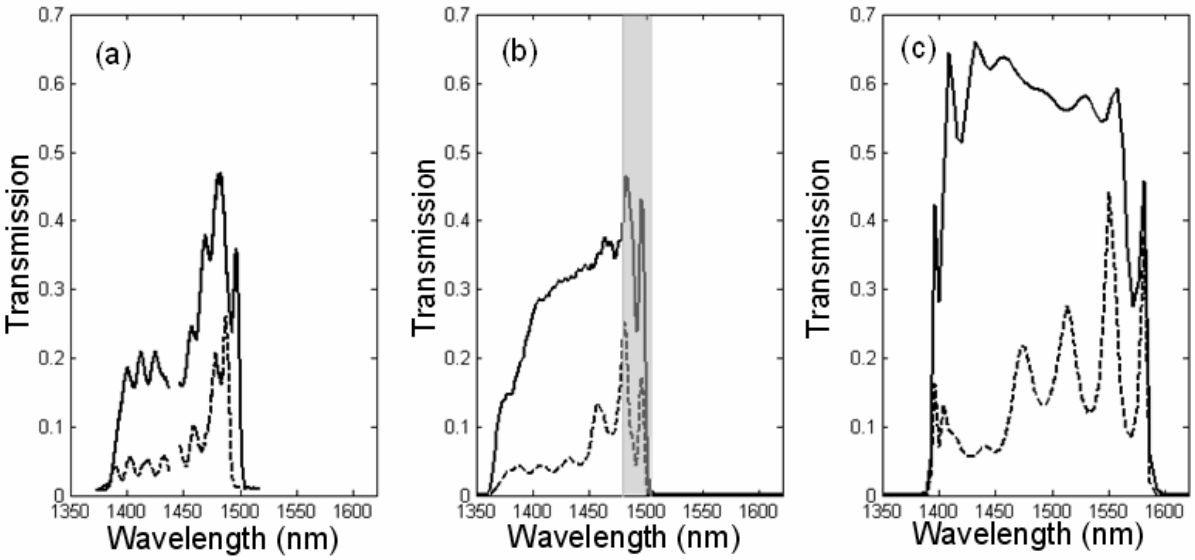

Figure 6.14.- (a) Experimental, (b) 3D FDTD simulated and (c) 2D FDTD simulated transmission spectra for the photonic crystal taper with defect structure (solid line) and the photonic crystal taper without defect structure (dashed line). The grey area shown in (b) corresponds to the wavelength range in which the guided mode is below the light line. The hole radius is R=130nm.

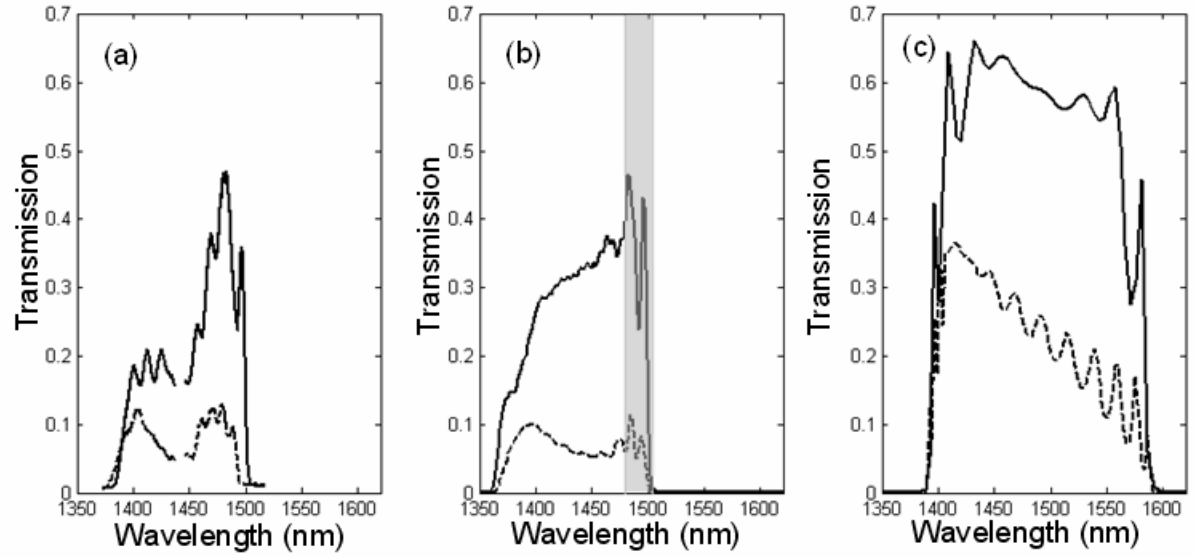

Figure 6.15.- (a) Experimental, (b) 3D FDTD simulated and (c) 2D FDTD simulated transmission spectra for the photonic crystal taper with defect structure (solid line) and the butt-coupled structure (dashed line). The grey area shown in (b) corresponds to the wavelength range in which the guided mode is below the light line. The hole radius is R=130nm.

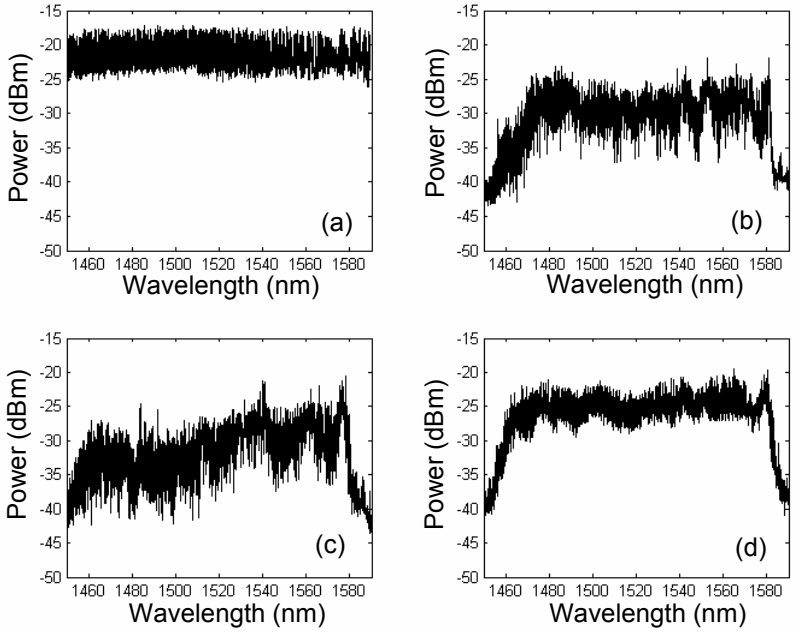

Figure 6.16.- Experimental transmission spectrum for (a) the unpatterned structure, (b) the butt-coupled structure and the photonic crystal taper structure (c) without and (d) with the optimized defect. The photonic crystal is formed by a triangular lattice of air holes. The hole radius is R=115nm while the lattice constant is a=435nm.

In this region, the transmission efficiency discrepancies between 2D and 3D simulation results are directly those determined by the coupling efficiency between the ridge dielectric waveguide and the photonic crystal waveguide since there are no out-of-plane losses in the waveguide. It can be seen that the best agreement between 2D and 3D results is achieved for the photonic crystal taper with defect.

However, the waveguide mainly operates above the light line, as it can be observed in figure 6.14(b) and 6.15(b). In this region, radiation modes can be excited in the vertical direction giving rise to out-of-plane losses. Therefore, discrepancies between 2D and 3D simulation results are mainly attributed due to out-of-plane losses and not due to higher coupling losses between the ridge dielectric waveguide and the photonic crystal waveguide. It is interesting to notice that 2D and 3D simulation results disagree more for wavelengths far away from the upper band edge, where the guided mode is below the light line. On the other hand, the discrepancies between experimental and 3D simulation results are due to the existence of sidewall roughness in the former which gives rise to higher out-of-plane losses thus increasing transmission losses.

Experimental results have also been obtained for the same photonic crystal structures but with a smaller hole radius (R=115nm), i.e. with a smaller filling ratio. The decrease of the hole radius increases the amount of dielectric in the

waveguides shifting the guided mode to higher wavelengths. Figure 6.16(a) shows the transmitted power as a function of the wavelength for the unpatterned structure. Figures 6.16(b)-6.16(d) show respectively the transmitted power as a function of the wavelength for the butt-coupled structure and photonic crystal taper without and with defect structures. It can be seen that the transmission spectra are similar to those previously obtained, shown in figure 6.13, in which the photonic crystal structures had a larger filling ratio.

Again, normalized experimental results have been obtained and compared to 3D FDTD simulation results. Figures 6.17(a)-6.17(b) show the results for the photonic crystal taper with and without defect structures while figures 6.18(a)-6.18(b) show the results for the photonic crystal with taper and the butt-coupled structures. It can be seen that there is also a very good agreement between experimental and 3D simulation results as well as that the transmission is significantly improved for the taper with defect structure with respect to the butt-coupled and taper without defect structures. The transmission efficiencies are higher than the ones obtained for the previous structures with larger filling ratio. Transmission efficiencies, t, up to 60% are achieved for the photonic crystal taper with defect structure. Thereby, the coupling efficiency between the ridge dielectric waveguide and the photonic crystal waveguide is obtained from $T = \sqrt{t}$ that yields to a transmission efficiency of 75%.

3D simulation results have also been compared to 2D results, which are shown in figures 6.17I and 6.18I. The same effective index (n_{eff}=2.8) has been used for the calculation of 2D simulation results[7]. Just as occurred in the previous photonic crystal structures with larger filling ratio, the transmission behaviour is similar for the three analyzed structures, although the bandwidth is also smaller and shifted to lower wavelengths for the 3D results with respect to the 2D results. The discrepancy between 2D and 3D results is higher for the photonic crystal taper with defect structure. The 2D simulated transmission spectrum is degraded at wavelengths around 1650nm. The lower transmission is attributed to the fact that the defect has been optimized at the wavelength of 1550nm. Therefore, in principle, the maximum transmission efficiency is only achieved at wavelengths around 1550nm, as it is corroborated in figures 6.17I and 6.18I. However, it is interesting to notice that the power drop is less accentuated in the 3D simulated transmission spectrum. This behaviour may be explained from the fact that the 3D spectrum is, in this case, more centred at wavelengths around 1550nm.

[7] Although the transmission band is shifted to higher wavelengths due to the smaller filling ratio, the effective index does not significantly change when higher wavelengths are considered. For instance, the effective index at the wavelength of 1600nm is 2.78.

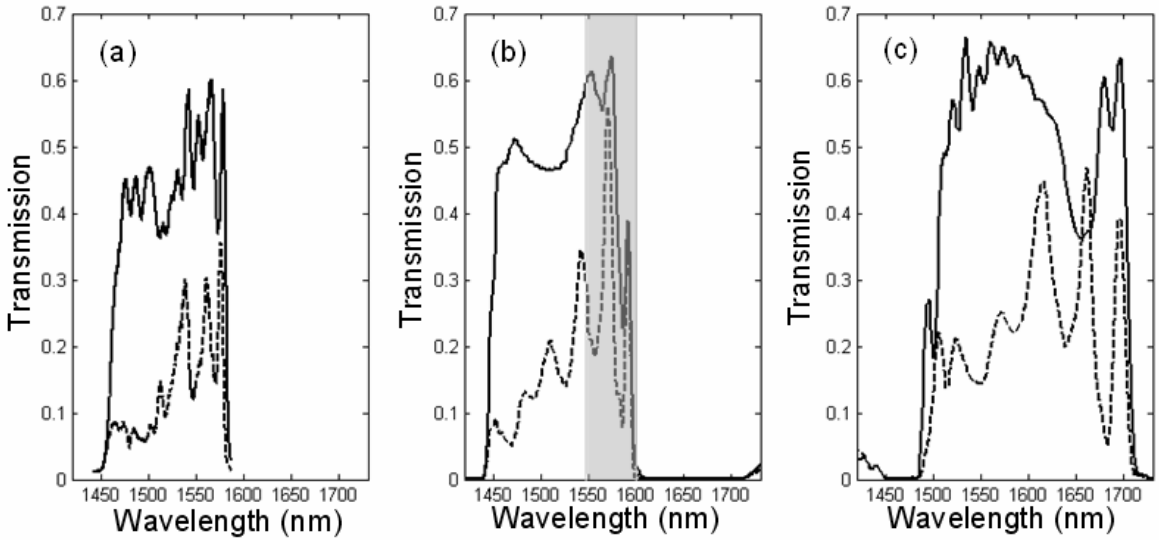

Figure 6.17.- (a) Experimental, (b) 3D FDTD simulated and (c) 2D FDTD simulated transmission spectra for the photonic crystal taper with defect structure (solid line) and the photonic crystal taper without defect structure (dashed line). The grey area shown in (b) corresponds to the wavelength range in which the guided mode is below the light line. The hole radius is R=115nm.

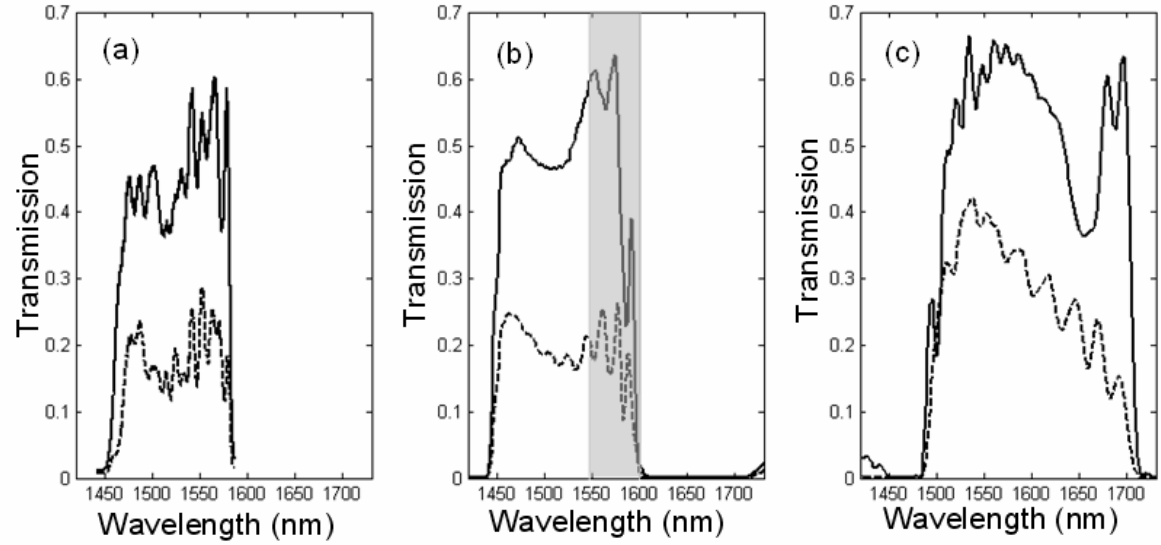

Figure 6.18.- (a) Experimental, (b) 3D FDTD simulated and (c) 2D FDTD simulated transmission spectra for the photonic crystal taper with defect structure (solid line) and the butt-coupled structure (dashed line). The grey area shown in (b) corresponds to the wavelength range in which the guided mode is below the light line. The hole radius is R=115nm.

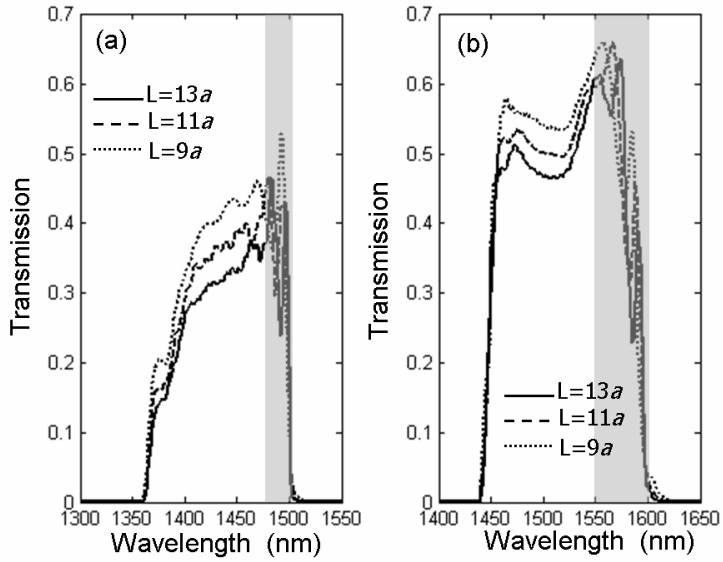

Figure 6.19.- 3D FDTD simulated transmission efficiency as a function of the wavelength for the photonic crystal taper with defect structure for (a) R=130nm (R=0.3a) and (b) R=115nm (R=0.264a) by considering three different lengths, L, of the photonic crystal waveguide.

On the other hand, the 2D and 3D transmission efficiencies for the three analyzed structures agree much better than for the previous structures with larger filling ratio. This better agreement is even given at the wavelength range in which the guided mode operates above the light line. The grey area shown in figure 6.17(b) and 6.18(b) depicts the wavelength range in which the mode is below the light line. In this case, this range is broader than the one achieved by taking into account a larger filling ratio. However, the guided mode still operates mainly above the light line. The good agreement between 2D and 3D simulation results indicates that out-of-plane losses in the photonic crystal waveguide are lower than the one obtained for the previous structures with larger filling ratio. This behaviour is expected due to the fact that out-of plane radiation increases as the hole size is enlarged.

In order to better analyze out-of-plane losses, the transmission spectrum for the photonic crystal taper with defect structure has been calculated by considering different lengths of the photonic crystal waveguide. Figure 6.19 shows the transmission spectrum considering (a) R=130nm and (b) R=115nm. It can be seen that below the light line, the transmission efficiency is not worsen as the photonic crystal waveguide increases. Propagation losses for wavelengths below the light line may only be produced due to fabrication imperfections such as sidewall roughness, which have not been taken into account in the 3D simulations. However, when the photonic crystal waveguide length is increased, the transmission efficiency decreases for wavelengths above the light line due to out-of-plane losses.

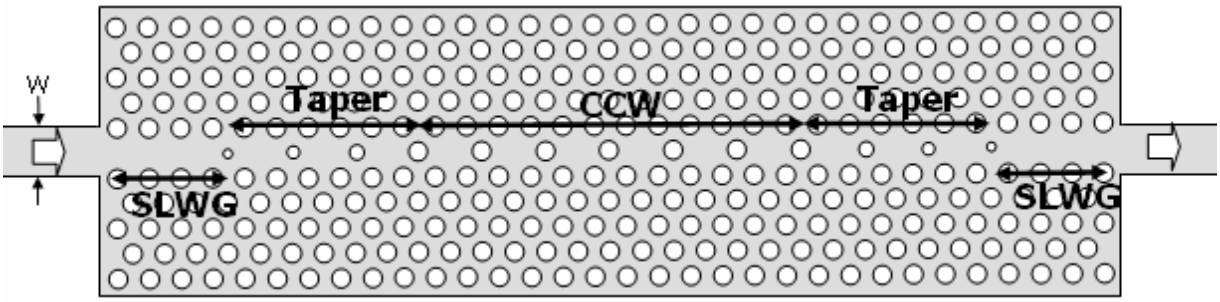

Figure 6.20.- Adiabatic coupling technique for efficient light transmission from single-line defect waveguides (SLWGs) into and out of a coupled-cavity waveguide (CCW) of finite length. The taper is based on gradually varying the radii of the spacing holes between cavities.

Propagation losses have been estimated by using the so-called cut-back method [Mcn03]. The method is based on comparing the transmission efficiency for different waveguide lengths. Propagation losses are then calculated as the line slope that best fits the data points for each wavelength. For both cases shown in figure 6.19, almost constant propagation losses were obtained for a broad wavelength range located above the light line. The estimated propagation losses are 0.6dB/μm for R=130nm and 0.35dB/μm for R=115nm. The larger propagation losses in the former confirm that out-of-plane losses are higher as the filling ratio increases. However, propagation losses are rather high in both cases so the optimum performance will be given for wavelengths located below the light line. On the other hand, it can be seen in figure 6.19(a) that the transmission efficiency is much less attenuated as the photonic crystal waveguide length increases for wavelengths located close to the lower band edge. Therefore, in this case the low transmission efficiency is mainly attributed to larger coupling losses instead of to higher propagation losses.

6.4.4 Coupling into coupled-cavity waveguides

The adiabatic coupling technique proposed in chapter five has also been used to achieve efficient coupling into photonic crystal coupled-cavity waveguides created in an air holes lattice etched into a high index dielectric background. The coupling technique is based on gradually varying the radii of the spacing holes between cavities. Thus, efficient light transmission from single-line defect waveguides (SLWGs) into and out of a coupled-cavity waveguide (CCW) of finite length is achieved.

The bulk photonic crystal is a two-dimensional triangular array of air holes in a dielectric background of silicon. The lattice constant is a=445nm while the hole radius is R=0.26a.

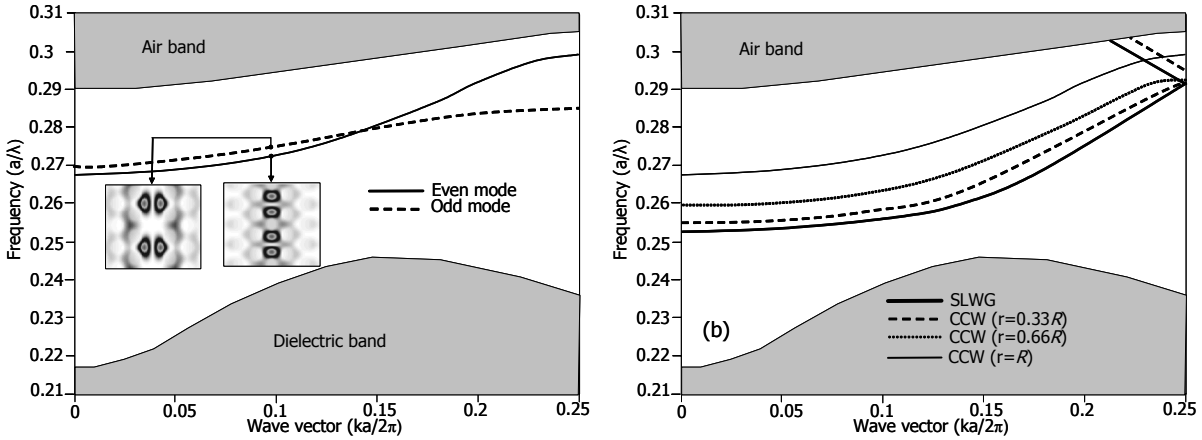

Figure 6.21.- (a) Dispersion diagram of the coupled-cavity waveguide (CCW). The insets show the mode profile for the even and odd modes for a given wave vector value. (b) Dispersion diagram of the SLWG and the CCWs with r=0.33*R*, r=0.66*R* and r=*R*. Only the even mode is shown.

The effective index approximation (n_{eff}=2.8) has also been used to initially analyze the proposed structure by means of 2D FDTD simulations. The analyzed structure is shown in figure 6.20. A silicon waveguide with an air cladding is used to couple light into and out of the SLWGs. The thickness of the waveguide (*w*=0.6μm) has been chosen to achieve negligible coupling losses into the SLWG.

The taper behavior can also be analyzed by calculating the independent dispersion diagrams at intermediate points in the taper, as described in chapter five. Figure 6.21(a) shows the dispersion diagram of the CCW formed by single missing hole cavities with a spacing of one hole between neighbouring cavities. In this case, the CCW supports two guided modes with odd and even symmetries in the transversal direction. It can be obtained that the SLWG supports also odd and even modes. However, as the fundamental mode of the dielectric waveguide has an even symmetry, only the even mode is excited in both the SLWG and CCW. Figure 6.21(b) shows the dispersion diagram for the even mode of the SLWG and of three different CCWs with r=0.33*R*, r=0.66*R* and r=*R*, being *r* the radius of the spacing single hole between cavities. It can be seen that the modes are pulled towards higher frequencies when the radius of the spacing hole is increased. This effect is just the opposite of that occurred in the rod structure because in this case we are removing dielectric material from the waveguide instead of adding it. However, there is also a mode splitting at the edge of the Brillouin zone that is enlarged as the radius of the spacing hole increases. Therefore, there are frequency ranges in which the mode is not allowed to propagate at intermediate points of the taper. This violates the condition of adiabaticity of the taper so the transmission at those frequencies is degraded [Joh02]. The same behavior occurred in the rod structure. However, in this case, the condition of adiabaticity is violated at the high frequencies of the band instead of at the low frequencies.

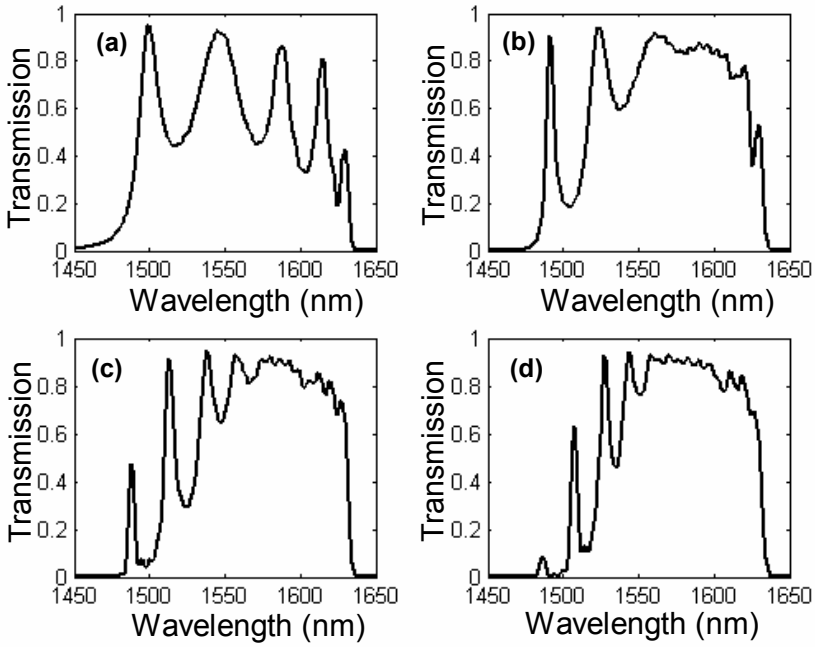

Figure 6.22.- Transmission efficiency as a function of the wavelength for a CCW length of five cavities and for different taper lengths: (a) without taper, (b) L=3, (c) L=6 and (d) L=9. The parameter *L* refers to the number of intermediate holes with a linear variation of their radius used in the taper.

Figure 6.22 shows the transmission efficiency as a function of the wavelength for a CCW length of five cavities and for different taper lengths. The vertical scale is in linear units to enhance the variations of the transmission spectra shape. When no taper is used, a number of resonances peaks equal to the number of cavities appear in the transmission spectrum, as it can be seen in figure 6.22(a). The spacing between adjacent resonance peaks is smaller at higher wavelengths, i.e. at lower frequencies, because the dispersion relation of the CCW is flatter in that region, as it is shown in figure 6.21(b). This region is more suitable for implementing functionalities based on the high dispersion of the CCW and therefore the elimination of these resonance peaks is especially desired when ultrashort pulses are transmitted through the structure.

The peak-to-valley ratio of the undesired resonance peaks is reduced when the adiabatic taper is inserted into the structure. The wavelength range, in which a rather flat transmission is observed, grows as the taper length increases. However, it can also be seen that the bandwidth is reduced at lower wavelengths and sharper resonance peaks appear when the taper length increases. This is originated due to the violation of the condition of adiabaticity occurred for those wavelengths at intermediate points in the taper.

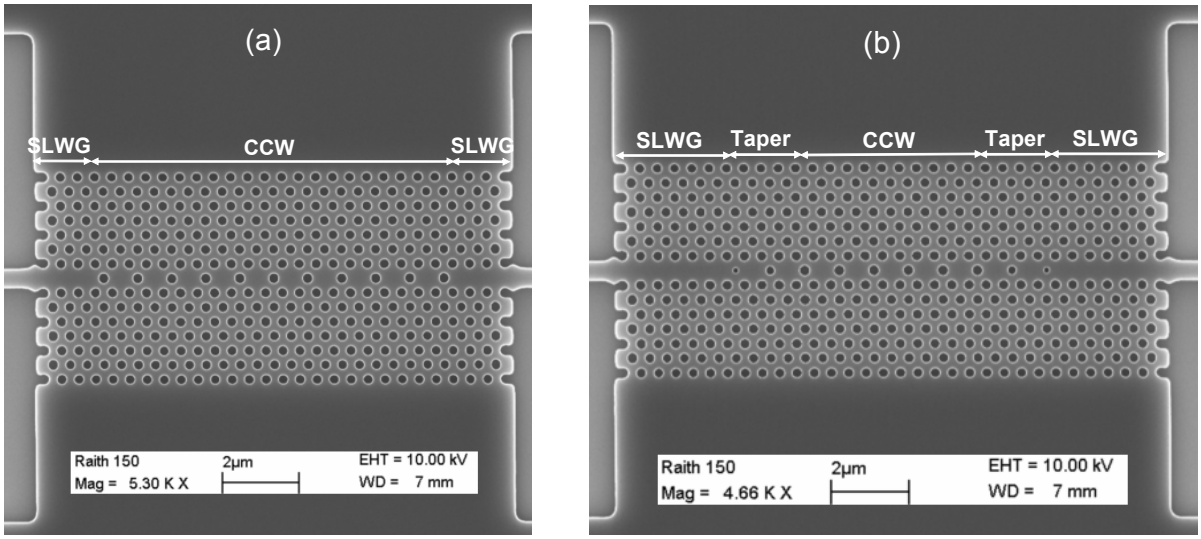

Figure 6.23.- Scanning electronic microscope (SEM) images of the coupled cavity waveguide (CCW) coupled to the single-line defect waveguides (SLWGs) (a) without and (b) with the adiabatic taper. The taper is based on gradually varying the radii of the spacing holes between cavities.

CCWs of different lengths coupled to the SLWGs with and without taper have been fabricated. Figure 6.23(a) shows a SEM image of a 10 cavities-long CCW while figure 6.23(b) shows a SEM image of a 9 cavities-long taper/CCW/taper structure. The adiabatic taper is formed by two intermediate holes. The input and output SLWGs have a different length in the CCW with and without taper structures because the taper was initially designed by using a length of three intermediate holes. However the smaller hole was too close to the allowed minimum size so it was not fabricated.

The transmission as a function of wavelength was measured using the measurement set-up previously described in section 6.3. The sample was formed by a 3µm-wide ridge waveguide tapered down to a 500nm-wide waveguide. The output power of the laser was 1mW (0dBm) and the polarizer was adjusted for only measuring TE polarized light.

Figure 6.24 shows the experimental transmitted power as a function of the wavelength for (a) a 10 cavities-long CCW and a 9 cavities-long taper/CCW/taper structure (structures shown in figure 6.23) and for (b) a 15 cavities-long CCW and a 14 cavities-long taper/CCW/taper structure. The Fabry-Perot resonances that appear at the transmission spectra are due to the inefficient coupling into and out of the 3µm-wide ridge waveguide. However, it can be seen that the transmitted power is improved at higher wavelengths when the adiabatic taper, of only two intermediate holes, is used to couple light into and out the CCW. This transmission improvement is in agreement to the one obtained from the previous 2D analysis.

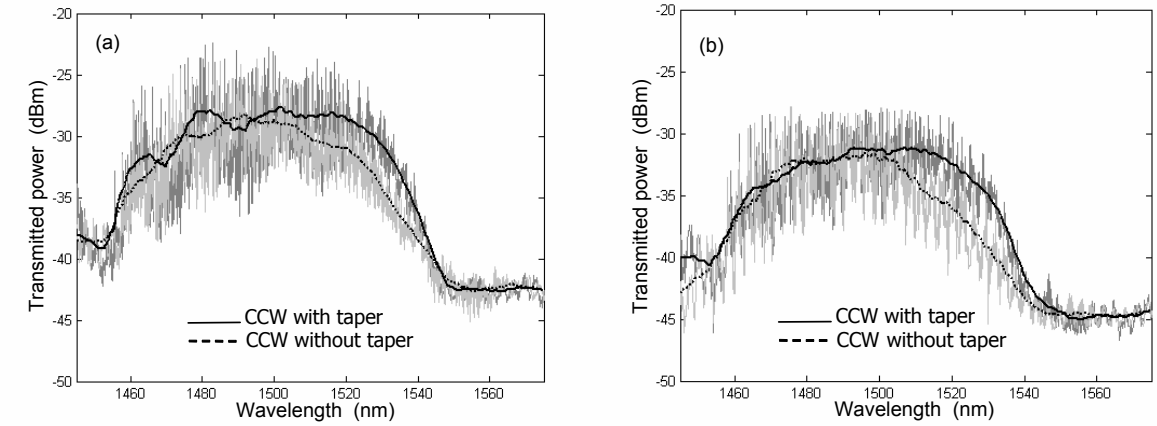

Figure 6.24.- Experimental transmitted power as a function of the wavelength for (a) a 10 cavities-long CCW and a 9 cavities-long taper/CCW/taper structure and for (b) a 15 cavities-long CCW and a 14 cavities-long taper/CCW/taper structure. The thicker lines depict the medium value obtained after filtering the Fabry-Perot resonances.

However, although the lower band edge of the transmission spectra is also in agreement between experimental and 2D simulation results, the bandwidth is narrowed for the experimental results, which restricts the transmission improvement provided by the taper.

Experimental results have been compared to 3D FDTD simulation results. Figure 6.25 shows the transmission efficiency as a function of the wavelength for the 10 cavities-long CCW and the 9 cavities-long taper/CCW/taper structure while figure 6.26 shows the transmission spectra for the 15 cavities-long CCW and the 14 cavities-long taper/CCW/taper structure. Experimental results have been normalized by the averaged transmission spectrum of the unpatterned structure. It can be seen that a very good agreement between experimental and 3D FDTD results is obtained. The transmission efficiency is improved when the adiabatic taper, of only two intermediate holes, is used to couple light into and out of the CCW. However, transmission losses are still very high.

The only difference between the results shown in figure 6.25 and 6.26 is that the CCW has a different length since the taper length is not changed. Therefore, transmission losses are only increased in figure 6.26 due to the propagation losses in the CCW. Concretely, the transmitted power is decreased around 3dB when the CCW length is increased by 4.45μm (10a) so propagation losses of the CCW are roughly estimated at 0.67dB/μm. These rather high propagation losses are attributed to the out-of-plane losses originated from the fact that the CCW operates above the light line, which implies that the guided mode is intrinsically lossy. It is important to remark that propagation losses due to sidewall roughness are not taken into account in the 3D simulations.

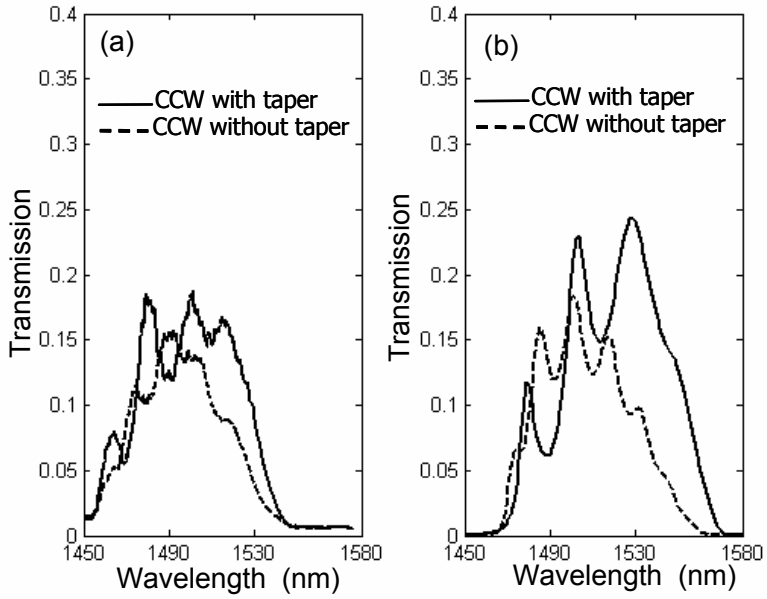

Figure 6.25.- (a) Experimental and (b) 3D FDTD simulated transmission efficiency as a function of the wavelength for the 10 cavities-long CCW and the 9 cavities-long taper/CCW/taper structure. Experimental results have been normalized by the averaged transmission spectra of the unpatterned structure.

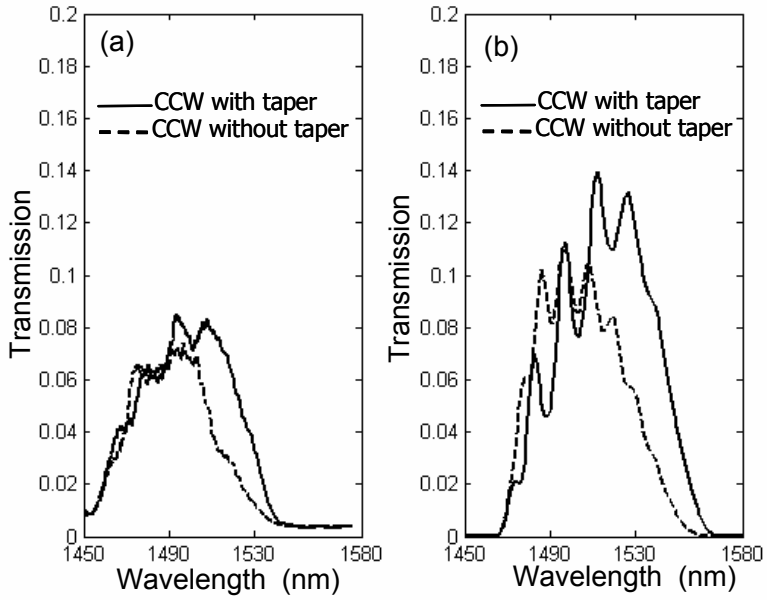

Figure 6.26.- (a) Experimental and (b) 3D FDTD simulated transmission efficiency as a function of the wavelength for the 15 cavities-long CCW and the 14 cavities-long taper/CCW/taper structure.

The transmission losses due to the estimated propagation losses are of 6.3dB (23% transmission) for a 10 cavities-long CCW and of 9.3dB (11.75% transmission) for a 15 cavities-long CCW. These values are close to those obtained for the CCW without taper structure, depicted as dashed lines in figures 6.25 and 6.36, which means that the propagation losses of the CCW are clearly dominant in the overall transmission losses. However, the transmission is higher for the CCW with taper structure, especially at the high wavelengths of the band. This transmission improvement is attributed to the effect of the taper but also because the CCW length is actually shorter in the CCW with taper structure since the total number of cavities including the input and output tapers is almost the same to that of the CCW without taper structure.

In order to better analyze the taper performance, the transmission spectra for a CCW of the same length coupled to the SLWG with and without the adiabatic taper have been calculated by means of 3D FDTD simulations. The photonic crystal has also the same length in both structures so the adiabatic taper has been replaced by a SLWG in the CCW without taper structure. Furthermore, 3D simulation results have been compared to 2D simulation results.

Figure 6.27 shows the transmission spectra calculated by means of (a) 2D and (b) 3D FDTD simulations for a 5 cavities-long CCW coupled to the SWLGs without taper (dashed line) and with a taper formed by two intermediate holes (solid line). On the other hand, figure 6.28 shows the 2D and 3D transmission spectra for a 5 cavities-long CCW coupled to the SWLGs with a taper formed by two (dashed line) and four (solid line) intermediate holes. In both figures 6.27 and 6.28, the transmission spectrum is also shown for a 12*a*-long SLWG (dotted line), which corresponds to the total length of the input and output SLWGs used in the CCW with taper structure considering a taper length of two intermediate rows.

It can be seen that the transmission improvement provided by the taper is not so evident for the 3D results compared to the 2D results. However, this is not due to a bad performance of the taper. In figures 6.27 and 6.28, it can be seen that the transmission efficiency decreases in the 12*a*-long SLWG structure as the wavelength is closer to the band edge due to the larger coupling losses between the external dielectric waveguide and the SLWG. Furthermore, the cut-off wavelength is shorter than the one given for the 2D results. These higher coupling losses besides the high propagation losses in the CCW make negligible the transmission efficiency at the high wavelengths of the CCW band, which restricts the transmission improvement provided by the taper.

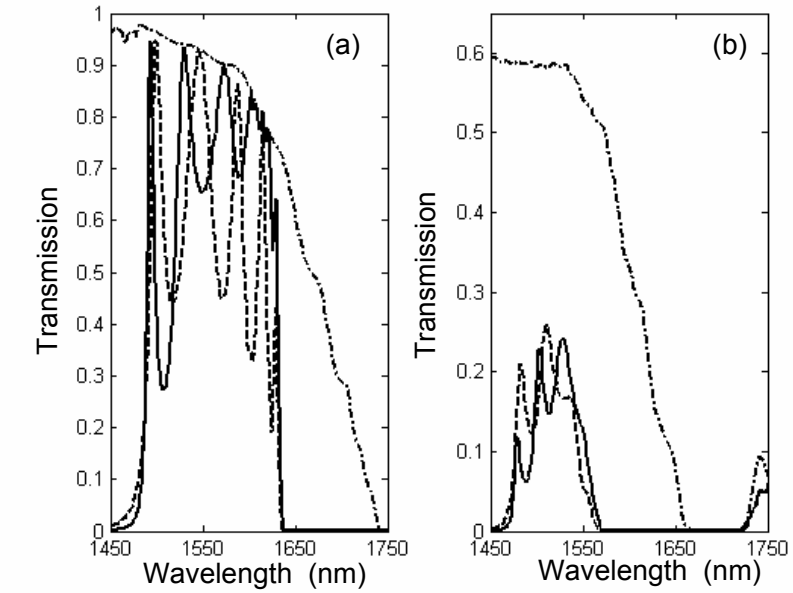

Figure 6.27.- (a) 2D and (b) 3D FDTD simulated transmission efficiency as a function of the wavelength for a 5 cavities-long CCW coupled to the SWLGs without taper (dashed line) and with a taper formed by two intermediate holes (solid line). The dotted line depicts the transmission spectrum for a 12*a*-long SLWG, which corresponds to the total length of the input and output SLWGs used in the CCW with taper structure.

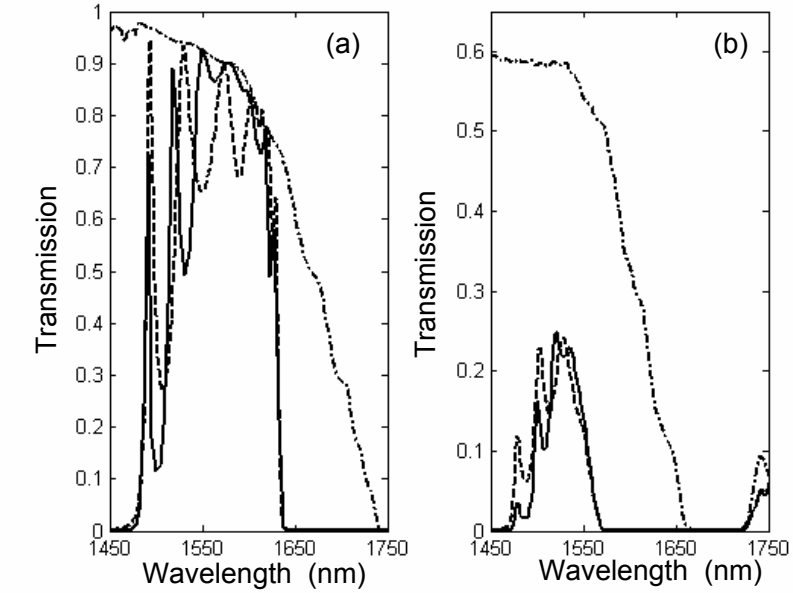

Figure 6.28.- (a) 2D and (b) 3D FDTD simulated transmission efficiency as a function of the wavelength for a 5 cavities-long CCW coupled to the SWLGs with a taper formed by two (dashed line) and four (solid line)intermediate holes. The dotted line depicts the transmission spectrum for a 12*a*-long SLWG.

The transmission efficiency is also attenuated at higher wavelengths in the 2D results, as it can bee seen in figure 6.27(a) and 6.28(a). However, it is much less critical due to the lack of out-of-plane losses. Thus, the 3D simulated transmission efficiency is improved at higher wavelengths while it is degraded at lower wavelengths due to the effect of the taper, which agrees with the results predicted by the 2D simulations. This behaviour is enhanced as the taper length increases, as it can be seen in figure 6.28(b). Furthermore, the transmission improvement due to the taper explains why the cut-off wavelength of the upper band edge of the CCW with taper structure is above than that of the CCW without taper structure while the cut-off wavelength of the lower band edge is the same in both cases, as it can be seen in figure 6.25(b), 6.26(b) or 6.27(b).

The previous analysis confirms that the transmission improvement shown at higher wavelengths in the experimental results for the CCW with taper structures is attributed to the higher coupling efficiency between the SLWG and the CCW. However, the overall transmission losses are lower because the propagation losses in the taper are lower than the propagation losses in the CCW. Therefore, it can be observed in figure 6.27 and 6.28 that the transmission losses are similar in both the CCW with and without taper structures when the CCW has the same length. This result also indicates that the propagation losses in the taper are similar to the propagation losses in the SLWG since the photonic crystal has also the same length in both the CCW with and without taper structures.

6.5 Rod structure: Silicon rods embedded in silica

6.5.1 Fabrication process

The planar photonic crystal structure consists of a borophosphosilicate glass (BPSG) layer on top of a silica layer. The BPSG layer has a higher index of refraction than the silica layer to ensure the index confinement in the vertical dimension. Both layers are deposited on top of a bare silicon wafer. The photonic crystal is formed by a lattice of rods of polycrystalline silicon or polysilicon inserted on the BPSG layer. An upper cladding of silica is deposited over the core layer to achieve a symmetric structure in the vertical dimension. The fabrication process is still under development. The main challenge is the minimum achievable rods diameter since there are not standard solutions for diameters smaller than 500nm.

The fabrication process flow is illustrated in figure 6.29. Low pressure chemical vapour deposition (LPCVD) is used for hard mask deposition prior to etching. The hard mask layer improves the selectivity of the further etching into the BPSG layer and it is firstly deposited on top of this layer.

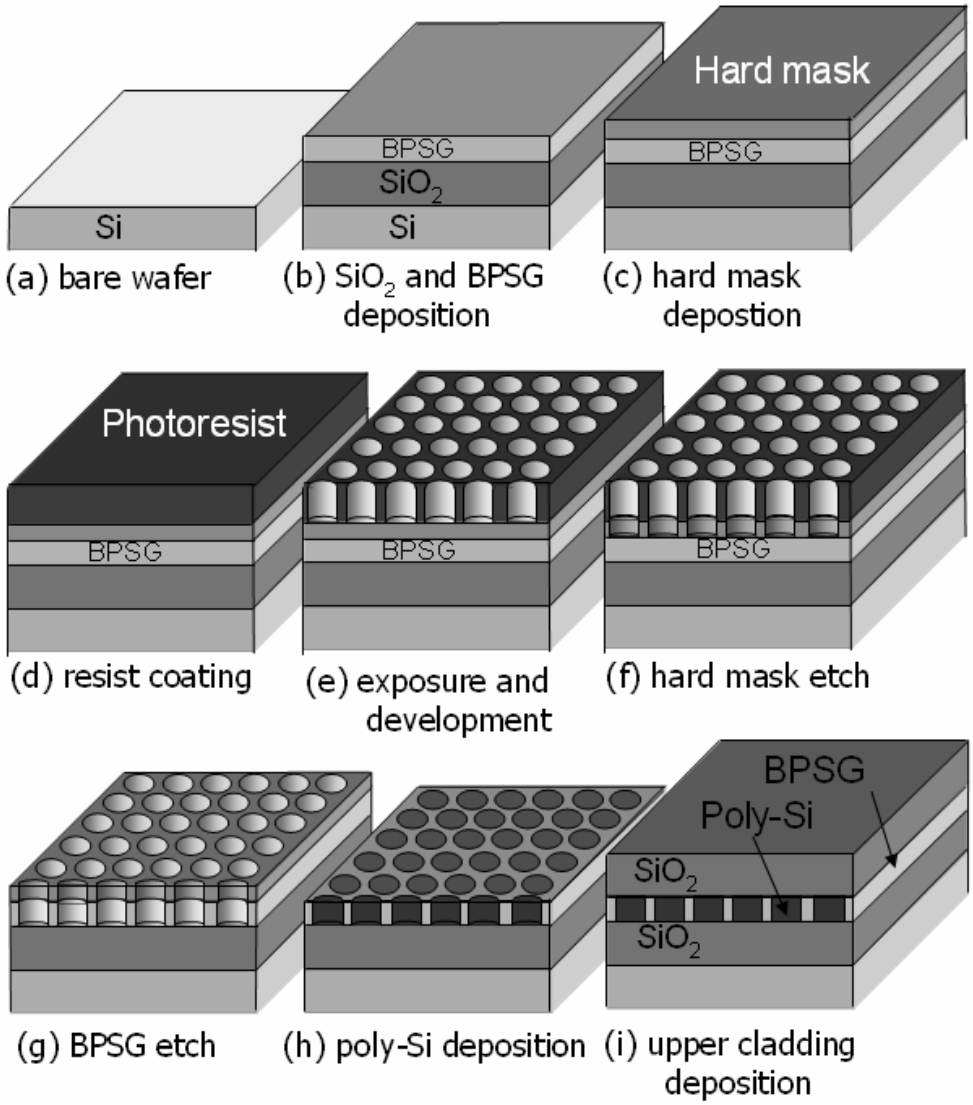

Figure 6.29.- Description of the fabrication process of the planar photonic crystal based on a rod structure. The planar photonic crystal structure consists of a doped silica layer on top of a silica layer of a lower index of refraction to ensure the index confinement in the vertical dimension. The photonic crystal is formed by a lattice of rods of polycrystalline silicon or polysilicon on the doped silica layer. An upper cladding of the same material than that of the lower cladding is deposited over the core layer in the final step to achieve a symmetric structure in the vertical dimension.

After deposition of the hard mask layer, the photoresist is coated over the wafer and electron beam lithography is used to illuminate the photoresist with the pattern. The photoresist is then developed and reactive ion etching (RIE) is firstly used for etching the hard mask layer. High aspect ratio etching (HARE) is then used for etching the holes in the BPSG layer. The holes are filled with the deposition of polysilicon by means of LPCVD. Finally, the extra polysilicon is removed and an upper cladding is deposited on top of polysilicon rods lattice.

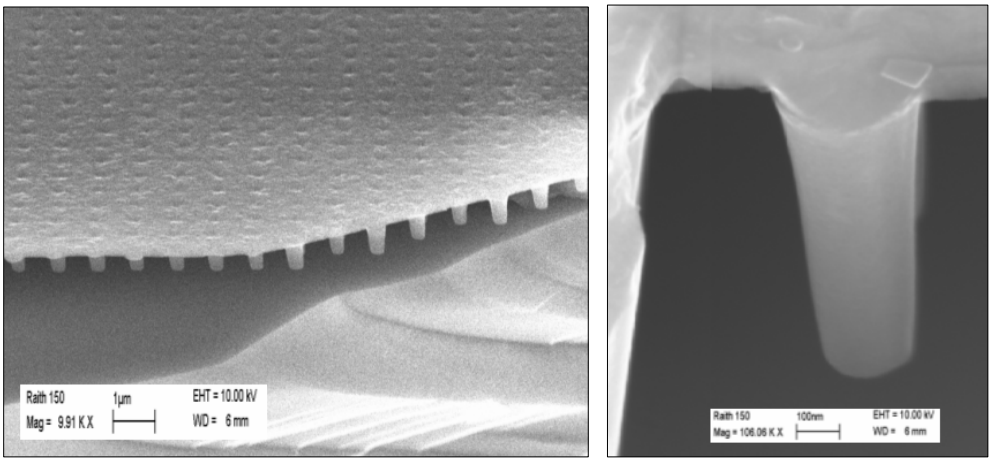

Figure 6.30.- SEM pictures of the planar photonic crystals based on a rod structure. The surrounding BPSG has been removed for highlighting the rods.

Figure 6.30 shows SEM pictures of a recently fabricated sample. The surrounding BPSG has been removed for highlighting the rods. Rods of a diameter up to 200nm are currently achieved.

6.5.2 Coupling into photonic crystal waveguides

The proposed coupling technique to achieve efficient coupling between dielectric waveguides and line defect photonic crystal waveguides has been evaluated for the rod structure by means of 3D FDTD simulations due to the lack of experimental results. For the sake of comparison, the same parameters as that used in the 2D analysis carried out in chapter four have been taken into account. The photonic crystal is formed by a triangular array of silicon rods with radius R=0.2a and lattice constant a=465nm surrounded by a homogenous dielectric medium of silica. The thickness of the planar photonic crystal structure is 2a while an air medium is used as upper and lower claddings. A 1.5µm-wide silica dielectric waveguide is coupled to a single line defect photonic crystal waveguide.

The analyzed structure consists of a photonic crystal waveguide of finite length coupled to input and output dielectric waveguides by means of a photonic crystal taper optimized with the suitable configuration of defects. Thus, the transmission spectrum of the whole structure may be calculated in only one FDTD simulation. The a-long photonic crystal taper optimized with the one defect configuration (r_{def}=0.5R, z_{def}=0.6a) has been first simulated. Figure 6.31 shows the transmission spectra calculated by means of (a) 2D and (b) 3D FDTD simulations for the taper with defect (solid line), without defect (dashed line) and also for the butt-coupling case (dotted line). The length of the photonic crystal is 11a for the three analyzed structures. It can be seen that almost negligible transmission is achieved by the butt-coupling case.

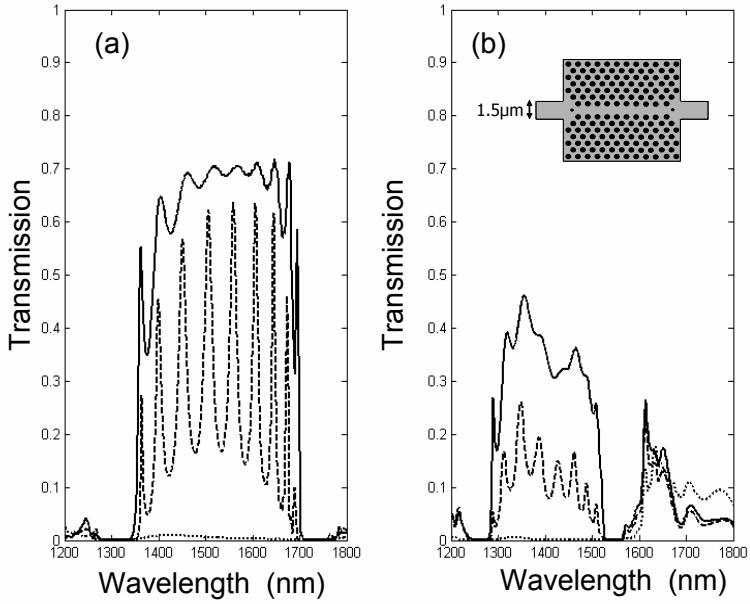

Figure 6.31.- (a) 2D and (b) 3D FDTD simulated transmission efficiency as a function of the wavelength considering a photonic crystal taper with defect (solid line), without defect (dashed line) and the butt-coupling case (dotted line). The *a*-long photonic crystal taper is depicted in the inset and the parameter of the defect are r_{def}=0.5R, and z_{def}=0.6a. The length of the photonic crystal is 11a for the three analyzed structures.

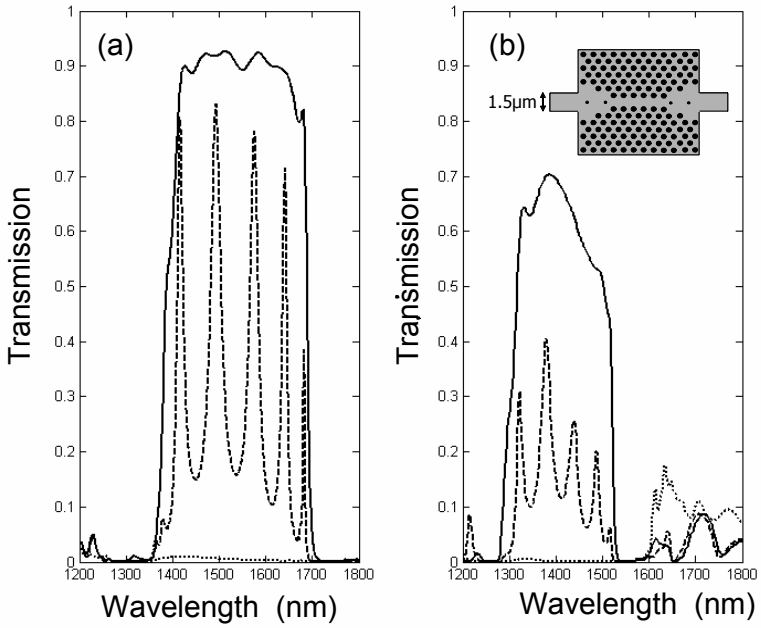

Figure 6.32.- (a) 2D and (b) 3D FDTD simulated transmission efficiency as a function of the wavelength considering a 3a-long photonic crystal taper, depicted in the inset, with a two defects configuration of parameters r_{int}=0.5R, z_{int}=2.6a and r_{ext}=0.6R, z_{ext}=0.2a (solid line), without defects (dashed line) and the butt-coupling case (dotted line) The length of the photonic crystal is 11a for the three analyzed structures.

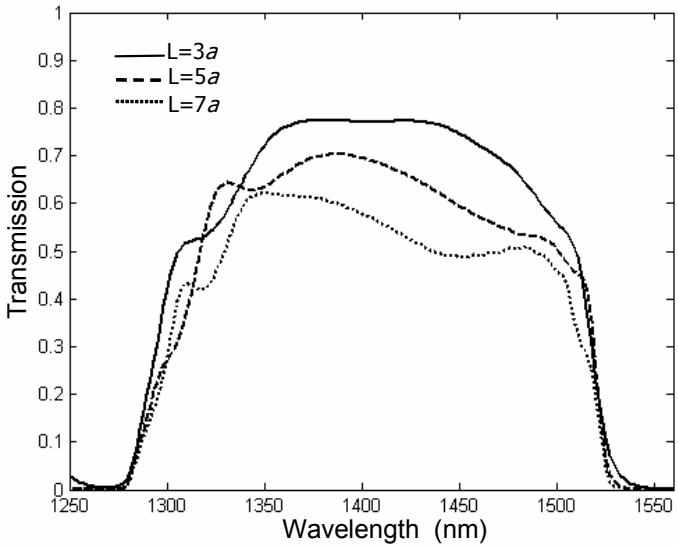

Figure 6.33.- 3D FDTD simulated transmission efficiency as a function of the wavelength for the 3*a*-long photonic crystal taper with the two defects configuration by considering three different lengths, *L*, of the photonic crystal waveguide.

The transmission is significantly improved when the photonic crystal taper is used. However, a number of resonance peaks appears in the transmission spectrum of the taper without defect structure due to Fabry-Perot like cavity originated from the mode mismatch at the input and output interfaces. The resonance peaks are eliminated from the transmission spectrum when the taper with defect is used. On the other hand, it can be seen in figure 6.31 that there is a good agreement between 2D and 3D results in the transmission behaviour for the three analyzed structures although a narrower bandwidth and lower transmission efficiency is observed for the 3D results.

The 3*a*-long photonic crystal taper analyzed in chapter four has also been evaluated. A broad transmission spectrum with efficiencies above 90% was predicted when a two defects configuration (r_{int}=0.5R, z_{int}=2.6a and r_{ext}=0.6R, z_{ext}=0.2a) was placed within the taper. Figure 6.32 shows the transmission spectra calculated by means of (a) 2D and (b) 3D FDTD simulations for the taper with the two defects configuration (solid line), without defects (dashed line) and for the butt-coupling case (dotted line). The length of the photonic crystal is also 11a in the three analyzed structures, the same as the one previously considered. A good agreement in the transmission behaviour is also observed between 2D and 3D results. Therefore, higher transmission efficiency is achieved with respect to the *a*-long photonic crystal taper.

The discrepancy of the transmission efficiency between 2D and 3D results is mainly attributed to the out-of-plane losses in the photonic crystal waveguide.

Therefore, in order to evaluate the effect of out-of-plane losses on the transmission efficiency, the transmission spectrum for the 3*a*-long taper with the two defects configuration structure has been calculated by considering three different lengths of the photonic crystal waveguide. Figure 6.33 shows the results. It can be seen that the transmission efficiency decreases as the length of the photonic crystal waveguide is increased. Propagation losses, which have been estimated by using the cut-back method, vary from 0.2dB/μm up to 1dB/μm as a function of the wavelength. These high propagation losses are mainly attributed to the fact that the guided mode is above the light line so out-of-plane losses are unavoidable.

Out-of-plane radiation may be avoided by using a different sort of photonic crystal waveguide that support a guided mode below the light line. One approach is to use rods of smaller radius instead of completely removing them to form the waveguide [Joh00a]. In this case, propagation losses below 0.005dB/μm have been experimentally obtained [Tok04]. Therefore, further work by properly designing the photonic crystal waveguide and optimizing the proposed coupling technique for that waveguide will be required to minimize propagation losses.

6.6 Conclusion

The coupling techniques proposed in chapters four and five for a rod structure have been demonstrated in this chapter for a hole structure. Furthermore, a 3D analysis have been carried out for both structures and compared to 2D simulation results. The main discrepancies between 2D and 3D simulation results are due to out-of-plane losses, which are not taken into account in the 2D simulations. Therefore, 2D simulations can be a good instrument to obtain preliminary results and demonstrate new concepts, although a 3D analysis must be carried out to accurately design real structures and analyze out-of-plane losses. On the other hand, the fabrication processes of both hole and rod structures have also been described. However, experimental results have only been provided for the hole structure since the fabrication process of the rod structure is still under development.

Experimental coupling efficiencies up to 75% from a 3μm-wide ridge waveguide into a line defect photonic crystal waveguide have been demonstrated for the hole structure. The coupling efficiency could be improved by using better optimization tools, such as genetic algorithms, to design the optimum configuration of defects, as it was shown in chapter four. On the other hand, it has also been obtained that out-of-plane losses may seriously degrade the transmission performance in both hole and rod structures when the photonic crystal waveguide operates above the light line. Therefore, alternative waveguides designs with a larger bandwidth below the light line should be investigated to reduce out-of-plane losses.

Finally, the experimental implementation of the proposed adiabatic coupling technique to improve the coupling efficiency from single line defect photonic crystal waveguides into CCWs has also been reported for the hole structure. High out-of-plane losses were also obtained in the CCW thus increasing propagation losses and restricting the transmission improvement provided by the taper. Therefore, the analysis of out-of-plane losses and techniques to avoid them will become necessary to improve the CCW performance.

Part of the obtained results has been published in the following peer-reviewed journal:

- P. Sanchis, J. García, J. Martí, W. Bogaerts, P. Dumon, D. Taillaert, R. Baets, V. Wiaux, J. Wouters and S. Beckx, "Experimental demonstration of high coupling efficiency between wide ridge waveguides and single-mode photonic crystal waveguides", *IEEE Photon. Tech. Lett.*, vol. 16, pp. 2272-2274, 2004.

- P. Sanchis, J. Martí, W. Bogaerts, P. Dumon, D. Van Thourhout and R. Baets, "Experimental results on adiabatic coupling into SOI photonic crystal coupled-cavity waveguides", *IEEE Photon. Techn. Lett.*, vol. 17, pp. 1199-1201, 2005.

And in the following conferences:

- P. Sanchis, J. Garcia, F. Cuesta-Soto, A. Martinez, J. Blasco, J. Marti, W. Bogaerts, P. Dumon, D. Taillaert, R. Baets, "Experimental demonstration of a high efficiency coupling technique for planar photonic crystal circuits", *Photonic and Electromagnetic Crystal Structures (PECS-V)*, Tu-P34, Kyoto, Japan, March 2004.

- P. Sanchis, J. Martí, W. Bogaerts, P. Dumon, and R. Baets, "Experimental implementation of an adiabatic coupling technique for SOI photonic crystal coupled-cavity waveguides", 2nd NanoSpain Workshop, Barcelona, 2005.

- P. Sanchis, A. Martínez, J. García, F. Cuesta-Soto, J. Martí, W. Bogaerts, P. Dumon, D. Van Thourhout and R. Baets, "Experimental demonstration of adiabatic coupling into SOI photonic crystal coupled-cavity waveguides", *Conference on Lasers and Electro-Optics (CLEO)*, CtuDD2, Baltimore, USA, 2005.

Chapter 7

Conclusions and Future Work

7.1 Conclusions

The aim of this work has been primary focused to minimize coupling losses between dielectric waveguides and line defect photonic crystal waveguides. The simplest way to couple them is butt-coupling, which has been firstly analyzed. Closed form expressions for the reflection and transmission matrices that completely characterize the scattering that occurs at the interface have been derived. Furthermore, an efficient approach has been proposed for a semi-analytic treatment of complex photonic crystal structures thus reducing the computation time with respect to other conventional numerical methods such as the widely used FDTD method. Coupling losses are originated due to the mode mismatch between dielectric and photonic crystal waveguides. However, mode properties in photonic crystals can significantly change within the basic period. Thus, it has been shown that the coupling efficiency can be improved by choosing the optimum cut position within the basic period of the photonic crystal.

However, even at the optimum cut position, the coupling efficiency gets worse when the dielectric waveguide becomes broader due to the mode profile mismatch. Furthermore, high resolution fabrication accuracies are required to achieve the target cut position. Therefore, a coupling technique has been proposed to maximize the transmission efficiency from both narrow and broad dielectric waveguides into line defect photonic crystal waveguides. The proposed coupling technique is based on setting a number of localized defects within a photonic crystal taper. Genetic algorithms have been demonstrated to be a very efficient tool to design the optimum number of defects as well as their radii and position within the photonic crystal taper. Transmission efficiencies above 90% over a large frequency range have been achieved significantly improving the results obtained by the same photonic crystal taper but without defects.

Once the problem of coupling from an external medium into line defect photonic crystal waveguides has been resolved, efficient coupling from line defect photonic crystal waveguides into coupled-cavity waveguides has been investigated. An adiabatic coupling technique based on progressively varying the radii of the spacing defects between cavities has been proposed and analyzed. Flat transmission spectra with transmission efficiencies above 90% have been achieved by using short tapers. Furthermore, the dynamic performance of the proposed coupling technique has been investigated by analyzing the propagation of ultra short pulses. A theoretical model based on the Fabry-Perot formula has been proposed for efficiently analyzing a large variety of parameters, such as the group delay, FWHM and peak amplitude of the transmitted pulse, thus avoiding the large computation times associated to the FDTD method.

Finally, the fabrication and experimental demonstration of the previously proposed coupling techniques and structures have been provided. Photonic crystals have been fabricated in the form of planar structures, known as planar photonic crystals or photonic crystal slabs. Two different planar photonic crystal structures named as rod and hole structures have been considered. In the former, the photonic crystal is formed by a triangular lattice of silicon rods surrounded by a silica material, which has a lower refractive index. In the latter, the photonic crystal is formed by a triangular lattice of air holes etched into a Silicon-on-insulator (SOI) substrate. Experimental results have only been provided for the hole structure since the fabrication process of the rod structure is still under development. However, the usefulness of the proposed coupling techniques have been demonstrated for both hole and rod structures by means of 3D simulation results. Furthermore, the discrepancies between 2D and 3D simulation results have been analyzed. It has been obtained that 2D simulations can be a good instrument to obtain preliminary result and demonstrate new concepts. However, 3D simulations must be carried out for a rigorous design and to analyze out-of-plane losses, which are not taken into

account by the 2D analysis and can significantly increase transmission losses. A very important advantage of the proposed coupling techniques is that the optimum performance is achieved in very short coupling lengths. Therefore, coupling losses due to out-of-plane losses are minimized and compact photonic crystal structures are achieved.

7.2 Main original contributions

The main original contributions of this work are:

- Modeling of the interface between dielectric waveguides and photonic crystal circuits.
- High efficiency coupling technique between dielectric waveguides and line defect photonic crystal waveguides.
- High efficiency coupling technique between line defect photonic crystal waveguides and coupled-cavity waveguides.

7.3 Future work

The proposed coupling techniques have been exhaustively analyzed through this work by means of 2D simulation tools. Only in the last term, we were able to perform 3D simulation results that corroborated the results obtained by the 2D analysis. However, an exhaustive 3D analysis will become necessary to optimize the proposed coupling technique making them useful for implementing future devices based on photonic crystals. Furthermore, the experimental demonstration of the proposed coupling techniques for the rod structure should be carried out.

The 3D implementation of the closed form expressions derived in chapter three would be very useful for a 3D analysis in a shorter computation time with respect to FDTD. Furthermore, it would also be interesting to repeat a similar derivation to obtain closed form expression for the butt-coupling between two different periodic media. These expressions would be useful to analyze a large variety of functionalities based on photonic crystals, such as directional couplers or Y-junctions.

Finally, future work should also be devoted to minimize out-of-plane losses in photonic crystal waveguides, especially in coupled-cavity waveguides. It is worth mentioning that the analysis of out-of-plane radiation in coupled-cavity waveguides has been almost untreated until now in the literature. On the other hand, conventional line defect photonic crystal waveguide should also be properly designed to mainly operate above the light line thus minimizing out-of-plane losses.

Appendix A

Publications

A.1 Peer-reviewed journals

1. P. Sanchis, J. Martí, A. García, A. Martínez and J. Blasco, "High efficiency coupling technique for planar photonic crystal waveguides", *Electron. Lett.*, vol. 38, pp. 961-962, 2002.
2. P. Sanchis, J. Martí, J. Blasco, A. Martínez and A. García, "Mode matching technique for highly efficient coupling between dielectric waveguides and planar photonic crystal circuits", *Opt. Express*, vol. 10, pp. 1391-1397, 2002.
3. P. Sanchis, J. Garcia, A. Martínez, F. Cuesta, A. Griol, J. Martí, "Analysis of adiabatic coupling between photonic crystal single-line-defect and coupled-resonator optical waveguides", *Optics Letters*, vol. 28, pp. 1903-1905, 2003.
4. P. Sanchis, P. Bienstman, B. Luyssaert, R. Baets, and J. Marti, "Analysis of Butt-Coupling in Photonic Crystals", *IEEE Journal of Quantum Electronics*, vol. 40, pp. 541-550, 2004.
5. P. Sanchis, J. García, J. Martí, W. Bogaerts, P. Dumon, D. Taillaert, R. Baets, V. Wiaux, J. Wouters and S. Beckx, "Experimental demonstration of high coupling efficiency between wide ridge waveguides and single-mode photonic crystal waveguides", *IEEE Photon. Tech. Lett.*, vol. 16, pp. 2272-2274, 2004.

6. P. Sanchis, J. García, A. Martinez, J. Martí, "Pulse Propagation in Adiabatically Coupled Photonic Crystal Coupled Cavity Waveguides", *Journal of Applied Physics*, vol. 97, pp. 013101, 2005.
7. P. Sanchis, J. Martí, B. Luyssaert, P. Dumon, P. Bienstman and R. Baets, "Analysis and design of efficient coupling in photonic crystal circuits", to be published in *Optical and Quantum Electronics*, March 2005.
8. P. Sanchis, J. Martí, W. Bogaerts, P. Dumon, D. Van Thourhout and R. Baets, "Experimental results on adiabatic coupling into SOI photonic crystal coupled-cavity waveguides", *IEEE Photon. Techn. Lett.*, vol. 17, pp. 1199-1201, 2005.

A.2 Conferences

9. P. Sanchis, J. Martí, A. Martínez J. Blasco and A. Griol, "A novel high efficiency coupling technique for planar photonic crystal circuits", *Conferencia de dispositivos electrónicos (CDE)*, pp. IV10.1-IV10.4, Calella, Barcelona, 2003.
10. P. Sanchis, J. Garcia, F. Cuesta-Soto, A. Martinez, J. Blasco, J. Marti, W. Bogaerts, P. Dumon, D. Taillaert, R. Baets, "Experimental demonstration of a high efficiency coupling technique for planar photonic crystal circuits", *Photonic and Electromagnetic Crystal Structures (PECS-V)*, Tu-P34, Kyoto, Japan, March 2004.
11. P. Sanchis, J. Martí, P. Bienstman, B. Luyssaert, R. Baets, "Analytic expressions for transmission and reflection from semi-infinite photonic crystal waveguides", *Photonic and Electromagnetic Crystal Structures (PECS-V)*, Tu-P31, Kyoto, Japan, March 2004.
12. P. Sanchis, J. Marti, B. Luyssaert, P. Dumon, P. Bienstman, R. Baets, "Analysis and design of efficient coupling into photonic crystal circuits", *XII Int. Workshop on Optical Waveguide Theory and Numerical Modelling*, Ghent, Belgium, pp.27, March 2004.
13. P. Sanchis, A. Martínez, J. García, F. Cuesta-Soto, J. Martí, W. Bogaerts, P. Dumon, D. Van Thourhout and R. Baets, "Experimental demonstration of adiabatic coupling into SOI photonic crystal coupled-cavity waveguides", *Conference on Lasers and Electro-Optics (CLEO)*, CtuDD2, Baltimore, USA, 2005.
14. P. Sanchis, J. Martí, J. García, P. Bienstman, R. Baets, "Semi-analytic analysis of complex photonic crystal structures", *12th European Conference on Integrated Optics*, FrB1-4, pp. 347-350, Grenoble, France, 2005.
15. P. Sanchis, J. Martí, W. Bogaerts, P. Dumon, and R. Baets, "Experimental implementation of an adiabatic coupling technique for SOI photonic crystal coupled-cavity waveguides", 2nd NanoSpain Workshop, Barcelona, 2005.

16. P. Sanchis, A. Håkansson, J. Sánchez-Dehesa, and J. Marti, "High efficiency defect-based photonic-crystal-tapers designed by a genetic algorithm", *Photonic and Electromagnetic Crystal Structures (PECS-VI)*, Crete, Greece, 2005.
17. P. Sanchis, J. Martí, J. García, P. Bienstman, R. Baets, "Semi-analytic approach for coupling issues in photonic crystal structures", *Photonic and Electromagnetic Crystal Structures (PECS-VI)*, Crete, Greece, 2005.

A.3 Other contributions

A.3.1 Peer-reviewed journals

18. A. Martínez, A. Garcia, P. Sanchis, J. Martí, "Group velocity and dispersion model of coupled-cavity waveguides in photonic crystals", *Journal of the Optical Society of America*, vol. 20, pp. 147-150, 2003.
19. A. Martínez, A. Griol , P. Sanchis, J. Martí , "Mach-Zehnder interferometer employing coupled-resonator optical waveguides", *Optics Letters*, vol. 28, pp. 405-407, 2003.
20. P. Sanchis, V. Polo, J, Herrera, J.L. Corral, Moon-Soon Choi, J. Martí, "Experimental Demonstration of a Direction of Arrival Estimation Algorithm for Millimeter-Wave Switched-Beam Array Antennas", *Microwave and Optical Technology Letters*, vol. 39, pp. 199-201, 2003.
21. A. Martínez, F. Cuesta, A. Griol, D. Mira, J. Garcia, P. Sanchis, R. Llorente, J. Martí, "Photonic crystal 180º power splitter based on coupled-cavity waveguides", *Applied Physics Letters*, vol. 83 pp. 3033-3035, 2003.
22. F. Cuesta-Soto, A. Martínez, J. Garcia, F. Ramos, P. Sanchis, J. Blasco, J. Martí, "All-optical switching structure based on a photonic crystal directional coupler", *Optics Express*, vol. 12, pp. 161-167, 2004.
23. A. Martinez, A. Griol, P. Sanchis, J. Marti, "Photonic Band Gap", *Encyclopedia of RF and and Microwave Engineering*, vol. 4, pp. 3823-3838, 2005.
24. A. Martinez, P. Sanchis and J. Marti, "Mach-Zehnder interferometers in photonic crystals", to be published in *Optical and Quantum Electronics*.
25. J. García, A. Martínez, F. Cuesta-Soto, P. Sanchis, J. Blasco, and J. Martí, "Broadening compensation for ultrashort pulses in photonic crystals", to be published in *Optical and Quantum Electronics*.

A.3.2 Conferences

26. P. Sanchis, J. Herrera, V. Polo, J. L. Corral, J. Marti, "Simultaneous Tracking and DoA Estimation Algorithm for Millimeter-Wave Broadband Wireless Access Networks employing Optically Beamformed Antennas", *International*

workshop on EU cooperation in the field of development of mobile personal communication – IST projects, pp. 113., Moscow, May 2002.

27. P. Sanchis, J. M. Martinez, J. Herrera, V. Polo, J. L. Corral, J. Marti, "A Novel Simultaneous Tracking and Direction of Arrival Estimation Algorithm for Beam-Switched Base Station Antennas in Millimeter-Wave Wireless Broadband Access Networks", *IEEE Antennas and Propagation International Symposium*, San Antonio, USA, vol. 1, pp. 594-597, June 2002.
28. P. Sanchis, J. M. Martinez, J. Herrera, V. Polo, J. L. Corral, J. Marti, "Reduction of Carrier-to-Interference Ratio in Fixed Broadband Wireless Access Networks Employing Beam-Switched Base Station Antennas", *IEEE Antennas and Propagation International Symposium*, San Antonio, USA, vol. 1, pp. 598-601, June 2002.
29. P. Sanchis, J.M. Martinez, J. Herrera , V. Polo, J. L. Corral, J. Marti, G. Nuñez" "Smart Functionalities for TDD/TDMA Broadband Wireless Access Networks Employing Optically Beamformed Base-Station Antenn"s", *IST Mobile Summit 2002*, Thessaliniki, Greece, pp. 695-699, June 2002.
30. P. Sanchis, V. Polo, J. Herrera, J. L. Corral, M.Choi, J. Marti, "Experimental Demonstration of a Direction of Arrival Estimation Algorithm for mm-wave Broadband Communication Systems", *IEEE MTT-S Int. Microwave Symposium*, TH4A-3, pp. 1534-1536, Philadelphia, USA, June 2003.
31. P. Sanchis, V. Polo, J. Herrera, J.L. Corral, Moon-Soon Choi, J. Martí, "Performance Analysis of Optically Beamformed Base-Station Antennas for Broadband Wireless Access Networks", *IST Mobile Communications Summit 2003*, Aveiro, Portugal, pp.12-16, June 2003.
32. A. Martínez, A. Griol, D. Mira, F. Cuesta, J. Garcia, P. Sanchis, R. Llorente, J. Martí, "180° power splitting in photonic crystals", *European Conference on Communications (ECOC)*, vol. 5, pp. 42-43, Rimini, Italy, 2003.
33. A. Griol, D. Mira, J. Martí, J.L. Corral, A. Martínez and P. Sanchis, "Microstrip multistage coupled ring bandpass filters using defected ground structures for harmonic suppression", *Conferencia de dispositivos electrónicos (CDE)*, pp. VII03.1-VII03.3, Calella, Barcelona, 2003.
34. J. Garcia, A. Martinez, G. Sanchez, F. Cuesta-Soto, P. Sanchis, J. Blasco, J. Martí, "Large-bandwidth and lossless single-mode waveguides in Si-on-SiO2 planar photonic crystal structures", *Photonic and Electromagnetic Crystal Structures (PECS-V)*, Tu-P40, Kyoto, Japan, March 2004.
35. F. Cuesta-Soto, F. Ramos, A. Martinez, P. Sanchis, J. Garcia, J. Blasco, J. Martí, "All-optical switching in a directional coupler", *Photonic and Electromagnetic Crystal Structures (PECS-V)*, Th-P22, Kyoto, Japan, 2004
36. A. Martinez, P. Sanchis, J. Marti, "Mach-Zehnder interferometers in photonic crystals", *XII Int. Workshop on Optical Waveguide Theory and Numerical Modelling*, Ghent, March 2004.

37. J. Garcia, A. Martinez, F. Cuesta, P. Sanchis, J. Blasco, J. Marti, "Analysis of photonic crystal waveguides as dispersion compensators", *XII Int. Workshop on Optical Waveguide Theory and Numerical Modelling*, Ghent, Belgium, March 2004.
38. B. Luyssaert, P. Vandersteegen, W. Bogaerts, P. Dumon, P. Sanchis, J. Marti, R. Baets, "A Versatile Optical Spot-Size Converter Design", *European Conference on Optical Communication (ECOC)*, We(3), Sweden, pp.468-469, 2004.
39. F. Cuesta-Soto, B. García-Baños, A. Håkanson, J. García, P. Sanchis and J. Martí, "Intermodal dispersion conpensation in a PhC directional coupler", *Photonic and Electromagnetic Crystal Structures (PECS-VI)*, Crete, Greece, 2005.
40. J. García, P. Sanchis, and J. Martí, "Using dispersion relationships for finite length PhC waveguides characterisation", *Photonic and Electromagnetic Crystal Structures (PECS-VI)*, Crete, Greece, 2005.

Bibliography

[Adi00] A. Adibi, R.K. Lee, Y. Xu, A. Yariv and A. Scherer , "Design of photonic crystal optical waveguides with singlemode propagation in the photonic bandgap", *Electron. Lett.*, vol. 36, pp. 1376-1378, 2000.

[Adi00a] A. Adibi, X. Yong, R. K. Lee, A. Yariv, A. Scherer, "Properties of the slab modes in photonic crystal optical waveguides", *IEEE J. Lightwave Technology*, vol. 18, pp. 1554-1564, 2000.

[Adi01] A. Adibi, Y. Xu, R.K. Lee, M. Loncar, A. Yariv and A. Scherer, "Role of distributed Bragg reflection in photonic-crystal optical waveguides", *Phy. Rev. B*, vol. 64, 041102I, 2001.

[Alm03] V.A. Almeida, R. Panepucci, and M. Lipson, "Nanotaper for compact mode conversion", *Optics Lett.*, vol. 28, pp. 1302-1304, 2003.

[Asa04] T. Asano, K. Kiyota, D. Kumamoto, B.S. Song, and S. Noda, "Time-domain measurement of picosecond light-pulse propagation in a two-dimensional photonic crystal-slab waveguide", *Appl. Phys. Lett.*, vol. 84, pp. 4690-4693, 2004.

[Ass04] S. Assefa P. T. Rakich, P. Bienstman, S. G. Johnson, G. S. Petrich, J. D. Joannopoulus, L. A. Kolodziejski, E. P. Ippen, and H. I. Smith, "Guiding 1.5 μm light in photonic crystals based dielectric rods", *Appl. Phys. Lett.*, vol. 85, pp. 6110-6112, 2004.

[Bab99] T. Baba, N. Fukaya, and J. Yonekura, "Observation of light propagation in photonic crystal optical waveguides with bends", *Electron. Lett.*, vol. 35, pp. 654-655, 1999.

[Bab01] T. Baba, and D. Ohsaki, "Interfaces of photonic crystals for high efficiency light transmission", *Jpn. J. Appl. Phys.*, vol. 40, pp. 5920-5924, 2001.

[Bar04] P.E. Barclay, K. Srinivasan, M. Borselli, O. Painter, "Efficient input and output fiber coupling to a photonic crystal waveguide", *Opt. Lett.*, vol. 27, pp. 697-6994, 2004.

[Bay00] M. Bayindir, B. Temelkuran, and E. Ozbay, "Propagation of photons by hopping: A waveguiding mechanism through localized coupled-cavities in three dimensional photonic crystals," *Phys. Rev. B*, vol. 61, R11 855, 2000.

[Bay00a] M. Bayindir, B. Temelkuran, and, "Tight-Binding Description of the Coupled Defect Modes in Three-Dimensional Photonic Crystals," *Phys. Rev. Lett.*, vol. 84, pp. 2140-2143, 2000.

[Ben00] H. Benisty, D. Labilloy, C. Weisbuch, C. Smith, T.F. Krauss, D. Cassagne, A. Beraud, C. Jouanin, "Radiation losses of waveguide-based two-dimensional photonic crystals: Positive role of the substrate", *Appl. Phys. Lett.*, vol. 76, pp. 532-534, 2000.

[Ber94] J. P. Berenger, "A Perfectly Matched Layer for the Absorption of Electromagnetic Waves", *J. Comput. Phys.*, vol. 114, pp. 185-200, 1994.

[Bie01] P. Bienstman, "Rigorous and efficient modeling of wavelength scale photonics components", Ph.D. dissertation, Ghent Univ.,Gent, Belgium, 2001.

[Bie03] P. Bienstman , S. Assefa, S.G. Johnson, J. D. Joannopoulos, G. S. Petrich and L. A. Kolodziejski, "Taper structures for coupling into photonic crystal slab waveguides", *J. Opt. Soc. Am. B*, vol. 20, pp. 1817-1821, 2003.

[Bis04] R. Biswas, Z.Y. Li, and K.M. Ho, "Impedance of photonic crystals and photonic crystal waveguides", *Appl. Phy. Lett.*, vol. 84, pp. 1254-1256, 2004.

[Bla00] A. Blanco, E. Chomski, S. Grabtchak, M. Ibisate, S. John, S. W. Leonard, C. Lopez, F. Meseguer, H. Miguez, J. P. Mondia, G. A. Ozin, O. Toader, and H. M. van Driel, "Large-scale synthesis of a silicon photonic crystal with a complete three-dimensional bandgap near 1.55 micrometres", *Nature*, vol. 405, pp. 437-440, 2000.

[Blo28] F. Bloch, "Über die quantenmechanik der electronen in kristallgittern", *Z. Physik*, vol. 52, pp. 555-600, 1928.

[Blu03] D. J. Blumenthal, J.E. Bowers, L. Rau, H.F. Chou, S. Rangarajan, W. Wang, amd H.N. Poulsen, "Optical signal processing for optical packet switching networks", *IEEE Optical Communications*, pp. 523-529, February 2003.

[Bog01] W. Bogaerts, P. Bienstman, D. Taillaert, R. Baets, D. De Zutter, "Out-of-plane scattering in photonic crystal slabs", *IEEE Photon. Technol. Lett.*, vol. 13, pp. 565-567, 2001.

[Bog02] W. Bogaerts, V. Wiaux, D. Taillaert, S. Beckx, B. Luyssaert, P. Bienstman, R. Baets, "Fabrication of photonic crystals in silicon-on-insulator using 248-nm deep UV lithography", *IEEE J. Sel. Top. Quantum Electron.*, vol. 8, pp. 928-934, 2002.

[Bog03] W. Bogaerts, V. Wiaux, P. Dumon, D. Taillaert, J. Wouters, S. Beckx, J. Van Campenhout, B. Luyssaert, D. Van Thourhout and R. Baets, "Large-scale production techniques for photonic nanostructures", *Proc. SPIE*, San Diego, United States, vol. 5225, pp. 101-112, 2003.

[Bog04] Wim Bogaerts, "Nanopotonic waveguides and photonic crystal in silicon-on-insulator", Ph.D. dissertation, Ghent Univ.,Gent, Belgium, 2004.

[Bor04] P. Borel, A. Harpoth, L. Frandsen, and M. Kristensen, "Topology optimization and fabrication of photonic crystal structures," *Opt. Exp.*, vol. 12, pp. 1996–2001, 2004.

[Bos02] S. Boscolo, M. Midrio, and T.F. Krauss, "Y-junctions in photonic crystal channel waveguides: high transmission and impedance matching", *Opt. Lett.*, vol. 27, pp. 1001-1003, 2002.

[Bos02a] S. Boscolo, M. Midrio, and C.G. Someda, "Coupling and decoupling of electromagnetic waves in parallel 2-D photonic crystal waveguides", *IEEE J. Lightwave Tech.*, vol. 38, pp. 47-53, 2002.

[Bos02c] S. Boscolo, C. Conti, M. Midirio and C.G. Someda, "Numerical analysis of propagation and impedance matching in 2-D photonic crystal waveguides with finite length", *IEEE J. Lightwave Technol.*, vol. 20, pp. 304-310, 2002.

[Bot01] L. C. Botten, N. A. Nicorovici, R. C. McPhedran, C. Martijn de Sterke, and A. A. Asatryan, "Photonic band structure calculations using scattering matrices", *Phys. Rev. E*, vol.64**,** 046603, 2001.

[Bot03] L.C. Botten, A. Asatryan, T. N. Langtry, T. P. White, C. Martijn de Sterke, and R. C. McPhedran, "Semianalytic treatment for propagation in photonic crystal waveguides", *Opt. Lett.*, vol. 28, pp. 854-859, 2003.

[Che95] C. Cheng, and A. Scherer, "Fabrication of photonic band-gap crystals", *J. Vac. Sci. Technol. B*, vol. 13, pp. 2696-2700, 1995.

[Che05] Chii-Chang Chen, Chih-Tu Chen, Wen-Kai Wang, Fan-Hsiu Huang, Cheng-Kuo Lin, Wei-Yi Chiu, Yi-Jen Chan, "Photonic crystal couplers formed by InAlGaAs nano-rods", Opt. Express, vol. 13, pp. 38-43 ,2005.

[Chu00] A. Chutinan, and S. Noda, "Waveguides and waveguide bens in two-dimensional photonic crystal slabs", *Phys. Rev. B*, vol. 62, pp. 4488-4492, 2000.

[Chu05] L.M. Chuand, H.K. Fu, and Y.F. Chen, "Fabrication and optical properties of two-dimensional photonic crystals of CdSe pillars", *Appl. Phys. Lett.*, vol. 86, pp. 061902, 2005.

[Cue04] F. Cuesta-Soto, A. Martínez, J. Garcia, F. Ramos, P. Sanchis, J. Blasco, J. Martí, "All-optical switching structure based on a photonic crystal directional coupler", *Optics Express*, vol. 12, pp. 161-167, 2004.

[Din03] M. Dinu, R.L. Willett, K. Baldwin, L.N. Pfeiffer and K.W. West, "Waveguide tapers and waveguide bends in AlGaAs-based two-dimensional photonic crystals", *Appl. Phys. Lett.*, vol. 83, pp. 4471-4473, 2003.

[Ele94] G. V. Eleftheriades, A. S. Omar, L. P. B. Katehi, G. M. Rebeiz, "Some important properties of waveguide junction generalized scattering matrices in the context of the mode matching technique", *IEEE Trans. Microwave Theor. Tech.*, vol. 42, pp. 1896-1903, 1994.

[Fan97] S. H. Fan, P. R. Villeneuve, J. D. Joannopoulos, and E. F. Schubert, "High extraction efficiency of spontaneous emission from slabs of photonic crystals", *Phys. Rew. Lett.*, vol. 78, pp. 3294-3297, 1997

[Fan98] S. Fan, P. R. Villeneuve, J. D. Joannopoulos, and H. A. Haus, "Channel drop tunneling through resonant states", *Phys. Rev. Lett.*, vol. 80, pp. 960-963, 1998.

[Fle99] J.G. Fleming, and S.Y. Lin, "Three-dimensional photonic crystal with a stop band from 1.35 to 1.95 μm", *Opt. Lett.*, vol. 24, pp. 49-51,1999.

[Flo83] G. Floquet, "Sur les équations différentielles linéaries à coefficients périodiques", *Ann. École Norm. Sup.*, vol. 12, pp. 47-88, 1883.

[For97] S. Foresi, P. R. Villeneuve, J. Ferrara, E. R. Thorn, G. Steinmeyer, S. Fan, J. D. Joannopoulos, L. C. Kimerling, H. I. Smith, and E. P. Ippen, "Measurement of photonic band gap waveguide microcavities", *Nature*, vol. 390, pp. 143, 1997.

[Fot03] S. Foteinopoulou, E. N. Economou, C. M. Soukoulis, "Refraction in media with a negative refractive index", *Phys. Rev. Lett.*, vol. 90, pp. 107402, 2003.

[Gol89] D. Goldberg, Genetic Algorithms in Search, Optimization and Learning, Addison Wesley, Reading, MA, 1989.

[Grü95] U. Grüning, V. Lehmann, and C. M. Engelhardt, "Two-dimensional infrared photonic band gap structure based on porous silicon", *Appl. Phys. Lett.*, vol. 66, pp. 3254-3256, 1995.

[Hak04] A. Håkansson, J. Sánchez-Dehesa, and L. Sanchis**, "**Acoustic lens design by genetic algorithms", *Phys. Rev. B*, vol. 70, pp. 214302, 2004.

[Hak05] A. Håkansson, F. Cervera, and J. Sánchez-Dehesa, "Sound focusing by flat acoustic lens without negative refraction", to be published in *Appl. Phys. Lett.*, 2005.

[Hak05a] A. Håkanson, José Sánchez-Dehesa, and L. Sanchis "Inversed design of photonic crystal devices", to be published *IEEE J. Sel. Areas in Commun*, 2005.

[Hap01] T.D. Happ, M. Kamp and A. Forchel, "Photonic crystal tapers for ultracompact mode conversion", *Opt. Lett.*, vol. 26**,** pp. 1102-1104, 2001.

[Hau84] H. A. Haus, Waves and Fields in Optoelectronics, Prentice-Hall, Englewood Cliffs, 1984.

[Ho90] K.M. Ho, C.T. Chan and C.M. Soukoulis, "Existence of photonic gaps in periodic dielectric structures", *Phys. Rev. Lett.*, vol. 65 pp. 3152, 1990.

[Holl75] J. Holland, Adaptation in natural and Artificial Systems, The University of Michigan Press, Ann Arbor, 1975.

[Hos02] K. Hosomi, and T. Katsuyama, "A dispersion compensator using coupled defects in a photonic crystal", *IEEE J. Quantum Electron.*, vol. 38, 825, 2002.

[Imh99] A. Imhof, W.L. Vos, R. Sprik R, and Ad. Lagendijk, "Large dispersive effects near the band edges of photonic crystals", *Phys. Rev. Lett.*, vol. 83, pp. 2942-2945, 1999.

[Jia03] J. Jiang, J. Cai, G.P. Nordin and L. Li, "Parallel microgenetic algorithm design for photonic crystal and waveguide structures", *Opt. Lett.*, vol. 28, pp. 2381-2383, 2003.

[Joa95] J. D. Joannopoulos, R. D. Meade, N. J. Winn, Photonic Crystals: Molding the flow of light, Princeton, 1995.

[Joa97] J. D. Joannopoulos, P. R. Villeneuve, S. Fan, "Photonic crystals: putting a new twist on light", *Nature*, vol. 386, pp. 143-149, 1997.

[Joh87] S. John, "Strong localization of photons in certain disordered dielectric superlattices", *Phys. Rev. Lett.*, vol. 58, pp. 2486-2489, 1987.

[Joh99] S. G. Johnson, S. Fan, P. R. Villeneuve, J. D. Joannopoulos, "Guided modes in photonic crystal slabs", *Phys. Rev. B*, vol. 60, no. 8, pp. 5751-5758, 1999.

[Joh00] S. G. Johnson and J. D. Joannopoulos, "Three-dimensionally periodic dielectric layered structure with omnidirectional photonic band gap", *Appl. Phys. Lett.*, vol. 77, pp. 3490-3492, 2000.

[Joh00a] S.G. Johnson, S. Fan, P.R. Villeneuve and J.D. Joannopoulus, "Linear waveguides in photonic crystal slabs", *Physical Review B*, vol. 62, pp. 8212-8222, 2000.

[Joh01] S. G. Johnson and J. D. Joannopoulos, "Block-iterative frequency-domain methods for Maxwel's equations in a planewave basis", Opt. *Express*, vol. 8, pp. 173-190, 2001.

[Joh02] S. G. Johnson, P. Bienstman, M. A. Skrorobogatiy, M. Ibanescu, E. Lidorikis, and J. D. Joannopoulus, "Adiabatic theorem and continuous coupled-mode theory for efficient taper transitions in photonic crystals," *Phys. Rev. E*, vol. 66, 066608, 2002.

[Kan97] M. Kanskar, P. Paddon, V. Pacradouni, R. Morin, A. Busch, J. F. Young, S. R. Johnson, J. MacKenzie, T. Tiedje, "Observation of leaky slab modes in an air-bridged semiconductor waveguide with a two-dimensional photonic lattice", *Appl. Phys. Lett.*, vol. 70, pp. 1438-1440, 1997.

[Kar02] T.J. Karle, D.H. Brown, R. Wilson, M. Steer, and T.F. Krauss, "Planar photonic crystal coupled cavity waveguides", *IEEE J. Sel. Top. Quant. Electron.*, vol. 8, pp 909-918, 2002.

[Kar04] T.J. Karle, Y.J. Chai, C.N. Morgan, I.H. White, and T.F. Krauss, "Observation of pulse compression in photonic crystal coupled cavity waveguides", *IEEE J. Lightwave Technol.*, vol. 22, pp. 514-519, 2004.

[Kaw01] N. Kawai, K. Inoue, N. Carlsson, N. Ikeda, Y. Sugimoto, K. Asakawa, T. Takemori, "Confined Band Gap in an Air-Bridge Type of Two-Dimensional AlGaAs Photonic Crystal", *Phys. Rev. Lett.*, vol. 86, pp. 2289-2292, 2001.

[Kos99] H.Kosaka, T. Kawashima, A. Tomita, M. Notomi, T. Tamamura, T. Sato and S. Kawakami, "Superprism phenomena in photonic crystals: toward microscale lightwave circuits", *IEEE J. Lightwave Techn. Rev.*, vol. 17, pp. 2032-2038, 1999.

[Kos00] H. Kosaka, T. Kawashima, A. Tomita, T. Sato, S. Kawakami, "Photonic-crystal spot-size converter", *Appl. Phys. Lett.*, vol. 76, pp. 268-270 , 2000.

[Kos01] M. Koshiba, "Wavelength division multiplexing and demultiplexing with photonic crystal waveguide couplers", *IEEE J. Lightwave Technol.*, vol. 19, pp. 1970-1975, 2001.

[Kra96] T. F. Krauss, R. M. de la Rue, S. Brand, "Two-dimensional photonic-bandgap structures operating at near-infrared wavelengths", *Nature*, vol. 382, pp. 699-702, 1996.

[Kra99] T.F. Krauss, and R. M. de La Rue, "Photonic crystals in the optical regime – past, present and future", *Progress in Quantum Electron.*, vol. 23, pp. 51-96, 1999.

[Kua02] W. Kuang, C. Kim, A. Stapleton and J.D.'O'Brien, "Grating-assisted coupling of optical fibers and photonic crystal waveguides", *Opt. Lett.*, vol. 27, pp. 1604-1606, 2002.

[Lal02] Ph. Lalanne and A. Talneau, "Modal conversion with artificial materials for photonic-crystal waveguides," *Opt. Express*, vol. 10, pp. 354, 2002.

[Lan01] S. Lan, S. Nishikawa, H. Ishikawa, and O. Wada, "Design of impurity band-based photonic crystal waveguides and delay lines for ultrashort optical pulses", *J. Appl. Phys.*, vol. 90, pp. 4321-4327, 2001.

[Lan02] S. Lan and H. Ishikawa, "Coupling of defect pairs and generation of dynamical band gaps in the impurity bands of nonlinear photonic crystals for all-optical switching", *J. Appl. Phys.*, vol. 91, pp. 2573-2577, 2002.

[Lan04] Ph. Lalanne, J.P. Hugonin, "Bloch-wave engineering for high Q´s, small V´s microcavitites", *IEEE J. Quantum. Electron.*, vol. 18, pp.1554-1564, 2000.

[Lau02] W.T. Lau and S. Fan. "Creating large bandwidth line defects by embedding dielectric waveguides into photonic crystal slabs", *App. Phys. Lett.*, vol. 81, pp. 3915-3917, 2002

[Leu90] K. M. Leung and Y. F. Liu, "Photonic band structures: the plane wave method", *Phys. Rev. B*, vol. 41, pp. 10188-10190, 1990.

[Leu90a] K. M. Leung and Y. F. Liu, "Full vector wave calculation of photonic band structure in face-centered-cubic dielectric media", *Phys. Rev. Lett.*, vol. 65, pp. 2646-2649, 1990.

[Lid98] E. Lidorikis, M. M. Sigalas, E. N. Economou, and C. M. Soukoulis, "Tight-binding parametrization for photonic band gap materials," *Phys. Rev. Lett.*, vol. 81, pp. 1405–1408, 1998.

[Lin96] H. B. Lin, R. J. Tonucci, and A. J. Campillo, "Observation of two-dimensional photonic band behavior in the visible", *Appl. Phys. Lett.*, vol. 68, pp. 2927-2929, 1996.

[Lin98] S. Y. Lin, J. G. Fleming, D. L. Hetherington, B. K. Smith, R. Biswas, K. M. Ho, M. M. Sigalas, W. Zubrzycki, S. R. Kurtz and J. Bur, "A three-dimensional photonic crystal operating at infrared wavelengths", *Nature*, vol. 394, pp. 251-253, 1998.

[Lin02] S. Y. Lin, E. Chow, J. Bur, S.G. Johnson, and J.D. Joannopoulos, "Low-loss, wide-angle Y splitter at similar to 1.6-μm wavelengths built with a two-dimensional photonic crystal", *Opt. Lett.*, vol. 27, pp. 1400-1403, 2002.

[Liu04] A. Liu, R. Jones, L. Liao, D. Samara-Rubio, D. Rubin, O. Cohen, R. Nicolaescu, and M. Paniccia, "A high-speed silicon optical modulator based on a metal-oxide-semiconductor capacitor", *Nature*, vol. 427, pp. 615, 2004.

[Lon00] M. Lonçar, D. Nedeljkoviç, T. Doll, J. Vuçkoviç, A. Scherer, T. P. Pearsall, "Waveguiding in planar photonic crystals", *Appl. Phys. Lett.*, vol. 77, pp.1937-1939, 2000.

[Man99] C. Manolatou, S.G. Johnson, S. Fan, P. R. Villeneuve, H. A. Haus and J. D. Joannopoulos, "High-density integrated optics", *IEEE J. Lightwave Technol.*, vol. 17, pp. 1682-1692, 1999.

[Mar97] J. Martorell, R. Vilaseca, and R. Corbalan, "Second harmonic generation in a photonic crystal", *Appl. Phys. Lett.*, vol. 70, pp. 702-704, 1997.

[Mar99] Mark A. McCord, Introduction to Electron-Beam Lithography, Short Course Notes Microlithography, SPIE's International Symposium on Microlithography 14-19, March 1999.

[Mar03] A. Martínez, A. Griol, P. Sanchis, and J. Martí, "Mach-Zehnder interferometer employing coupled-resonator optical waveguides", *Opt. Lett.*, vol. 28, pp. 405-407, 2003.

[Mar03a] A. Martinez, J. Garcia G. Sanchez,, and J. Marti, "Planar photonic crystal structures with inherently single-mode waveguides", *J. Opt. Soc. Am. A*, vol. 20, pp. 2131-2136, 2003.

[Mar04] A. Martínez, H. Míguez , A. Griol, and J. Martí, "Experimental and theoretical analysis of the self-focusing of light by a photonic crystal lens", *Phys, Rev, B*, vol. 69, pp. 165119, 2004.

[Mcn03] S. J. McNab, N. Moll, and Y. A. Vlasov, "Ultra-low loss photonic integrated circuit with membrane-type photonic crystal waveguides", *Opt. Express*, vol. 11, pp. 2927-2939, 2003.

[Mek96] A. Mekis, J. C. Chen, I. Kurland, P. R. Villeneuve, and J. D. Joannopoulos "High transmission through sharp bends in photonic crystal waveguides", *Phys. Rev. Lett.*, vol. 77, pp. 3787-3791, 1996.

[Mek01] A. Mekis and J. D. Joannopoulos, "Tapered couplers for efficient interfacing between dielectric and photonic crystal waveguides", *IEEE J. Lightwave Technol.*, vol. 19, pp. 861-865, 2001.

[Mig97] H. Míguez, C. López, F. Meseguer, A. Blanco, L. Vázquez, R. Mayoral, M. Ocaña, V. Fornés and A. Mifsud, "Photonic crystal properties of packed submicrometric SiO_2 spheres", *Appl. Phys. Lett.*, vol. 71, pp. 1148-1150, 1997.

[Miy02] E. Miyai, M. Okano, M. Mochizuki, S. Noda, "Analysis of coupling between two-dimensional photonic crystal waveguide and external waveguide", *Appl. Phys. Lett.*, vol. 81, pp. 3729-3731, 2002.

[Moe97] M. Moerman, P. Van Daele, and P.M. emeester, "A review on fabrication technologies for the monolithic integration of tapers with III-V semiconductor devices", *IEEE J. Sel. Top. Quantum Electron.*, vol. 3, pp. 1308-1320, 1997.

[Mol03] N. Moll, G. L. Bona, "Comparison of three-dimensional photonic crystal slab waveguides with two-dimensional photonic crystal waveguides: Efficient butt coupling into these photonic crystal waveguides", *J. Appl. Phys.*, vol. 93, pp. 4986-4991, 2003.

[Moo02] S. Mookherjea and A. Yariv, "Coupled resonator optical waveguides", *IEEE J. Sel. Top. Quantum Electron.*, vol. 8, pp. 448-456, 2002.

[Moo02a] S. Mookherjea, and A. Yariv, "Pulse propagation in a coupled resonator optical waveguide to all orders of dispersion", *Phys. Rev. E*, vol. 65, pp. 056601 Part 2, 2002.

[Mur88] E. J. Murphy, "Fiber attachment for guided devices", *IEEE J. Light. Tech.*, vol. 6, pp.862-871, 1988.

[Nod00] S. Noda, K. Tomoda, N. Yamamoto, and A. Chutinan, "Full three-dimensional photonic bandgap crystals at near-infrared wavelengths", *Science*, vol. 289, pp. 604-606, 2000.

[Nod00a] S. Noda, A. Chutinan, and M. Imada, "Trapping and emission of photons by a single defect in a photonic band gap structure", *Nature*, vol. 407, pp. 608-610, 2000.

[Not00] M. Notomi, "Theory of light propagation in strongly modulated photonic crystals: Refraction like behaviour in the vicinity of the photonic band gap", *Phys. Rev. B*, vol. 62, pp. 10696–10705, 2000.

[Not01] M. Notomi, A. Shinya, K. Yamada J. Takahashi, C. Takahashi and I. Yokohama, "Singlemode transmission within photonic bandgap of width-varied single-line-defect photonic crystal waveguides on SOI substrates", *Electron. Lett.*, vol. 37, pp. 293-295, 2001.

[Och02] T. Ochiai and J. Sánchez-Dehesa, "Localized defect modes in finite metallic two-dimensional photonic crystals", *Phys. Rev. B*, vol. 65, pp. 245111, 2002.

[Oht79] K. Ohtaka, "Energy band of photons and low-energy photon diffraction", *Phys. Rev. B*, vol. 19, pp. 5079, 1979.

[Oli01] S. Olivier, C. Smith, M. Rattier, H. Benisty, C. Weisbuch, T. Krauss, R. Houdré and U. Oesterlé, "Miniband transmission in a photonic crystal coupled-resonator optical waveguide", *Opt. Lett.*, vol. 26, pp. 1019-1021, 2001.

[Ozb02] E. Ozbay, M. Bayindir, I. Bulu, and E. Cubukcu, "Investigation of localized coupled-cavity modes in two-dimensional photonic bandgap structures", *IEEE J. of Quantu Electron.*, vol. 38, pp.837-842, 2002.

[Pai99] O. Painter, R. K. Lee, A. Scherer, A. Yariv, J. D. O'Brien, P. D. Dapkus, I. Kim, "Two-dimensional photonic bad-gap defect mode laser", *Science*, vol. 284, pp. 1819-1821, 1999.

[Pal01] M. Palamaru, and P. Lalanne, "Photonic crystal waveguides: Out-of plane losses and adiabatic modal conversion", *Appl. Phys. Lett.*, vol. 78, pp. 1466-1468, 2001.

[Pat02] M. Patrini, M. Galli, F. Marabelli, M. Agio, L. C. Andreani, D. Peyrade, and Yong Chen, "Photonic Bands in Patterned Silicon-on-Insulator Waveguides", *IEEE Journal of Quantum Electron.*, vol. 38, pp. 885-890, 2002.

[Pen00] J. B. Pendry, "Negative Refraction Makes a Perfect Lens", *Phys. Rev. Lett.*, vol. 18, pp. 3966-3969, 2000.

[Pot02] M.E. Potter and R.W. Ziolkowski, "Two compact structures for perpendicular coupling of optical signals between dielectric and photonic crystal waveguides," *Opt. Express*, vol. 10, pp. 691-698, 2002.

[Pot03] P. Pottier, I. Ntakis, R.M. De La Rue, "Photonic crystal continuous taper for low-loss direct coupling into 2D photonic crystal channel waveguides and further device functionality", *Optics Communications*, 223, pp. 339-347, 2003.

[Pra02] D.W. Prather, J. Murakowski, S. Shi, S. Venkataram, A. Sharkawy, C. Chen and D. Pustai, "High-efficiency coupling structure for a single-line-defect photonic-crystal waveguide", *Opt. Lett.*, vol. 27, pp.1601-1603, 2002.

[Qiu01] M. Qiu, K. Azizi, A. Karlsson, M. Swillo, B. Jaskorzynska, "Numerical studies of mode gaps and coupling efficiency for line-defect waveguides in two-dimensional photonic crystals", *Phys. Rev. E*, vol. 64, 155113, 2001.

[Qiu02] M. Qiu, "Band gap effects in asymmetric photonic crystal slabs", *Phys, Rev. B*, vol. 66, pp. 033103, 2002.

[Qiu02a] M. Qiu, "Effective index method for heterostructure-slab-waveguide-based two-dimensional photonic crystals", *Appl. Phys. Lett.*, vol. 81, pp. 1163-1165, 2002.

[Rip99] D.J. Ripin, Lim Kuo-Yi, G.S. Petrich, P.R. Villeneuve, Fan Shanhui, E.R. Thoen, J.D. Joannopoulos, E.P. Ippen and L.A. Kolodziejski, "One-dimensional photonic bandgap microcavities for strong optical confinement in GaAs and GaAs/Al_xO_y semiconductor waveguides", *IEEE J. Lightwave Tech*., vol. 17, pp. 2152-2160, 1999.

[Ryu02] H. Y. Ryu, J. K. Hwang, Y. J. Lee, and Y. H. Lee, "Enhancement of light extraction from two-dimensional photonic crystal slab structures", *IEEE J. Sel. Top. Quant. Electron.*, vol. 8, pp. 231-237, 2002.

[Sak99] K. Sakoda, K. Ohtaka, and T. Ueta, "Low-threshold laser oscillation due to group-velocity anomaly peculiar to two- and three-dimensional photonic crystals", *Opt. Express*, vol. 4, pp. 481-489, 1999.

[San02] P. Sanchis, J. Martí, A. García, A. Martínez and J. Blasco, "High efficiency coupling technique for planar photonic crystal waveguides", *Electron. Lett.*, vol. 38, pp. 961-962, 2002.

[San03] P. Sanchis, J. Martí, J. Blasco, A. Martínez and A. García, "Mode matching technique for highly efficient coupling between dielectric waveguides and planar PhC circuits", *Opt. Express*, vol. 10, pp. 1391-1397, 2002.

[San04] L. Sanchis, A. Håkanson, D. López-Zanón, J. Bravo-Abad, and José Sánchez-Dehesa, "Integrated optical devices design by genetic algorithm", *Appl. Phys. Lett.*, vol. 84, pp. 4460-4462, 2004.

[Sat90] S. Satpathy, Z. Zhang, and M. R. Salehpour, "Theory of photon bands in three-dimensional periodic dielectric structures", *Phys. Rev. Lett.*, vol. 64, pp. 1239-1242, 1990.

[Sca96] M. Scalora, R.J. Flynn, S.B. Reinhardt, R.L. Fork, M.J. Bloemer, M.D. Tocci, C.M. Bowden, H.S. Ledbetter, J.M. Bendickson, J.P. Dowling and R.P. Leavitt, "Ultrashort pulse propagation at the photonic band edge: Large tunable group delay with minimal distortion and loss", *Phys. Rev. E*, vol. 54, pp. R1078, 1996.

[She03] L. Shen, Z. Ye, and S. He, "Design of two-dimensional photonic crystals with large absolute band gaps using a genetic algorithm", *Phys. Rev. B*, vol. 68, no. 035109, 2003.

[Sho02] T. Shoji, T. Tsuchizawa, T. Watanabe, K. Yamada,and H. Morita, "Low loss mode size converter from 0.3-μm square Si wire waveguides to singlemode fibres", *Electron. Lett.*, vol. 38, pp. 1669-167, 2002.

[Ste98] N. Stefanou and A. Modinos, "Impurity bands in photonics insulators", *Phys. Rev. B*, 57, pp. 12127-12133, 1998.

[Sto00] R. Stoffer, H. Hoekstra, R. M. De Ridder, E. V. Groesen, and F. P. H. Van Beckum, "Numerical studies of 2D photonic crystals: Waveguides, coupling between waveguides and filters", *Opt. Quantum. Electron.*, vol. 32, pp. 947-961, 2000.

[Sug02] Y. Sugimoto , N. Ikeda, N. Carlsson, K. Asakawa, N. Kawai, and K. Inoue, Light-propagation characteristics of Y-branch defect waveguides in AlGaAs-based air-bridge-type two-dimensional photonic crystal slabs, *Opt. Lett.*, 27: 388-390, 2002.

[Sum03] M. Sumetsky, and B.J. Eggleton, "Modeling and optimization of complex photonic resonant cavity circuits", *Opt. Express*, 11, pp 381-391, 2003.

[Taf95] A. Taflove, Computational Electrodynamics: The Finite-Difference Time-Domain Method, Norwood, MA: Artech House 1995.

[Tai02] D. Taillaert, W. Bogaerts, P. Bienstman, T. F. Krauss, P. Van Daele, I. Moerman, S. Verstuyft, K. De Mesel and R. Baets, "An out-of-plane grating coupler for efficient butt-coupling between compact planar waveguides and single-mode fibers," *IEEE Journal of Quantum Electronics*, vol. 38, pp. 949-955, 2002.

[Tal02] A. Talneau, Ph. Lalanne, M. Agio, and C.M. Soukoulis, "Low-reflection photonic-crystal taper for efficient coupling between guide sections of arbitrary widths," *Opt. Lett.*, 27, pp. 1522-1524, 2002.

[Tal03] A. Talneau, M. Mulot, S. Anand, Ph. Lalanne, "Compound cavity measurements of transmission and reflection of a tapered single-line photonic crystal waveguide", *Appl. Phys. Lett.*, vol. 82, pp. 2577-2579, 2003.

[Tal04] A. Talneau, M. Agio, C. M. Soukoulis, M. Mulot, S.Anand, and Ph. Lalanne, "High-bandwidth transmission of an efficient photonic-crystal mode converter", Opt. Lett., vol. 29, pp. 1745-1747, 2004.

[Tan02] T. Tanaka, S. Noda, A. Chutinan, T. Asano and N. Yamamoto, "Ultra-short pulse propagation in 3D GaAs photonic crystals", *Opt. Quantum Electron.*, vol. 34, pp. 37-43, 2002.

[Tan04] Y. Tanaka, Y. Sugimoto, N. Ikeda, H. Nakamura, K. Asakawa, K. Inoue and S.G. Johnson, "Group velocity dependence of propagation losses in single-line-defect photonic crystal waveguides on GaAs membranes", Electron. Lett., vol. 40, pp. 174-176, 2004.

[Tok04] M. Tokushima, H. Yamada, and Y. Arakawa, "1.5-μm-wavelength light guiding in waveguides in square-lattice-of-rod photonic crystal slab", *Appl. Phys. Lett.*, vol. 84, pp. 4298-4301, 2004.

[Ush03] J. Ushida, M. Tokushima, M. Shirane, A. Gomyo, and H. Yamada, "Immittance matching for multidimensional open-system photonic crystal", *Phys. Rev. B*, vol. 68, 155115, 2003.

[Vil92] P. R. Villeneuve, M. Piché, "Photonic band gaps in two-dimensional square and hexagonal lattices", *Phys. Rev. B*, vol. 46, pp. 4969-4972, 1992.

[Vla01] Yu. A. Vlasov, X. Z. Bo, J. C. Sturm, and D. J. Norris, "On-chip natural assembly of silicon photonic band gap crystals", *Nature*, 414, pp. 289-293, 2001.

[Wu02] L.J. Wu M. Mazilu, T. Karle, and T.F. Krauss, "Superprism phenomena in planar photonic crystals", *IEEE J. Quant. Electron.*, vol. 38, pp. 915-918, 2002.

[Xu00] Y. Xu, R. K. Lee, A. Yariv, "Propagation and second-harmonic generation of electromagnetic waves in a coupled-resonator optical waveguide", *J. Opt. Soc. Amer. B*, vol. 17, pp. 387-400, 2000.

[Xu00] Y. Xu, R. Lee, and A. Yariv, "Adiabatic coupling between conventional dielectric waveguides and waveguides with discrete translational symmetry", *Opt. Lett.*, vol. 25, pp. 755-757, 2000.

[Yab87] E. Yablonovitch, "Inhibited spontaneous emission in solid-state physics and electronics", *Phys. Rev. Lett.*, vol. 58, pp. 2059-2062, 1987.

[Yab89] E. Yablonovitch and T. J. Gmitter, "Photonic band structure: The face-centered-cubic case", *Phys. Rev. Lett.*, vol. 63, pp.1950–1953, 1989.

[Yab91] E. Yablonovitch, T. J. Gmitter, and K. Leung, "Photonic band structure: The face-centered-cubic case employing nonspherical atoms", *Phys. Rev. Lett.*, vol. 67, pp.2295-2298, 1991.

[Yam02] K. Yamada, M. Notomi, A. Shinya, C. Takahashi, J. Takahashi, H. Morita, "Singlemode lightwave transmission in SOI-type photonic crystal line-defect waveguides with with phase-shifted holes", *Electron. Lett.*, vol. 38, pp. 74-75, 2002.

[Yam03] S. Yamada, Y. Watanabe, Y. Katayama, and J.B. Cole, "Simulation of optical pulse propagation in a two-dimensional photonic crystal waveguide using a high accuracy finite-difference time-domain algorithm", *J. Appl. Phys.*, 93, pp. 1859-1864, 2003.

[Yan03] T. Yang, Y. Sugimoto, S. Lan, N. Ikeda, Y. Tanaka, and K. Asakawa, "Transmission properties of coupled-cavity waveguides based on two-dimensional photonic crystals wit a triangular lattice of air holes", *J. Opt. Soc. Am. B*, vol. 20, pp. 1922-1926, 2003.

[Yar99] A. Yariv, Y. Xu, R. K. Lee, and A. Scherer, "Coupled resonator optical waveguides: A proposal and analysis," *Opt. Lett.*, vol. 24, pp.711-713, 1999.

[Ye04] Y.H. Ye, J. Ding, D.Y. Jeong, I.C. Khoo, and Q.M. Zhang, "Finite-size effect on one-dimensional coupled resonator optical waveguides", *Phys. Rev. E*, vol. 69, pp. 056604, 2004.

[Yeh98] P. Yeh and A. Yariv, Optical wave is layered media, J. Wiley, NY, 1988.

[Zak88] K. A. Zaki, S. Chen, C. Chen, "Modeling discontinuities in dielectric-loaded waveguides", *IEEE Trans. Microwave Theor. Tech.*, vol. 36, pp. 1804-1810, 1988.

[Zha90] Z. Zhang, S. Satpathy, "Electromagnetic wave propagation in periodic structures: Bloch wave solution of Maxwell's equations", *Phys. Rev. Lett.*, vol. 65, pp. 2650-2653, 1990.